



UNIVERSIDAD DE CHILE  
FACULTAD DE CIENCIAS FÍSICAS Y MATEMÁTICAS  
DEPARTAMENTO DE GEOLOGÍA

A TALE OF A LAVA FROM ITS SHALLOW ZONED RESERVOIR  
TO SURFACE: THE CASE OF AZUFRE VOLCANO IN THE  
CONTEXT OF THE ALTIPLANO PUNA MAGMA BODY  
(NORTHERN CHILE)

TESIS PARA OPTAR AL GRADO DE DOCTOR EN CIENCIAS,  
MENCIÓN GEOLOGÍA

DARÍO SALVADOR HÜBNER GONZÁLEZ

**PROFESOR GUÍA:**

MIGUEL ÁNGEL PARADA REYES

**PROFESOR CO-GUÍA:**

EDUARDO MORGADO BRAVO

**MIEMBROS DE LA COMISIÓN:**

PHILIPPE ROBIDOUX

ÁNGELO CASTRUCCIO ÁLVAREZ

SANTIAGO DE CHILE

2024

**Resumen de la tesis para optar al grado de:** Doctor en Ciencias, mención Geología  
**Por:** Darío Salvador Hübner González  
**Fecha:** 2024  
**Profesor guía:** Miguel Ángel Parada Reyes

## EL CUENTO DE UNA LAVA DESDE SU RESERVORIO ZONADO SOMERO HASTA LA SUPERFICIE: EL CASO DEL VOLCÁN AZUFRE EN EL CONTEXTO DEL ALTIPLANO PUNA MAGMA BODY (NORTE DE CHILE)

El volcán Azufre (21°47'S; 68°14'O) se encuentra emplazado sobre un alineamiento volcánico NO-SE de 70 km de largo por sobre el margen occidental del *Aльтиplano Puna Magma Body (APMB)*, el cual es el cuerpo magmático activo más grande del planeta Tierra (~500.000 km<sup>3</sup>). El depósito de lava más joven del volcán Azufre fue seleccionado para su estudio debido a la relevante información petrológica que puede entregar su reservorio como una potencial fuente de calor del adyacente sistema geotermal Cerro Pabellón. La lava corresponde a una andesita-dacita (61 – 63 SiO<sub>2</sub> wt%) con una edad estimada de 50 – 331 ka compuesta por fenocristales de plagioclasa, anfíbol (Grupo 1), biotita y ortopiroxeno (15, 4, 4, 2 vol%, respectivamente); marginalmente por fenocristales de clinopiroxeno, cuarzo, olivino y óxidos de Fe-Ti (~1 vol% cada uno). El depósito también contiene enclaves afaníticos de andesita (58 – 60 SiO<sub>2</sub> wt%), cuya masa fundamental posee la misma mineralogía y química mineral que la masa fundamental de la lava, siendo ambas constituidas por microfenocristales de anfíbol (Grupo 2) y microlitos de plagioclasa, piroxeno y óxidos de Fe-Ti. Abundantes texturas de desequilibrio fueron identificadas en las muestras estudiadas, tales como disolución de fenocristales de plagioclasa y cuarzo, descomposición en cristales de anfíbol y biotita, zonación inversa en fenocristales de piroxeno y plagioclasa entre otras.

Variables intensivas (P, T,  $fO_2$ ) fueron determinadas a partir de condiciones de equilibrio por diferentes geobarómetros, geotermómetros y oxibarómetros. Presiones de en torno a los 2 kbar (1 – 3,3 kbar) fueron estimadas a partir de anfíboles y pares de anfíbol-plagioclasa (Grupo 1), mientras que un amplio rango de temperatura entre 712 – 1097 °C fue obtenido a partir de diferentes fases minerales. Las temperaturas más altas (916 – 1097 °C) corresponden a fenocristales de piroxeno ricos en Mg y cristales de plagioclasa ricas en Ca (An<sub>≥66</sub>), mientras que las menores (712 – 827 °C) corresponden a los pares de anfíbol-plagioclasa (Grupo 1). La composición de los anfíboles del Grupo 1 y su cristalización a temperaturas cercanas al *solidus* indican una saturación desde un líquido evolucionado (63 – 79 wt% of SiO<sub>2</sub>). Condiciones de oxidación en el rango de QFM+ 0.9 – 2.5 unidades logarítmicas fueron registradas en anfíbol (Grupo 1), microlitos de óxidos de Fe-Ti y enclaves. Adicionalmente, modelamientos de Rhyolite-MELTS reproducen la composición de la mineralogía de alta temperatura a similares condiciones de P-T- $fO_2$  para una cristalización en equilibrio con un fundido inicial de la misma composición que un enclave andesítico representativo. Las texturas de desequilibrio observadas podrían desarrollarse después de la intrusión de un nuevo magma (más caliente) con una composición similar a la de los enclaves dentro de un reservorio félsico somero tipo *crystal-mush* cuya temperatura es cercana al *solidus*. En este escenario, la variación de temperatura podría corresponder a un reservorio zonado con temperaturas decrecientes hacia sus paredes y techo. Finalmente, como resultado de los procesos combinados de *magma mixing* y aumento de temperatura, se desencadenó la última erupción del volcán Azufre, registrando en sus microlitos de óxidos de Fe-Ti temperaturas de enfriamiento (742 – 866 °C) para el emplazamiento del flujo de lava a condiciones subáreas. La lava estudiada tendría su origen en una cámara magmática con un volumen máximo de 106 km<sup>3</sup>.


*A PAOLA, PAMELA, JUAN;  
AMIGOS, AMIGAS;  
PROFESORES Y PROFESORAS  
DE TODA LA VIDA.*

## AGRADECIMIENTOS

Especial agradecimiento a todos los lugares e instituciones que me vieron pasar por sus salas, talleres, gimnasios, canchas y piscinas. La gente que conocí en dichos espacios ha aportado en mi formación humana y profesional, forjando mi carácter y espíritu, mis emociones, mi visión de la vida y mis sueños. Especiales recuerdos me dejan el Kumon, los scouts, los equipos de fútbol y natación, así como también los colegios República de Siria, Salvador San Fuentes y el Glorioso Instituto Nacional. El Plan Común y el Departamento de Geología de la Facultad de Ciencias Físicas y Matemáticas de la Universidad de Chile dejan también vivencias imborrables, muchas de las cuales tuve el gusto de compartir con mis amigos del Instituto que también entraron a este “manicomio” llamado Beauchef, y a los cuales, también se sumaron nuevos amigos y amigas que forjé en la facultad. Imposible olvidar los míticos terraceos, fiestas y terrenos de geología.

Especiales agradecimientos también a los Profesores Miguel Ángel Parada, Luis Aguirre y Reynaldo Charrier, quienes fueron los artífices en el despertar de mi pasión por las rocas y sus misterios. La cátedra de Fundamentos de Petrología del Profesor Miguel Ángel fue el primer gran desafío académico que enfrenté en la Universidad y del cual casi no salgo vivo. Con el Profesor Aguirre tuve la oportunidad de profundizar aún más mis conocimientos de petrología, y en especial con los tópicos relacionados al metamorfismo de bajo grado. Posteriormente la cátedra de Geología de Chile del Profesor Charrier, fue la instancia que unificó todos los conocimientos adquiridos durante la carrera, madurando de manera superlativa mi entendimiento de la geología. En este selecto grupo no puedo dejar de incluir a mi Profesor Co-Guía Eduardo y a Fran Mallea, quienes a pesar de los difíciles momentos que vivimos como sociedad durante octubre del 2019 y en la pandemia del COVID-19, me acompañaron con mucha amistad durante este largo camino de 4 años. Nuevamente agradecer a mi Profesor Guía por darme la oportunidad de trabajar y aprender de él, por brindarme el espacio para desarrollar ideas propias, por su continuo apoyo y consejos durante este proceso, y sobre todo por las excelentes clases que me brindó en los ramos de Fundamentos de Petrología, Petrología Ígnea y Metamórfica e Introducción al Trabajo de Título.

Quiero expresar también mi agradecimiento y cariño a quienes me acompañaron en el trabajo de terreno: Lorena Olivares, Rodrigo Espinoza y Vicente Méndez, quienes

permitieron que fuera posible extraer las mejores muestras del volcán Azufre  a pesar de las dos ruedas pinchadas. Muchos cariños también para Fran Aguilera por su compañía y buena onda en todos los terrenos que tuvimos juntos (creo que fueron al menos 5). Especiales cariños a mis amigos y colegas Lucas Navarro, Claudia Magerkurth, Rodolfo Cuevas, Sebastián Menares, Cristian Bastías, Gabriel Fernández, Franco “Matías” Robbiano “Barrobiano”, Nico “Roto” Cadiz y Sebastián Plaza.

Tampoco puedo dejar de agradecer a las distintas personas que hacen posible el trabajo del Departamento de Geología, a las secretarias Blanca, Maritza, Bernardette y Karin, a Julio por su trabajo en el taller de cortes, a Cristian Nieves por su ayuda en el SEM, a Don Luis por su ayuda técnica con los PC del Departamento y a William por mantener las cuentas claras.

Finalmente, quiero expresar todo mi amor y gratitud a mi familia, a mi mamá Paola, a mi tía Pamela y a mi tío Juan.

# TABLA DE CONTENIDO

TABLA DE CONTENIDO.....	vi
ÍNDICE DE TABLAS .....	xi
ÍNDICE DE FIGURAS .....	xiii
CAPÍTULO 1: INTRODUCCIÓN.....	1
1.1.    La tesis.....	1
1.2.    Motivación.....	4
1.3.    Ubicación y vías de acceso a la zona de estudio.....	7
1.4.    Objetivos.....	8
1.4.1. Hipótesis de trabajo.....	8
1.4.2. Objetivo general .....	9
1.4.3. Objetivos específicos .....	10
CAPÍTULO 2: MAGMATISMO EN LA ZONA VOLCÁNICA CENTRAL DE LOS ANDES Y SU ROL COMO FUENTE DE CALOR EN LA CORTEZA SUPERIOR .....	11
2.1.    Magmatismo en ambientes de subducción.....	11
2.2.    Magmatismo en la Zona Volcánica Central de los Andes.....	17
2.3.    Sistema geotermal de Cerro Pabellón .....	22
2.4.    Magmas como fuentes de calor en la corteza superior.....	26
2.4.1. Emplazamiento ( $\Delta t = 1$ Ma) y etapa convectiva ( $t = 2 - 9$ ka).....	27
2.4.2. Etapa advectiva ( $t = 2 - 20$ ka).....	28
2.4.3. Perturbación termal de la roca caja ( $t = 2 - 30$ ka).....	30
2.4.4. Síntesis del rol de los plutones como fuentes de calor.....	31
CAPÍTULO 3: A tale of a lava from its shallow zoned reservoir to surface: the case Azufre volcano in the context of the Altiplano Puna Magma Body (northern Chile) .....	32
Abstract.....	34

3.1. Introduction .....	35
3.2. The Azufre volcano and its geologic setting.....	37
2.3. Methodology .....	40
2.3.1 Sampling and analytical methods.....	40
3.4. Results.....	47
3.4.1. Geochemistry, petrography, and mineral chemistry .....	47
Geochemistry .....	47
Petrography .....	48
Plagioclase .....	50
Amphibole.....	52
Pyroxenes.....	57
Biotite.....	59
Fe-Ti oxides.....	59
Olivine and quartz.....	60
3.4.2. Equilibrium tests.....	63
Plagioclase .....	63
Amphibole.....	63
Olivine.....	64
Pyroxenes.....	64
Fe-Ti oxides.....	64
3.4.3. Pressure conditions.....	66
3.4.4. Temperature conditions.....	68
Amphibole.....	68
Pyroxenes.....	69
Plagioclase .....	69

Fe-Ti oxides.....	69
3.4.5. Felsic melt in equilibrium with Group 1 amphiboles.....	71
3.4.6. Oxygen fugacity ( $fO_2$ ).....	72
3.4.7. Thermodynamic model: MELTS.....	74
3.5. Discussion .....	80
3.5.1 Shallow depth magmatic evolution: magma mixing and zonation of the reservoir .....	80
3.5.2. $fO_2$ and $H_2O$ conditions in the reservoir.....	84
3.5.3. Temperatures of eruption and cooling in the lava .....	85
3.6. Conclusions .....	87
Acknowledgments.....	89
Author contributions.....	89
CAPÍTULO 4: APROXIMACIÓN DEL VOLUMEN DE LA CÁMARA MAGMÁTICA QUE ORIGINÓ EL DEPÓSITO DE LAVA ESTUDIADO .....	90
4.1. Introducción .....	90
4.2. Cálculo de volúmenes y densidades.....	93
4.3. Volumen de la cámara magmática del volcán Azufre .....	97
CAPÍTULO 5: SUPPLEMENTARY MATERIAL .....	103
5.1. Inferred age of last eruptive stage of the Azufre volcano .....	103
5.2. Sample locations .....	106
5.3. Geochemistry analyses.....	108
5.4. EMPA analyses .....	116
Plagioclase.....	116
Microlites in contact with Amp microphenocrysts .....	116
Cores.....	122



External rims.....	125
Internal rings.....	128
Intermediate zones .....	130
Plg inclusions in Amp microphenocrysts.....	136
Plg inclusions in Amp phenocrysts .....	138
Plg inclusions in Bt phenocrysts .....	139
Amphibole .....	141
Phenocrysts and inclusions in Plg .....	141
Microphenocrysts .....	145
Biotite .....	153
Phenocrysts.....	153
Pyroxenes .....	155
Microlites .....	155
Mg-rich rims.....	161
Mg-poor cores .....	167
Mg-rich Opx patches in Mg-rich rims of Cpx.....	170
Fe-Ti oxides .....	172
Paired Fe-Ti oxides microlites .....	172
Olivine .....	175
Standards.....	177
5.5. P-T- felsic melt composition-fO <sub>2</sub> - Solubility calculations.....	180
Pressure calculations (kbar).....	180
Amphibole.....	180
Amphibole-plagioclase.....	181
Temperature calculations (°C).....	182

Amphibole-plagioclase.....	182
Amphibole.....	184
Orthopyroxene-clinopyroxene.....	185
Plagioclase-liquid.....	192
Fe-Ti oxides.....	193
$f_{O_2}$ (log units).....	194
Amphibole.....	194
Fe-Ti oxides.....	195
Liquid.....	195
H <sub>2</sub> O solubility (wt%).....	196
Liquid.....	196
5.6. Cr <sub>2</sub> O <sub>3</sub> (wt%) contents in pyroxenes.....	203
5.7. Equilibrium tests.....	204
5.8. Temperatures not considered for amphiboles of Group 1.....	206
5.9. Felsic melt composition.....	208
5.10. MELTS simulations.....	210
5.11. Shallow Mg-rich pyroxenes and olivine crystallization data.....	214
5.12. Equilibrium time of ilmenite and titanomagnetite.....	217
CAPÍTULO 6: CONCLUSIÓN.....	219
BIBLIOGRAPHY.....	222
ANEXOS.....	244
Anexo A: Otras publicaciones asociadas al PhD.....	244
Anexo B: Participación en congresos.....	246

## ÍNDICE DE TABLAS

Table 3.1: Modal mineralogy and crystals size of the youngest lava deposit samples of the Azufre volcano and their enclaves.....	43
Table 3.2: Whole-rock compositions of representative samples from the studied lava and enclaves of the Azufre volcano. Mg-number (Mg#) was calculated as molar $Mg/(Mg+Fe^{2+})$ . d.l. corresponds to detection limit. Details of calculation used in the table can be found in the supplementary material “Geochemistry analyses” .....	44
Table 3.3: Representative microprobe analyses of plagioclase from the studied lava and enclaves. Anorthite (An), albite (Ab), and orthoclase (Or) contents in mol%.....	54
Table 3.4: Representative microprobe analyses of amphibole and biotite from the studied lava and enclaves. Equivalent oxygen ( $O=F+Cl$ ) and recalculations of $FeO^*$ , $Fe_2O_3^*$ , and $H_2O^*$ were performed using Locock (2014) spreadsheet and Li’s et al. (2020) method for amphibole and biotite, respectively. Total (wt%) does not include $FeO_T$ measured by EMPA. ....	56
Table 3.5: Representative microprobe analyses of pyroxene phenocrysts from the studied lava and enclaves. Recalculations of $FeO^*$ and $Fe_2O_3^*$ were performed with the Putirka (2008) method. Total (wt%) does not include $FeO_T$ measured by EMPA. Mg-number (Mg#) was calculated as molar $Mg/(Mg+Fe^{2+})$ . Wollastonite (Wo), enstatite (En), and ferrosilite (Fs) contents in mol%.....	61
Table 3.6: Representative microprobe analyses of Fe-Ti oxides microlites and olivine phenocrysts from the studied lava and enclaves. The Stormer’s (1983) method was used to calculate the $FeO^*$ and $Fe_2O_3^*$ contents and the titanomagnetite and ilmenite mole fractions ( $X_{Usp}$ and $X_{Ilm}$ , respectively). Forsterite (Fo) content in mol%. Excepting olivine (all its Fe content is considered ferrous), total (wt%) does not include $FeO_T$ measured by EMPA. ....	62

Table 3.7: Summary of calculated intensive conditions and H <sub>2</sub> O content for the last eruptive stage of the Azufre volcano .....	77
Table 5.1: Dating of young volcanic units (<140 ka) of the Ascotán-Inacaliri district that show rough morphologies, volcanic craters and structures flow as levees, ogives, and steep flow front. The location of these units is displayed in Fig. 5.1 .....	104
Table 5.2: Coordinates of sample sites (UTM zone 19K) .....	107
Table 5.3: Features of the melting experiments on andesite (spessartite) and basaltic andesite of Moore and Carmichael (1998). .....	215
Table 5.4: Features of the melting experiment on basaltic andesite of Groove et al. (1997). .....	216

## ÍNDICE DE FIGURAS

- Fig. 1.1: Imagen satelital del volcán Azufre donde se muestra su cercanía geográfica con la planta de energía geotérmica Cerro Pabellón. El graben de Inacaliri evidencia el carácter extensional del lineamiento volcánico NW-SE (imagen satelital obtenida de Google Earth). .....2
- Fig. 1.2: Imagen satelital con una visión amplia del lineamiento volcánico NW-SE de 70 km donde se encuentra emplazado el volcán Azufre (en amarillo) y la planta de energía geotérmica Cerro Pabellón (estrella verde). El lineamiento se encuentra delimitado por el volcán Palpana y el graben de Inacaliri en sus extremos NO y SE, respectivamente (imagen satelital obtenida de Google Earth). .....3
- Fig. 1.3: Esquema general del contexto geodinámico Andino (A), en el cual se destaca en (B) su Zona Volcánica Central, el Altiplano Puna Volcanic Complex (línea punteada azul) y la ubicación del volcán Azufre. En (C) se proyecta el perfil geológico esquemático de la Zona Volcánica Central, indicando: T, Fosa; AB, Cuenca de Arica; CC, Cordillera de la Costa; CD, Depresión Central; FP, Antearco de la Precordillera; WC, Cordillera Occidental; EC, Cordillera Oriental; SS, Sierras Subandinas (imágenes modificadas de Stern et al. 2007 y Charrier et al. 2007). .....5
- Fig. 1.4: Modelo 3D de inversión sísmica para definir la distribución espacial del Altiplano Puna Magma Body (APMB) y su manifestación exógena en el Altiplano Puna Volcanic Complex (APVC). Se destaca también la ubicación geográfica de los volcanes Azufre y Uturuncu, los cuales se encuentran emplazados con relación al APMB sobre su borde occidental y centro (imagen modificada de Ward et al. 2014). .....6
- Fig. 1.5: Mapa rutero con la vía de acceso "ruta CH 21" al volcán Azufre a partir de la ciudad de Calama (imagen modificada de la Red Caminera de Chile, MOP). .....7
- Fig. 2.1: Esquema conceptual de los principales procesos magmáticos asociados a un margen convergente por subducción. Entre ellos se puede destacar la deshidratación del *slab*, la fusión parcial del manto astenosférico junto con procesos ocurridos en la transición manto-corteza como el *underplating* de magmas de composición basáltica y

los procesos MASH. También se destaca el emplazamiento final en la corteza superior de magmas intermedios a félsicos previo a un eventual evento eruptivo (imagen tomada de Richards 2003). ..... 12

Fig. 2.2: Representación de un sistema magmático transcortical tipo *mush* con lentes de material fundido a diferentes niveles de la corteza. La degradación de color destaca la diferenciación (aumento del contenido de SiO<sub>2</sub>) y enfriamiento que sufren los fundidos generados en la corteza baja a medida que ascienden (imagen tomada de Cashman et al. 2017). ..... 13

Fig. 2.3: Gráfico indicando el grado de cristalización óptima para extraer fundidos desde un reservorio magmático en torno a una fracción de cristales de 0,6. Se observa que dicha extracción es independiente de la composición del magma (imagen tomada de Dufek and Bachmann)..... 14

Fig. 2.4: Gráfico indicando el cambio reológico de un magma a medida que cristaliza. Un aumento drástico en la viscosidad se da a una fracción de cristales entre 0,4 y 0,6. El *inset* expone como también aumenta la resistencia de un magma al alcanzar una fracción volumétrica de cristales de 0,6 (imagen modificada de Cashman et al. 2017)..... 15

Fig. 2.5: Gráficos para diferentes sistemas volcánicos de los cuales se infiere como la presión óptima de almacenamiento de reservorios magmáticos activos (con más de un 25% de fundido) previo a una erupción se da en la corteza somera en torno a los  $2 \pm 0.5$  kbar. Los métodos utilizados corresponden a análisis petrológicos experimentales (estrellas rojas), inclusiones vítreas y anfíboles junto con métodos geofísicos de inversión sísmica en ondas V<sub>p</sub>, V<sub>s</sub> y magnetotelúrica (imagen tomada de Huber et al. 2019). .... 16

Fig. 2.6: Perfiles geofísicos de sismicidad y gravimetría realizados en el Altiplano Puna Plateau que interpretan la existencia de diferentes reservorios magmáticos activos a partir de la correlación entre anomalías de Bouguer negativas y zonas con una atenuación en la velocidad de ondas S. Las líneas punteadas negras de figura de la izquierda corresponden de norte a sur a cada uno de los perfiles geofísicos, mientras que la línea blanca presente en cada uno de estos últimos representa el Moho. Los cuerpos de magma se identifican como Altiplano Puna Magma Body (APMB), Lazufre Magma Body

(LMB), Cerro Galan Magma Body (CGMB); Incahuasi Magma Body (IMB); Incapillo-Bonete Magma Body (IBMB) (imagen modificada de Ward et al. 2017). ..... 19

Fig. 2.7: Gráfico con el volumen acumulado de material volcánico eruptado en el APVC (~13.000 km<sup>3</sup>) donde se destacan tres pulsos magmáticos principales (Salisbury et al. 2010). A modo de comparación, se presenta también el volumen acumulado de otros campos volcánicos como Southern Rocky Mountain (SRMVF), Southwest Nevada (SWNVF), Yellowstone y Taupo.....21

Fig. 2.8: Esquemas con las distribuciones de los principales depósitos ignimbríticos y calderas del APVC en función de su edad (Salisbury et al. 2010). Entre estos se destacan las ignimbritas Sifón (B), Toconao y Atana (E). Los depósitos se encuentran distribuidos en torno al punto trifinio entre Chile, Bolivia y Argentina cubriendo un área de ~70.000 km<sup>2</sup>. .....21

Fig. 2.9: Mapa del margen continental chileno donde se exponen la Zona Geotermal Norte (izquierda) y la Zona Geotermal Centro-Sur (derecha), las cuales se encuentran controladas por el magmatismo, volcanismo y lineamientos estructurales de la Cordillera de Los Andes. Las zonas de mayor potencial para la explotación de energía geotérmica se encuentran señalados con la magnitud (±incertidumbre) de sus recursos indicados e inferidos (Aravena et al. 2016). .....24

Fig. 2.10: Sección representativa del sistema geotermal de Cerro Pabellón en la cual se expone la variación de temperatura y resistividad en profundidad. En la imagen se destaca el pozo PAE-1 descubridor del sistema junto con las fumarolas y zonas de alteración fósil presentes en el volcán Apacheta (llamado también Cerro Aguilucho; imagen tomada de Urzúa et al. 2002). .....25

Fig. 2.11: Gráficos asociados a la evolución del Plutón La Gloria. En A) se destaca la cristalinidad total de la cámara, la temperatura a la cual comienza la cristalización (rojo), el conteo del tiempo desde t=0 (azul) y la formación del frente cristalino o *mush* (verde). En el gráfico B) se expone la evolución heterogénea de la cámara en un magma caliente y otro frío al momento de comenzar la formación del frente cristalino (verde). En el *inset*

se destaca el momento en que el magma caliente alcanza el *solidus* a los  $t=20$  ka (modificado de Gutiérrez et al. 2013). .....28

Fig. 2.12: Gráficos asociados a la evolución del Plutón La Gloria. En A) se destaca la evolución cristalina del magma frío y caliente, destacando el instante en que comienza la formación del frente cristalino (línea verde) y la etapa advectiva para cada uno de los magmas una vez alcanzado el 60 vol% de cristalinidad (línea rosada). En B) se expone la evolución termal de la roca caja, destacando que la mayor perturbación en cuanto a tiempo y temperatura se alcanza en el centro del techo de la cámara (punto “a”) debido a la mayor cantidad de líquido extraído desde el núcleo del reservorio (modificado de Gutiérrez et al. 2013, Aravena et al. 2018)......29

Fig. 2.13: Esquema representativo del estado físico de la cámara magmática del Plutón La Gloria a  $t=3,5$  ka. Se destaca en rojo la zona de cristalinidad crítica a partir de la cual comienza la extracción del fundido (flechas rosadas) y por tanto la etapa advectiva (modificado de Gutiérrez et al. 2013). .....30

Fig. 3.1: Images showing: **a** The location of Altiplano Puna Volcanic Complex (APVC), the maximum extension of Altiplano Puna Magma Body (APMB; after Ward et al. 2014), and the volcanic alignment where the Azufre volcano, dacitic domes, and Cerro Pabellón geothermal power plant are emplaced. **b** The geologic map of the Azufre volcano (modified from Sellés and Gardeweg 2017; Godoy et al. 2022). **c** The volcanic crater and flow structures of the studied lava (within the red contour), which are also drawn in the geologic map **b**. We omit tags of sampling sites (white circles in **c**) to highlight the volcanic structures. To consult coordinates and samples tags see supplementary material “Sample locations”. Digital elevation model (DEM) of 12.5 m resolution (DEM ALOS-PALSAR; <https://vertex.daac.asf.alaska.edu>, date of data 17 July 2010) was used to make the elevation and geologic map of **a** and **b**, respectively. Satellite images **a** and **c** were obtained from Google Earth® freeware.....39

Fig. 3.2: Image showing an aphanitic enclave within a representative lava sample of the studied deposit and their compositions (and other related ones) in the total alkalis versus



silica diagram (le Bas et al. 1986). The black-dashed line corresponds to the alkaline and sub-alkaline magmatic series boundary (Irvine and Baragar 1971).....49

Fig. 3.3: Compositional and textural features of plagioclase crystals from lava and enclave samples. **a, b** Diagrams show the Ca-poor and Ca-rich textural-compositional features of plagioclase phenocrysts, which are indicated by tag colors in **c** and **d** BSE images. Different dissolution effects in plagioclase phenocrysts are shown in **c, f,** and **g** images. Microlite composition is shown in **e** .....51

Fig. 3.4: Compositional and textural features of amphibole crystals from the lava and enclave samples. Compositional groups of the studied amphiboles after Hawthorne’s et al. (2012) classification (**a**) and major oxide composition (**b**). BSE photomicrographs showing: **c** Group 1 amphibole crystal as inclusions within the Ca-poor intermediate zone of plagioclase phenocrysts. **d** Group 1 amphibole phenocryst with apatite and Ca-poor plagioclase inclusions. **e** Group 2 amphibole microphenocrysts in contact with microlites and inclusions of Ca-rich plagioclase. Optical microscope photomicrograph **f** showing amphibole crystals of both compositional groups. Group 2 crystal shows opaque rim (left) and Group 1 crystal is completely pseudomorphed (right). Tag colors of amphibole correspond to those in **a** plot, while tag colors of plagioclase are related with the Ca-poor and microlite compositions of Fig. 3.3b and e .....53

Fig. 3.5: Compositional and textural features of pyroxenes from the lava and enclave samples. **a** Pyroxene composition diagrams show the differences between cores and rims of orthopyroxenes and clinopyroxenes phenocrysts. Composition of orthopyroxene patches in clinopyroxene phenocrysts are also displayed in the diagrams in figure **a**. Tag colors in BSE images **c** and **d** are related to those of the diagrams in figure **a**. Pyroxene microlite compositions are exhibited in the diagram of figure **b**.....58

Fig. 3.6: BSE images obtained from lava samples that show: **a** Biotite phenocryst with thin reaction rim containing inclusions of Ca-poor plagioclase and apatite. **b** Paired ilmenite-titanomagnetite microlites. **c** Olivine phenocryst with orthopyroxene corona. **d** Embayed-quartz phenocryst with clinopyroxene corona (inset).....60

Fig. 3.7: Equilibrium test plots for mineral-liquid and mineral-mineral pairs. The liquid composition corresponds to the enclave sample Azu 7 EN. The exchange coefficient  $K_D$  (continuous black line) and its standard deviation (dotted black line) are presented on each diagram. **a** Mineral-liquid test show that plagioclase with compositions of  $An_{66-83}$  are in equilibrium with the assumed liquid composition (additional mineral-liquid test can be found in Fig. 6.5 to Fig. 6.8 of supplementary material “Equilibrium test”). Mineral-mineral tests (**b**, **c**) indicate that most of the orthopyroxene-clinopyroxene pairs are in equilibrium irrespectively of their textural features and that all paired titanomagnetite-ilmenite microlites pass the test.....65

Fig. 3.8: **a** The box plots display the pressures calculated by three different geobarometers for Group 1 amphiboles and associated phases. The average pressure and standard deviation ( $1\sigma$ ) determined by these methods is  $2 \pm 0.6$  kbar. Box plot symbology is shown in **b**. The data of pressure ranges, average values, standard deviation, and total uncertainty of each method are shown in Table 3.7 .....67

Fig. 3.9: Box plots displaying the temperature results from different thermometric methods (**a – h**). The phases and equation references involved in the calculations are on the left side of the diagram. Box plot symbology is the same used in Fig. 3.8. The data of temperature ranges, average values, standard deviation, and total uncertainty of each method are shown in Table 3.7 .....70

Fig. 3.10: Oxygen fugacity buffer results for the studied lava samples. Temperatures of Group 1 amphibole correspond to those calculated using the equation B of Holland and Blundy (1994). QFM buffer line was calculated according to Frost (1991) at  $P= 2$  kbar. The data of oxygen fugacity ranges, average values, standard deviation and total uncertainty of each method are shown in Table 3.7 .....73

Fig. 3.11: **a** Diagram showing Rhyolite-MELT models that reproduce the observed compositions of high-temperature mineralogy from the studied lava samples, i.e., olivine cores, Mg-rich pyroxenes (Mg-rich rims of both pyroxene phenocrysts and Mg-rich orthopyroxenes patches in Mg-rich rims of clinopyroxene phenocrysts), and Ca-rich plagioclase ( $An_{\geq 66}$ ). **a** Diagram also exhibits the evolution of initial water contents (wt%;

black crosses) and mineral compositions in terms of An% and Mg#. Initial water contents of 3.9 and 4.8 wt% (instead of 4 and 5 wt%) are due to the normalization of melt composition to 100% at the beginning of simulations. **b** Diagram displays percentage evolution of crystallinity in the system .....76

Fig. 3.12: Equilibration times plot for paired titanomagnetite-ilmenite microlites. The crystals were modeled as spheres with a representative radius of 5  $\mu\text{m}$  through interdiffusion coefficient models of FH78 (Freer and Hauptman 1978), A84 (Aragon et al. 1984), and P20 (Prissel et al. 2020) following the  $f\text{O}_2$  parameters fixed by van Orman and Crispin (2010). The dashed lines correspond to the maximum uncertainty of Fe-Ti oxides thermometry (i.e.,  $\pm 50$   $^\circ\text{C}$ ), while X<sub>Ti</sub> is the titanium mole fraction in titanomagnetite ...86

Fig. 3.13: Schematic representation (not to scale) of the processes associated with the last eruptive stage of the Azufre volcano. The intruded andesitic liquids (from APMB or lower crust zones) are mixed with hosted magma and differentiated in the shallow crust, producing a crystal mush and residual felsic melts, which give rise to thermal and compositional zonation of the reservoir .....88

Fig. 4.1: Extracto de la tabla de dataciones de Roobol et al. (1974), en la cual se expone la unidad, lugar y ubicación cartográfica para estas.....91

Fig. 4.2: Imagen satelital que exhibe el punto de coordenadas sexagesimales de la muestra datada por Roobol et al. (1974) más la interpretación del lugar datado según el presente documento, siendo asociado al domo DI (Hübner 2018) (modificado de Google Earth). .....92

Fig. 4.3: Imagen satelital que expone las diferencias morfológicas en el domo Chanka. En a) vista en planta del domo. En b) vista lateral hacia el E, en la cual se aprecia una morfología cónica con cúspide en forma de punta para el domo DI (en rojo) y una cónica con cúspide plana para el domo DII (en azul) (modificado de Google Earth). .....92

Fig. 4.4: Modelo de superficie TIN del volcán Azufre y perfil de elevación AB del domo I. En el perfil se destaca la cota de 4.100 m.s.n.m. como la base para el cálculo del volumen (modificado de ArcGIS). .....93

Fig. 4.5: Curvas de nivel asociadas al flanco norte del volcán Azufre y a su depósito de lava joven (delimitado en rojo; modificado de ArcGIS).....	94
Fig. 4.6: Superficie TIN asociada al flanco norte del volcán Azufre y a su depósito de lava joven (delimitado en rojo). Gradación de colores corresponde a elevación según escala de la Fig. 5.4 (modificado de ArcGIS). .....	95
Fig. 4.7: Superficie TIN asociada al flanco norte del volcán Azufre sin su depósito de lava joven (delimitado en rojo). Gradación de colores corresponde a elevación según escala de la Fig. 5.4 (modificado de ArcGIS). .....	95
Fig. 4.8: Volumen de material eruptable (modificado de Townsend and Huber 2020), en el cual se destaca (cuadro rojo) que cámaras magmáticas entre 10 y 30 km <sup>3</sup> pueden producir erupciones con volúmenes de 0.1 a 2 km <sup>3</sup> .....	100
Fig. 4.9: Perfil de resistividad a partil del cual los autores (Comeau et. al 2016) establecen que las estructuras tipo dique “C3” poseen un volumen aproximado de 500 km <sup>3</sup> . Estas estructuras, que se correlacionan con hipocentros sísmicos (círculos blancos en la figura), conectarían el APMB (C2) con reservorios someros o zonas de fluido hidrotermal (C1). .....	101
Fig. 4.10: Perfil geofísico cortical de resistividad en el cual se destaca en un cuadrado negro la ubicación del volcán Azufre y su anomalía de baja resistividad (color amarillo de ~20 km de largo). P2 y W2 corresponden a zonas de baja resistividad ubicadas debajo de la Precordillera (P) y Cordillera Occidental (W) (modificado de Araya Vargas et al. 2019). .....	102
Fig. 5.1: Location of young volcanic units (50 – 140 ka) of the Ascotán-Inacaliri district that show rough morphologies, which correspond to structures as volcanic craters (studied lava deposit and La Poruña scoria cone) and flow structures as levees, ogives, and steep flow front (studied lava deposit, Chac Inca dome, young lava deposits of the San Pedro volcano, and La Poruña scoria cone). The satellite images were obtained from Google Earth® freeware .....	104

Fig. 5.2: Satellite image obtained from Google Earth® freeware that shows an eroded lava deposit of the Azufre volcano (inset), whose age is  $331 \pm 33$  ka (Bertin and Amigo 2019) ..... 105

Fig. 5.3: Sample sites along the front of the studied lava deposit..... 106

Fig. 5.4: Diagram displaying the contrasting  $\text{Cr}_2\text{O}_3$  (wt%) concentrations between Mg-poor and Mg-rich (including patches) pyroxene phenocrysts. Although we did not use a secondary standard to quantify the uncertainty of  $\text{Cr}_2\text{O}_3$  (wt%) measurement, the data show a notorious difference in  $\text{Cr}_2\text{O}_3$  (wt%) concentration. ....203

Fig. 5.5: Mineral-liquid test plots considering the composition of the enclave sample Azu 7 EN as liquid composition. The results show that cores of plagioclase phenocryst ( $\text{An}_{66-83}$ ) and olivine phenocrysts ( $\text{Fo}_{80-81}$ ) are in equilibrium with the considered liquid composition, whereas amphiboles are in disequilibrium.....204

Fig. 5.6: Mineral-liquid test plots considering the composition of the enclave sample Azu 8 EN as liquid composition. The results show that cores of plagioclase phenocryst ( $\text{An}_{74-83}$ ) and olivine phenocrysts ( $\text{Fo}_{80-81}$ ) are in equilibrium with the considered liquid composition, whereas amphiboles are in disequilibrium.....204

Fig. 5.7: Mineral-liquid test plots considering the composition of the enclave sample Azu 10 EN as liquid composition. The results show that cores and external rims of plagioclase phenocrysts and plagioclase microlites with composition between  $\text{An}_{71-83}$  are in equilibrium with the considered liquid composition. Cores of olivine phenocrysts ( $\text{Fo}_{80-83}$ ) are also in equilibrium, whereas amphiboles are in disequilibrium .....205

Fig. 5.8: Mineral-liquid test plots considering the composition of the enclave sample Azu 14 EN as liquid composition. The results show that cores and external rims of plagioclase phenocrysts and plagioclase microlites with composition between  $\text{An}_{69-83}$  are in equilibrium with the considered liquid composition. Cores of olivine phenocrysts ( $\text{Fo}_{80}$ ) are also in equilibrium, whereas amphiboles are in disequilibrium .....205

Fig. 5.9: Box plots showing temperature crystallization of Group 1 amphiboles according to different geothermometers (**a – h**) at 2 kbar of pressure. The phases and equation references involved in the calculations are on the left side of the diagram.....207

Fig. 5.10: Diagrams showing the SiO<sub>2</sub> (wt%) content in the liquid equilibrated with Group 1 amphiboles at different P-T conditions. X axis represents different spot analysis of amphibole (triangles and diamond). The uncertainties associated with Ridolfi and Renzulli's (2012) method is ± 1.3 wt% (smaller than symbols), while those of Putirka (2016) and Zhang et al. (2017) are ± 3.6 wt% for both. In (a) plot the pressure curves at 2, 3, 4, and 5 kbar are superposed.....209

Fig. 5.11: Diagrams showing P-T-fO<sub>2</sub> conditions and initial H<sub>2</sub>O contents in which Rhyolite-MELT modellings reproduced crystallization sequence of olivine, Mg-rich pyroxenes (co-crystallized orthopyroxene and clinopyroxene), and Ca-rich plagioclase with An≥66, which is consistent with the composition observed in lava samples .....210

Fig. 5.12: Diagrams showing P-T-fO<sub>2</sub> conditions and initial H<sub>2</sub>O contents in which Rhyolite-MELT modellings reproduced Ca-rich plagioclase (An≥66).....211

Fig. 5.13: Diagrams showing P-T-fO<sub>2</sub> conditions and initial H<sub>2</sub>O contents in which Rhyolite-MELT modellings reproduced the Mg-rich pyroxenes compositions (co-crystallized ortho- and clinopyroxene) consistent with those observed in lava samples.....212

Fig. 5.14: Continued diagram of Fig. 5.13 .....213

Fig. 5.15: Paired titanomagnetite-ilmenite microlites founded in the lava samples of the Azufre volcano. Different ellipses are drawn next to the small ilmenite crystals with the length of their minor and major axis to determine a representative sphere geometry with a radius of 5 μm.....218

Fig. 6.1: Modelo conceptual que plantea al reservorio magmático del volcán Azufre como una posible fuente de calor del sistema geotermal de Cerro Pabellón. Adicionalmente, se destaca también el posible rol que podría jugar el lineamiento NW-SE (estructura extensiva) en el ascenso de los magmas que originaron los domos dacíticos y la lava andesítica estudiada del volcán Azufre a partir de un mismo reservorio.....221

# CAPÍTULO 1: INTRODUCCIÓN

## 1.1. La tesis

La presente investigación busca determinar entre otros parámetros, las variables termodinámicas intensivas de presión y temperatura de un reservorio magmático con el fin de contextualizar la posible fuente de calor que alimentó o se encuentran alimentando el sistema geotermal de Cerro Pabellón, lugar donde se encuentra operando la primera planta de energía geotérmica de Sudamérica desde el año 2017. Para lo anterior, se determinó estudiar el origen del depósito de lava más joven del volcán Azufre (<140 ka), el cual se encuentra a ~10 km de la planta geotérmica y dentro de un lineamiento estructural extensional NW-SE de 70 km (Fig. 1.1 y Fig. 1.2). De esta forma, por medio de un detallado estudio petrológico, fue posible establecer un modelo para el reservorio magmático que dio origen al depósito estudiado, el cual se emplazó durante la última etapa eruptiva del volcán Azufre.

En el CAPÍTULO 2 se expone una síntesis de los principales procesos magmáticos presentes en las zonas de subducción y se entregan antecedentes generales de la evolución tectonomagmática de la Zona Volcánica Central de Los Andes. Adicionalmente, en el CAPÍTULO 2, también se presentan antecedentes del contexto geológico en el cual se encuentra el sistema geotermal de Cerro Pabellón y se discute respecto al rol que tendrían los intrusivos como posibles fuentes de calor en la corteza superior. En el CAPÍTULO 3 se presenta el manuscrito del *paper* “*A tale of a lava from its shallow zoned reservoir to surface: the case of the Azufre volcano in the context of the Altiplano Puna Magma Body (northern Chile)*”, el cual sintetiza toda la investigación realizada durante el proyecto de Doctorado, mientras que en el CAPÍTULO 4 se aplica una metodología volcanológica para aproximar el volumen de la cámara magmática del volcán Azufre. En el CAPÍTULO 5 se adjunta el *supplementary material* asociado al *paper* que profundiza en ciertas discusiones y cálculos relevantes dentro del contexto de la presente investigación, mientras que en el CAPÍTULO 6 se presentan las conclusiones generales

de la investigación. Finalmente, en los anexos se exhiben otras publicaciones asociadas a la investigación doctoral.

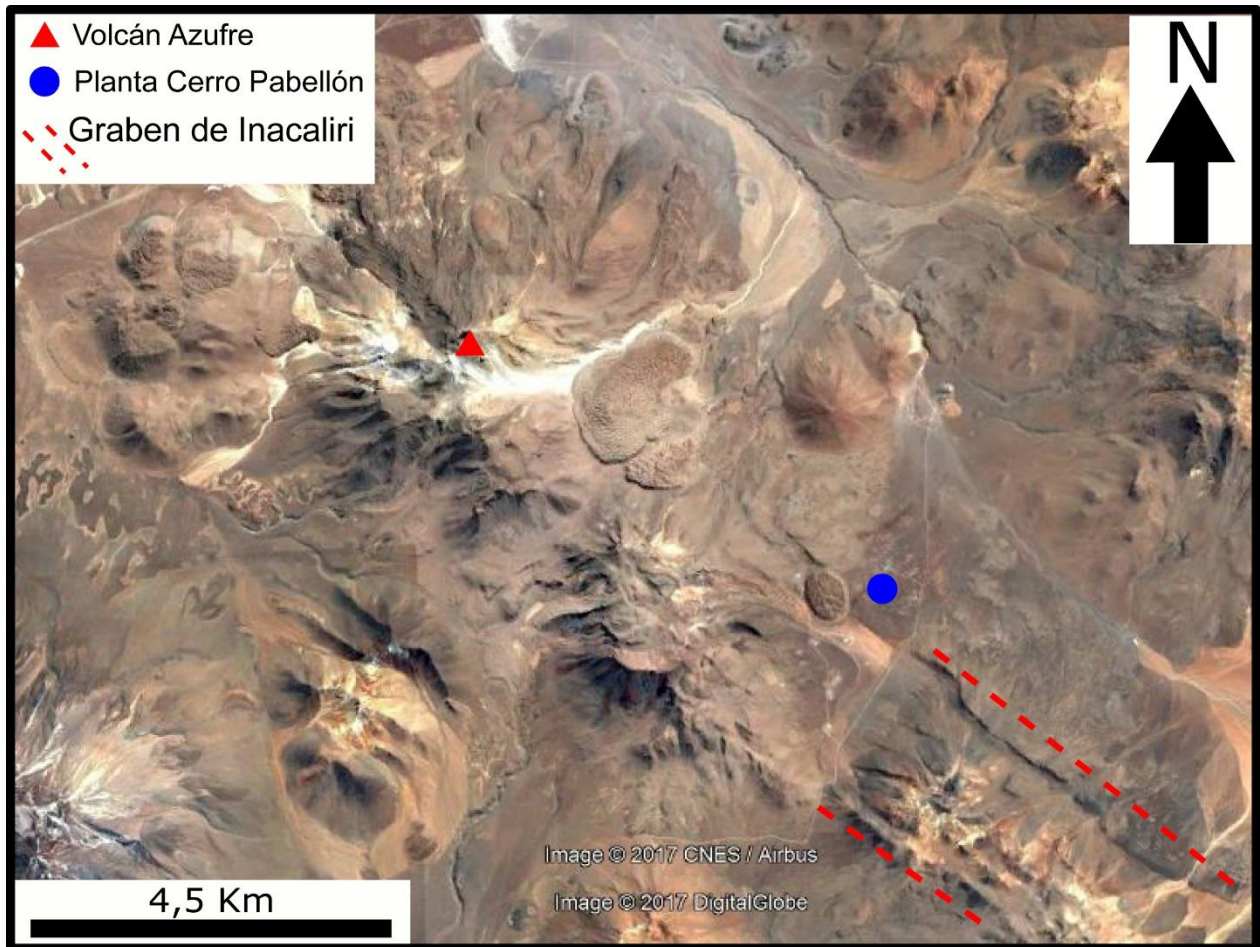


Fig. 1.1: Imagen satelital del volcán Azufre donde se muestra su cercanía geográfica con la planta de energía geotérmica Cerro Pabellón. El graben de Inacaliri evidencia el carácter extensional del lineamiento volcánico NW-SE (imagen satelital obtenida de Google Earth).



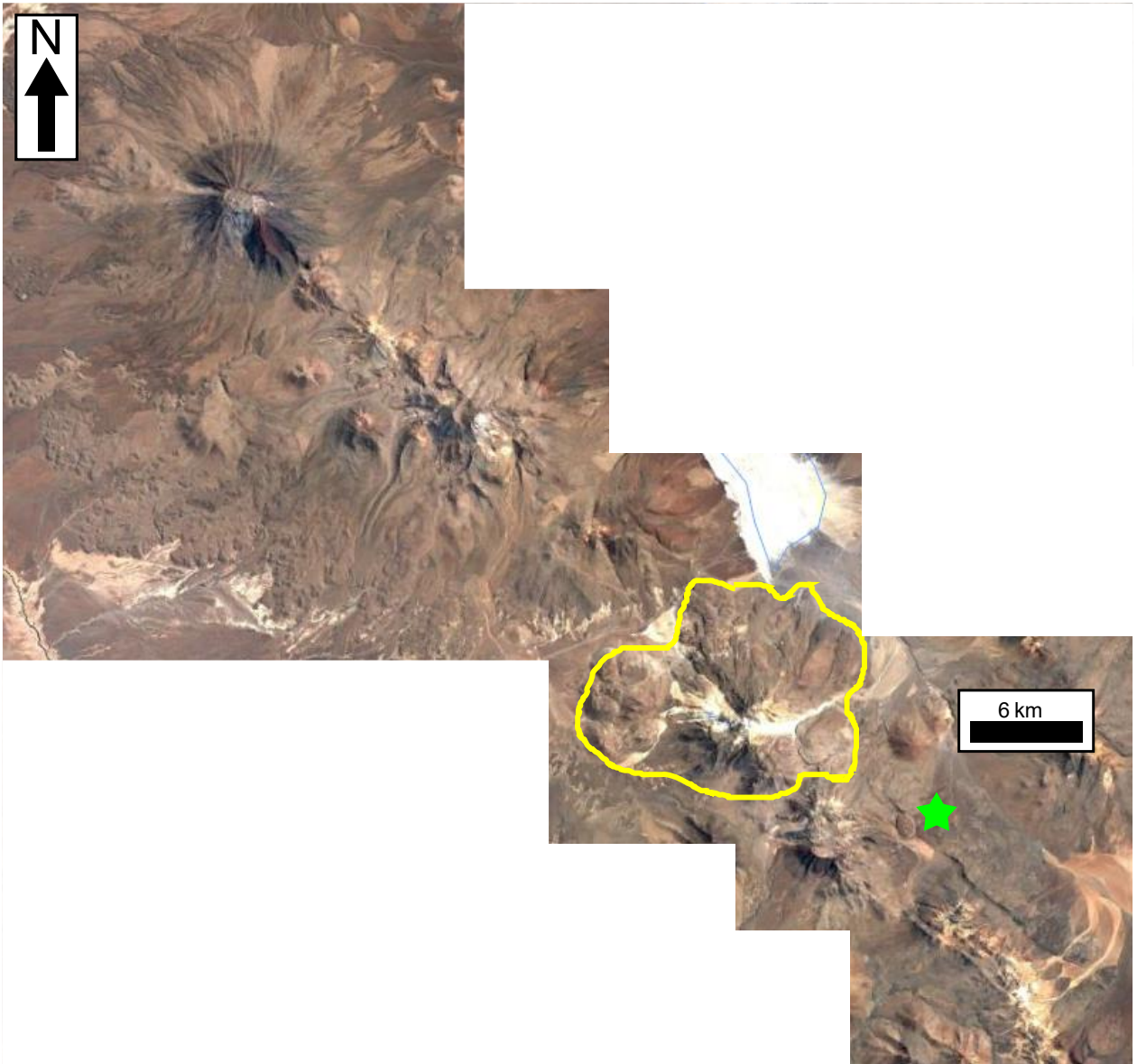


Fig. 1.2: Imagen satelital con una visión amplia del lineamiento volcánico NW-SE de 70 km donde se encuentra emplazado el volcán Azufre (en amarillo) y la planta de energía geotérmica Cerro Pabellón (estrella verde). El lineamiento se encuentra delimitado por el volcán Palpana y el graben de Inacaliri en sus extremos NO y SE, respectivamente (imagen satelital obtenida de Google Earth).

## 1.2. Motivación

El magmatismo, y su expresión exógena por medio del volcanismo, juegan un rol fundamental en diversos procesos naturales tales como la formación de la corteza y el granito (Petford et al. 2000; Castro 2014), la evolución de la atmósfera (Mather et al. 2004; Trail et al. 2011; Lee and Dee 2019), la formación de depósitos minerales (Hedenquist and Lowenstern 1994; Sillitoe 2010; Audétat and Simon 2012; Chelle-Michou et al. 2017) y el control sobre diversos peligros geológicos (Wilson et al. 2014). Otra manifestación significativa del magmatismo es su rol como fuente de calor en la energía geotérmica de alta entalpía (temperatura de fluidos  $>200^{\circ}\text{C}$ ; Lee 2001; Moeck 2014), la cual es una energía renovable que representa una posibilidad factible de ser desarrollada en contextos geológicos donde el magmatismo posee un control significativo. Un ejemplo de lo anterior dentro del territorio nacional es el Altiplano Puna Magma Body (APMB; Chmielowski et al. 1999; Ward et al. 2014; Wörner et al. 2018), el cual es un gran cuerpo magmático activo localizado entre los  $21^{\circ}$  y  $23^{\circ}$  S dentro de la Zona Volcánica Central de Los Andes (Fig. 1.3 y Fig. 1.4), y cuya manifestación exógena es el volcanismo del Altiplano Puna Volcanic Complex (de Silva 1989a, b; de Silva and Kay 2018). Así mismo, también se han identificado otras provincias volcánicas de Chile con potencial para el desarrollo de geotermia, tales como El Tatio, La Torta y Tolhuaca (Aravena et al. 2016).

Para poder entender el rol del magmatismo como fuente de calor, es necesario preguntarse la profundidad en que se encuentran los principales reservorios magmáticos, la evolución de la temperatura en dichos reservorios, la longevidad y volumen de tales reservorios y cómo es la difusión termal hacia la corteza. Adicionalmente, corresponde preguntarse sobre la existencia de otras fuentes de calor además del magmatismo tales como el calor latente debido a la cristalización o el decaimiento radioactivo.

La búsqueda de respuestas a estas pocas, pero no menores interrogantes, son la principal motivación por realizar la presente investigación. Sin embargo, dada la complejidad del problema, ahondaremos sólo en dar respuestas parciales a las dos primeras interrogantes planteadas.

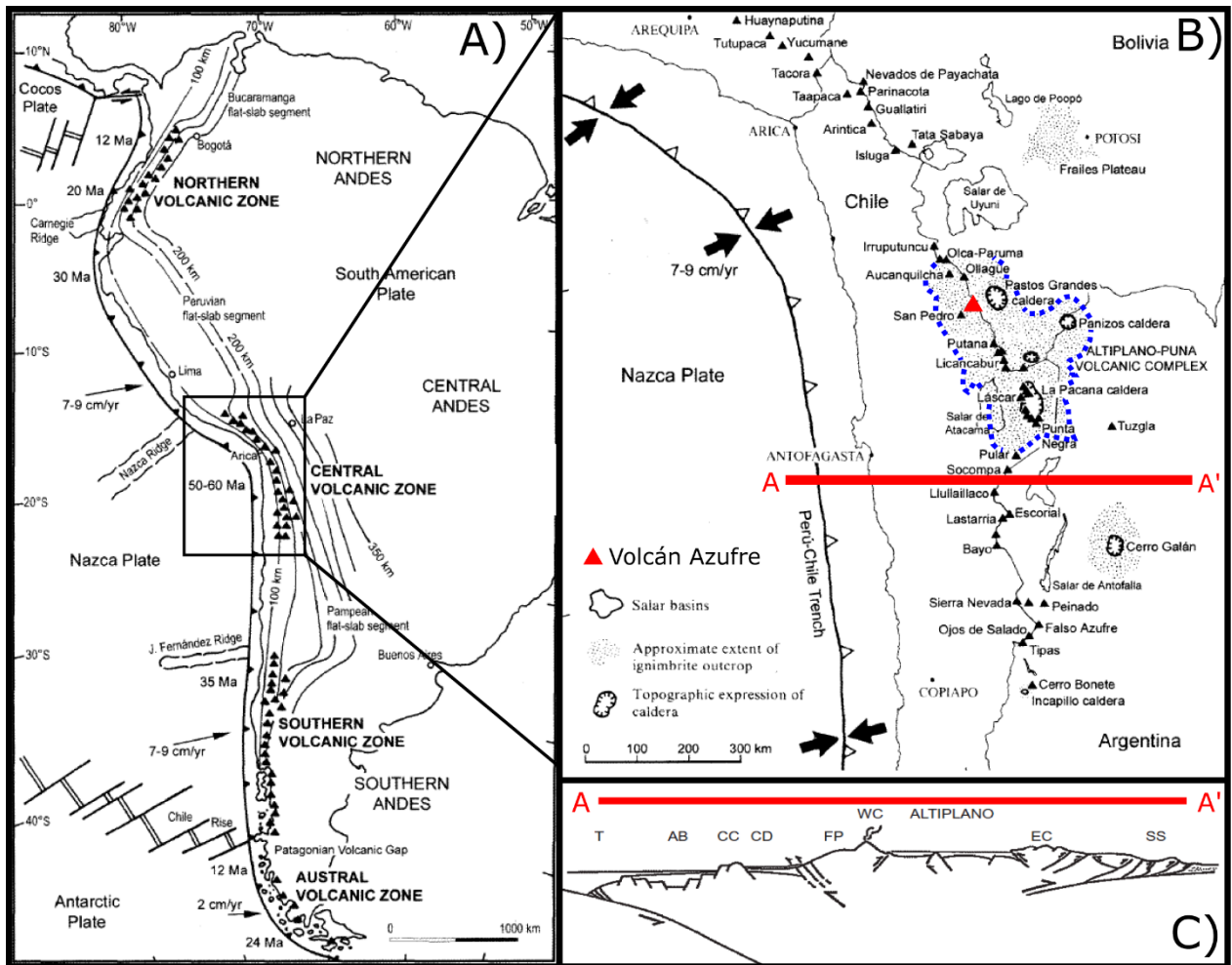


Fig. 1.3: Esquema general del contexto geodinámico Andino (A), en el cual se destaca en (B) su Zona Volcánica Central, el Altiplano Puna Volcanic Complex (línea punteada azul) y la ubicación del volcán Azufre. En (C) se proyecta el perfil geológico esquemático de la Zona Volcánica Central, indicando: T, Fosa; AB, Cuenca de Arica; CC, Cordillera de la Costa; CD, Depresión Central; FP, Antearco de la Precordillera; WC, Cordillera Occidental; EC, Cordillera Oriental; SS, Sierras Subandinas (imágenes modificadas de Stern et al. 2007 y Charrier et al. 2007).

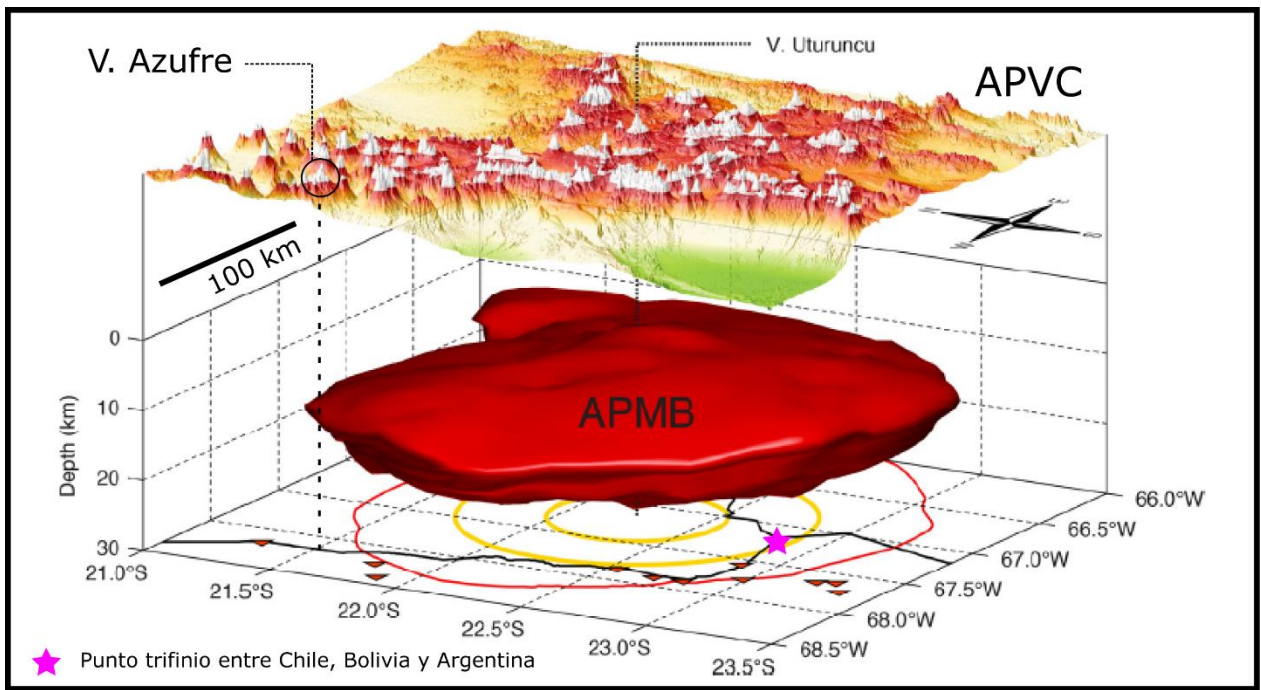


Fig. 1.4: Modelo 3D de inversión sísmica para definir la distribución espacial del Altiplano Puna Magma Body (APMB) y su manifestación exógena en el Altiplano Puna Volcanic Complex (APVC). Se destaca también la ubicación geográfica de los volcanes Azufre y Uturuncu, los cuales se encuentran emplazados con relación al APMB sobre su borde occidental y centro (imagen modificada de Ward et al. 2014).

### 1.3. Ubicación y vías de acceso a la zona de estudio

Geográficamente el volcán Azufre se ubica a los 21°47' de latitud S y a los 68°14' de longitud O; mientras que políticamente se encuentra en la comuna de Ollagüe, provincia de El Loa en la Segunda Región de Antofagasta, Chile.

La ciudad más cercana al volcán Azufre es Calama, a partir de la cual se debe tomar la ruta CH 21 para llegar a él (Fig. 1.5). Sin embargo, para acceder a sus depósitos de lavas, a la altura del kilómetro 120 se deben tomar con dirección SE caminos secundarios y huellas.

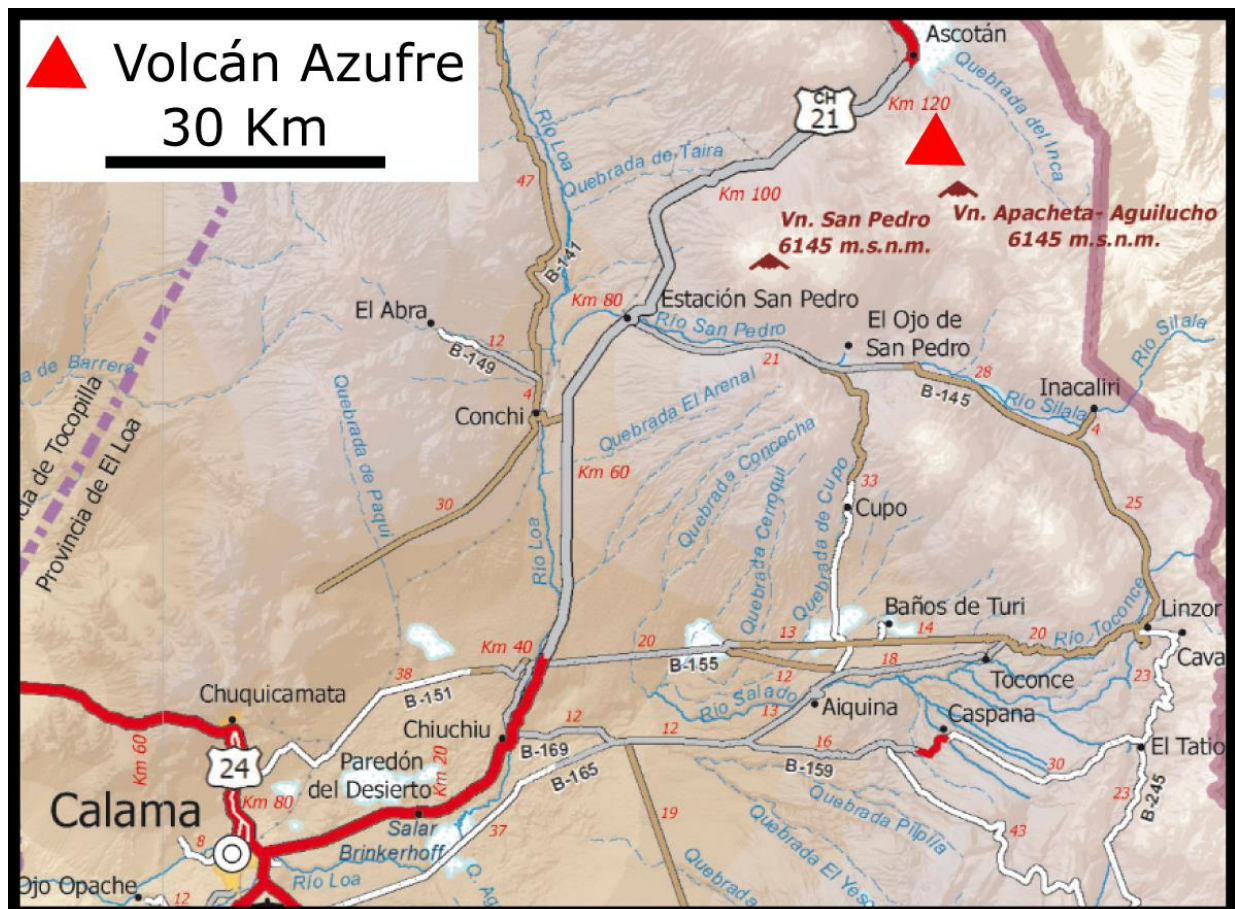


Fig. 1.5: Mapa rutero con la vía de acceso "ruta CH 21" al volcán Azufre a partir de la ciudad de Calama (imagen modificada de la Red Caminera de Chile, MOP).

## 1.4. Objetivos

### 1.4.1. Hipótesis de trabajo

Basado en el contexto tectónico (que incluye la segunda corteza más engrosada del planeta Tierra y la más gruesa dentro de un ambiente de subducción con un espesor de ~70 km) y magmático (que considera la presencia del *Altiplano Puna Magma Body*, el cuerpo magmático más voluminoso del planeta Tierra con ~500.000 km<sup>3</sup>) en el cual se desarrolla el volcán Azufre, se plantea que los procesos magmáticos en torno a su origen y desarrollo son complejos.

Consistentemente, lo anterior se evidencia en el depósito de lava más joven del volcán Azufre (i.e., el objeto de estudio de la presente investigación) por medio de la presencia de enclaves y una mineralogía contrastante con presencia de fases máfica y félsica que presentan distintos tipos de texturas de desequilibrio.

Así, la evolución magmática que dio origen al depósito de lava estudiado considera al menos dos reservorios (uno somero y otro que forma parte del *Altiplano Puna Magma Body*) entre los cuales hay transferencia de masa y energía (i.e., presencia de un sistema magmático abierto). De esta forma, se plantea que el proceso de mezcla magmática (i.e., *magma mixing*), el cual involucran también procesos de zonación química y termal, juega un rol fundamental en la evolución del reservorio magmático somero del volcán Azufre y también en los mecanismos eruptivos que dan origen al depósito estudiado.

### **1.4.2. Objetivo general**

Identificar cuáles fueron los principales procesos magmáticos que dieron origen al depósito estudiado, para así proponer un modelo petrogenético de la lava y sus enclaves desde su reservorio hasta la superficie.

Particularmente, basado en las texturas de disequilibrio y los enclaves presentes en la lava, se pretende definir el rol de estos últimos en los procesos de mezcla magmática, zonación química y termal del reservorio por medio de la determinación de las condiciones termodinámicas intensivas ( $P$ - $T$ - $fO_2$ ) y químicas de los fundidos en interacción. Adicionalmente, se busca también evaluar el efecto de los enclaves en el proceso eruptivo de la lava estudiada.

Junto con lo anterior, se pretende también caracterizar el reservorio de la lava estudiada por medio de aproximaciones numéricas volcanológicas. De esta forma, se pretende evaluar y contrastar algunos de los resultados obtenidos a partir de los métodos petrológicos.

### 1.4.3. Objetivos específicos

1. Definir la petrografía de la lava y sus enclaves, reconociendo sus principales texturas y posibles asociaciones de minerales en equilibrio.
2. Determinar condiciones intensivas (P-T- $fO_2$ ) a partir de las diferentes asociaciones minerales (mineral-mineral o mineral-líquido) para establecer así diferentes etapas de cristalización en equilibrio durante la evolución del reservorio que da origen al depósito de lava estudiado.
3. Determinar la química de los fundidos que son mezclados dentro del reservorio (i.e., *end members* del *magma mixing*).
4. Realizar modelamientos termodinámicos con el *software* Rhyolite-Melts para definir el ambiente (i.e., condiciones de P-T- $fO_2$ -H<sub>2</sub>O) más favorable para cristalizar la mineralogía observada y su composición.
5. Determinar el mecanismo(s) eruptivo que originó el depósito de lava estudiado.
6. Determinar el volumen de la cámara magmática que dio origen al depósito de lava estudiado mediante parámetros físicos y modelos volcanológicos.
7. Establecer un modelo petrogenético para el reservorio que originó el depósito de lava más joven del volcán Azufre.



# CAPÍTULO 2: MAGMATISMO EN LA ZONA VOLCÁNICA CENTRAL DE LOS ANDES Y SU ROL COMO FUENTE DE CALOR EN LA CORTEZA SUPERIOR

## 2.1. Magmatismo en ambientes de subducción

El paradigma actual establece que los procesos magmáticos en un contexto de subducción calco alcalino como el de la Zona Volcánica Central de los Andes (ZVCA) parten por la deshidratación del *slab* subductante, el cual libera los fluidos y volátiles presentes en sus sedimentos al ser arrastrados dentro del canal de subducción hacia la cuña del manto astenosférico que sobreyace al *slab* (Fig. 2.1; Tatsumi et al. 1986; Peacock 1993; Pearce and Peate 1995). La liberación de dichos fluidos produce la metasomatización y fusión parcial por hidratación del manto astenosférico dado que la adición de volátiles (H<sub>2</sub>O principalmente) baja el punto de fusión de las lherzolitas presentes en dicha zona (Hirose and Kawamoto 1995). Adicionalmente, la fusión parcial por hidratación produciría el carácter oxidado de los magmas de arco calco alcalino (Kelley and Cottrell 2009; Evans et al. 2012) y el enriquecimiento de elementos LILE (*large ion lithophile elements*) por sobre los de tipo HFSE (*high field strength elements*). A pesar de los procesos globales mencionados previamente, los magmas producidos en el manto astenosférico pueden variar su composición de acuerdo con las configuraciones particulares que se presenten en el margen convergente tales como el ángulo de subducción, tasa de convergencia, el estado termal del *slab*, y el contenido de sedimentos entre otros.

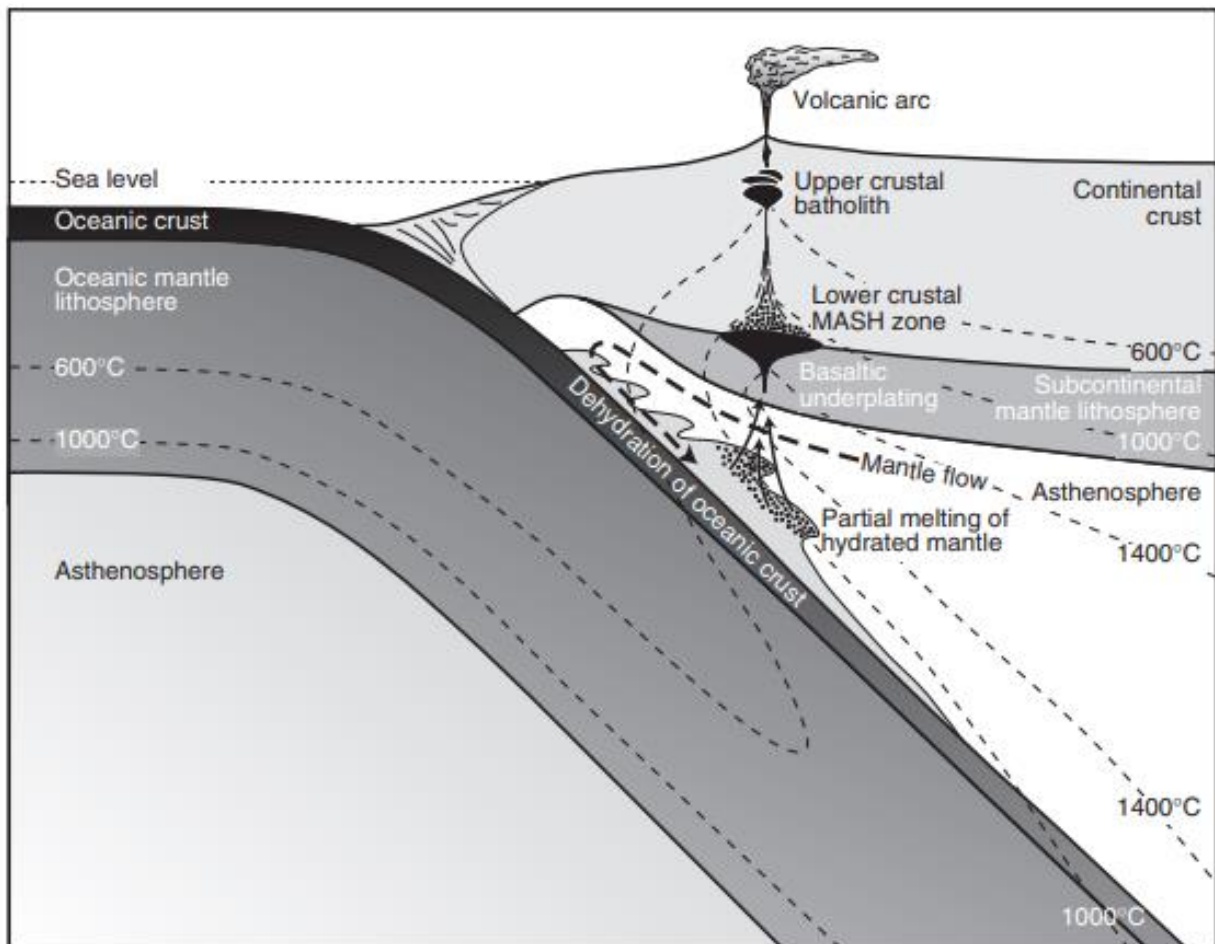


Fig. 2.1: Esquema conceptual de los principales procesos magmáticos asociados a un margen convergente por subducción. Entre ellos se puede destacar la deshidratación del *slab*, la fusión parcial del manto astenosférico junto con procesos ocurridos en la transición manto-corteza como el *underplating* de magmas de composición basáltica y los procesos MASH. También se destaca el emplazamiento final en la corteza superior de magmas intermedios a félsicos previo a un eventual evento eruptivo (imagen tomada de Richards 2003).

Una vez el manto sufre la fusión parcial, comienza el ascenso de los fundidos a través del manto astenosférico y manto litosférico hasta la discontinuidad manto-corteza, lugar donde se produce un cambio brusco en la composición y densidad de las rocas. En dicha transición se plantea la hipótesis de los procesos MASH (*melting, assimilation, storage y homogenization*) por parte de Hildreth and Moorbath (1988). Estos procesos MASH serían los causantes de la hibridación de los basaltos hacia composiciones más intermedias y evolucionadas tipo andesitas-dacitas por medio del fraccionamiento de fases minerales densas de alta temperatura (olivino, piroxeno, espinela y plagioclasa tipo

anortita-bytownita) y la asimilación de material cortical de menor densidad relativa a dichas fases fraccionadas. Luego de un tiempo de almacenamiento los magmas hibridados logran disminuir su densidad para continuar su ascenso hacia la corteza superior, formando reservorios magmáticos altamente cristalizados (i.e., reservorios tipo *mush*) que se emplazan a distintos niveles de la corteza. Dicho emplazamiento polibárico tipo columna de destilación se ha denominado *transcrustal magmatic system* (Fig. 2.2; Kiser et al. 2016; Cashman et al. 2017; Samrock et al. 2018; Giordano and Caricchi 2022).

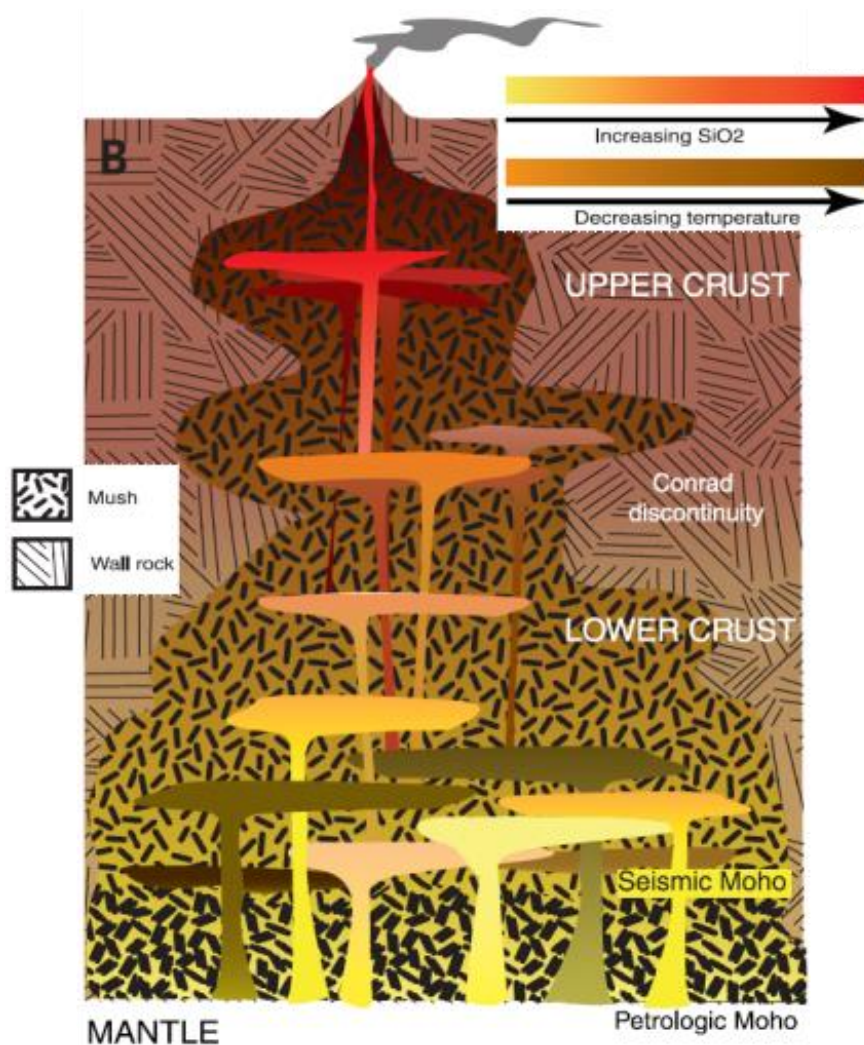


Fig. 2.2: Representación de un sistema magmático transcortical tipo *mush* con lentes de material fundido a diferentes niveles de la corteza. La degradación de color destaca la diferenciación (aumento del contenido de SiO<sub>2</sub>) y enfriamiento que sufren los fundidos generados en la corteza baja a medida que ascienden (imagen tomada de Cashman et al. 2017).

Se ha planteado que la formación de dichos reservorios magmáticos polibárnicos tipo *mush* está gobernada principalmente por la cristalización, debido a que los magmas ascienden a modo general, y en particular dentro de la corteza, por el control que la cristalización tiene sobre la composición, densidad y viscosidad del líquido residual (Dufek and Bachmann 2010; Solano et al. 2012; Jackson et al. 2018). En particular, se ha propuesto que una ventana de cristalización entre el 50 – 70% configura una dinámica cristal-fundido óptima para el ascenso por la compactación y permeabilidad de la red cristalina, el calor latente generado por la cristalización y la velocidad relativa alcanzada entre los cristales y el fundido (Fig. 2.3; Dufek and Bachmann 2010). Dentro de esa misma ventana de cristalización, se da también un cambio reológico en el reservorio al aumentar su viscosidad efectiva, pasando de un magma que se comporta como un fluido a un reservorio magmático tipo *mush* que se comporta como un sólido al aumentar su resistencia a la deformación (Fig. 2.4).

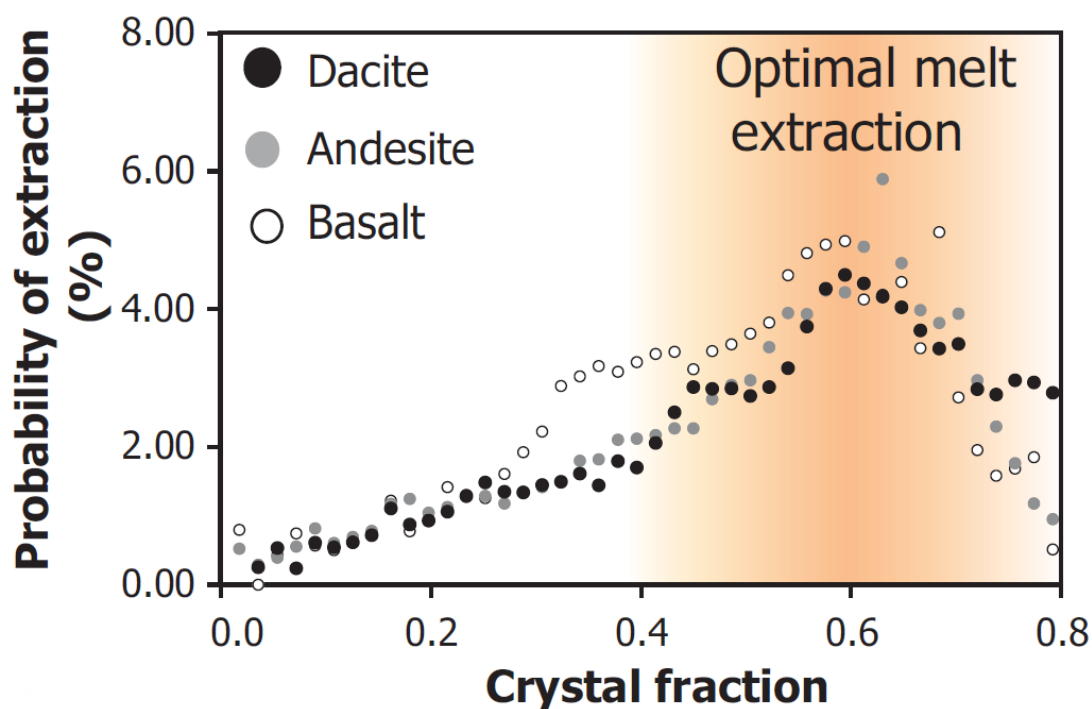


Fig. 2.3: Gráfico indicando el grado de cristalización óptima para extraer fundidos desde un reservorio magmático en torno a una fracción de cristales de 0,6. Se observa que dicha extracción es independiente de la composición del magma (imagen tomada de Dufek and Bachmann).

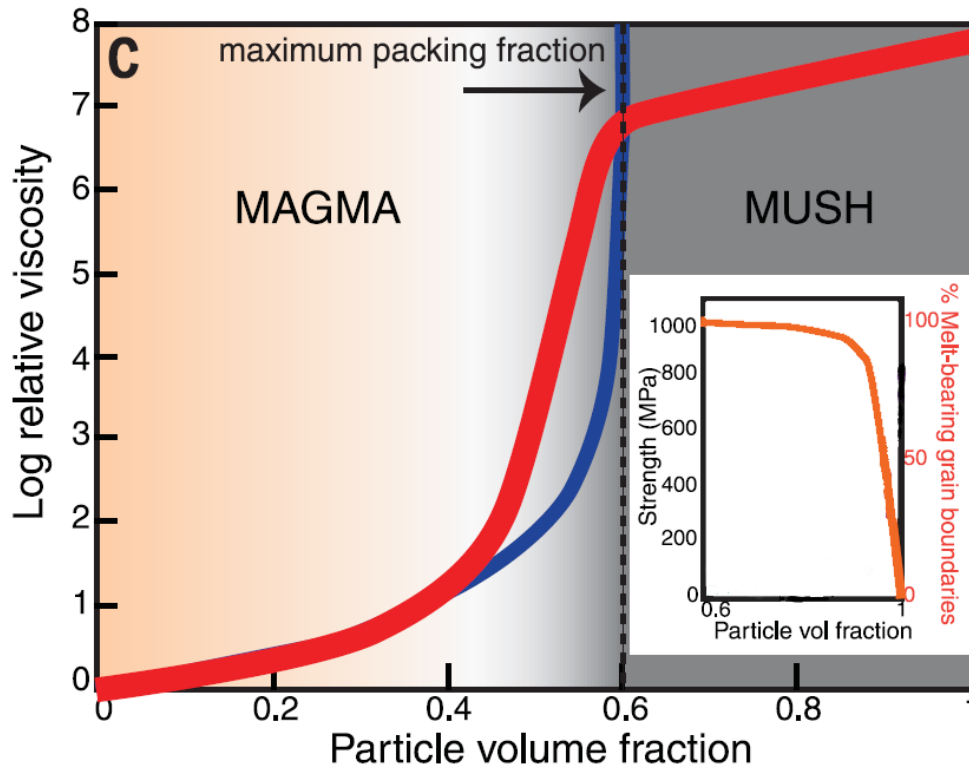


Fig. 2.4: Gráfico indicando el cambio reológico de un magma a medida que cristaliza. Un aumento drástico en la viscosidad se da a una fracción de cristales entre 0,4 y 0,6. El *inset* expone como también aumenta la resistencia de un magma al alcanzar una fracción volumétrica de cristales de 0,6 (imagen modificada de Cashman et al. 2017).

A medida que los magmas son “destilados” en los sucesivos reservorios transcorticales, los fundidos residuales se desgasifican y aumentan su contenido de  $\text{SiO}_2$ , incrementando así su grado de polimerización (i.e., aumento de enlaces entre los tetraedros de las moléculas de sílice). Lo anterior, junto con una progresiva disminución de la temperatura (Fig. 2.2), da como resultado un aumento en la viscosidad de los fundidos, lo cual resulta en una limitante reológica para continuar su ascenso a través de la corteza (McBirney and Murase 1984; Giordano et al. 2008).

A partir de modelos numéricos que consideran la viscosidad de un diapiro de material fundido ascendiendo por la corteza, diferentes geotermas para esta última, el contraste de densidad entre el diapiro y su roca caja, la difusión termal del primero sobre la segunda y el efecto en la deformación de la roca caja por la sobre presión generada por el diapiro y sus volátiles exsueles, se ha deducido que existe una transición dúctil-frágil para la

corteza a los  $2 \pm 0.5$  kbar (i.e.,  $\sim 6,5 \pm 1,5$  km considerando  $2,7 \text{ g/cm}^3$  como la densidad de la corteza; Burov et al. 2003; Huber et al. 2019). Dicha transición, cuya existencia es sustentada también por estudios petrológicos y geofísicos (Fig. 2.5), representa una zona óptima para el emplazamiento final de los fundidos ascendentes en la corteza superior *priori* a una eventual erupción.

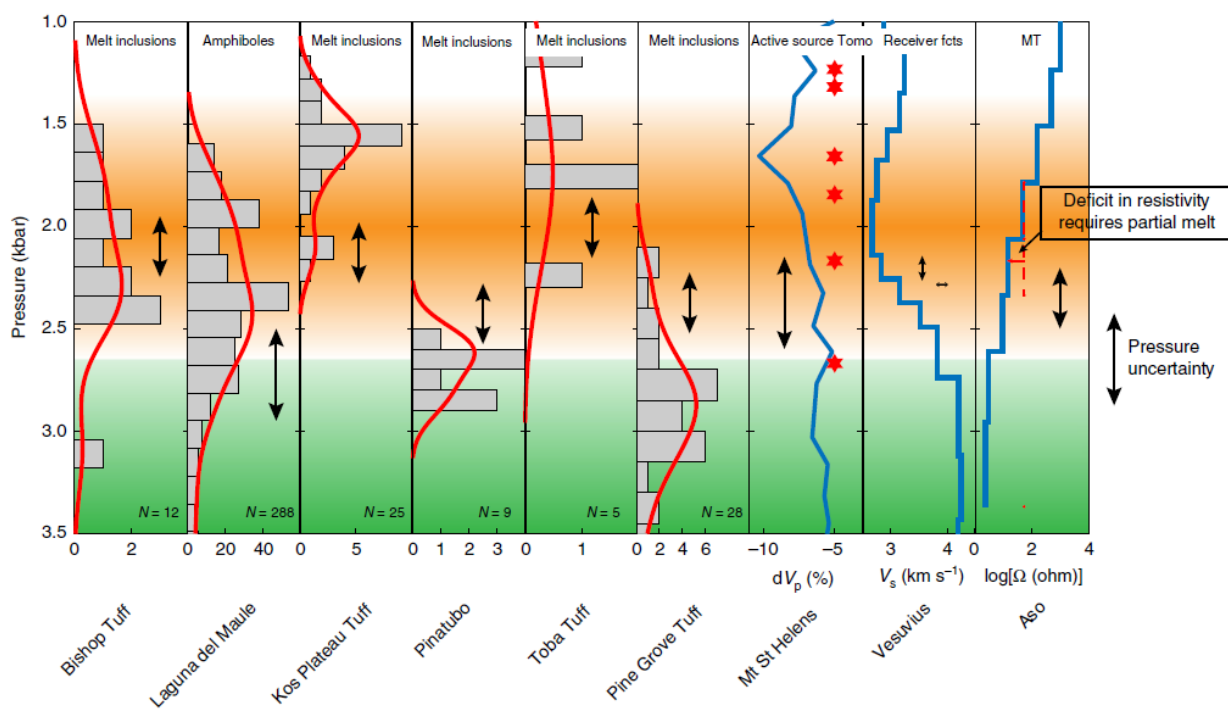


Fig. 2.5: Gráficos para diferentes sistemas volcánicos de los cuales se infiere como la presión óptima de almacenamiento de reservorios magmáticos activos (con más de un 25% de fundido) previo a una erupción se da en la corteza somera en torno a los  $2 \pm 0.5$  kbar. Los métodos utilizados corresponden a análisis petrológicos experimentales (estrellas rojas), inclusiones vítreas y anfíboles junto con métodos geofísicos de inversión sísmica en ondas  $V_p$ ,  $V_s$  y magnetotelúrica (imagen tomada de Huber et al. 2019).

## 2.2. Magmatismo en la Zona Volcánica Central de los Andes

La evolución geológica del margen continental Andino de Sudamérica se ha caracterizado por una abundante actividad magmática y volcánica como consecuencia de una subducción que se remonta al Paleozoico (en particular al Carbonífero; ca. 330 Ma), la cual luego de un gap durante el Triásico, fue retomada de forma casi ininterrumpida desde el Jurásico hasta la actualidad (Charrier et al. 2007). La evidencia de este proceso de subducción ha quedado registrada en diferentes afloramientos de roca que han sido interpretados como el desarrollo de sucesivos arcos magmáticos que progresivamente han migrado desde el este hacia oeste del continente (Mpodosis and Ramos 2008; Charrier and Muñoz 1994; Charrier et al. 2007). En la actualidad, la Zona Volcánica Central de los Andes (ZVCA), desarrolla entre los 14° y 27° de latitud sur, se configura por la subducción de la Placa de Nazca (ca. 50 a 60 Ma) bajo la Placa de Sudamérica a una tasa de ~8 cm/año y una convergencia oblicuidad variable entre los 0° a 24° oeste (Stern 2004; Stern et al. 2007 y referencias ahí establecidas). Lo anterior genera un frente volcánico a ~300 km de la fosa y a 135 km por sobre el *slab* subductado, el cual posee un ángulo de ~25°.

Sin embargo, los procesos tectonomagmáticos que configuraron los principales rasgos morfotectónicos de la ZVCA, y que son visibles en la actualidad (i.e., Oroclino Boliviano, *plateau* del Altiplano Puna y arco volcánico), se comenzaron a desarrollar hace ~25 Ma debido a un episodio deformacional denominado en la literatura como Fase Quechua (Isacks 1988; Allmendinger et al. 1997; Noble et al. 1997). Se ha planteado que una horizontalización en el ángulo de subducción (<20°) y un aumento en la tasa de convergencia de la placa oceánica de Nazca (>10 cm/año; Pardo-Casas and Molnar 1987) generó una mayor interacción termal entre la astenosfera sobreyacente al *slab* y la litósfera continental, produciendo que esta última se comportara de forma más dúctil por el aumento de su temperatura (i.e., debilitamiento termal; Isacks 1988). A consecuencia de lo anterior y por los esfuerzos tectónicos horizontales producto de la convergencia de placas, la corteza respondió engrosándose por el acortamiento en la dirección de su eje horizontal este-oeste hasta alcanzar cerca de 70 km de espesor (Beck

and Zandt 2002). Así, el debilitamiento termal de la litósfera sería el principal mecanismo formador de la flexura del Oroclino Boliviano, del alzamiento del Altiplano Puna Plateau y de la segunda corteza más gruesa del planeta Tierra después de la presente bajo los Himalayas (siendo, sin embargo, la corteza más gruesa del planeta con un arco volcánico activo).

Sin embargo, el proceso de acortamiento da cuenta solo del 70 – 80% del engrosamiento cortical que sustenta el *plateau* del Altiplano-Puna. Por lo anterior, se plantea también que un adelgazamiento del manto litosférico junto con una adición magmática podría haber contribuido a formar el otro 20% de la corteza de los Andes Centrales o en su defecto aportar la isostasia necesaria para sostener el alzamiento del *plateau* (Thorpe et al. 1981; Reymer and Schubert 1984; Allmendinger et al. 1997; Perkins et al. 2016). La hipótesis de la adición magmática es consistente con las evidencias de un aumento violento del flujo de magmatismo silíceo hacia la corteza (i.e., *flare-up*), lo cual se refleja en la generación de depósitos ignimbríticos masivos en la ZVCA, entre los cuales se destacan los pertenecientes al Altiplano Puna Volcanic Complex (APVC; Fig. 1.2; de Silva 1989a, b), y en la generación de grandes cuerpos magmáticos como el Altiplano Puna Magma Body (APMB; Fig. 1.3) o Cerro Galán Magma Body (Fig. 2.6; Ward et al. 2014; 2017; Perkins et al. 2016).



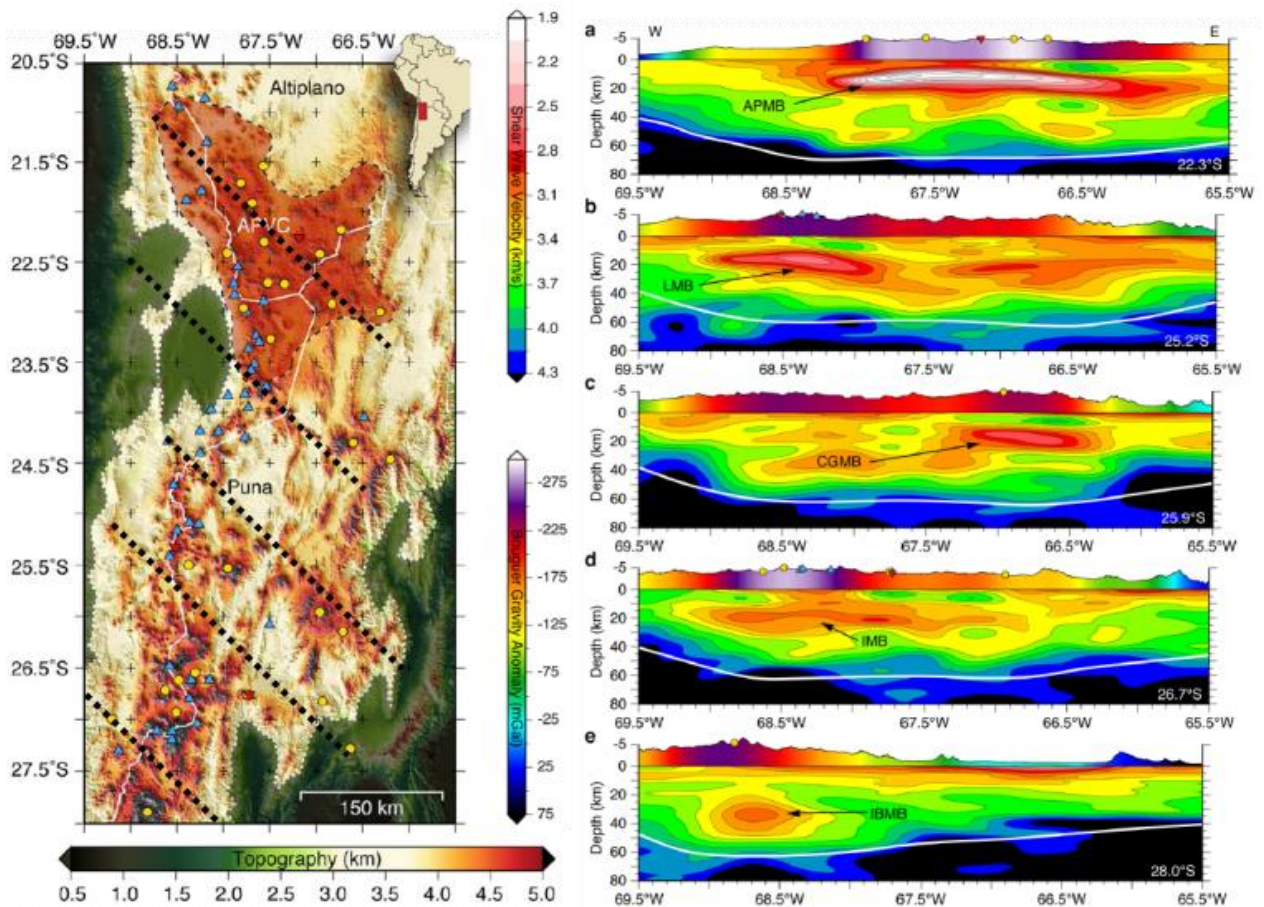


Fig. 2.6: Perfiles geofísicos de sismicidad y gravimetría realizados en el Altiplano Puna Plateau que interpretan la existencia de diferentes reservorios magmáticos activos a partir de la correlación entre anomalías de Bouguer negativas y zonas con una atenuación en la velocidad de ondas S. Las líneas punteadas negras de figura de la izquierda corresponden de norte a sur a cada uno de los perfiles geofísicos, mientras que la línea blanca presente en cada uno de estos últimos representa el Moho. Los cuerpos de magma se identifican como Altiplano Puna Magma Body (APMB), Lazufre Magma Body (LMB), Cerro Galan Magma Body (CGMB); Incahuasi Magma Body (IMB); Incapillo-Bonete Magma Body (IBMB) (imagen modificada de Ward et al. 2017).

El APVC es un campo volcánico andesítico-riolítico de 70.000 km<sup>2</sup> de extensión entre los 21° y 24° de latitud sur que comenzó a formarse hace ~11 Ma por medio de al menos tres pulsos magmáticos o *flare-up* a los 8, 6 y 4 Ma aproximadamente, los cuales acumularon ~13.000 km<sup>3</sup> de material volcánico (Fig. 2.7; Salisbury et al. 2010). Algunos de sus principales depósitos corresponden a las ignimbritas Sifón (ca. 8 Ma), Toconao (ca. 5 – 4 Ma) y Atana (ca. 4 Ma), las cuales poseen volúmenes entre los 1.000 – 2.500 km<sup>3</sup> cada una (Fig. 2.8; de Silva 1989a; Lindsay et al. 2001; de Silva et al. 2006).

Sincrónicamente, y posterior al emplazamiento de los grandes depósitos ignimbríticos, se desarrollaron otros tipos de estructuras volcánicas como estratovolcanes de composición andesítica a dacítica (Feeley and Davidson 1993; Sparks et al. 2008; Walker et al. 2013), domos tipo torta de composición dacítica a riolítica (de Silva et al. 1994; Watts et al. 1999) y conos de escoria con composición entre andesita basáltica y andesita (Mattioli et al. 2006; Gonzalez-Maurel et al. 2019).

El origen de los depósitos del APVC se ha relacionado estrechamente con la génesis y evolución del APMB debido a que este último se encuentra emplazado por debajo del APVC (Fig. 1.3; Ward et al. 2014). A partir de estudios de sísmica, conductividad eléctrica, gravimetría, petrología experimental entre otros (Chmielowski and Zandt 1999; del Potro et al. 2013; Ward et al. 2014; Perkins et al. 2016; Lauminier et al. 2017; Spang et al. 2021), se ha establecido que el APMB representa en la actualidad el cuerpo magmático activo (i.e., un reservorio tipo *mush* que contiene 14 – 27% de material fundido y 10% de agua disuelta) más grande del planeta Tierra con sus 500.000 km<sup>3</sup> de volumen. Este cuerpo magmático, cuyo centro se encuentra debajo del volcán Uturuncu (22°15'S y 67°11'O; Sparks et al. 2008), se emplaza entre 5 y 25 km bajo el nivel del mar con un radio de 200 km. El rol del APMB en el volcanismo del APVC, y el de otros cuerpos magmáticos como los presentados en la Fig. 2.6 en el volcanismo de la ZVCA, es ser zonas de *mixing* magmático entre fundidos poco evolucionados a intermedios (i.e., desde basaltos provenientes del manto a andesitas) con material cortical peraluminoso altamente evolucionado de composición dacítica a riolítica (Kay et al. 2010; Ward et al. 2017; Wörner et al. 2018). Mediante modelos geoquímicos, se ha estimado que el aporte de material cortical a los productos volcánicos de la ZVCA varía entre un 22% y 68% (Kay et al. 2010; Godoy et al. 2014; 2017; Freymuth et al. 2015).

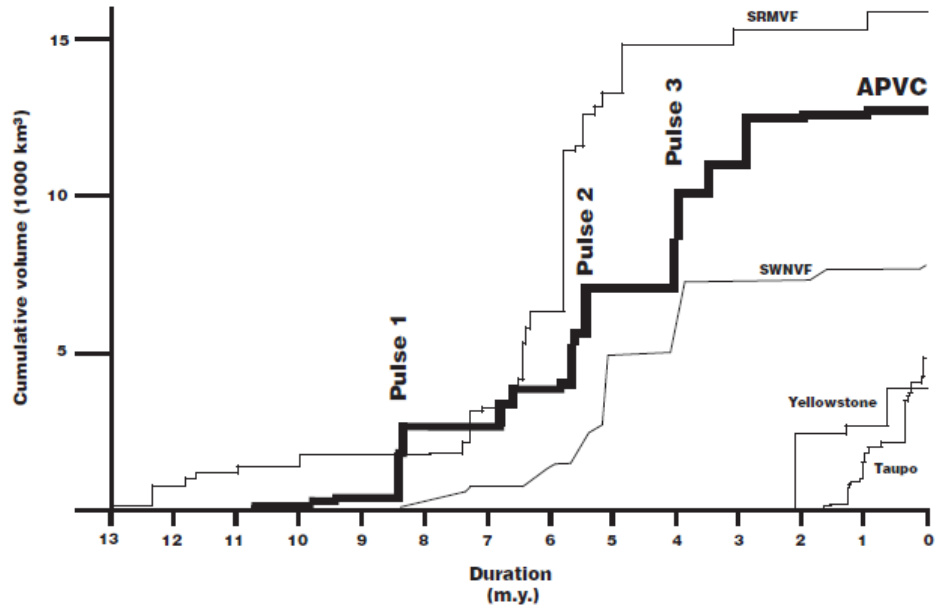


Fig. 2.7: Gráfico con el volumen acumulado de material volcánico eruptado en el APVC (~13.000 km<sup>3</sup>) donde se destacan tres pulsos magmáticos principales (Salisbury et al. 2010). A modo de comparación, se presenta también el volumen acumulado de otros campos volcánicos como Southern Rocky Mountain (SRMVF), Southwest Nevada (SWNVF), Yellowstone y Taupo.

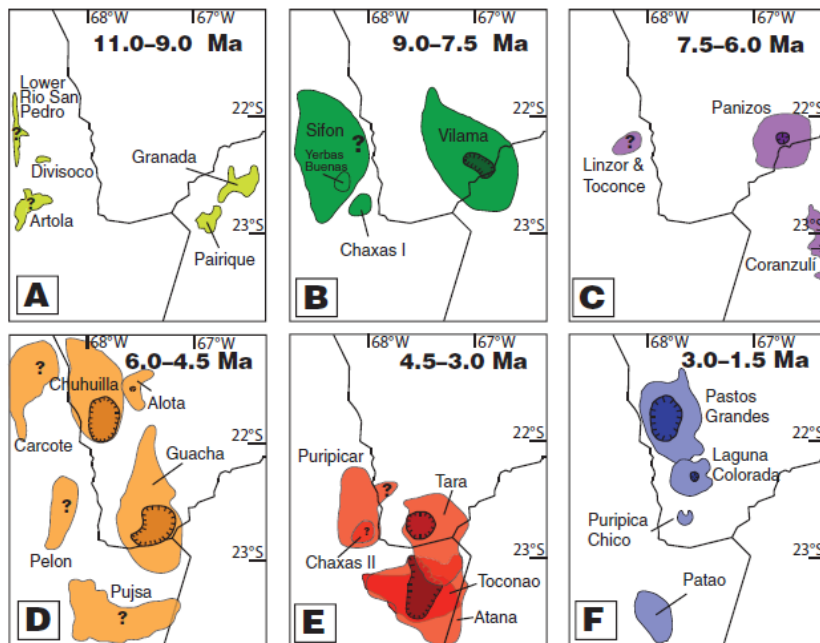


Fig. 2.8: Esquemas con las distribuciones de los principales depósitos ignimbríticos y calderas del APVC en función de su edad (Salisbury et al. 2010). Entre estos se destacan las ignimbritas Sifón (B), Toconao y Atana (E). Los depósitos se encuentran distribuidos en torno al punto trifinio entre Chile, Bolivia y Argentina cubriendo un área de ~70.000 km<sup>2</sup>.

### 2.3. Sistema geotermal de Cerro Pabellón

Debido al contexto geológico en que se encuentra la Cordillera de los Andes (i.e., un ambiente de subducción con magmatismo activo y ~200 volcanes de edad Pleistoceno-Holoceno), se ha propuesto que ella representa una de las provincias geotermales menos desarrolladas e inexploradas del mundo (Lahsen et al. 2015). En particular, Chile posee ~100 volcanes de edad Pleistoceno-Holoceno junto con ~60 campos volcánicos y mega calderas con registro de actividad Holocena (Stern et al. 2007). Dado el alto potencial de los Andes chilenos para el desarrollo de este tipo de energía renovable, lo cual se ha reflejado en exploraciones que comenzaron a principios del siglo XX y que han identificado más de 300 áreas geotermales (Lahsen et al. 2015; Aravena et al. 2016), se ha dividido su territorio en dos principales zonas volcánicas-geotermales (Aravena et al. 2016). Estas corresponden a la Zona Geotermal Norte (17°S – 28°S) y la Zona Geotermal Centro-Sur (33°S – 46°S; Fig. 2.9). Dichas zonas constituyen una conjunción entre magmatismo somero, lineamientos estructurales, zonas de permeabilidad en la corteza superior, volcanismo y emanaciones de aguas calientes en piscinas burbujeantes y/o géisers.

El año 2017 Cerro Pabellón se convirtió en la primera planta geotérmica de Chile y Sudamérica (denominada como Apacheta en Fig. 2.9). Su capacidad productiva por medio de 6 pozos de producción y 4 de reinyección, y posterior a su expansión del año 2020, quedó en 81 MWe (i.e., equivalente al consumo de 165.000 hogares), lo cual representa un 0,34% de la capacidad eléctrica instalada en Chile de 23.590 MWe (Cappeti et al. 2020).

Desde el descubrimiento del reservorio geotermal de Cerro Pabellón en el año 1999 se han realizado diferentes estudios que han determinado la presencia de un alto gradiente termal (~200 °C/km) respecto al que usualmente presenta la corteza continental (i.e., ~25 °C/km). Por medio del análisis de emanaciones de gases desde el volcán Apacheta (4 km al NW de Cerro Pabellón) y fluidos calientes provenientes de los pozos de exploración se determinó que entre la cota 4.500 y 3.000 m existe un aumento de temperatura hasta los ~300 °C (Fig. 2.10; Urzúa et al. 2002).

Este alto gradiente de temperatura estaría controlado por una componente magmática y una componente estructural. La primera, además de reflejarse en el contexto volcánico en que se encuentra el sistema geotermal de Cerro Pabellón, se evidencia en la naturaleza de los fluidos del reservorio. Estudios de isotopía de oxígeno e hidrógeno (i.e.,  $\delta^{18}\text{O}$  y  $\delta\text{D}$ ) en las fumarolas del volcán Apacheta han deducido que la génesis de los fluidos corresponde a aguas meteóricas mezcladas con un ~30% de aguas magmáticas (Urzúa et al. 2002). Por otro lado, la componente estructural se evidencia en un primer orden por el lineamiento NW-SE de ~70 km donde se encuentra el graben de Inacaliri y el sistema geotermal de Cerro Pabellón (Fig. 1.1 y 1.2). En coherencia con dicho lineamiento, se disponen también las fumarolas y zonas de alteración fósil del volcán Apacheta junto con la mineralogía de alteración presente en los núcleos de roca extraídos desde los pozos de exploración del sistema geotermal (Maza et al. 2021; Vidal et al. 2022; 2023). Cabe destacar que las estructuras con alineación NW-SE son comunes en el Altiplano Puna Plateau debido a los cambios en el campo de esfuerzos durante su evolución tectónica. Estas estructuras controlan el emplazamiento de cuerpos magmáticos, depósitos minerales, estructuras volcánicas y manifestaciones hidrotermales (Chernicoff et al. 2002; Tibaldi et al. 2009; 2017; Giambiagi et al. 2016). Lo anterior ha llevado a proponer que la conjunción entre magmatismo y estructuras son claves para entregar calor a los fluidos y permitir su ascenso por zonas de alta permeabilidad (Maza et al. 2021; Vidal et al. 2022; 2023).

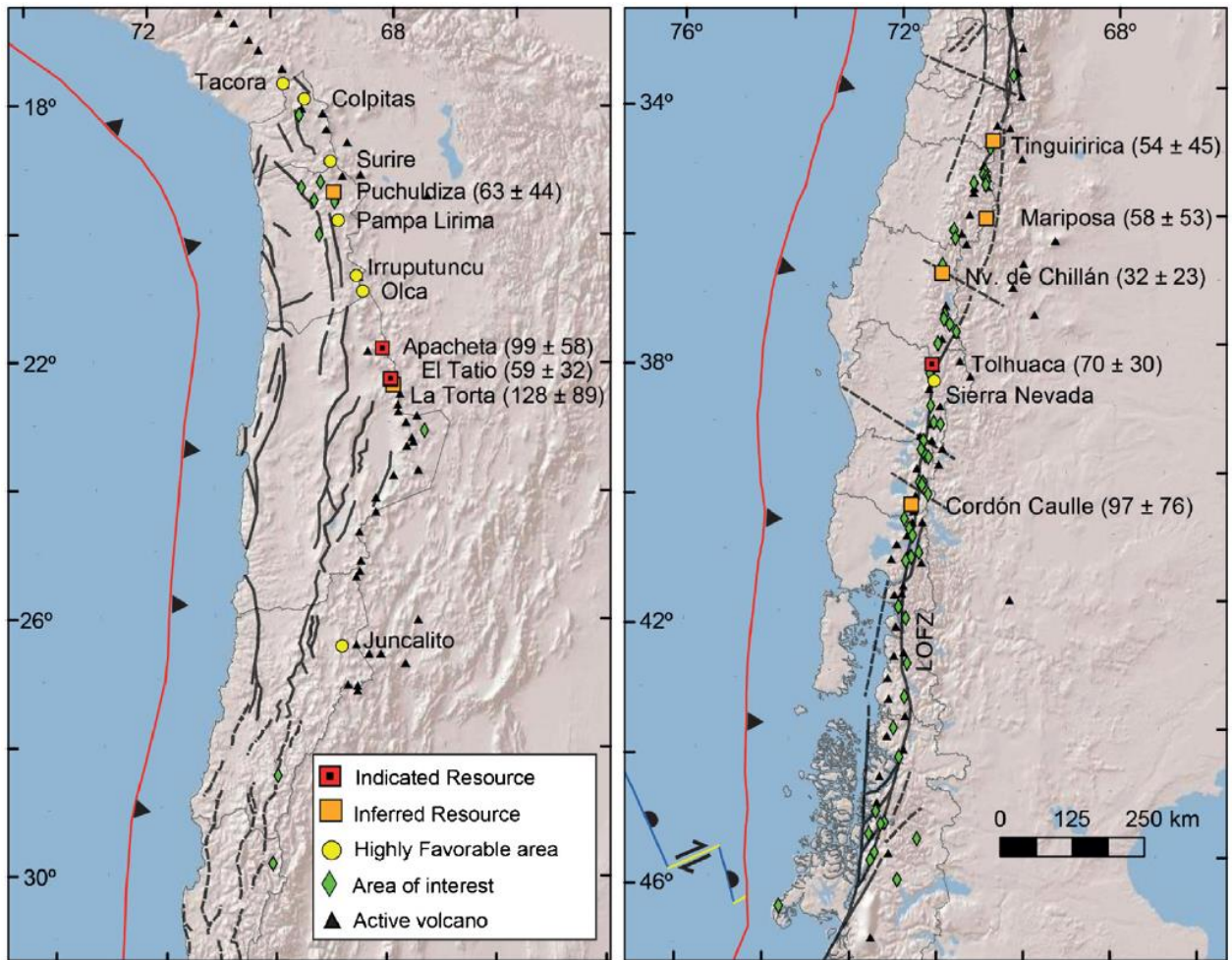


Fig. 2.9: Mapa del margen continental chileno donde se exponen la Zona Geotermal Norte (izquierda) y la Zona Geotermal Centro-Sur (derecha), las cuales se encuentran controladas por el magmatismo, volcanismo y lineamientos estructurales de la Cordillera de Los Andes. Las zonas de mayor potencial para la explotación de energía geotérmica se encuentran señalados con la magnitud ( $\pm$ incertidumbre) de sus recursos indicados e inferidos (Aravena et al. 2016).

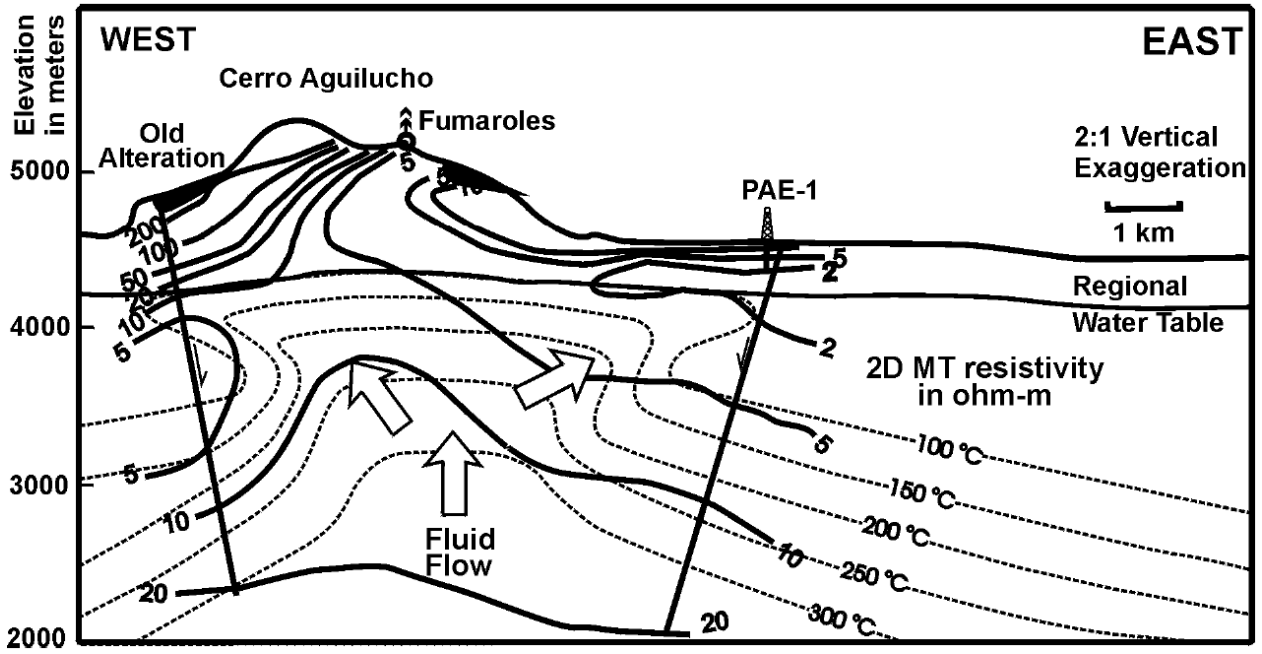


Fig. 2.10: Sección representativa del sistema geotermal de Cerro Pabellón en la cual se expone la variación de temperatura y resistividad en profundidad. En la imagen se destaca el pozo PAE-1 descubridor del sistema junto con las fumarolas y zonas de alteración fósil presentes en el volcán Apacheta (llamado también Cerro Aguilucho; imagen tomada de Urzúa et al. 2002).

## 2.4. Magmas como fuentes de calor en la corteza superior

Ante la dificultad de entender el rol que jugaría un volcán como fuente de calor para un sistema hidrotermal (e.g., volcán Azufre) debido, entre otros, a la complejidad de registrar la duración de su reservorio a temperaturas superiores al *solidus* y la imposibilidad de evaluar los mecanismos de transferencia de calor hacia la roca caja, se hace necesario recurrir al estudio de plutones que fueron emplazados a profundidades someras y que en la actualidad se encuentran exhumados. A partir de estos, es posible determinar con menor incertidumbre las condiciones de evolución y enfriamiento de un reservorio magmático.

Así, un modelo representativo de tales procesos y con atributos comparables a los evidenciados por el reservorio del volcán Azufre (*i.e.*, composición, profundidad y tiempo de emplazamiento) puede ser evaluado a partir del ampliamente estudiado plutón La Gloria (Cornejo and Mahood 1997; Gutiérrez et al. 2013; Payacán et al., 2014; Aravena et al. 2017; Gutiérrez et al. 2018). Este plutón que aflora en la zona central de Chile (33°30'S y 70°8'O), corresponde a un cuerpo félsico zonado (61 – 65 wt% SiO<sub>2</sub>) de ~200 km<sup>3</sup> que se emplazó en la corteza superior (~1 kbar) en un periodo de ~1 Ma durante el Mioceno (~10 Ma). Por medio de dataciones de alta precisión (ID-TIMS U-Pb en zircones; Gutiérrez et al. 2018), simulaciones numéricas (Gutiérrez et al. 2013; Aravena et al. 2018), y estudios de su fábrica magmática y magnética (Gutiérrez et al. 2013; Payacán et al., 2014), se ha logrado establecer que la evolución del plutón La Gloria se dio en cuatro etapas magmáticas principales que elevaron la temperatura de la roca caja sobreyacente a él de 200 a 500 °C.



### 2.4.1. Emplazamiento ( $\Delta t = 1 \text{ Ma}$ ) y etapa convectiva ( $t = 2 - 9 \text{ ka}$ )

A partir de dataciones  $U^{238}/Pb^{206}$  en zircones, Gutiérrez et al. (2018) determinaron que el emplazamiento del plutón La Gloria se dio en un periodo de 1 Ma por medio de una serie de pulsos magmáticos entre los 11,3 – 10,2 Ma. Una vez emplazado el plutón (primera etapa), y por tanto finalizados los eventos de rejuvenecimiento, comienza su segunda etapa, la cual considera el enfriamiento y cristalización a partir de una temperatura de  $\sim 1020 \text{ }^\circ\text{C}$  (línea punteada roja en Fig. 2.11A). Esta caída de temperatura produce un contraste de densidad entre las fases cristalizadas y el líquido residual, lo cual da paso a la formación de celdas convectivas dentro de la cámara. Sin embargo, en esta segunda etapa se da un fenómeno adicional, ya que a los  $850 \text{ }^\circ\text{C}$  se logra una cristalinidad del 47% que produce que el magma comience a evolucionar de manera heterogénea entre un fundido caliente y otro frío. Dada estas últimas condiciones, el modelamiento numérico de Gutiérrez et al. (2013) toma como referencia dicha temperatura y cristalinidad para establecer un tiempo  $t=0$  (línea punteada azul en Fig. 2.11A).

A medida que continua el enfriamiento hasta los  $800 \text{ }^\circ\text{C}$  a  $t=2 \text{ ka}$ , se forma un frente cristalino (magma frío) que cumple la función de alimentar y aislar termalmente el magma caliente y convectivo presente en el núcleo del reservorio por medio del calor latente que libera la cristalización. Por lo tanto, a los 2 ka ya se forma una barrera reológica (*crystal mush*) que inhibe la difusión termal desde el centro de la cámara hacia el medio exterior, prolongando así la vida del magma caliente hasta un  $t=20 \text{ ka}$  cuando alcanza el *solidus* (*inset* en Fig. 2.11B).

Dado que el paso a la tercera etapa evolutiva se da en diferentes momentos para cada uno de los magmas, se determinó un tiempo mínimo de 2,2 y 9 ka para la etapa convectiva en el magma frío y caliente, respectivamente.

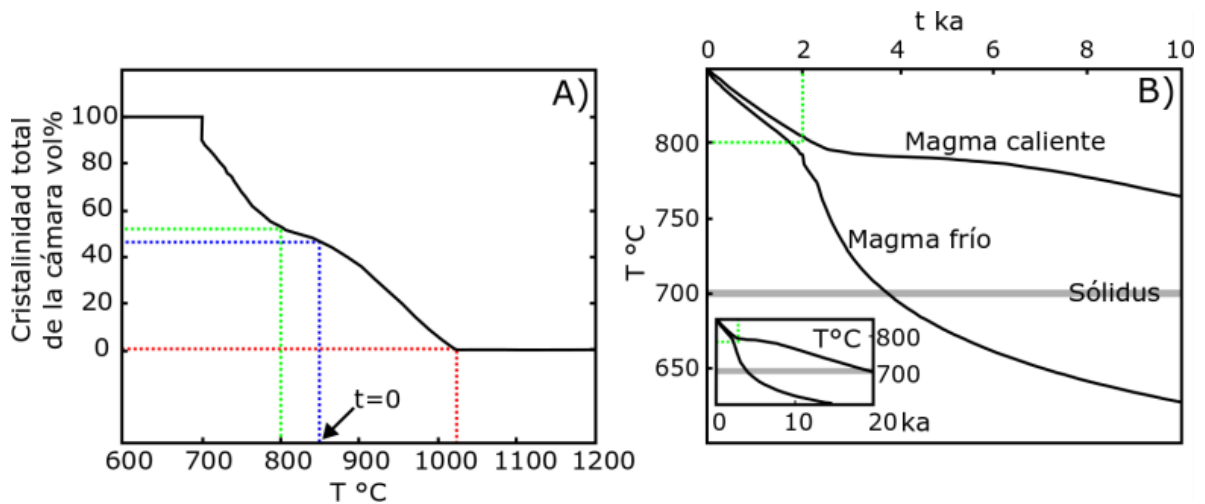


Fig. 2.11: Gráficos asociados a la evolución del Plutón La Gloria. En A) se destaca la cristalinidad total de la cámara, la temperatura a la cual comienza la cristalización (rojo), el conteo del tiempo desde  $t=0$  (azul) y la formación del frente cristalino o *mush* (verde). En el gráfico B) se expone la evolución heterogénea de la cámara en un magma caliente y otro frío al momento de comenzar la formación del frente cristalino (verde). En el *inset* se destaca el momento en que el magma caliente alcanza el *solidus* a los  $t=20$  ka (modificado de Gutiérrez et al. 2013).

#### 2.4.2. Etapa advectiva ( $t = 2 - 20$ ka)

El inicio de la etapa advectiva se da a diferentes momentos para cada uno de los magmas una vez alcanzado un nivel crítico de cristalinidad en torno al 60% de su volumen (línea punteada rosada en Fig. 2.12). De este modo, cuando los magmas frío y caliente decaen a una temperatura de 770 °C ( $t= 2,2$  y 9 ka, respectivamente; Fig. 2.11) alcanzan dicho grado de cristalinidad que inhibe el movimiento convectivo dentro de la cámara, coincidiendo también con el inicio de la exsolución de H<sub>2</sub>O. De esta forma, durante esta tercera etapa, el calor es removilizado mediante la advección del líquido residual hacia los niveles superiores de la cámara, lo cual se evidencia por medio del emplazamiento de diques aplíticos syn-plutónicos en el núcleo de la cámara, una mayor concentración de anfíbola en los márgenes de la cámara (por el H<sub>2</sub>O exsuelto), junto con un volumen de 7,5 km<sup>3</sup> de diques y sill leucograníticos en la roca caja circundante. Una sección transversal que simula el estado físico del reservorio magmático del Plutón La Gloria a  $t=3,5$  ka se ilustra en la Fig. 2.13.

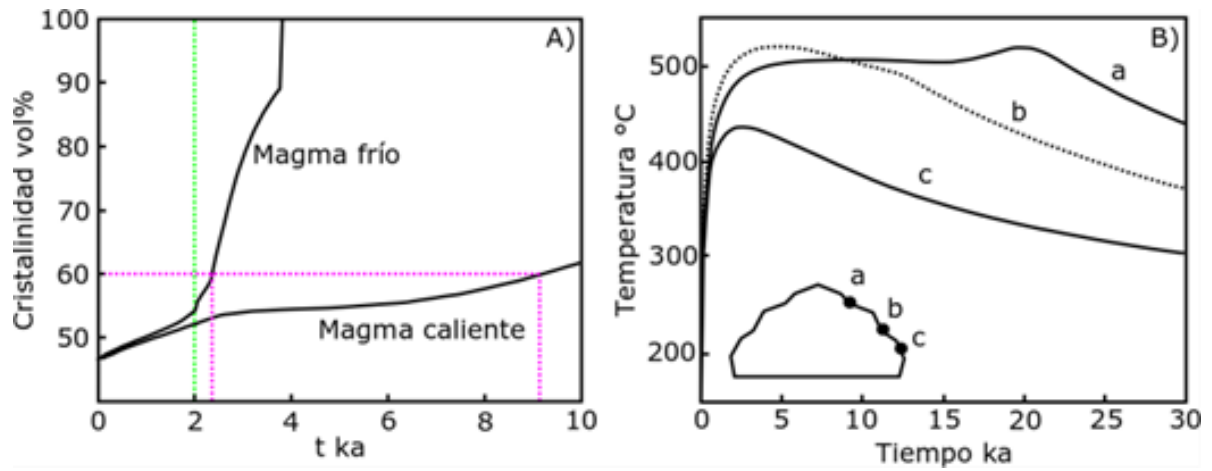


Fig. 2.12: Gráficos asociados a la evolución del Plutón La Gloria. En A) se destaca la evolución cristalina del magma frío y caliente, destacando el instante en que comienza la formación del frente cristalino (línea verde) y la etapa advectiva para cada uno de los magmas una vez alcanzado el 60 vol% de cristalinidad (línea rosada). En B) se expone la evolución termal de la roca caja, destacando que la mayor perturbación en cuanto a tiempo y temperatura se alcanza en el centro del techo de la cámara (punto "a") debido a la mayor cantidad de líquido extraído desde el núcleo del reservorio (modificado de Gutiérrez et al. 2013, Aravena et al. 2018).

### 2.4.3. Perturbación termal de la roca caja ( $t = 2 - 30$ ka)

Debido a la extracción de los líquidos residuales desde la cámara hacia los niveles superiores, es que la mayor perturbación termal se da en el techo del plutón a partir de los 2,2 ka, manteniéndose en el tiempo a medida que continua la cristalización hacia el centro del plutón (Fig. 2.12B). De esta forma, el gradiente termal de la roca caja que rodea la intrusión en su zona superior (i.e.,  $200\text{ }^{\circ}\text{C}$ ) se eleva a temperaturas que sobrepasan los  $500\text{ }^{\circ}\text{C}$  hasta los 20 ka en las zonas que se encuentran sobre el centro del plutón (ver curva 'a' en Fig. 2.12B).

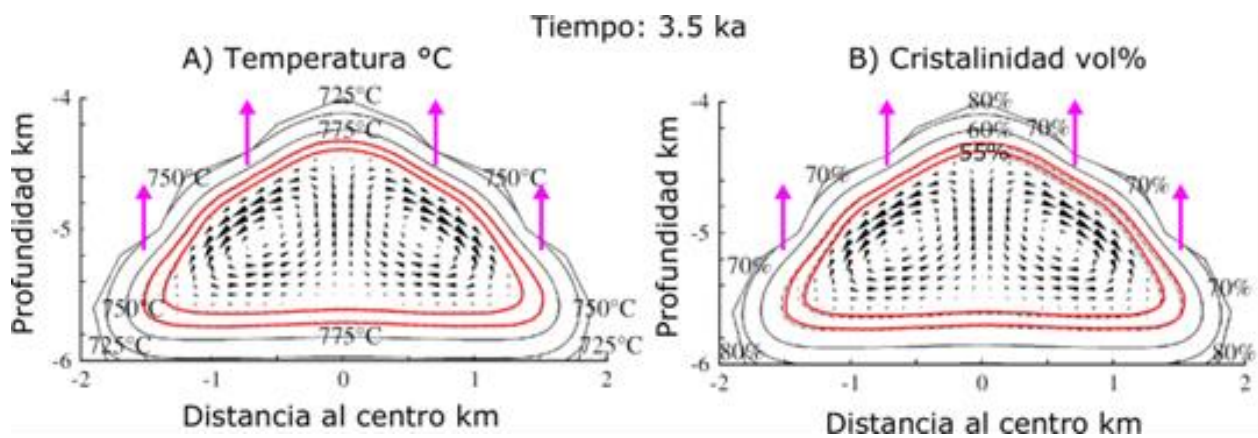


Fig. 2.13: Esquema representativo del estado físico de la cámara magmática del Plutón La Gloria a  $t=3,5$  ka. Se destaca en rojo la zona de cristalinidad crítica a partir de la cual comienza la extracción del fundido (flechas rosadas) y por tanto la etapa advectiva (modificado de Gutiérrez et al. 2013).

#### **2.4.4. Síntesis del rol de los plutones como fuentes de calor**

La importancia del estudio de los plutones en el contexto presentado radica en la estrecha relación que guarda el magmatismo como medio de transporte del calor hacia la corteza superior y superficie de la Tierra. Según lo expuesto, el Plutón La Gloria (~200 km<sup>3</sup>) presenta diques con un volumen de 7,5 km<sup>3</sup>, lo cual resulta suficientemente voluminoso como para generar erupciones volcánicas y transportar fluidos y calor hasta niveles aún más someros de la corteza (< 1 kbar ≈ 3,3 km). Adicionalmente, a partir de los modelamientos de Gutiérrez et al. (2013), es posible establecer un tiempo de 20 ka para la transferencia activa de calor hacia la roca caja, elevando el gradiente termal de 200 a 500 °C en el entorno cercano al techo del plutón.

# **CAPÍTULO 3: A tale of a lava from its shallow zoned reservoir to surface: the case Azufre volcano in the context of the Altiplano Puna Magma Body (northern Chile)**

Darío S. Hübner <sup>1,2,\*</sup>, Miguel-Ángel Parada <sup>1,2</sup>, Eduardo Morgado <sup>3</sup>, Francisca Mallea-Lillo <sup>1,2</sup>

<sup>1</sup> *Department of Geology, Faculty of Physical and Mathematical Sciences, University of Chile, 803 Plaza Ercilla, Santiago, Chile.*

<sup>2</sup> *Andean Geothermal Center of Excellence (CEGA), 803 Plaza Ercilla, Santiago, Chile.*

<sup>3</sup> *Escuela de Geología, Universidad Mayor, Manuel Montt 367, Providencia, Santiago, Chile.*

\*Corresponding author at: Department of Geology, University of Chile, 803 Plaza Ercilla, Santiago, Chile.

*E-mail addresses:* [dario.hubner@ing.uchile.cl](mailto:dario.hubner@ing.uchile.cl) (D. Hübner), [maparada@cec.uchile.cl](mailto:maparada@cec.uchile.cl) (M.A. Parada), [eduardo.morgado@umayor.cl](mailto:eduardo.morgado@umayor.cl) (E. Morgado), [francisca.mallea@ug.uchile.cl](mailto:francisca.mallea@ug.uchile.cl) (F. Mallea-Lillo).



# A tale of a lava from its shallow zoned reservoir to surface: the case of Azufre volcano in the context of the Altiplano Puna Magma Body (northern Chile)

Darío Salvador Hübner<sup>1,2</sup> · Miguel-Ángel Parada<sup>1,2</sup> · Eduardo Morgado<sup>3</sup> · Francisca Mallea-Lillo<sup>1,2</sup>

Received: 8 June 2022 / Accepted: 5 July 2023

© The Author(s), under exclusive licence to Springer-Verlag GmbH Germany, part of Springer Nature 2023

## Abstract

The Azufre volcano (21°47'S; 68°14'W) is emplaced above the western boundary of the Altiplano Puna Magma Body. The youngest lava of the Azufre volcano (50–331 ka) was selected for detailed studies because of the relevant petrological information that could emerge to understand its reservoir as a potential heat source of the neighboring Cerro Pabellón geothermal system. The studied lava corresponds to an andesite-dacite (61–63 SiO<sub>2</sub> wt%) with phenocrysts of plagioclase, amphibole (Group 1), biotite, pyroxenes, quartz, and olivine. The lava also contains aphanitic enclaves (58–60 SiO<sub>2</sub> wt%), whose groundmass have the same mineralogy of lava samples groundmass consisting of amphibole microphenocrysts (Group 2) and microlites of plagioclase, pyroxenes, and Fe–Ti oxides. Disequilibrium textures are commonly observed in the studied samples such as partially resorbed plagioclase phenocrysts, amphibole breakdown, and reverse zoning in pyroxene and plagioclase phenocrysts. Thermobarometry calculations indicated pressures of ~2 kbar for Group 1 amphiboles, temperatures of 905–1097 °C for Mg-rich pyroxene phenocrysts and Ca-rich plagioclase (An ≥ 66), and near-solidus temperatures of 712–788 °C for Group 1 amphibole-plagioclase pairs. Group 1 amphiboles also indicate crystallization from an evolved liquid (63–79 wt% of SiO<sub>2</sub>). Oxidation conditions of QFM + 0.9–2.5 log units were recorded in amphibole and Fe–Ti oxides. Rhyolite-MELTS models reproduce the composition of the high-temperature phases from a melt composition (andesitic enclave) at similar P–T–fO<sub>2</sub>. The arrival of new hot andesite magma into a crystal-rich shallow reservoir, thermally and compositionally zoned, would have triggered the studied eruption. Diffusion models in Fe–Ti oxides microlites indicated cooling temperatures of 742–866 °C during the sub-aerial emplacement of the lava.

**Keywords** Altiplano Puna Volcanic Complex · Crystal-mush reservoirs · Magma mixing · Magmatic enclaves

Communicated by Mark S Ghiorso.

✉ Darío Salvador Hübner  
dario.hubner@ing.uchile.cl

Miguel-Ángel Parada  
maparada@cec.uchile.cl

Eduardo Morgado  
eduardo.morgado@umayor.cl

Francisca Mallea-Lillo  
francisca.mallea@ug.uchile.cl

<sup>1</sup> Department of Geology, Faculty of Physical and Mathematical Sciences, University of Chile, 803 Plaza Ercilla, Santiago, Chile

<sup>2</sup> Andean Geothermal Center of Excellence (CEGA), 803 Plaza Ercilla, Santiago, Chile

<sup>3</sup> Escuela de Geología, Universidad Mayor, Manuel Montt 367, Providencia, Santiago, Chile

## Introduction

Current research indicates that magmatic evolution in subduction zones involves open systems of interconnected networks of molten lenses hosted in crystal-rich reservoirs (i.e., crystal-mush reservoirs; Marsh 1996; Bachmann and Bergantz 2004; Hildreth 2004; Bergantz et al. 2015), which could be developed at different depths in the crust (Kiser et al. 2016; Bachmann and Huber 2016; Cashman et al. 2017). Roots of these magmatic systems are typically thought to be at the mantle-crust transition (MASH zone; Hildreth and Moorbath 1988) or within deep crustal hot zones (Annen et al. 2006), where H<sub>2</sub>O-rich parental magmas of basaltic composition must modify their compositions and densities to gain enough buoyancy to rise. Processes such as mixing, crystallization, and lesser degree assimilation of crustal rocks could produce differentiated

## Abstract

The Azufre volcano (21°47'S; 68°14'W) is emplaced above the western boundary of the Altiplano Puna Magma Body. The youngest lava of the Azufre volcano (50 – 331 ka) was selected for detailed studies because of the relevant petrological information that could emerge to understand its reservoir as a potential heat source of the neighboring Cerro Pabellón geothermal system. The studied lava corresponds to an andesite-dacite (61 – 63 SiO<sub>2</sub> wt%) with phenocrysts of plagioclase, amphibole (Group 1), biotite, pyroxenes, quartz, and olivine. The lava also contains aphanitic enclaves (58 – 60 SiO<sub>2</sub> wt%), whose groundmass have the same mineralogy of lava samples groundmass consisting of amphibole microphenocrysts (Group 2) and microlites of plagioclase, pyroxenes, and Fe-Ti oxides. Disequilibrium textures are commonly observed in the studied samples such as partially resorbed plagioclase phenocrysts, amphibole breakdown, and reverse zoning in pyroxene and plagioclase phenocrysts.

Thermobarometry calculations indicated pressures of ~2 kbar for Group 1 amphiboles, temperatures of 905 – 1097 °C for Mg-rich pyroxene phenocrysts and Ca-rich plagioclase (An<sub>≥66</sub>), and near-solidus temperatures of 712 – 788 °C for Group 1 amphibole-plagioclase pairs. Group 1 amphiboles also indicate crystallization from an evolved liquid (63 – 79 wt% of SiO<sub>2</sub>). Oxidation conditions of QFM+ 0.9 – 2.5 log units were recorded in amphibole and Fe-Ti oxide. Rhyolite-MELTS models reproduce the composition of the high-temperature phases from a melt composition (andesitic enclave) at similar P-T-fO<sub>2</sub>. The arrival of new hot andesite magma into a crystal-rich shallow reservoir, thermally and compositionally zoned, would have triggered the studied eruption. Diffusion models in Fe-Ti oxides microlites indicated cooling temperatures of 742 – 866 °C during the sub-aerial emplacement of the lava.

Keywords: Altiplano Puna Volcanic Complex, crystal-mush reservoirs, magma mixing, magmatic enclaves.



### 3.1. Introduction

Current research indicates that magmatic evolution in subduction zones involves open systems of interconnected networks of molten lenses hosted in crystal-rich reservoirs (i.e., crystal-mush reservoirs; Marsh 1996; Bachmann and Bergantz 2004; Hildreth 2004; Bergantz et al. 2015), which could be developed at different depths in the crust (Kiser et al. 2016; Bachmann and Huber 2016; Cashman et al. 2017). Roots of these magmatic systems are typically thought to be at the mantle-crust transition (MASH zone; Hildreth and Moorbath 1988) or within deep crustal hot zones (Annen et al. 2006), where H<sub>2</sub>O-rich parental magmas of basaltic composition must modify their compositions and densities to gain enough buoyancy to rise. Processes such as mixing, crystallization, and lesser degree assimilation of crustal rocks could produce differentiated melt pockets of andesitic-dacitic composition that would rise in near adiabatic conditions to store at different levels of the crust (Annen et al. 2006; Dufek and Bachmann 2010; Solano et al. 2012; Laumonier et al. 2014; Jackson et al. 2018). The magma transport continues until decompression- and degassing-driven crystallization increase the melt viscosity, stalling it in shallow magma reservoirs located in the ductile-brittle transition of the upper crust ( $2 \pm 0.5$  kbar; Burov et al. 2003; Huber et al. 2019). In this locus, magma chambers (i.e., the volume of melt, exsolved volatiles, and crystals-dominated zones able to erupt) can form if enough rate of magma recharge is supplied to sustain the magma chamber above the solidus. Eventually, the magma chamber can be erupted due to internal or external triggers (e.g., magma mixing and earthquakes, respectively) that modify the magma rheology, thermal regime, and magma pressure (Tait et al. 1989; Tramontano et al. 2017; Caricchi et al. 2021).

Long-term storage conditions of magmatic reservoirs are thought to be cold (i.e., near to solidus temperatures on a scale of ka to Ma) from the evidence of uranium-series disequilibria coupled with Sr diffusion models in plagioclase, data of zircon and titanite, and numeric models (Cooper and Kent 2014; Szymanowski et al. 2017; Jackson et al. 2018). This hypothesis is consistent with the scarcity of geophysics surveys that have identified molten bodies even in active volcanic regions (see discussion in Glazner et al. 2004; Cooper and Kent 2014; Cashman et al. 2017). However, to build small- to super-

sized magma chambers ( $10^{-1} - 10^4 \text{ km}^3$ ), a continuous recharge of basaltic-intermediate liquids has also been suggested as a condition to generate or maintain bodies above the solidus (Gelman et al. 2013; Menand et al. 2015; Karakas et al. 2017; Jackson et al. 2018). Depending on the thermal maturity of the crusts, the rates to build magma chambers can vary between  $10^{-4} - 10^{-2} \text{ km}^3/\text{yr}$  (Karakas et al. 2017). Thus, although cold magma storage seems to be the rule in the long-term, magma reservoirs can be intruded by high-temperature liquids in determined narrow-span times to form ephemeral thermal zoned crystal-mush reservoirs with high melt content able to erupt (Hildreth 1981; Bachmann and Bergantz 2008).

The Azufre is a Pleistocene volcano ( $<1.1 \text{ Ma}$ ; Sellés and Gardeweg 2017; and references therein) that forms part of the Altiplano Puna Volcanic Complex (APVC; de Silva 1989a, b; de Silva and Kay 2018), which is one of the youngest ( $<10 \text{ Ma}$ ) and most voluminous felsic volcanic provinces of the Central Volcanic Zone of the Andes (CVZA; Stern 2004). The Azufre volcano is also located above the western margin of the Altiplano Puna Magma Body (APMB), the largest magma body on Earth ( $\sim 500,000 \text{ km}^3$  of volume), extending between  $21^\circ$  and  $23^\circ\text{S}$  in the CVZA (Chmielowski et al. 1999; Ward et al. 2014; Perkins et al. 2016; Wörner et al. 2018). Despite numerous regional-scale geochemical, isotopic, and geochronological studies have been carried out nearby of the Azufre volcano and on itself, particularly motivated by the spatial relationship of different volcanic centers with APMB (Godoy et al. 2017, 2022; Taussi et al. 2019; González-Maurel et al. 2019), no attempts have been made to understand the reservoir conditions that give rise to their different volcanic units.

We selected the volcanic materials of the youngest Azufre volcano eruption, because it could provide clues about the heat source of the Cerro Pabellón geothermal system, where the first geothermal power plant of South America has been working since 2017. This paper provides detailed petrographic data, mineral textures and compositions, P-T- $f\text{O}_2$  calculations, felsic-melt-composition calculation, and thermodynamic models to understand the conditions of the reservoir before the eruption of the studied lava. In addition, we also performed diffusion models to account for cooling temperatures during the emplacement of studied lava at sub-aerial conditions.

### 3.2. The Azufre volcano and its geologic setting

The CVZA includes the Altiplano-Puna Plateau, a major morphotectonic unit that has been building since ~25 Ma from the subduction of the oceanic Nazca Plate beneath the continental South American plate (Isacks 1988; Allmendinger et al. 1997). This morphotectonic unit and their associated volcanoes form the highest volcanic arc plateau on Earth (~70 km of crustal thickness; Beck and Zandt 2002), displaying average elevations of 3.7 and 4.7 km a.s.l. for the Altiplano and Puna, respectively, and volcano summits over 6 km a.s.l. (Allmendinger et al. 1997). In this context, APVC comprises the most voluminous and one youngest ignimbrite deposits of the CVZA (<10 Ma; de Silva et al. 2006; Wörner et al. 2018), covering an area of ~70,000 km<sup>2</sup> (Fig. 3.1a). The source of ignimbrites and other volcanic units such as the Azufre volcano could be associated with the APMB, which is currently considered a network of crystal-mush reservoirs (10 – 25% vol. of andesitic melt) that together form a batholithic size body emplaced in the upper crust (i.e., 5 – 8 kbar; de Silva and Gosnold 2007; del Potro et al. 2013; Ward et al. 2014; Laumonier et al. 2017; Spang et al. 2021). Recently, above the roof of APMB, have been detected shallow dacitic magma reservoirs ( $1 \pm 0.5$  kbar) feeding volcanic centers such as the Uturuncu volcano (Muir et al. 2014a, b; Comeau et al. 2015).

The Azufre volcano, located in the Ascotán-Inacaliri district (Northern Chile at 21°47'S; 68°14'W; Sellés and Gardeweg 2017), is a 2 km high stratovolcano above its surrounding plateau that is emplaced over a 70 km long NW-SE volcanic alignment between Palpana volcano and Inacaliri graben (Fig. 3.1a). The Azufre volcano started its volcanic activity ~1.1 Ma (Sellés and Gardeweg 2017; and references therein), forming four volcanic units (Fig. 3.1b; Godoy et al. 2022). Its volcanic products correspond to ~50 km<sup>3</sup> of andesite and dacite blocky lavas (60 – 69 SiO<sub>2</sub> wt%; Godoy et al. 2022) that contain andesitic enclaves with ellipsoidal shapes (major-axis length between 4 – 15 cm), forming smooth and chilled boundaries with the lava. Next to the Azufre volcano are emplaced the Chanca, Chac Inca, and Cerro Pabellón dacitic domes (65 – 67 SiO<sub>2</sub> wt%; Taussi et al. 2019), whose lavas deposits also display andesitic enclaves (57 – 62 SiO<sub>2</sub> wt%; Taussi et al. 2019).

We infer an age of the last eruptive stage of the Azufre volcano of 50 – 331 ka based on preservation of its crater and flow structures (such as levees, ogives, and steep flow front as is showed in Fig. 3.1b and Fig. 3.1c). These volcanic structures are comparable with those observed in <140 ka lavas of the Ascotán-Inacaliri district as the neighboring dacitic domes (Fig. 3.1b), whose ages are between 114 and 50 ka (Renzulli et al. 2006; Rivera et al. 2015; Tierney et al. 2016; see details of structures correlation in supplementary material “Inferred age of the last eruptive stage of the Azufre volcano”). Thus, the studied lava could represent one of the youngest volcanic products of the NW-SE volcanic alignment.

Currently, the Azufre volcano displays a low resistivity zone ( $\sim 5 \Omega\text{m}^{-1}$ ) at <10 km below the surface, which is interpreted as magma or hydrothermal fluid storage (Araya Vargas et al. 2019). It is consistent with the presence of paleo-hydrothermal vents on its west flank (Godoy et al. 2022), hot spring pools on its north flank (42°C; Risacher et al. 2011), and would be related to three fumaroles in the neighboring Apacheta volcano (109 – 118 °C; Urzua et al. 2002; Maza et al. 2021).

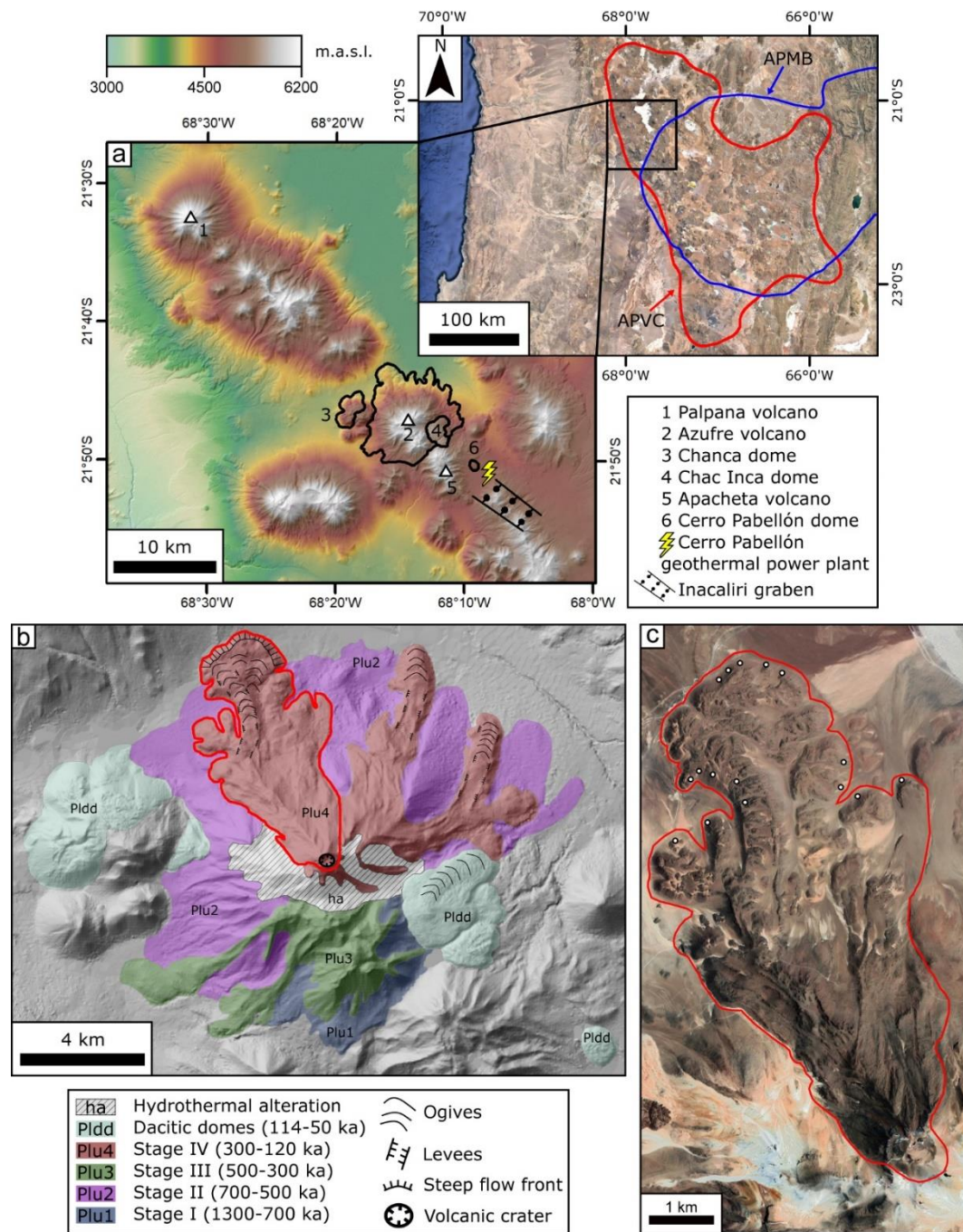


Fig. 3.1: Images showing: **a** The location of Altiplano Puna Volcanic Complex (APVC), the maximum extension of Altiplano Puna Magma Body (APMB; after Ward et al. 2014), and the volcanic alignment where the Azufre volcano, dacitic domes, and Cerro Pabellón geothermal power plant are emplaced. **b** The geologic map of the Azufre volcano (modified from Sellés and Gardeweg 2017; Godoy et al. 2022). **c** The volcanic crater and flow structures of the studied lava (within the red contour), which are also drawn in the geologic map **b**. We omit tags of sampling sites (white circles in **c**) to highlight the volcanic structures. To consult coordinates and samples tags see supplementary material “Sample locations”. Digital elevation model (DEM) of 12.5 m resolution (DEM ALOS-PALSAR; <https://vertex.daac.asf.alaska.edu>, date of data 17 July 2010) was used to make the elevation and geologic map of **a** and **b**, respectively. Satellite images **a** and **c** were obtained from Google Earth® freeware

## 2.3. Methodology

### 2.3.1 Sampling and analytical methods

Polished thin sections were prepared from the sixteen fresh lava samples and sixteen fresh enclave samples collected along the front of the studied lava flow deposit (Fig. 3.1c; see supplementary material “Sample locations”). Mineral and their textural recognition were determined using the Scanning Electron Microscope (SEM) FEI Quanta 250 at the University of Chile. Due to the isotropic fabric of samples, we estimated the volume (vol%) of mineral phases and vesicles (Table 3.1) as their relative area spread using image processing techniques and the JMicroVision® freeware. We carried out the volume estimations of both crystals and vesicles with major-axis lengths  $>500\ \mu\text{m}$  using scanned polished thin sections images that have an area of  $20 \times 40\ \text{mm}^2$ . Also, we performed volume estimations of those with major-axis lower than  $500\ \mu\text{m}$  with backscatter electron (BSE) images ( $3.7 \times 3.2\ \text{mm}^2$ ). We selected five and four representative samples of lava and enclave, respectively, for whole-rock and mineral chemistry analyses.

Whole-rock compositions of selected samples (Table 3.2) were obtained employing an Arcos Spectro ICP-OES (for major and minor elements) and a Perkin Elmer ELAN 9000 ICP-MS (for trace elements) at Bureau Veritas Mineral Laboratories (Vancouver, Canada) using SO-19 standard. The sample preparation includes a pulverization of less than 200 mesh (i.e.,  $\geq 85\%$  of sampled at grain size  $\leq 75\ \mu\text{m}$ ), loss on ignition (LOI) determination by the weight change showed by samples after being heated for one hour at  $1000^\circ\text{C}$ , the employ of  $\text{LiBO}_2/\text{Li}_2\text{B}_4\text{O}_7$  as flux, and digestion of glass bead with nitric acid. Accuracy on the standard was better than 1.5% (relative) for major and minor elements analyses (except for  $\text{P}_2\text{O}_5$ , whose accuracy was 3%) and lower than 6% (relative) in the case of trace element analyses (except for Ga and W, whose accuracy was 12% and 7%, respectively). In the same laboratory, FeO contents of samples were measured through titration via cold acid digestion of sulfuric and hydrofluoric acids, using potassium dichromate as titrant agent and a mix of distilled water, sulfuric acid, phosphoric acid, boric acid, and diphenylamine sulfonate as indicator solution. Due to the lava and enclave

samples do not exhibit macroscopic supergene or hydrothermal alteration (nor microscopic at the SEM analysis scale), we determined their Fe<sub>2</sub>O<sub>3</sub> content from FeO and Fe<sub>2</sub>O<sub>3</sub>T measured by titration and ICP-OES, respectively. Thus, as samples are fresh, the calculated Fe<sub>2</sub>O<sub>3</sub> belongs to the crystal lattice of magmatic minerals that form each sample. Fe<sub>2</sub>O<sub>3</sub> calculation and detailed values for uncertainties ( $2\sigma$ ), quality control, and blanks can be found in the supplementary material “Geochemistry analyses”, while detection limits are listed in Table 3.2.

The mineral compositions were obtained from an Electron MicroProbe JEOL JXA-8230 (EMPA) equipped with three wavelength-dispersive detectors at LAMARX laboratory, National University of Córdoba, Argentina. To obtain high quality measurements of major elements, we used an accelerating potential of 15 kV and an electron beam current of 20 nA as analytical conditions. Counting times for all elements were 10 s on peak and 5 s at each background position. In addition, different natural and synthetic standards were used at the beginning of each session to calibrate and ensure the quality of EMPA analyses, meaning accuracies better than 2% (relative) for major element analyses on analyzed standards. In addition, a focused beam (<5  $\mu\text{m}$ ) was used for all EMPA analyses except for plagioclases, which were performed with a defocused beam ( $\sim 10 \mu\text{m}$ ) to minimize alkali loss (Fiedrich et al. 2018). Some minor and trace elements were also measured as part of EMPA analysis routine for determined mineral phases (e.g., FeO and SrO in plagioclase), but without the proper analytical conditions (i.e., with an unknown uncertainty). Representative analyses are listed in Table 3.3 to Table 3.6, where the EN code in sample number identifies enclave samples and n indicates the number of measurements. The complete set of EMPA results can be found in supplementary material “EMPA analyses”.

We determine the pre-eruptive intensive conditions (i.e., T, P,  $f\text{O}_2$ ) using different geothermometers (Holland and Blundy 1994; Putirka 2005, 2008, 2016; Sauerzapf et al. 2008; Ghiorso and Evans 2008; Ridolfi et al. 2010; Ridolfi and Renzulli 2012), geobarometers (Anderson and Smith 1995; Ridolfi et al. 2010; Ridolfi and Renzulli 2012; Mutch et al. 2016), and oxybarometers (Sauerzapf et al. 2008; Ghiorso and Evans 2008; Ridolfi et al. 2010). The complete results obtained are in supplementary material “P-T-felsic melt composition- $f\text{O}_2$ -Solubility calculations”. The pre-eruptive conditions are also

obtained from equilibrium crystallization simulations using the 1.0.2 version of Rhyolite-MELTS freeware (Gualda et al. 2012). Additionally, to justify the cooling temperatures of the studied lava during its emplacement at sub-aerial conditions, we applied the interdiffusion coefficient models of Freer and Hauptman (1978), Aragon et al. (1984), and Prissel et al. (2020) in paired titanomagnetite-ilmenite microlites.

Finally, to determine the total uncertainty of the formerly mentioned techniques, we considered the inherent uncertainty of each one together with the propagated effect of the errors of calculated temperatures and pressures where applicable. As the analytical uncertainties of major elements analyses are low (<2%), we propagated their errors in specific cases that are mentioned in the text. Additional considerations about uncertainty propagations are highlighted in the text.



Table 3.1: Modal mineralogy and crystals size of the youngest lava deposit samples of the Azufre volcano and their enclaves

	Phase	Average vol% ( $\pm 2\sigma$ )			Size
		Porphyritic lava	Porphyritic enclaves	Aphanitic enclaves	
Phenocrysts	Plagioclase	15 (2.6)	9 (2.1)	0.5 (0.8)	0.3 – 7 mm
	Amphibole	3.5 (2)	1 (0.8)	0.6 (0.8)	0.5 – 2.3 mm
	Biotite	3.5 (2.4)	1 (0.5)	0.6 (1.2)	0.5 – 1.7 mm
	Pyroxene <sup>a</sup>	2 (0.8)	1 (0.5)	0.5 (0.8)	0.3 – 1 mm
	Quartz	1 (1)	-	-	0.5 – 2.3 mm
	Total <sup>b</sup>	25 (5)	12 (3)	2 (2.6)	
Groundmass	Plagioclase	66 (3.4)	70 (2.6)	73 (4.4)	< 250 $\mu\text{m}$
	Amphibole	4 (1.2)	9 (0.5)	13 (4.6)	70 – 500 $\mu\text{m}$
	Pyroxene <sup>c</sup>	4 (1.8)	6 (0.1)	10 (6)	< 100 $\mu\text{m}$
	Fe-Ti oxides	1 (0.6)	2 (0.3)	2 (0.6)	< 100 $\mu\text{m}$
	Total	75 (3.8)	87 (2.4)	98 (1.8)	
Total crystals		100	100	100	
Vesicles <sup>d</sup>		3 (0.6)	26 (0.5)	20 (4.4)	

<sup>a</sup>Orthopyroxene and clinopyroxene phenocrysts distribution in lava samples are around 70% and 30%, whereas in enclave samples are around 95% and 5%, respectively

<sup>b</sup>Total porphyritic lava samples also include trace amount of olivine and Fe-Ti oxides phenocrysts (0.2 – 1 mm), whose total volume does not exceed ~1 vol%. In enclave samples, only includes trace amount of olivine and quartz phenocrysts

<sup>c</sup>Orthopyroxene and clinopyroxene microlites distribution is almost the same (~50% each one) in the groundmass of lava and enclave samples

<sup>d</sup>Vesicularity was determined based on lava volume (or enclave) vesicle-free volume. Major-axis length of vesicles (ellipsoid shape) reach 160 and 600  $\mu\text{m}$  in lava and enclaves samples, respectively

Table 3.2: Whole-rock compositions of representative samples from the studied lava and enclaves of the Azufre volcano. Mg-number (Mg#) was calculated as molar Mg/(Mg+Fe<sup>2+</sup>). d.l. corresponds to detection limit. Details of calculation used in the table can be found in the supplementary material “Geochemistry analyses”

Sample:		Lava Azu 2	Lava Azu 3	Lava Azu 4	Lava Azu 7	Enclave Azu 7 EN	Enclave Azu 8 EN	Enclave Azu 10 EN	Lava Azu 14	Enclave Azu 14 EN
Major oxide (wt%)	d.l. (wt%)									
ICP-OES										
SiO <sub>2</sub>	0.01	60.4	61.0	60.8	60.9	58.9	56.3	56.5	61.9	58.6
Al <sub>2</sub> O <sub>3</sub>	0.01	16.3	16.4	16.2	16.0	16.1	16.2	16.7	16.4	17.1
Fe <sub>2</sub> O <sub>3T</sub>	0.04	5.7	5.6	5.6	5.3	6.3	6.5	6.9	5.1	6.0
FeO	0.2	2.8	2.8	2.9	2.8	3.5	3.4	3.7	2.1	2.2
Fe <sub>2</sub> O <sub>3</sub> <sup>a</sup>		2.6	2.5	2.4	2.2	2.4	2.8	2.8	2.8	3.5
MgO	0.01	3.3	3.1	3.1	3.3	3.7	3.7	4.3	2.3	2.9
CaO	0.01	5.5	5.3	5.2	5.3	5.8	7.0	6.5	4.8	6.0
Na <sub>2</sub> O	0.01	3.6	3.6	3.6	3.5	3.4	3.0	3.3	3.6	3.3
K <sub>2</sub> O	0.01	2.7	2.8	2.8	2.6	2.2	2.5	2.4	3.1	2.2
TiO <sub>2</sub>	0.01	0.7	0.7	0.8	0.7	0.9	0.8	1.0	0.7	0.8
P <sub>2</sub> O <sub>5</sub>	0.01	0.2	0.2	0.2	0.2	0.2	0.2	0.2	0.2	0.2
MnO	0.01	0.1	0.1	0.1	0.1	0.1	0.1	0.1	0.1	0.1
Cr <sub>2</sub> O <sub>3</sub>	0.002	0.02	0.02	0.01	0.02	0.02	0.01	0.02	0.01	0.01
LOI		1.5	1.3	1.7	2.1	2.5	3.8	2.3	1.8	2.8
Total <sup>b</sup>		99.7	99.7	99.7	99.7	99.7	99.7	99.7	99.7	99.7
Mg#		0.67	0.66	0.65	0.68	0.65	0.66	0.68	0.67	0.71

<sup>a</sup>Fe<sub>2</sub>O<sub>3</sub> was calculated from Fe<sub>2</sub>O<sub>3T</sub> and FeO concentrations obtained by ICP-OES and titration, respectively

<sup>b</sup>Sum of major oxides without considering Fe<sub>2</sub>O<sub>3T</sub>

Table 3.2: (continued)

Sample:		Lava Azú 2	Lava Azú 3	Lava Azú 4	Lava Azú 7	Enclave Azú 7 EN	Enclave Azú 8 EN	Enclave Azú 10 EN	Lava Azú 14	Enclave Azú 14 EN
Minor and trace elements (ppm)	d.l. (ppm)									
ICP-OES										
Ni	20	33	45	27	39	54	36	31	20	<20
Sc	1	14	13	13	12	14	15	15	12	14
ICP-MS										
Ba	1	654	644	665	635	672	757	631	684	744
Be	1	3	3	<1	1	2	<1	<1	<1	<1
Co	0.2	46.9	33.8	28.3	32.3	39.2	34.9	37.2	25.6	40.5
Cs	0.1	5.4	5.7	5.4	5.2	3.2	3.7	1.3	6.2	2.8
Ga	0.5	17.5	18.1	18	17.6	18.2	17	18.7	17.4	17.9
Hf	0.1	4.3	4.3	4.3	4.1	4.3	3.9	4	4.8	3.7
Nb	0.1	8.8	9.2	9.2	8.8	8.3	6.9	7.6	9.3	6.5
Rb	0.1	98.6	100.2	101.9	90.2	71.8	91.7	58.2	118.9	77.7
Sn	1	3	1	1	1	1	1	1	1	1
Sr	0.5	509.7	494.5	482.5	487.6	540	578.6	592.3	466.3	621.8
Ta	0.1	0.8	0.8	0.7	0.8	0.7	0.4	0.5	0.8	0.5
Th	0.2	13.4	14.2	14.8	13.1	8.5	5	5	16.2	5.5
U	0.1	4.6	5	4.8	4.3	2.6	1.1	1.3	5.4	1.3
V	8	145	129	134	123	149	164	175	119	146
W	0.5	129.8	133	90.5	152.4	178.5	123.6	119.8	113.5	187.6
Zr	0.1	153.6	148.9	157.3	144.5	151.7	156	152.9	178.7	140.5
Y	0.1	17.1	17.1	17.2	15.8	15.6	15.2	16.5	16.5	15.3
La	0.1	29.1	29.8	30.4	28.9	29.5	27.6	27.9	32.3	28.8
Ce	0.1	54.9	54.9	57.4	55.3	54.1	52	54.1	59.1	46.9
Pr	0.02	6.23	6.47	6.5	6.37	6.53	6.12	6.4	6.78	6.09
Nd	0.3	23.1	24.4	24.2	24.3	24.8	22.8	26.3	25	23.1
Sm	0.05	4.26	4.51	4.53	4.35	4.62	4.22	5.27	4.62	4.19
Eu	0.02	1.03	1.04	1.06	1	1.12	1.06	1.32	0.97	1.13
Gd	0.05	3.84	3.79	3.75	3.76	3.84	3.61	4.37	3.77	3.69
Tb	0.01	0.55	0.55	0.54	0.55	0.56	0.52	0.62	0.54	0.52
Dy	0.05	3.1	3.1	3.08	2.8	2.91	2.85	3.38	3.05	3.02
Ho	0.02	0.6	0.58	0.6	0.54	0.52	0.55	0.59	0.64	0.57
Er	0.03	1.66	1.59	1.6	1.49	1.51	1.54	1.56	1.71	1.45
Tm	0.01	0.24	0.24	0.23	0.21	0.21	0.2	0.2	0.24	0.19

Yb	0.05	1.57	1.47	1.46	1.43	1.29	1.3	1.37	1.59	1.26
Lu	0.01	0.26	0.22	0.23	0.22	0.19	0.2	0.18	0.25	0.18

---

## 3.4. Results

### 3.4.1. Geochemistry, petrography, and mineral chemistry

#### Geochemistry

The samples were taken from the selected andesite-dacite lava (61 – 63 SiO<sub>2</sub> wt%) that contains aphanitic enclaves of less evolved andesitic composition (58 – 60 SiO<sub>2</sub> wt%; Fig. 3.2) and porphyritic enclaves (not analyzed). All samples display Mg# values between 0.65 – 0.71 (Table 3.2) and the typical trend of calc-alkaline magmas from arc setting with negative Nb and Ta anomalies (see spider diagram in the supplementary material “Geochemistry analyses”). This arc setting is also evidenced by Ba/La ratios between 21.2 – 22.5 and 22.6 – 27.4 in lava and enclave samples, respectively (cf. Fig. 7 of Kay et al. 2010). Trace elements of the lava samples exhibit higher contents in Th and U (13.1 – 16.2 and 4.3 – 5.4) together with lower values of La/Yb (18.5 – 20.8), Sm/Yb (2.7 – 3.1), and Sr/Y (28 – 30.9) than aphanitic enclave samples (5 – 8.5, 1.1 – 2.6, 20.4 – 22.9, 3.2 – 3.8, and 34.6 – 40.6, respectively). Finally, E<sub>N</sub>/E<sub>u\*</sub> anomalies and La/Yb ratios normalized (i.e., La<sub>N</sub>/Yb<sub>N</sub>) by CI chondrite composition of Sun and McDonough (1989) are higher in enclaves (0.8 – 0.9 and 14.6 – 16.4) than lava samples (0.7 – 0.8 and 13.3 – 14.9).

## Petrography

The lava samples are porphyritic with phenocrysts (~25 vol%) in a holocrystalline groundmass (~75 vol%). The dominant phenocryst phase is plagioclase (~15 vol%), followed by small amount of amphibole, biotite, orthopyroxene, clinopyroxene, and quartz phenocrysts (Table 3.1). Phenocrysts of all phases are commonly observed as isolated grains, but plagioclase is also found in crystal clots with amphibole and biotite or as inclusions in crystals of these mafic phases together with apatite crystals. Some samples show trace amounts (<1 vol%) of olivine and Fe-Ti oxides phenocrysts together with accessory phases of titanite and zircon (<200  $\mu\text{m}$ ) immersed in the lava groundmass. The latter was also observed within plagioclase and amphibole phenocrysts.

The groundmass of lava samples includes microlites (<250  $\mu\text{m}$ ) of plagioclase, amphibole, orthopyroxene, clinopyroxene, and Fe-Ti oxides. We also include in the lava groundmass larger amphibole crystals (<500  $\mu\text{m}$ ) that have similar composition than amphibole microlites (hereafter we refer to all amphibole crystals <500  $\mu\text{m}$  as microphenocrysts). Pyroxenes and Fe-Ti oxide microlites occur as isolated grains in an intergranular texture between the spaces left by plagioclase microlites and amphibole microphenocrysts.

The andesitic enclave samples show nearly aphanitic to porphyritic textures with variable amounts of phenocrysts between 2 and 13 vol%, immersed in a holocrystalline groundmass with diktytaxitic texture. The phenocrysts observed in the enclaves have similar size, chemistry, and textural features than those found in lava samples. They mainly correspond to plagioclase, amphibole, biotite, and orthopyroxene phenocrysts, together with trace amounts of clinopyroxene, quartz, and olivine phenocrysts (<1 vol%). In porphyritic enclaves, plagioclase is the most common mineral phase (~9 vol%), whereas the other phenocrysts do not reach 1 vol% (Table 3.1).

Although the holocrystalline groundmass mineralogy of enclaves is similar to lava samples, there are differences in the shape of microlites and microphenocrysts. While crystals in lava groundmass samples display euhedral to subhedral shapes, those from enclaves show crystals with quenching (cf. Shea and Hammer 2013). Within enclave samples, plagioclase microlites are ubiquitous and are found as prismatic laths. Similarly,

amphibole microphenocrysts and pyroxene microlites are found with elongate to acicular grains shape. The length of these crystals rarely exceeds 200  $\mu\text{m}$ .

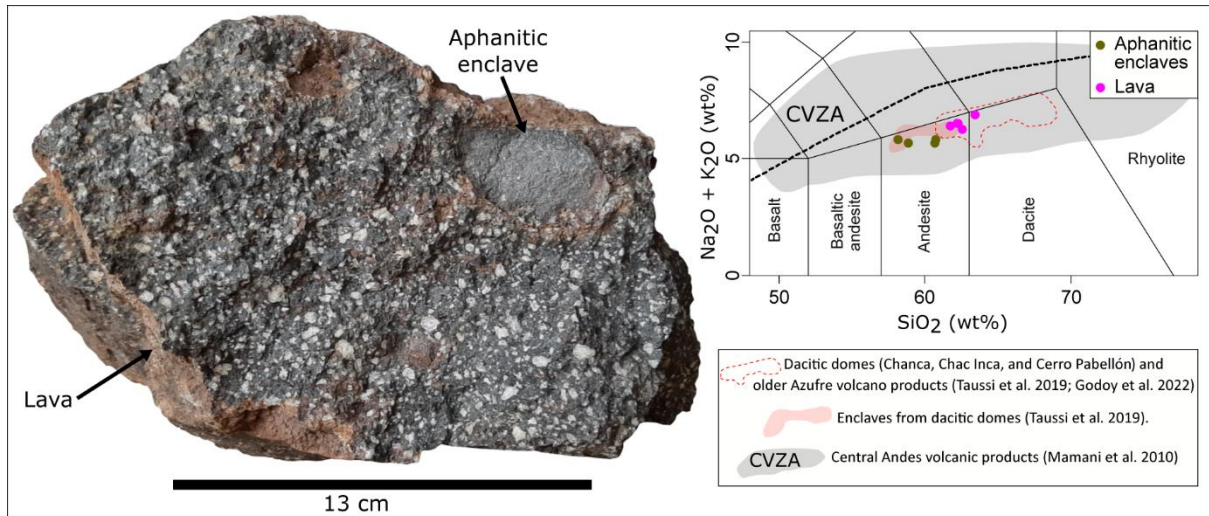


Fig. 3.2: Image showing an aphanitic enclave within a representative lava sample of the studied deposit and their compositions (and other related ones) in the total alkalis versus silica diagram (le Bas et al. 1986). The black-dashed line corresponds to the alkaline and sub-alkaline magmatic series boundary (Irvine and Baragar 1971)

## Plagioclase

Plagioclase phenocrysts from lava and enclave samples show similar textural-compositional features as cores, intermediate zones with internal rings (i.e., oscillatory zoning), and rims. Compositionally, we grouped these textures into: Ca-poor and Ca-rich (Fig. 3.3a, b). The Ca-poor group displays an andesine composition ( $An_{34-47}$ ), whereas the Ca-rich group exhibits a labradorite composition ( $An_{55-70}$ ) and, in some cases, bytownite composition ( $An_{70-83}$ ).

The Ca-poor compositions are in the intermediate zones of plagioclase phenocrysts (zones that comprises the major volume of plagioclase phenocrysts), whereas the Ca-rich are found in the cores ( $An_{56-83}$ ), internal rings ( $An_{55-65}$ ), and rims ( $An_{62-72}$ ) (Fig. 3.3b, c, d). Among these Ca-rich textures, the most ubiquitous are the rims and internal rings, while the cores are less frequent. Plagioclase microlites in both lava and enclave samples have similar Ca-rich composition ( $An_{57-71}$ ; Fig. 3.3e). Representative analyses of plagioclase composition for each textural feature are presented in Table 3.3.

In addition to the textural-compositional features, plagioclase phenocrysts can exhibit variable degrees of dissolution (Tsuchiyama 1985). Thus, while some phenocrysts are weakly resorbed (Fig. 3.3c), others are mantled with their outer zone partially resorbed (Fig. 3.3f), and others correspond to rounded-embayed phenocrysts strongly resorbed (Fig. 3.3g). The percentages distribution of these dissolution textures are 40%, 40%, and 20%, respectively.



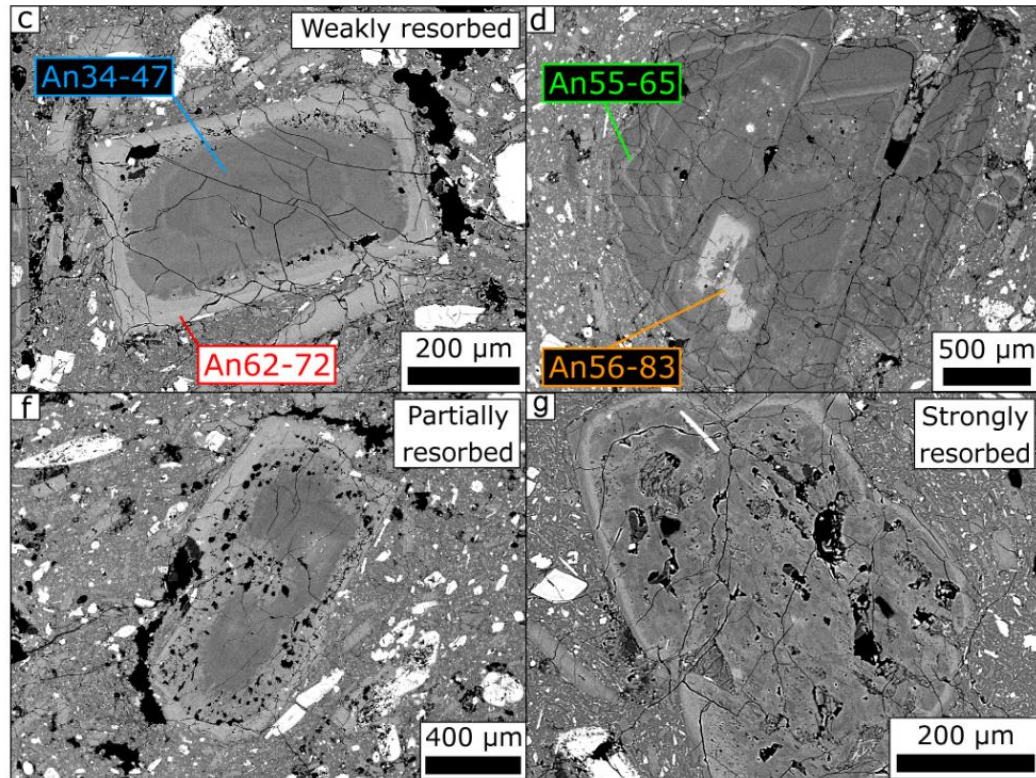
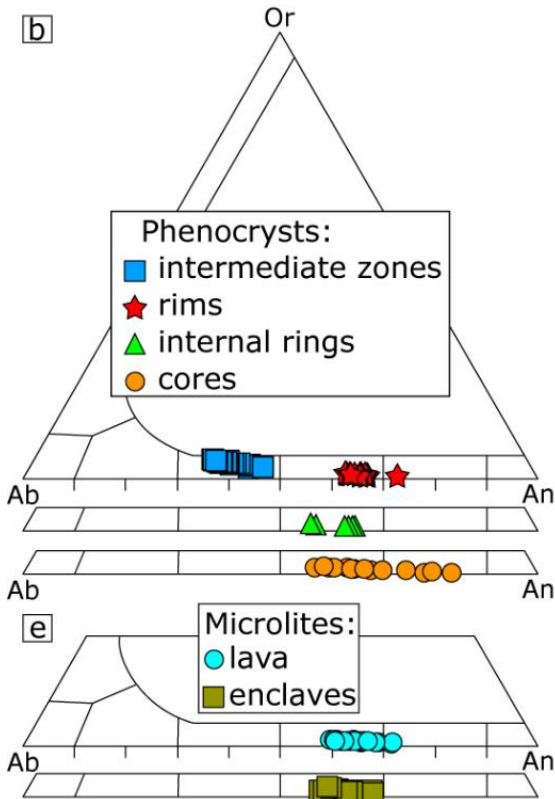
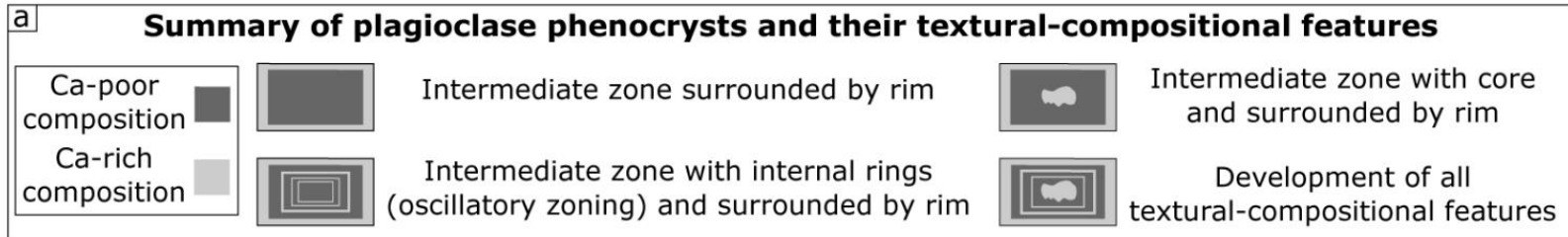


Fig. 3.3: Compositional and textural features of plagioclase crystals from lava and enclave samples. **a, b** Diagrams show the Ca-poor and Ca-rich textural-compositional features of plagioclase phenocrysts, which are indicated by tag colors in **c** and **d** BSE images. Different dissolution effects in plagioclase phenocrysts are shown in **c, f,** and **g** images. Microlite composition is shown in **e**

## Amphibole

Two groups of amphibole were identified following the Hawthorne et al.'s (2012) classification scheme (Fig. 3.4a) and major oxide compositions (Fig. 3.4b). Group 1 corresponds to magnesio-hastingsite and magnesio-ferri-hornblende with high SiO<sub>2</sub> (45 – 48.6 wt%) contents relative to magnesio-hastingsite and magnesio-Ti-hastingsite that form Group 2 (SiO<sub>2</sub> between 40.1 – 45.5 wt%). The high SiO<sub>2</sub> values are correlated with low contents of Al<sub>2</sub>O<sub>3</sub> (6.3 – 8.8 wt%), TiO<sub>2</sub> (1.3 – 2 wt%), and NaO (1.1 – 1.6 wt%) together with high contents of FeO<sub>T</sub> (13.1 – 15.1 wt%) and CaO (12.3 – 12.6 wt%) relative to Group 2 amphiboles (9.2 – 13.6, 1.8 – 4.4, 2 – 2.6, 10.8 – 14.2, and 11.4 – 12.2 wt%, respectively).

Texturally, Group 1 consists of amphiboles found as isolated phenocrysts or phenocrysts and inclusions in contact with Ca-poor intermediate zone of plagioclase phenocrysts (An<sub>35</sub> – 43; Fig. 3.4c). Conversely, Group 2 comprises amphibole microphenocrysts of the groundmass of lava and enclave samples that are in contact with Ca-rich plagioclase microlites (An<sub>57</sub> – 71). These relationships between amphibole groups and plagioclase composition are also evidenced in plagioclase inclusions within amphiboles. In fact, Group 1 phenocrysts display Ca-poor plagioclase inclusions (An<sub>38</sub> – 42; Fig. 3.4d), whereas Group 2 microphenocrysts show Ca-rich plagioclase inclusions (An<sub>59</sub> – 66; Fig. 3.4e). Additionally, amphibole crystals of both compositional groups can be found free of breakdown texture or partially to wholly pseudomorphed by fine-grained plagioclase, Fe-Ti oxides, orthopyroxene, and clinopyroxene intergrowths (Fig. 3.4f). Representative analyses of amphibole composition are available in Table 3.4.

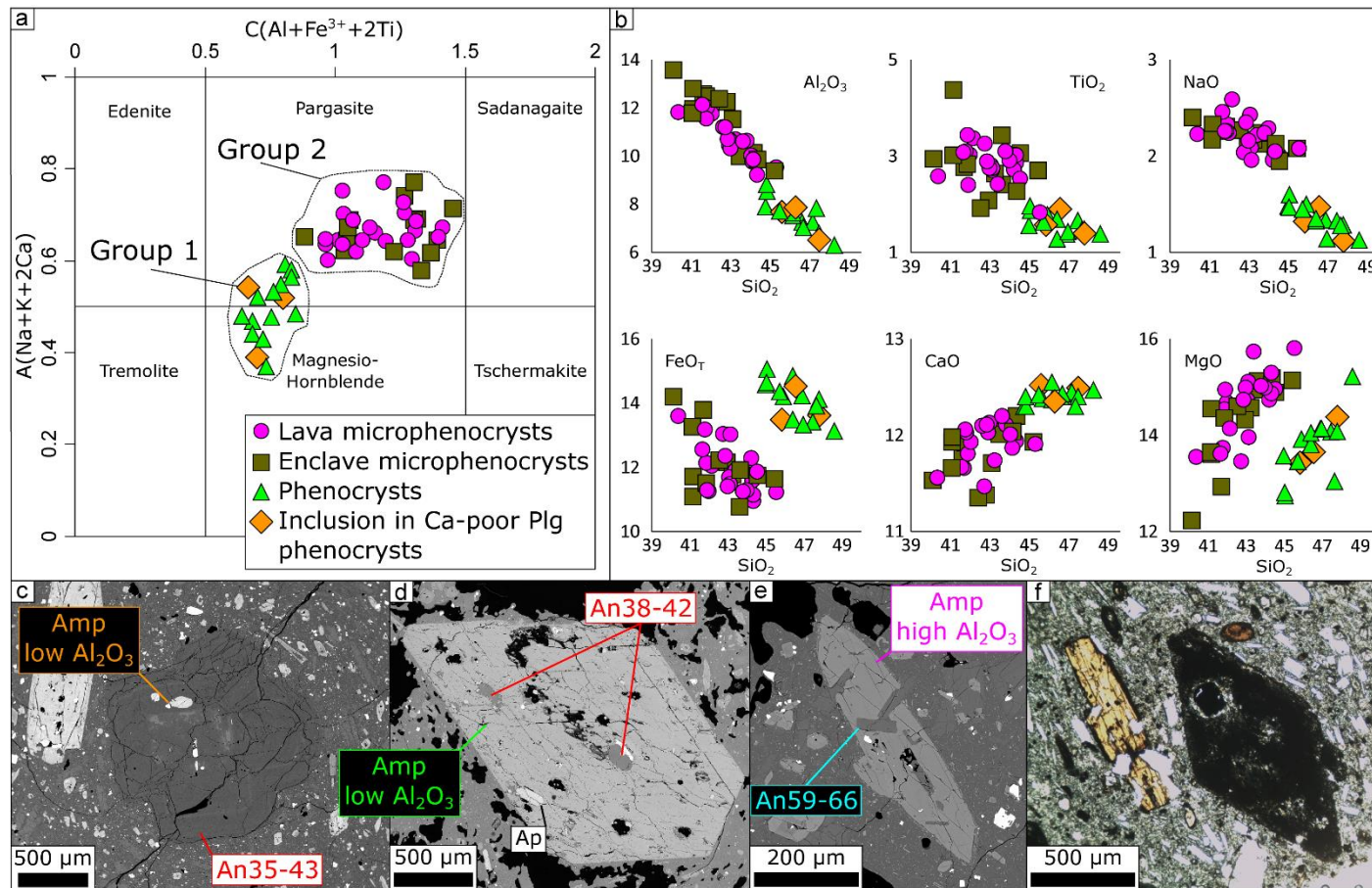


Fig. 3.4: Compositional and textural features of amphibole crystals from the lava and enclave samples. Compositional groups of the studied amphiboles after Hawthorne's et al. (2012) classification (a) and major oxide composition (b). BSE photomicrographs showing: c Group 1 amphibole crystal as inclusions within the Ca-poor intermediate zone of plagioclase phenocrysts. d Group 1 amphibole phenocryst with apatite and Ca-poor plagioclase inclusions. e Group 2 amphibole microphenocrysts in contact with microlites and inclusions of Ca-rich plagioclase. Optical microscope photomicrograph f showing amphibole crystals of both compositional groups. Group 2 crystal shows opaque rim (left) and Group 1 crystal is completely pseudomorphed (right). Tag colors of amphibole correspond to those in a plot, while tag colors of plagioclase are related with the Ca-poor and microlite compositions of Fig. 3.3b and e

Table 3.3: Representative microprobe analyses of plagioclase from the studied lava and enclaves. Anorthite (An), albite (Ab), and orthoclase (Or) contents in mol%.

Sample	Plagioclase											
	Intermediate zones of phenocrysts (n= 48)			Cores of phenocrysts (n= 16)			Internal rings of phenocrysts (n= 8)			Rims of phenocrysts (n= 20)		
	Azu 1-2	Azu 1-3	Azu 10 EN-1	Azu 2-14	Azu 3-1	Azu 7 EN-8	Azu 3-3	Azu 4-11	Azu 7 EN-6	Azu 1-21	Azu 2-7	Azu 7 EN-7
SiO <sub>2</sub>	60.0	59.4	60.2	51.5	47.3	50.6	54.5	52.5	54.4	52.9	52.2	52.4
Al <sub>2</sub> O <sub>3</sub>	24.8	25.3	24.6	30.1	33.0	30.5	28.0	29.5	28.3	28.9	29.5	29.4
CaO	7.4	7.8	7.4	14.4	17.7	14.8	11.7	13.5	12.0	13.0	13.8	13.6
Na <sub>2</sub> O	7.2	7.1	7.2	3.8	1.9	3.5	5.1	4.2	4.8	4.3	4.0	4.2
K <sub>2</sub> O	0.7	0.7	0.7	0.2	0.1	0.2	0.3	0.2	0.3	0.2	0.2	0.3
FeO <sub>T</sub>	0.28	0.23	0.24	0.29	0.32	0.39	0.2	0.29	0.27	0.7	0.64	0.52
BaO	0.12	0.0	0.05	0.2	0.4	0.0	0.0	0.0	0.12	0.0	0.0	0.0
SrO	0.0	0.04	0.0	0.0	0.09	0.09	0.08	0.07	0.04	0.13	0.0	0.11
Total (wt%)	100.6	100.4	100.5	100.5	100.9	100.2	100	100.3	100.3	100.3	100.4	100.4
An	35	36	35	67	83	69	55	63	57	62	65	63
Ab	61	60	61	32	17	30	43	35	41	37	34	35
Or	4	4	4	1	0	1	2	1	2	1	1	2

Table 3.3 (continued)

Sample	Plagioclase								
	Microlites (n= 35)			Inclusions in amphibole phenocrysts (n= 3)		Inclusions in amphibole microphenocrysts (n= 11)		Inclusions in biotite phenocrysts (n= 11)	
	Azu 2-8	Azu 3-14	Azu 7 EN-1	Azu 1-10	Azu 4-31	Azu 3-6	Azu 3-5	Azu 2-4	Azu 2-9
SiO <sub>2</sub>	51.5	53.0	53.7	59.6	58.5	53.0	53.1	57.7	59.1
Al <sub>2</sub> O <sub>3</sub>	30.2	28.9	28.2	25.5	26.0	28.9	29.1	26.0	25.5
CaO	14.5	13.1	12.3	8.1	8.9	12.7	13.1	9.0	8.1
Na <sub>2</sub> O	3.6	4.2	4.7	6.8	6.3	4.2	4.4	6.5	6.9
K <sub>2</sub> O	0.2	0.2	0.4	0.7	0.6	0.3	0.24	0.5	0.7
FeO <sub>T</sub>	0.73	0.76	0.67	0.4	0.31	1.02	0.68	0.3	0.38
BaO	0.0	0.02	0.02	0.0	0.1	0.0	0.17	0.0	0.0
SrO	0.11	0.15	0.17	0.03	0.05	0.8	0.17	0.5	0.0
Total (wt%)	100.9	100.6	100.3	101.3	100.8	101	100.8	100.2	100.6
An	68	62	58	38	42	59	60	42	38
Ab	31	36	40	58	54	39	38	55	58
Or	1	1	2	4	3	1	1	3	4

Table 3.4: Representative microprobe analyses of amphibole and biotite from the studied lava and enclaves. Equivalent oxygen (O=F+Cl) and recalculations of FeO\*, Fe<sub>2</sub>O<sub>3</sub>\*, and H<sub>2</sub>O\* were performed using Locock (2014) spreadsheet and Li's et al. (2020) method for amphibole and biotite, respectively. Total (wt%) does not include FeO<sub>T</sub> measured by EMPA.

Sample	Amphibole								Biotite	
	Phenocrysts (n= 13)		Inclusions in plagioclase phenocrysts (n= 3)		Microphenocrysts (n= 36)				Phenocrysts (n= 6)	
	Azu 1-2	Azu 1-3	Azu 1-7	Azu 4-9	Azu 2- 2	Azu 2-3	Azu 10 EN-1	Azu 10 EN-3	Azu 2- 1	Azu 2-2
SiO <sub>2</sub>	45.9	45.0	46.6	45.8	40.4	43.4	43.6	41.7	36.7	37.1
TiO <sub>2</sub>	1.8	1.6	1.9	1.6	2.6	2.4	3.4	2.8	5.1	4.7
Al <sub>2</sub> O <sub>3</sub>	7.8	7.9	7.9	7.7	11.8	10.7	10.0	12.6	13.4	13.5
FeO <sub>T</sub>	14.2	14.6	14.5	13.5	13.6	11.9	10.8	13.8	16.7	14.6
MgO	13.9	13.6	13.7	13.4	13.6	15.7	15.1	12.9	13.7	15.3
MnO	0.4	0.5	0.5	0.4	0.2	0.2	0.2	0.3	0.2	0.3
CaO	12.4	12.3	12.4	12.5	11.6	11.7	12.0	11.8	0.0	0.0
Na <sub>2</sub> O	1.5	1.5	1.5	1.3	2.2	2.2	2.1	2.3	0.5	0.9
K <sub>2</sub> O	0.9	0.9	0.8	0.9	0.6	0.5	0.7	0.7	9.3	9.0
F	0.1	0.2	0.3	0.3	0.2	0.2	0.2	0.2	0.1	0.1
Cl	0.1	0.1	0.1	0.2	0.0	0.0	0.0	0.0	0.2	0.2
O=F+Cl	-0.1	-0.1	-0.2	-0.2	-0.1	-0.1	-0.1	-0.1	-0.1	-0.1
FeO*	11.1	10.7	11.9	12.0	7.4	5.6	8.8	9.9	5.6	6.0
Fe <sub>2</sub> O <sub>3</sub> *	3.4	4.3	3.0	1.6	6.9	7.1	2.2	4.3	12.4	9.4
H <sub>2</sub> O*	2.0	1.9	1.9	1.9	1.9	2.0	2.0	1.9	2.5	2.4
Total (wt%)	101.2	100.4	102.2	99.5	99.3	101.8	100.4	101.4	99.6	98.8

## Pyroxenes

Reverse zonation has been identified in orthopyroxene and clinopyroxene phenocrysts of the lava samples (Fig. 3.5a, c, d). Mg-poor cores of orthopyroxene have Mg# between 0.67 and 0.78 ( $\text{En}_{65-76}\text{Fs}_{21-32}\text{Wo}_{1-3}$ ), while Mg-poor cores of clinopyroxene have Mg# between 0.72 and 0.74 ( $\text{En}_{40-42}\text{Fs}_{14-15}\text{Wo}_{42-45}$ ). By contrast, the Mg-rich rims display Mg# between 0.79 and 0.84 for orthopyroxene ( $\text{En}_{77-82}\text{Fs}_{16-20}\text{Wo}_{2-4}$ ) and Mg# between 0.79 and 0.85 for clinopyroxene ( $\text{En}_{43-51}\text{Fs}_{9-14}\text{Wo}_{35-47}$ ). Unzoned pyroxene phenocrysts show compositions that match with those Mg-rich compositions. Some clinopyroxene phenocrysts show Mg-rich orthopyroxene patches in their Mg-rich rims (Fig. 3.5d), with Mg# that varies between 0.78 and 0.88 ( $\text{En}_{75-77}\text{Fs}_{19-21}\text{Wo}_{3-5}$ ). Mg-poor and Mg-rich (including patches) pyroxene phenocrysts also differ in their contrasting  $\text{Cr}_2\text{O}_3$  concentrations, displaying values between 0.01 – 0.24 and 0.02 – 0.6 (wt%), respectively (see Fig. 5.4 in supplementary material). Additionally, orthopyroxene phenocrysts of enclave samples exhibit similar reverse zonation texture to those in orthopyroxene phenocrysts from the lava samples.

Mg# of the orthopyroxene and clinopyroxene microlites are in the range of 0.68 – 0.82 ( $\text{En}_{66-80}\text{Fs}_{17-31}\text{Wo}_{2-5}$ ) and 0.73 – 0.84 ( $\text{En}_{40-55}\text{Fs}_{10-15}\text{Wo}_{33-46}$ ), respectively (Fig. 3.5b). Representative analyses for each textural-compositional zone of pyroxenes are in Table 3.5.

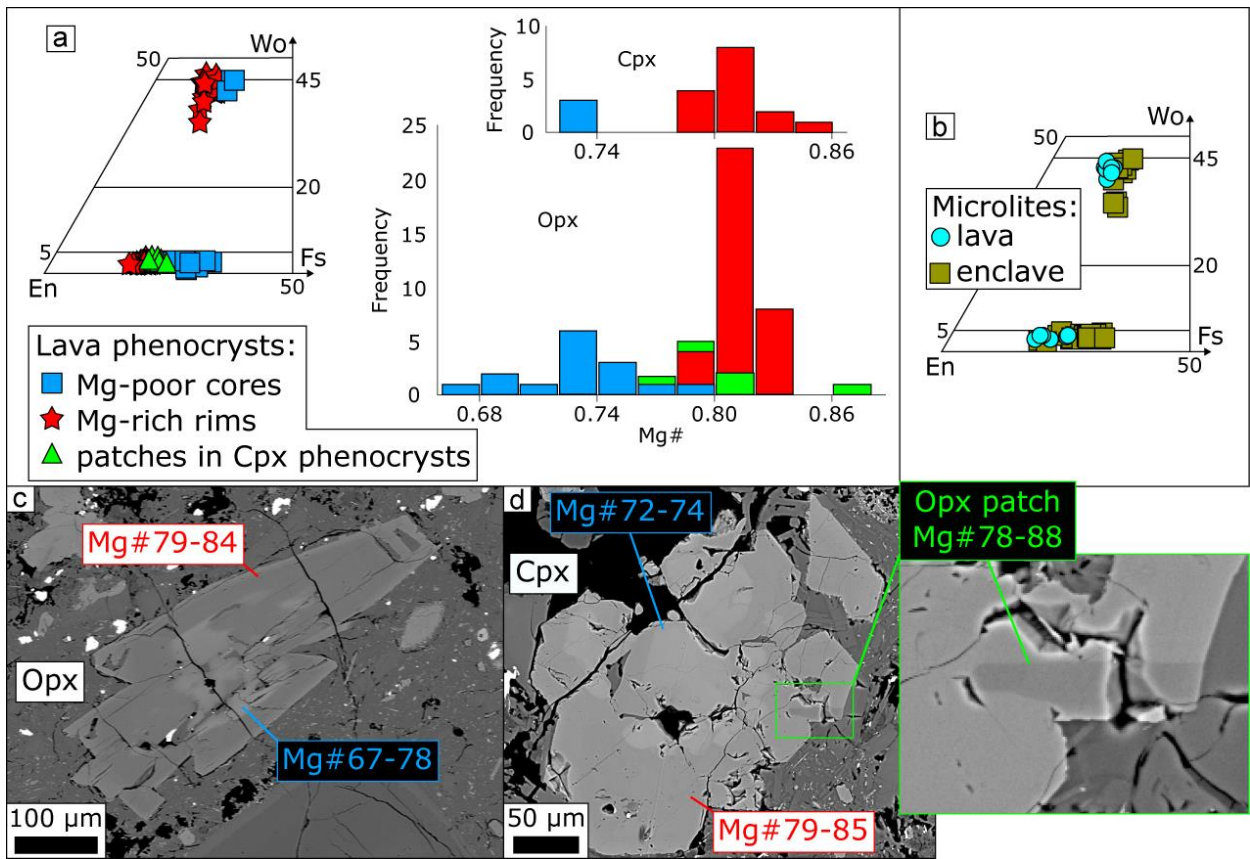


Fig. 3.5: Compositional and textural features of pyroxenes from the lava and enclave samples. **a** Pyroxene composition diagrams show the differences between cores and rims of orthopyroxenes and clinopyroxenes phenocrysts. Composition of orthopyroxene patches in clinopyroxene phenocrysts are also displayed in the diagrams in figure **a**. Tag colors in BSE images **c** and **d** are related to those of the diagrams in figure **a**. Pyroxene microlite compositions are exhibited in the diagram of figure **b**



## **Biotite**

Using the machine learning method of Li et al. (2020) for the biotite formula as  $A_1M_3T_4O_{10}W_2$ , we determined a nearly homogeneous cationic distribution of major elements. Based on Deer et al.'s (1992) classification scheme, biotite phenocrysts correspond to Mg-rich compositions close to phlogopite end member ( $Mg\#_{0.68 - 0.77} (\pm 0.06)$ ), showing aluminum content in the tetrahedral ( $Al^{IV}$ ) and octahedral ( $Al^{VI}$ ) sites in the range of  $0.92 - 0.99 (\pm 0.2)$  and  $0.24 - 0.3 (\pm 0.3)$  atoms per formula unit. Errors showed in the compositional ranges correspond to uncertainty propagation of  $Al^{IV}$  content in the T site;  $Fe^{2+}$  and  $Al^{VI}$  content in the M site according to Li et al.'s (2020) method. These compositional features, together with the normalized mol contents of  $10Na_2O$ ,  $TiO_2$ , and  $10MnO$  (values ranging between  $71 - 84.1$ ,  $8.5 - 14.3$ , and  $6.5 - 14.8$  for each molecule), correlate biotite phenocrysts with a magmatic origin (Samadi et al. 2021). Representative analyses of biotite composition are presented in Table 3.4.

Texturally, and similarly to amphibole phenocrysts, biotite phenocrysts show inclusions of Ca-poor plagioclase ( $An_{38 - 42}$ ) and apatite (Fig. 3.6a). Additionally, biotite phenocrysts occur as euhedral crystals almost free of reaction textures (Fig. 3.6a) or as subhedral crystals with breakdown rims.

## **Fe-Ti oxides**

Titanomagnetite and ilmenite occur as phenocrysts and microlites. In lava samples, phenocrysts of both series display exsolution lamellae. Fe-Ti oxides microlites usually occur as titanomagnetite single crystals in lava and enclave samples. However, scarce paired titanomagnetite-ilmenite microlites also occur (Fig. 3.6b). Consequently, we used the Stormer's (1983) method to determine Fe speciation and to perform the cationic distribution of these Fe-Ti oxides pairs (Table 3.6). Accordingly, paired titanomagnetite and ilmenite microlites exhibit mole fractions in the range of  $X_{Usp_{0.18 - 0.34}}$  and  $X_{Ilm_{0.76 - 0.87}}$ , respectively.

## Olivine and quartz

Phenocrysts of olivine and quartz in lava and enclave samples exhibit disequilibrium textures as resorption and reaction rims (Fig. 3.6c and d). Olivine phenocrysts display orthopyroxene reaction rims and, in some cases, a second rim of amphibole surrounding the orthopyroxene corona. Compositionally, olivine phenocrysts are normally zoned with contents of  $Fo_{79-84}$  and  $Fo_{76}$  in cores and rims, respectively (Table 3.6). On the other hand, phenocrysts of quartz are euhedral to subhedral with deep embayments and a finely crystalline clinopyroxene rim overgrowth.

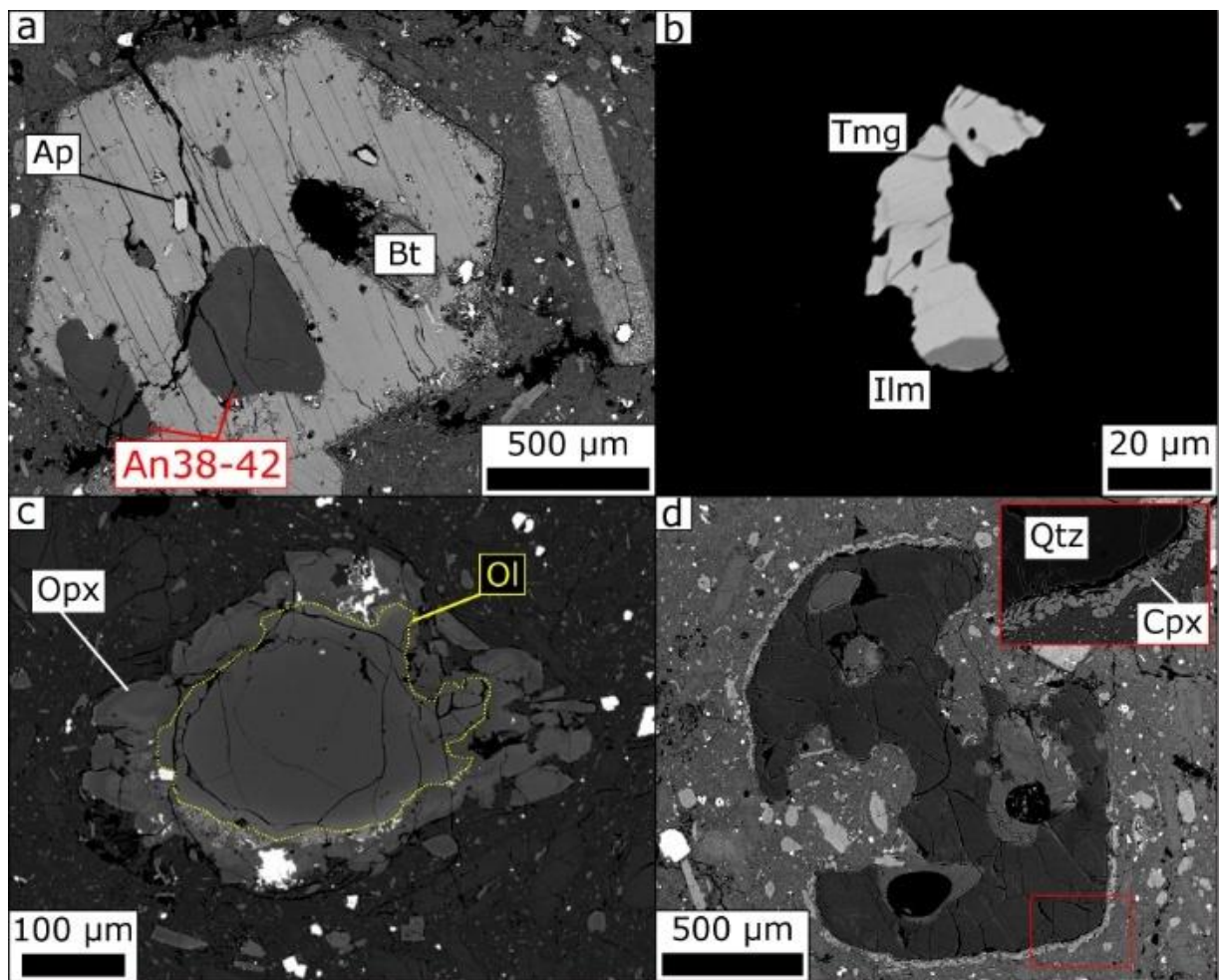


Fig. 3.6: BSE images obtained from lava samples that show: **a** Biotite phenocryst with thin reaction rim containing inclusions of Ca-poor plagioclase and apatite. **b** Paired ilmenite-titanomagnetite microlites. **c** Olivine phenocryst with orthopyroxene corona. **d** Embayed-quartz phenocryst with clinopyroxene corona (inset)

Table 3.5: Representative microprobe analyses of pyroxene phenocrysts from the studied lava and enclaves. Recalculations of FeO\* and Fe<sub>2</sub>O<sub>3</sub>\* were performed with the Putirka (2008) method. Total (wt%) does not include FeO<sub>T</sub> measured by EMPA. Mg-number (Mg#) was calculated as molar Mg/(Mg+Fe<sup>2+</sup>). Wollastonite (Wo), enstatite (En), and ferrosilite (Fs) contents in mol%

Sample	Pyroxene													
	Orthopyroxene Mg-poor cores (n= 15)		Clinopyroxene Mg-poor cores (n= 3)		Orthopyroxene Mg-rich rims (n= 35)		Clinopyroxene Mg-rich rims (n= 15)		Orthopyroxene patches (n= 9)		Microlites (n= 46)			
	Azu 1-7	Azu 7 EN-1	Azu 2-26	Azu 2-33	Azu 1-3	Azu 7 EN-2	Azu 1-5	Azu 1-12	Azu 1-11	Azu 1-17	Azu 1-22	Azu 7 EN-18	Azu 2-8	Azu 7 EN-16
SiO <sub>2</sub>	50.3	54.2	53.1	50.3	54.2	54.4	48.5	52.6	54.8	52.5	54.0	54.0	50.5	50.4
TiO <sub>2</sub>	0.5	0.0	0.2	1.0	0.3	0.2	1.1	0.3	0.1	0.2	0.4	0.5	1.2	0.9
Al <sub>2</sub> O <sub>3</sub>	7.3	1.9	1.6	3.7	2.4	2.9	5.2	2.3	1.7	3.6	3.0	3.4	5.1	3.9
Cr <sub>2</sub> O <sub>3</sub>	0.0	0.0	0.0	0.0	0.4	0.3	0.1	0.1	0.3	0.3	0.1	0.4	0.0	0.0
FeO <sub>T</sub>	15.4	17.0	10.3	10.7	12.7	13.1	9.0	8.8	12.5	13.5	13.0	12.4	9.2	10.7
MgO	25.2	25.3	14.7	13.4	28.7	27.8	15.0	17.3	28.0	27.0	27.9	27.7	15.1	14.0
MnO	0.3	0.7	0.4	0.4	0.3	0.2	0.2	0.2	0.3	0.4	0.3	0.2	0.2	0.3
CaO	1.4	0.7	20.5	20.7	1.4	1.3	20.0	18.7	2.4	2.0	1.5	1.2	19.6	20.1
Na <sub>2</sub> O	0.1	0.0	0.3	0.4	0.0	0.0	0.3	0.2	0.0	0.0	0.0	0.1	0.4	0.3
FeO*	13.2	17.0	9.5	8.4	11.7	13.1	4.9	7.1	12.2	11.8	13.0	12.4	7.7	8.9
Fe <sub>2</sub> O <sub>3</sub> *	2.4	0.0	0.8	2.5	1.1	0.0	4.6	1.8	0.3	1.8	0.0	0.0	1.7	2.0
Total (wt%)	100.7	99.7	101.1	100.8	100.5	100.2	99.8	100.8	100.2	99.8	100.0	99.8	101.3	100.7
Mg#	0.77	0.73	0.73	0.74	0.81	0.79	0.85	0.81	0.88	0.80	0.79	0.80	0.78	0.74
Wo	3	1	42	45	3	3	45	39	5	4	3	2	42	43
En	75	72	42	41	79	77	47	50	77	77	77	78	45	42
Fs	22	27	15	14	18	20	9	12	19	19	20	20	13	15

Table 3.6: Representative microprobe analyses of Fe-Ti oxides microlites and olivine phenocrysts from the studied lava and enclaves. The Stormer's (1983) method was used to calculate the FeO\* and Fe<sub>2</sub>O<sub>3</sub>\* contents and the titanomagnetite and ilmenite mole fractions (XUsp and XIlm, respectively). Forsterite (Fo) content in mol%. Excepting olivine (all its Fe content is considered ferrous), total (wt%) does not include FeO<sub>T</sub> measured by EMPA.

Sample	Fe-Ti oxides				Olivine		
	Titanomagnetite microlites (n= 6)		Ilmenite microlites (n= 4)		Cores of phenocrysts (n= 7)		Rims of phenocrysts (n= 2)
	Azu 2-8	Azu 2-16	Azu 8 EN-2	Azu 2-15	Azu 3-1	Azu 3-2	Azu 3-3
SiO <sub>2</sub>	0.1	0.2	0.1	0.1	38.8	39.2	38.4
TiO <sub>2</sub>	7.0	7.5	45.9	46.4	0.0	0.0	0.0
Al <sub>2</sub> O <sub>3</sub>	1.8	1.7	0.2	0.1	0.0	0.0	0.0
Cr <sub>2</sub> O <sub>3</sub>	0.0	0.0	0.1	0.1	0.0	0.0	0.0
V <sub>2</sub> O <sub>3</sub>	0.7	0.8	0.6	0.5	-	-	-
FeO <sub>T</sub>	82.2	82.2	48.6	48.7	18.9	15.8	21.8
MgO	1.1	1.0	2.7	2.2	42.1	44.8	39.6
MnO	0.5	0.5	0.6	0.7	0.3	0.2	0.6
CaO	0.1	0.1	0.2	0.1	0.1	0.1	0.1
NiO	0.0	0.0	0.0	0.0	0.1	0.2	0.2
ZnO	0.3	0.2	0.0	0.1	-	-	-
FeO*	35.2	36.0	35.8	37.1	-	-	20.8
Fe <sub>2</sub> O <sub>3</sub> *	52.3	51.3	14.3	12.8	-	-	1
Total (wt%)	98.9	99.1	100.5	100.2	100.5	100.6	100.7
XUsp	0.21	0.22	-	-	Fo	80	84
XIlm	-	-	0.86	0.87			76

### 3.4.2. Equilibrium tests

To calculate the intensive thermodynamic conditions of the magma reservoir by different petrological techniques, we assess the possibility of equilibrium by applying mineral-liquid and mineral-mineral equilibrium tests. As liquid (melt) compositions, we consider the enclaves chemistry due to their aphanitic textures and to be representative of the lava groundmass composition as their microlites and microphenocrysts have similar chemistry (Fig. 3.3b, Fig. 3.4a, and Fig. 3.5b). Due to its relevance, Fig. 3.7a shows a plagioclase-liquid test with the representative enclave sample Azu 7 EN as liquid. The rest of the mineral-liquid tests (Fig. 5.5 to Fig. 5.8) are presented in supplementary material “Equilibrium test”.

#### Plagioclase

The Ab-An partition coefficient (Putirka 2008; Fig. 3.7a) shows that plagioclases with anorthite content of  $An_{66-83}$  pass the plagioclase-liquid test using the enclave sample Azu 7 EN as liquid. These anorthite compositions correspond to the more calcic microlites ( $n=10$ ), some of them ( $n=2$ ) as inclusions in amphibole microphenocrysts (Fig. 3.4d), and to the more calcic cores ( $n=8$ ) and external rims ( $n=6$ ) of phenocrysts. More restrictive anorthite contents ( $An_{69-83}$ ) pass the test with other enclave samples as a liquid representative (Fig. 5.6a to Fig. 5.8a).

#### Amphibole

Although Group 2 amphiboles form part of the groundmass of lava and enclave samples, they display disequilibrium conditions with the assumed liquid compositions when we use the amphibole-melt Fe-Mg exchange coefficient (Putirka 2016; Fig. 5.5b to Fig. 5.8b). This disequilibrium and the observed quenching textures of amphibole microphenocrysts found in enclave samples suggest the unreliability of Group 2 amphiboles to be used in P-T- $fO_2$  determinations (see other examples of unreliability in Gorini et al. (2018)). Group 1 also indicates disequilibrium conditions, but as we will discuss in the following sections,

amphiboles of this group were crystallized from a more differentiated liquid than those represented by enclave compositions.

### **Olivine**

The Fe-Mg exchange coefficients (Roeder and Emslie 1970) for olivine-melt indicate that olivine cores with  $Fo_{80-83}$  contents ( $n=4$ ) are in equilibrium with the assumed melt compositions (Fig. 5.5c to Fig. 5.8c).

### **Pyroxenes**

The orthopyroxene-clinopyroxene Fe-Mg exchange test (Putirka 2008; Fig. 3.7b) indicates that almost all Mg-rich orthopyroxene patches within Mg-rich rims of clinopyroxene phenocrysts are in equilibrium (15 pairs). Equilibrium conditions are also obtained in the Mg-rich rims of both clinopyroxene and orthopyroxenes (94 pairs). More than the half of the analyzed Mg-poor cores of orthopyroxene-clinopyroxene pairs exhibit equilibrium conditions (29 pairs).

### **Fe-Ti oxides**

The Mg-Mn partition coefficients (Bacon and Hirschmann 1988; Fig. 3.7c) for the six analyzed paired Fe-Ti oxide microlites indicate equilibrium conditions. These analyzed pairs were free from exsolution textures.

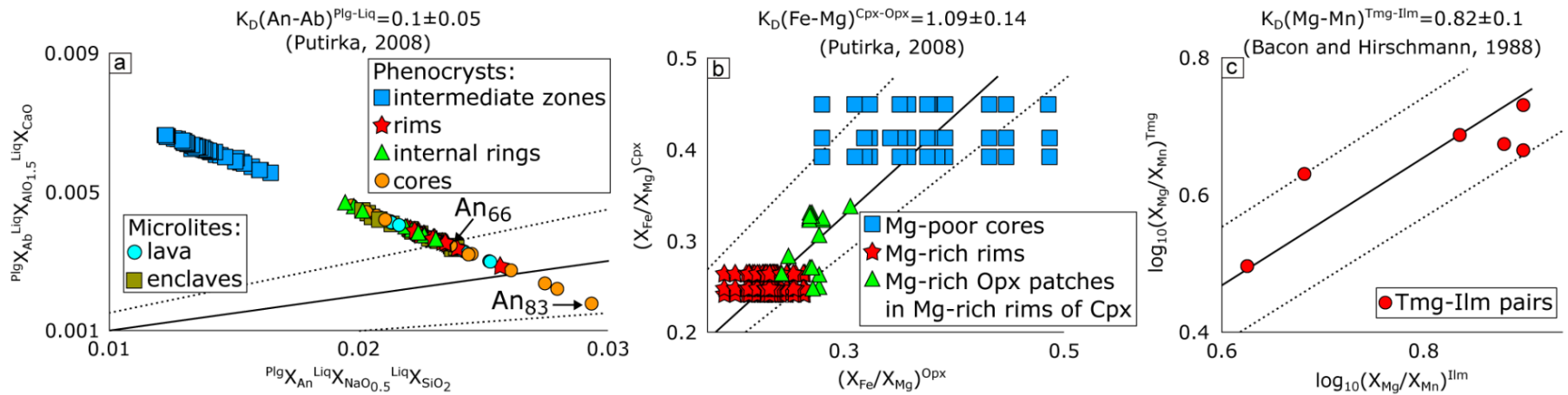


Fig. 3.7: Equilibrium test plots for mineral-liquid and mineral-mineral pairs. The liquid composition corresponds to the enclave sample Azu 7 EN. The exchange coefficient  $K_D$  (continuous black line) and its standard deviation (dotted black line) are presented on each diagram. **a** Mineral-liquid test show that plagioclase with compositions of  $\text{An}_{66-83}$  are in equilibrium with the assumed liquid composition (additional mineral-liquid test can be found in Fig. 5.5 to Fig. 5.8 of supplementary material "Equilibrium test"). Mineral-mineral tests (**b**, **c**) indicate that most of the orthopyroxene-clinopyroxene pairs are in equilibrium irrespectively of their textural features and that all paired titanomagnetite-ilmenite microlites pass the test

### 3.4.3. Pressure conditions

The presence of Ca-poor plagioclase inclusions in Group 1 amphibole and biotite phenocrysts, and Group 1 amphibole inclusions in Ca-poor intermediate zones of plagioclase phenocrysts (Fig. 3.4b, Fig. 3.4c, and Fig. 3.6a), suggest that crystallization of Group 1 amphiboles is related to plagioclase (Ca-poor zones) and biotite phenocrysts. Thus, despite the disequilibrium of Group 1 amphibole with the andesitic melts (Fig. 5.5b to Fig. 5.8b), we found the proper mineral assemblage to use the Al-in-hornblende barometer (Anderson and Smith 1995; Mutch et al. 2016). From the identification of titanite crystals together with quartz, titanomagnetite, and ilmenite phenocrysts, we infer that Group 1 amphiboles could have crystallized from a more differentiated magmatic system, forming a pressure buffering assemblage of plagioclase (Ca-poor) + amphibole + biotite + Fe-Ti oxides + titanite + quartz (Johnson and Rutherford 1989; Schmidt 1992).

To consider the temperature effect on the Al-in-hornblende barometer, we solve simultaneously the Anderson and Smith's (1995) geobarometer with the geothermometer of Holland and Blundy (1994) as an equation system of two variables (i.e., P and T). The results of temperatures are exhibited in the following section. As Group 1 amphibole crystallization is synchronous with Ca-poor plagioclase, we use the edenite-richterite geothermometer (equation B in Holland and Blundy 1994), which is for quartz-saturated or quartz-undersaturated systems. Accordingly, 23 amphibole-plagioclase pairs of Group 1 gave pressures between 1.6 – 3.1 ( $\pm 1$ ) kbar (Fig. 3.8a), where the total uncertainty considers the inherent uncertainty in the calibration (0.6 kbar) and the propagated effect of  $\pm 40$  °C geothermometer error (0.7 kbar), and 2% analytical error of Al in EMPA analysis (0.1 kbar). The formulation for uncertainty propagations corresponds to those of Lindsay et al.'s (2001). Additionally, using only the Group 1 amphibole compositions (n=16), we constrained pressure via the T-independent geobarometers of Mutch et al. (2016) and Ridolfi and Renzulli (2012), obtaining results in the range of 2 – 3.3 ( $\pm 0.4$ ) and 1 – 1.7 ( $\pm 0.5$ ) kbar, respectively. The analytical uncertainty of Al (2% relative) does not add a significant digit to the inherent uncertainty of these geobarometers. It is interesting to note that the range of pressure determined using the geobarometers of Ridolfi et al. (2010) and Ridolfi (2021) are identical to that obtained with Ridolfi and Renzulli (2012) method.



In summary, the average pressure value and standard deviation ( $1\sigma$ ) determined by the combined results of three methods above presented are  $2$  and  $\pm 0.6$  kbar, while the median value is  $1.8$  kbar. As we will discuss in the section “Thermodynamic model: MELTS”, this pressure result of  $2$  kbar appear to indicate a critical depth in the development of petrogenetic features of the studied lava, including the crystallization of its felsic a mafic mineralogy.

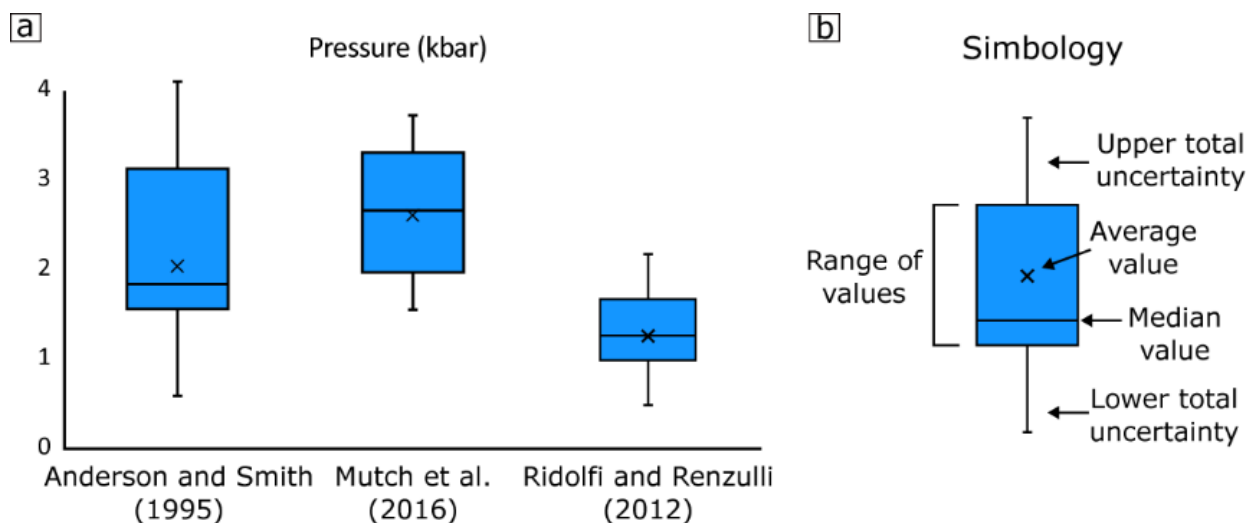


Fig. 3.8: **a** The box plots display the pressures calculated by three different geobarometers for Group 1 amphiboles and associated phases. The average pressure and standard deviation ( $1\sigma$ ) determined by these methods is  $2 \pm 0.6$  kbar. Box plot symbology is shown in **b**. The data of pressure ranges, average values, standard deviation, and total uncertainty of each method are shown in Table 3.7

### 3.4.4. Temperature conditions

We use twelve geothermometers to constrain the thermal evolution of the magmatic system associated with the last eruptive stage of the Azufre volcano (Fig. 3.9), which were selected according to our ability to use them with the collected data of mineral chemistry and whole-rock composition of enclaves (i.e., representative liquids) coming from the studied lava deposit. The selected geothermometers involve different methods that consider the compositions of amphibole (Ridolfi et al. 2010; Ridolfi and Renzulli 2012; Putirka 2016; Ridolfi 2021), amphibole-plagioclase pairs (Holland and Blundy 1994), orthopyroxene-clinopyroxene pairs (Putirka 2008), titanomagnetite-ilmenite pairs (Sauerzapf et al. 2008; Ghiorso and Evans 2008), and plagioclase-liquid (Putirka 2005). Although some of these geothermometers are pressure-dependent, they are nearly insensitive to its variations. For example, if pressure varies 1 kbar, the most sensitive geothermometers to pressure variations such as those of Ridolfi and Renzulli (2012) and the equation A of Holland and Blundy (1994), show a variation of up to 17 °C and 13 °C, respectively. Temperature variations lower than 10 °C are obtained from other geothermometers if the same pressure variation is considered. Consequently, we use the average pressure of 2 kbar to perform thermometry calculations, as another value in the range of determined pressures has no significant influence on temperature calculations.

#### **Amphibole**

Twenty-three amphibole-plagioclase pairs from Group 1 were used for thermometry calculations through both equations of Holland and Blundy (1994). The edenite-richterite calibration yielded temperatures in the range of 712 – 788 ( $\pm 40$ ) °C, while the edenite-tremolite calibration (for quartz-saturate magmas) gave temperatures between 747 – 827 ( $\pm 40$ ) °C (Fig. 3.9a, b). These low temperatures of crystallization are consistent with the presence of a felsic melt (see following sections). It should be noted that higher temperatures (774 – 874 ( $\pm 22$ ) °C) obtained from Ridolfi et al. (2010), Ridolfi and Renzulli (2012), Putirka (2016), and Ridolfi (2021) thermometers were not considered, as these methods tend to overestimate the temperature of amphiboles that crystallize below 800

°C (see our arguments in the supplementary material “Temperatures not considered for amphiboles of Group 1”). Similarly, some results of the edenite-tremolite calibration also appear to give overestimated temperatures. Therefore, we considered only the temperatures obtained through the edenite-richterite calibration.

## **Pyroxenes**

We calculated crystallization temperatures of 138 orthopyroxene-clinopyroxene pairs in equilibrium (Fig. 3.7b) using the equation 37 of Putirka (2008). Mg-poor core pairs yielded temperatures between 860 – 943 ( $\pm 38$ ) °C (Fig. 3.9c), while the Mg-rich rims of both pyroxene phenocrysts gave temperatures of 918 – 1071 ( $\pm 38$ ) °C (Fig. 3.9d). Mg-rich orthopyroxene patches within the Mg-rich rims of clinopyroxene phenocrysts gave similarly high temperatures in the range of 916 – 1097 ( $\pm 38$ ) °C (Fig. 3.9e).

## **Plagioclase**

Six rims and eight cores of plagioclase phenocrysts together with ten plagioclase microlites in equilibrium with the assumed liquid (i.e., composition of enclave sample Azu EN 7; Fig. 3.7a) were used to constrain crystallization temperatures of these Ca-rich plagioclases ( $An \geq 66$ ) through plagioclase-liquid thermometer (equation B) of Putirka (2005). The obtained temperature results are in the range of 957 – 1028 ( $\pm 53$ ) °C (Fig. 3.9f).

## **Fe-Ti oxides**

Six paired titanomagnetite-ilmenite microlites were used to calculate syn- to post-eruptive temperatures of the studied lava (later discussed). The Fe-Ti exchange thermometer of Ghiorso and Evans (2008) and the empirical thermometer of Sauerzapf et al. (2008) gave similar temperatures ranges of 742 – 866 ( $\pm 18$ ) °C and 750 – 859 ( $\pm 50$ ) °C, respectively (Fig. 3.9g, h). The total uncertainty of Ghiorso and Evans’s (2008) was calculated following the Morgado et al.’s (2019) method (see his supplementary material 2).

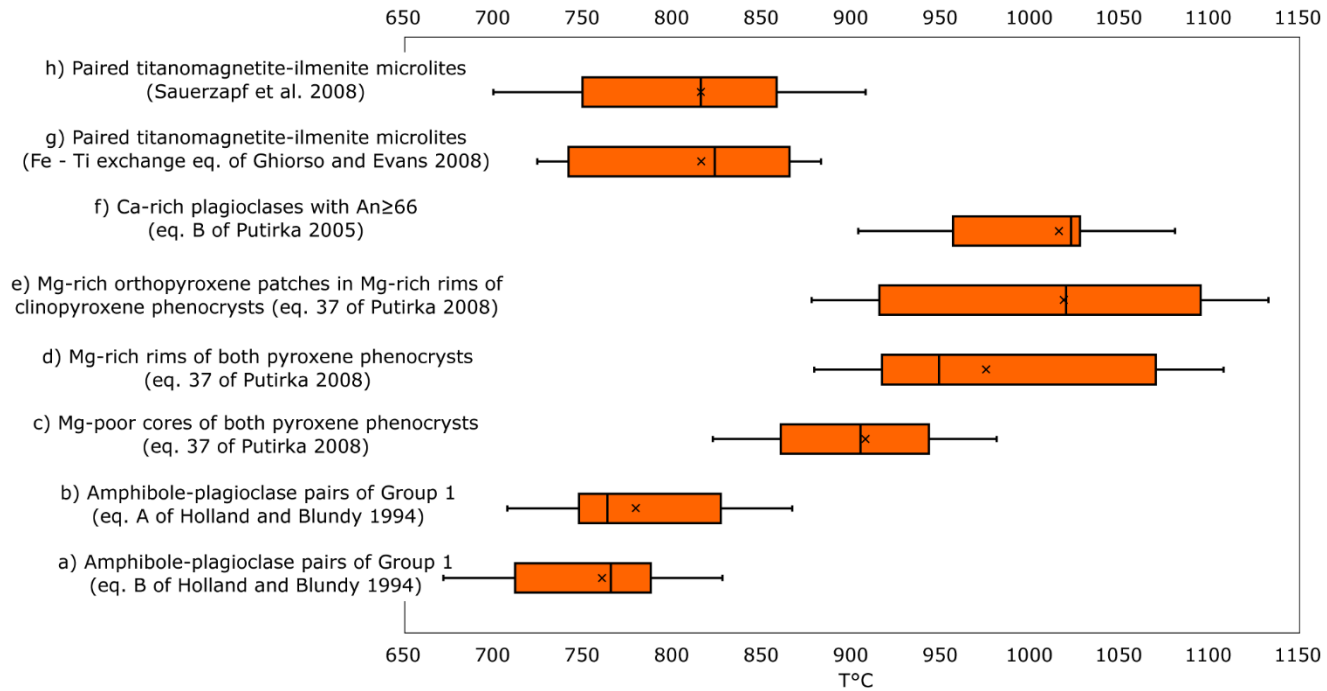


Fig. 3.9: Box plots displaying the temperature results from different thermometric methods (a – h). The phases and equation references involved in the calculations are on the left side of the diagram. Box plot symbology is the same used in Fig. 3.8. The data of temperature ranges, average values, standard deviation, and total uncertainty of each method are shown in Table 3.7

### 3.4.5. Felsic melt in equilibrium with Group 1 amphiboles

As we mentioned, textural relationships suggest that Group 1 amphiboles crystallized from an evolved magmatic system with a characteristic pressure buffering assemblage. Considering that the amphibole compositions of Group 1 represent equilibrium conditions, we use P-dependent, T-dependent, and P-T-independent chemometric equations (Ridolfi and Renzulli 2012; Putirka 2016; Zhang et al. 2017) to calculate the composition of the liquid in equilibrium with these Group 1 amphibole crystals. As we show in the supplementary material “Felsic melt composition”, the compositional results display minimal variance with changes in P (1 – 5 kbar) and T (700 – 900 °C). The results indicate that Group 1 amphiboles crystallized from an evolved liquid, which includes SiO<sub>2</sub> and K<sub>2</sub>O concentrations (wt%) of 63 – 79 ( $\pm$  3.8) and 3.4 – 5.6 ( $\pm$  0.6) at P-T conditions of 2 kbar and 758 °C (average temperature calculated from edenite-richtenite geothermometer). Other calculated compositions (wt%) at the same intensive conditions include Al<sub>2</sub>O<sub>3</sub> (12 – 14.5  $\pm$  0.93), CaO (0.7 – 2.4  $\pm$  1.4), FeO (0.6 – 1.4  $\pm$  1.8), MgO (0.0 – 0.5  $\pm$  1), and TiO<sub>2</sub> (0.1 – 0.2  $\pm$  0.7). All these results and the average SiO<sub>2</sub> value (wt%) with its standard deviation (1 $\sigma$ ) of 74.1 ( $\pm$  3.3) suggest a dacitic-rhyolitic composition for the liquid in equilibrium with Group 1 amphiboles.

### 3.4.6. Oxygen fugacity ( $fO_2$ )

We determined  $fO_2$  buffer conditions in the six paired titanomagnetite-ilmenite microlites in equilibrium. The results are in the range of QFM+ 0.9 – 2 ( $\pm 0.1$ ) log units and QFM+ 1.3 – 2.5 ( $\pm 0.4$ ) log units according to the methods of Ghiorso and Evans (2008) and Sauerzapf et al. (2008), respectively (Fig. 3.10). The total uncertainty of Ghiorso and Evans's (2008) oxybarometer was determined through Morgado et al.'s (2019) method. We also calculated oxidation conditions via Ridolfi et al. (2010) in amphibole crystals of Group 1, which yielded oxygen fugacity buffer in the range of QFM+ 1.3 – 2.1 ( $\pm 0.4$ ) log units. It is worth noting that Erdmann et al. (2014) show that Ridolfi et al.'s (2010) oxybarometer gives better results than that of Ridolfi and Renzulli (2012).

Taking all these data, the average  $fO_2$  buffer condition is QFM+ 1.7 log units. Additionally, considering  $XFe_2O_3/XFeO=0.3$  (mole fraction calculated from the representative Azu 7 EN enclave sample composition; Table 3.2) and the Kress and Carmichael's (1991) method, we obtained consistent oxidation conditions results between QFM+ 1.3 – 2.5 log units. This latter oxygen fugacity interval was calculated for the whole temperature range recorded in crystal phases (i.e., 712 – 1097 °C) as it is unknown at which temperature the liquid reached the calculated  $XFe_2O_3/XFeO$  ratio of the representative enclave sample.

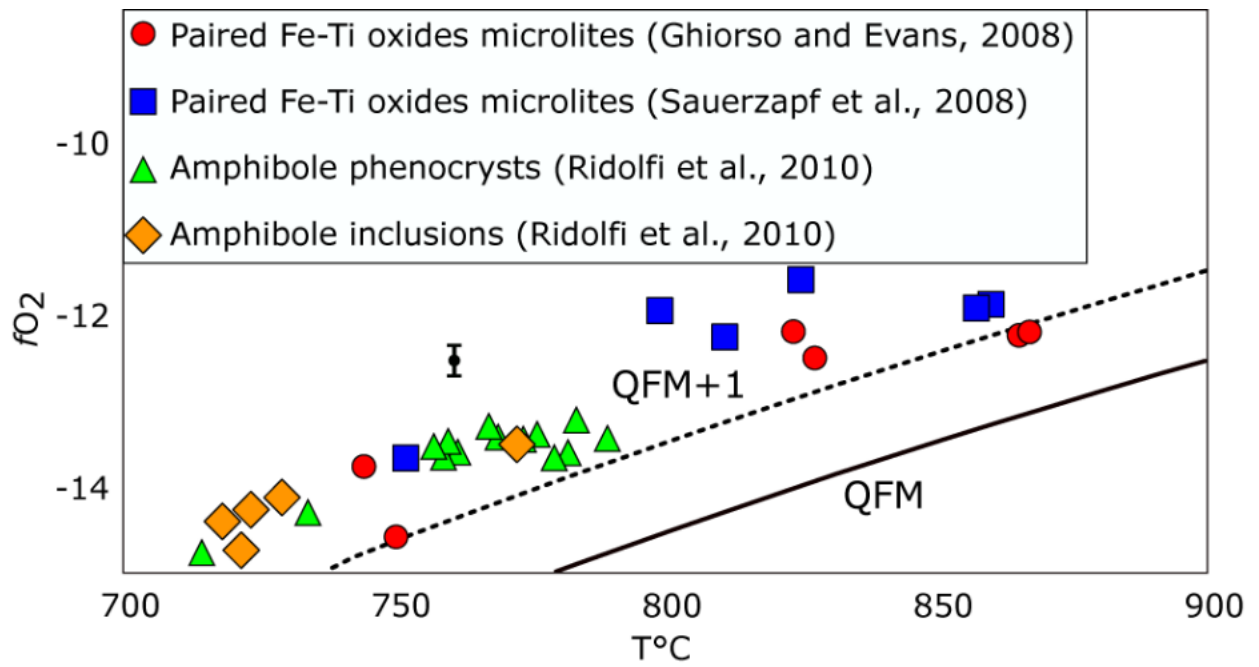


Fig. 3.10: Oxygen fugacity buffer results for the studied lava samples. Temperatures of Group 1 amphibole correspond to those calculated using the equation B of Holland and Blundy (1994). QFM buffer line was calculated according to Frost (1991) at P= 2 kbar. The data of oxygen fugacity ranges, average values, standard deviation and total uncertainty of each method are shown in Table 3.7

### 3.4.7. Thermodynamic model: MELTS

Due to Rhyolite-MELTS has not adequate thermodynamic models to reproduce hydrous-mafic silicates (Gualda et al. 2012), we only evaluated the equilibrium crystallization conditions (P-T- $fO_2$ -H<sub>2</sub>O) and chemical compositions of common high-temperature phases in calc-alkaline magmas, such as olivine and pyroxenes, whose saturation temperatures occur closer to the liquidus than amphibole or biotite crystallization (Blatter et al. 2013). This early crystallization of anhydrous-mafic minerals occurs even at low pressure conditions (minor to 2 – 3.5 kbar) for basaltic andesite and andesitic liquids (Grove et al. 1997; Moore and Carmichael 1998; Martel et al. 1999). Additionally, as some plagioclase microlites of composition  $An_{\geq 66}$  are inclusions in amphibole microphenocrysts (Fig. 3.4d), we also evaluated its crystallization conditions by multiple equilibrium conditions using the enclave sample Azu 7 EN as initial melt composition. To avoid bias to P-T- $fO_2$  conditions previously determined, we performed the equilibrium crystallization models at pressures between 1 and 5 kbar (considering intervals of 1 kbar), temperatures from 1300 °C (with cooling steps of 5 °C), oxidation conditions fixed at different buffers (QFM, QFM+1, and QFM+2), and with initial water contents (H<sub>2</sub>O wt%) between 1 wt% and saturation conditions (with intervals of 1 wt%). As H<sub>2</sub>O saturation is highly dependent on the pressure value fixed in each model, it can range between 4 and 9 wt% for the considered pressure interval. The details of simulations are presented in supplementary material “MELTS simulations”.

MELTS models indicated that the olivine formation ( $FO_{80 - 81}$ ) was followed as temperatures decrease by co-crystallized Mg-rich orthopyroxene ( $En_{77 - 79}Fs_{18 - 20}Wo_3$  and Mg#: 79 – 82) and Mg-rich clinopyroxene ( $En_{43 - 48}Fs_{9 - 10}Wo_{43 - 47}$  and Mg#: 81 – 84), and by Ca-rich plagioclase ( $An_{66 - 69}$ ). This crystallization sequence is modeled at initial water contents between 4 – 5 wt% and P- $fO_2$  conditions of 2 kbar and QFM+1 buffer (Fig. 3.11a). The simulating phase compositions are consistent with those of olivine cores, Mg-rich rims of pyroxene phenocrysts pairs, Mg-rich orthopyroxene patches, and Ca-rich plagioclases (cores and rims of phenocrysts and microlites with  $An_{\geq 66}$ ) recorded in the studied lava samples. In addition, modeled equilibrium temperatures obtained for co-crystallized Mg-rich orthopyroxene and clinopyroxene (980 – 1060 °C) are consistent with those



determined by two-pyroxene thermometry (Fig. 3.9d, e), while the temperature range of modeled plagioclase (905 – 940 °C) is within the lower uncertainty of the temperatures obtained from the plagioclase-liquid thermometry (Fig. 3.9f). In the case of modeled olivine, whose crystallization from liquids with enclave samples compositions is also supported by equilibrium tests, MELTS gave higher crystallization temperatures (1035 – 1070 °C) than the Mg-rich pyroxenes for each initial water content. The simulated crystallinities reach up to 27 – 30 vol% at 900 °C (Fig. 3.11b). Lastly, our thermodynamic models are also supported by experimental studies (Grove et al. 1997; Moore and Carmichael 1998). The supplementary material “Shallow Mg-rich pyroxenes and olivine crystallization data” shows comparable mineral chemistry synthesized at experimental conditions like our determined intensive conditions.

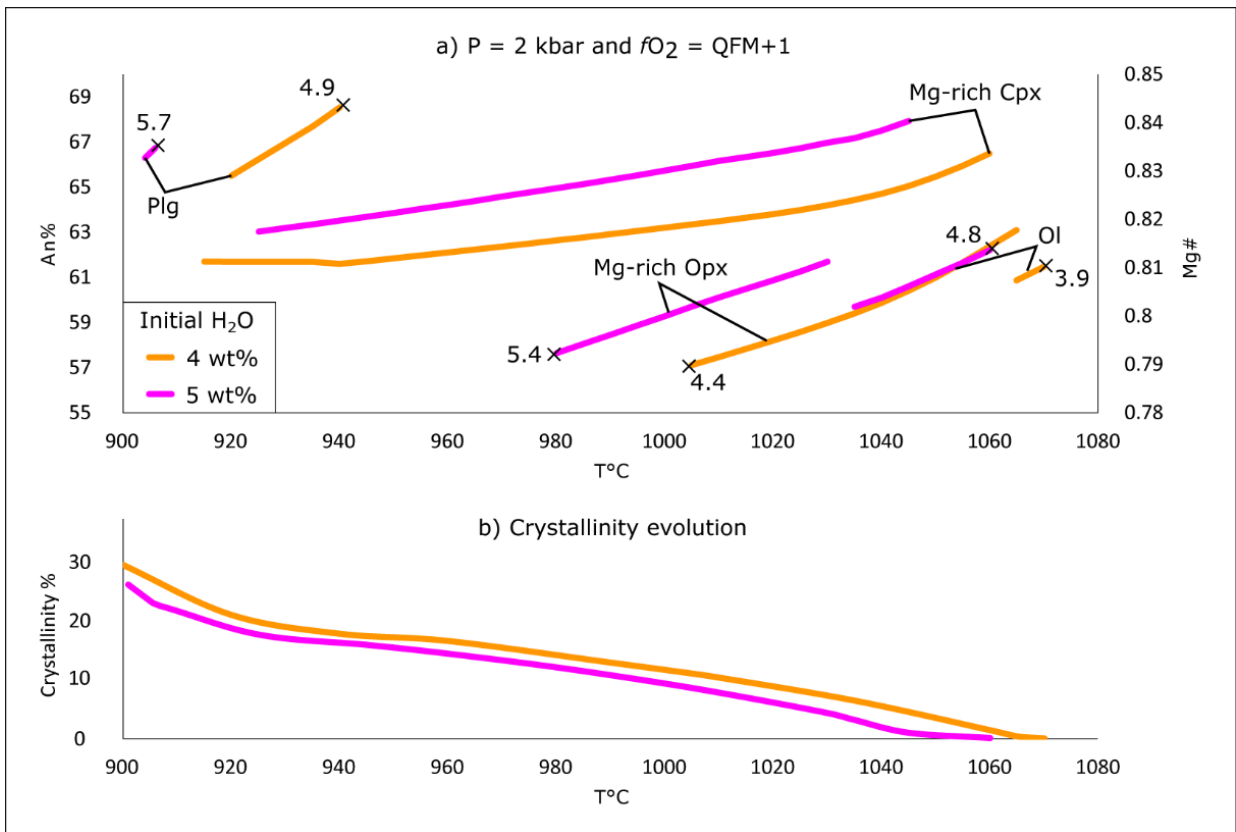


Fig. 3.11: **a** Diagram showing Rhyolite-MELT models that reproduce the observed compositions of high-temperature mineralogy from the studied lava samples, i.e., olivine cores, Mg-rich pyroxenes (Mg-rich rims of both pyroxene phenocrysts and Mg-rich orthopyroxenes patches in Mg-rich rims of clinopyroxene phenocrysts), and Ca-rich plagioclase ( $An \geq 66$ ). **a** Diagram also exhibits the evolution of initial water contents (wt%; black crosses) and mineral compositions in terms of An% and Mg#. Initial water contents of 3.9 and 4.8 wt% (instead of 4 and 5 wt%) are due to the normalization of melt composition to 100% at the beginning of simulations. **b** Diagram displays percentage evolution of crystallinity in the system

Table 3.7: Summary of calculated intensive conditions and H<sub>2</sub>O content for the last eruptive stage of the Azufre volcano

Method	Reference	Phases involved	P (kbar)	Total uncertainty of method ( $\pm\sigma_T$ )	Average	Standard deviation ( $\pm 1\sigma$ )
Al-in-hornblende	Anderson and Smith (1995)	Amphibole-plagioclase pairs of Group 1	1.6 – 3.1	1	2	0.4
Al-in-hornblende	Mutch et al. (2016)	Group 1 amphiboles	2 – 3.3	0.4	2.6	0.3
Amphibole	Ridolfi and Renzulli (2012)	Group 1 amphiboles	1 – 1.7	0.5	1.3	0.2
Rhyolite-MELTS	Gualda et al. (2012)	Ol – Mg-rich Pyx – Ca-rich Plg (An $\geq 66$ )	2	-	-	-
T (°C)						
Amphibole-plagioclase	Holland and Blundy (1994) (equation B)	Amphibole-plagioclase pairs of Group 1	712 – 788	40	758	24
Amphibole-plagioclase	Holland and Blundy (1994) (equation A)	Amphibole-plagioclase pairs of Group 1	747 – 827	40	779	26
Two-pyroxenes	Putirka (2008) (equation 37)	Mg-poor cores of phenocrysts	860 – 943	38	909	23
Two-pyroxenes	Putirka (2008) (equation 37)	Mg-rich rims of phenocrysts	918 – 1071	38	977	57
Two-pyroxenes	Putirka (2008) (equation 37)	Mg-rich orthopyroxene patches in Mg-rich rims of clinopyroxene phenocrysts	916 – 1097	38	1019	49
Plagioclase-liquid	Putirka (2005) (equation 3)	Ca-rich plagioclase (An $\geq 66$ )	957 – 1028	53	1016	17
Fe-Ti oxides	Ghiorso and Evans (2008) (Fe-Ti exchange equation)	Paired titanomagnetite-ilmenite microlites	742 – 866	18	811	50
Fe-Ti oxides	Sauerzapf et al. (2008)	Paired titanomagnetite-ilmenite microlites	750 – 859	50	816	37

Rhyolite-MELTS	Gualda et al. (2012)	Olivine	1035 – 1070	-	-	-
Rhyolite-MELTS	Gualda et al. (2012)	Mg-rich pyroxenes (co-crystallized orthopyroxene and clinopyroxene)	980 – 1060	-	-	-
Rhyolite-MELTS	Gualda et al. (2012)	Ca-rich plagioclase (An $\geq$ 66)	905 – 940	-	-	-

---

Table 3.7: (continued)

Method	Reference	Phases involved	$fO_2$ (QFM+)	Total uncertainty of method ( $\pm\sigma_T$ )	Average	Standard deviation ( $\pm 1\sigma$ )
Fe-Ti oxides	Ghiorso and Evans (2008)	Paired titanomagnetite-ilmenite microlites	0.9 – 2	0.1	1.1	0.2
Fe-Ti oxides	Sauerzapf et al. (2008)	Paired titanomagnetite-ilmenite microlites	1.3 – 2.5	0.4	1.6	0.3
Amphibole	Ridolfi et al. (2010)	Group 1 amphiboles	1.3 – 2.1	0.4	1.7	0.2
XFe <sub>2</sub> O <sub>3</sub> /XFeO	Kress and Carmichael (1991)	Liquid (Azu 7 EN composition)	1.3 – 2.5	-	-	-
Rhyolite-MELTS	Gualda et al. (2012)	Ol – Mg-rich Pyx – Ca-rich Plg (An $\geq$ 66)	1	-	-	-
H <sub>2</sub> O (wt%)						
Rhyolite-MELTS	Gualda et al. (2012)	Ca-rich plagioclase (An $\geq$ 66)	4.9 – 5.7	-	-	-
Rhyolite-MELTS	Gualda et al. (2012)	Ol – Mg-rich Pyx	3.9 – 5.4	-	-	-

## 3.5. Discussion

### 3.5.1 Shallow depth magmatic evolution: magma mixing and zonation of the reservoir

The consistent results obtained from three geobarometers (Fig. 3.8) and MELTS models (Fig. 3.11) suggest that the late-stage magmatic evolution of the Azufre volcano is developed at shallow crustal depths. We consider the average pressure of Group 1 amphiboles (and its standard deviation) of  $2 \pm 0.6$  kbar as the more likely range of crystallization. Similar pressure results between 1.4 – 2.2 kbar were obtained by Godoy et al. (2022) using Ridolfi and Renzulli's (2012) geobarometer in amphiboles. Our pressure range represents a magma chamber storage depth of  $5.4 \pm 2.2$  km below the surface if the volcanic edifice load is considered with its ~2 km height above its surrounding plateau and a crust density of  $2.7 \text{ g/cm}^3$  (Prezzi et al. 2009). This depth is consistent with a magnetotelluric survey that detected active storage of melt and fluids less than 10 km below the surface of the Azufre volcano (Araya Vargas et al. 2019). It is also consistent with the estimated depth for the brittle-ductile upper crust transition ( $2 \pm 0.5$  kbar), a mechanical level that has been widely recognized as the optimal subvolcanic depth for magma chamber growth (Burov et al. 2003; Huber et al. 2019). Our results appear to be consistent with pressure estimates for shallow reservoirs of other volcanic centers of the APVC such as Aguilucho-Apacheta Volcanic Complex (0.9 – 1.9 kbar; Gorini et al. 2018), Uturuncu volcano ( $1 \pm 0.5$  kbar; Muir et al. 2014b; Comeau et al. 2015), and Purico and Atana ignimbrites (1.1 – 3.3 kbar; Schmitt et al. 2001; Lindsay et al. 2001).

The evidence of magma mixing (and mingling) in the studied lava deposit includes the presence of andesitic enclaves, disequilibrium textures, and wide temperature variations (Fig. 3.9). We infer the existence of two compositional magma end members mixed in an open system. The felsic member would correspond to a dacitic-rhyolitic liquid with 63 – 79 wt%  $\text{SiO}_2$ , which contains in equilibrium Ca-poor plagioclase, Group 1 amphiboles, biotite, quartz, and Fe-Ti oxides phenocrysts together with apatite and titanite as accessory phases. The more primitive end member would correspond to an andesitic

liquid with 58 – 60 SiO<sub>2</sub> wt% (enclave compositions) equilibrated with mafic mineralogy of olivine, Mg-rich orthopyroxene and clinopyroxene phenocrysts, Ca-rich plagioclase (forming external rims and cores of phenocrysts and microlites), and non-equilibrated Group 2 amphibole microphenocrysts. According to petrologic models and geophysical surveys, the andesitic liquids could come from APMB (i.e., 20 – 30 km; Muir et al. 2014b; Ward et al. 2014; Comeau et al. 2015) or lower crust (50 – 80 km; Araya Vargas et al. 2019). In fact, the higher La<sub>N</sub>/Yb<sub>N</sub> and Sr/Y values showed by the enclave samples in relation to those of lava samples are consistent with a deeper source of andesitic liquid than those of shallow reservoir (45 – 60 km according to models of Profeta et al. (2015), and Lieu and Stern (2019)). The higher La<sub>N</sub>/Yb<sub>N</sub> and Sr/Y ratios in enclaves compared to lava samples could be attributed to contamination of felsic-low-pressure mineralogy into the andesitic liquid. It is supported by the microlites and microphenocrysts compositions (Fig. 3.3e, Fig. 3.4a, and Fig. 3.5b), indicating that the lava groundmass was composed of a melt resembling the composition of enclaves. Additionally, the Sm/Yb ratios of enclave samples provide further evidence of a deep source, as these values suggest a mid-crustal melting with amphibole as the residual phase (Kay et al. 2010).

The effects of magma mixing can be summarized by the presence of dissolution textures of plagioclase phenocrysts (Fig. 3.3e, f), breakdown textures in biotite and amphibole crystals of both groups (Fig. 3.4e), embayed rims in plagioclase and quartz phenocrysts (Fig. 3.3f, and Fig. 3.6d), and reaction rims in olivine and quartz phenocrysts (Fig. 3.6c, d). All these textures indicate that mixing involves, among other processes, the heating of the magma chamber and its decompression via eruption event (Tsuchiyama 1986; Rutherford and Hill 1993; Henton de Angelis et al. 2015). Although the magma mixing would be a continuous process in the evolution of the magma chamber, a more relevant mixing stage likely triggered the last eruption of the Azufre volcano after a high thermal perturbation (i.e., system rejuvenation). This is inferred from the reverse zoning in plagioclase and pyroxene phenocrysts (Fig. 3.3c, Fig. 3.5c, and Fig. 3.5d). In fact, the greater than 250°C differences in crystallization temperatures between Ca-poor intermediate zones and Ca-rich rims of plagioclase phenocrysts (Fig. 3.9a, f) and higher than 100°C between Mg-poor cores and Mg-rich rims of pyroxenes pairs (Fig. 3.9c – e) can be interpreted as evidence of the last heating prior to eruption. Due to the refractory

behavior of plagioclase with increasing temperature, and its consequent slow dissolution kinetics, the presence of reabsorption features is consistent with the wide temperature variation (i.e., 250 °C) recorded by the compositional changes of the analyzed crystals in a relatively protracted magmatic residence time. For example, in an experimental study, Tsuchiyama (1985) estimated for different plagioclase compositions that the time formation of a dusty zone (i.e., dissolution) with 0.1 mm of width is approximately 0.5 - 50 years at 1,100°C and 100 – 1,000 years at 1,000°C. Thus, plagioclase phenocrysts may have enough time to re-equilibrate to the new temperature and composition of the melt during the mixing stage and form their Ca-rich rims in a located place of the magma chamber, as felsic mineralogy also indicates that its remobilization before the eruption was fast enough to preserve low-temperature crystals (partially resorbed) of quartz, biotite, and Group 1 amphiboles.

Supported by thermometry results, MELTS models, and mineralogy associated with each magmatic end member, we propose that the shallow-magmatic reservoir was thermally and compositionally zoned during the mixing process. The presence of felsic mineralogy together with the low temperatures yielded by Group 1 amphiboles (712 – 788 ( $\pm$  40) °C) indicate a cool siliceous zone, whereas the consistent results from MELTS models and thermometry of Mg-rich pyroxenes and Ca-rich plagioclases with  $An \geq 66$  (Fig. 3.9d – f) suggest a hot andesitic zone (905 – 1097 ( $\pm$  38) °C).

Simple and more complex models have been invoked to explain compositional and thermal differences within a single magma reservoir. Simple-symmetric models consider a hot zone that would have settled in the lower levels of a magmatic reservoir, resulting from magma recharge coming from more deep reservoirs, whereas a cool zone would be developed at the walls of the reservoir as in situ solidification front with its associated boundary-layer flow. This simple visualization is supported by diverse methodologies used to research magma reservoirs evolution, such as theoretical and experimental studies (Turner 1980; Huppert and Sparks 1984; Marsh 1996) and numerical models of basaltic and felsic magmatic systems (Gutiérrez and Parada 2010; Gutiérrez et al. 2013; Aravena et al. 2017). By contrast, more complex models would also regard different geometric configurations of the reservoir (e.g., vertical, horizontal, oblate, or prolate shapes) and diverse points of magma injections at its bottom, displaying asymmetric rates and volumes



of recharge. These considerations would give rise to an irregular temperature variation within the reservoir and the consequent heterogeneous distribution of hot and cool zones. Thus, cool zones would exist in places of low intrusion frequency or small volumetrically. An example of complex processes developing a magma reservoir, and including an asymmetric geometric configuration, comes from some plutons that indicate lateral propagation as its growth mechanism (Johnson et al. 2003; Gutiérrez et al. 2018).

Whatever the distribution of both zones, the intruded andesitic melts would have fractionated in the hot zone, generating a cumulate of high-temperature mineralogy with a relative crystal content of ~30 vol% at 900 °C as is suggested by MELTS results (Fig. 3.11). The more evolved residual liquids would give rise to the crystallization of Mg-poor pyroxenes at intermediate-temperature (860 – 943 ( $\pm$  38) °C) and the felsic low-temperature mineralogy. The later crystallization of Mg-poor pyroxenes concerning Mg-rich pyroxenes is also supported by the low and high Cr<sub>2</sub>O<sub>3</sub> (wt%) concentration of each one, respectively. Considering the obtained low-temperatures (Group 1 amphiboles) near solidus conditions (i.e., ~680 °C for a water-saturated granitic system at 2 kbar of pressure; Holtz et al. 2001), the observed exsolution lamellae in Fe-Ti oxides phenocrysts (which could be related to subsolidus conditions; Buddington and Lindsley 1964), and the scarcity of molten bodies even in active volcanic regions (Cashman et al. 2017), it could infer that a crystal-mush was formed at some development stage of the reservoir.

Low-temperature results, pressure buffering assemblage, and calculated felsic-melt composition are also consistent with the presence of biotite and quartz phenocrysts, as both coexist in equilibrium with a dacitic liquid at water-saturated conditions below 800 °C (Venezky and Rutherford 1999; Holtz et al. 2005). Additionally, other authors (Schmitt et al. 2001; Lindsay et al. 2001) also reported similar low temperatures for amphibole crystallization (730 – 790 °C) in zoned dacitic reservoirs that generated ignimbrites deposits from the APVC (e.g., Atana, Toconao, and Purico ignimbrites). Considering all the aforementioned reasons and the similar composition of amphiboles presented by Godoy et al. (2022) to those of Group 1 of this study, it seems that amphibole temperatures determined by Godoy et al. (2022) using Ridolfi and Renzulli's (2012) geothermometer (~810 – 900 °C) appear to overestimate the temperature for the petrogenetic model of the Azufre volcano's shallow reservoir.

Finally, additional evidence supporting the reservoir zonation comes from the Ca-rich cores, Ca-rich internal rings, and dissolution textures of plagioclase phenocrysts (Fig. 3.3), which are widely recognized features indicative (not exclusive) of open magma systems with temperature, chemical, and volatile variations (Tsuchiyama 1985; Landi et al. 2004; Streck 2008; Cashman and Blundy 2013). Similarly, the observed breakdown textures in amphibole crystals, commonly attributed to decompression or heating events (Rutherford and Hill 1993; Buckley et al. 2006; Browne and Gardner 2006; Henton de Angelis et al. 2015), are also evidence of pressure and temperature gradients within the reservoir.

### **3.5.2. $fO_2$ and $H_2O$ conditions in the reservoir**

Oxygen fugacity results from Group 1 amphiboles,  $XFe_2O_3/XFeO$  ratio of the representative enclave sample, and MELTS models constrain the oxidation state of the reservoir (considering the uncertainties) to QFM+ 0.9 – 2.5 log units. Fe-Ti oxide microlites indicated that these conditions are kept even during the lava flow emplacement stage (discussed in the following subsection), with values between QFM+ 0.9 – 2.5 ( $\pm 0.4$ ) log units (Table 3.7). Although the goal of this study is not to explain the reason for the observed redox variation, it would be related to water, sulfur, and/or chlorine degassing (Bell and Simon 2011; Moussallam et al. 2014; Humphreys et al. 2015). For example, the MELT simulation at an initial water content of 5 wt% indicates that the system reaches water saturation at 5.3  $H_2O$  wt% and 1005 °C. This water-saturated content is also consistent with results coming from solubility models of both Moore et al. (1998) and Zhang et al. (2007), which stated at P-T conditions of 2 kbar and 1005 °C a water-saturated condition of 5.4 ( $\pm 0.5$ ) and 5.2 ( $\pm 0.7$ ) wt% for a liquid composition corresponding to enclave sample Azu EN 7 (see solubility model results in “P-T-felsic melt composition- $fO_2$ -Solubility calculations”). Whatever the causes of the recorded oxygen fugacities, the determined water contents (3.9 – 5.7 wt%) would be preserved during the high-temperature mineralogy fractionation (i.e., olivine, Mg-rich pyroxenes, and Ca-rich cores of plagioclase phenocrysts) and the crystallization of Ca-rich ( $An_{\geq 66}$ ) microlites and external rims of plagioclases phenocrysts in the final mixing stage (Fig. 3.11a).

Although mixing and heating seem to be the main eruption triggers, it is likely that the addition and exsolution of volatiles (water mainly) also played a role, such as evidenced by the diktytaxitic texture of enclaves and the possible water-saturated crystallization according to MELTS. Besides, an additional water input to the system could occur from the breakdown of biotite and amphibole crystals, as the destabilization of these phases releases the ~2 wt% of H<sub>2</sub>O housed in their crystalline structures (Bardintzeff and Bonin 1987; Buckley et al. 2006).

### **3.5.3. Temperatures of eruption and cooling in the lava**

Eruption temperatures can be inferred from microlites (despite rapid crystallization during the syn-eruptive stage with a high degree of undercooling) if equilibrium-crystallization conditions are tested and suggested by equilibrium tests. In our case, the late crystallization stage of plagioclases at the moment of the eruption (or immediately before it) is represented by their Ca-rich microlites and phenocrysts rims. Thus, based on these late plagioclase compositions in equilibrium ( $An \geq 66$ ) with the representative liquid (Fig. 3.7a), we deduce that the studied lava flowed at temperatures of up to 1028 ( $\pm 53$ ) °C when the eruption took place. This temperature result is also consistent with a direct provenience of lava from the andesitic hot zone and the mixing process as an eruption trigger. However, from paired titanomagnetite-ilmenite microlites, we also recorded lower temperatures (742 – 866 ( $\pm 18 - 50$ ) °C; Fig. 3.9g, h) that are interpreted as cooling temperatures during the lava flow emplacement at sub-aerial conditions. The latter is based on interdiffusion models (Fig. 3.12), which consider the small sizes of ilmenite crystals (<20  $\mu\text{m}$ ; Fig. 3.6b), the high interdiffusivity in Fe-Ti oxides (van Orman and Crispin 2010; Prissel et al. 2020), and the consequent capacity to record late stage of magmatic evolution (Hammond and Taylor 1982; Morgado et al. 2019). Interdiffusion models of Fe-Ti (Freer and Hauptman 1978; Aragon et al. 1984), Fe-Mn, and Fe-Mg (Prissel et al. 2020) indicated that titanomagnetite and ilmenite crystals with a representative radius of 5  $\mu\text{m}$  could be equilibrated (or re-equilibrated) in timescales of the order of minutes to days (Fig. 3.12). In particular, the slower interdiffusion rate based

on Aragon's et al. (1984) model gives equilibration times of 14 days at the representative temperature of 800 °C for titanomagnetites with 0.08 titanium mole fraction ( $X_{Ti}$ ). The details of interdiffusion calculations are in supplementary material "Equilibrium time of ilmenite and titanomagnetite".

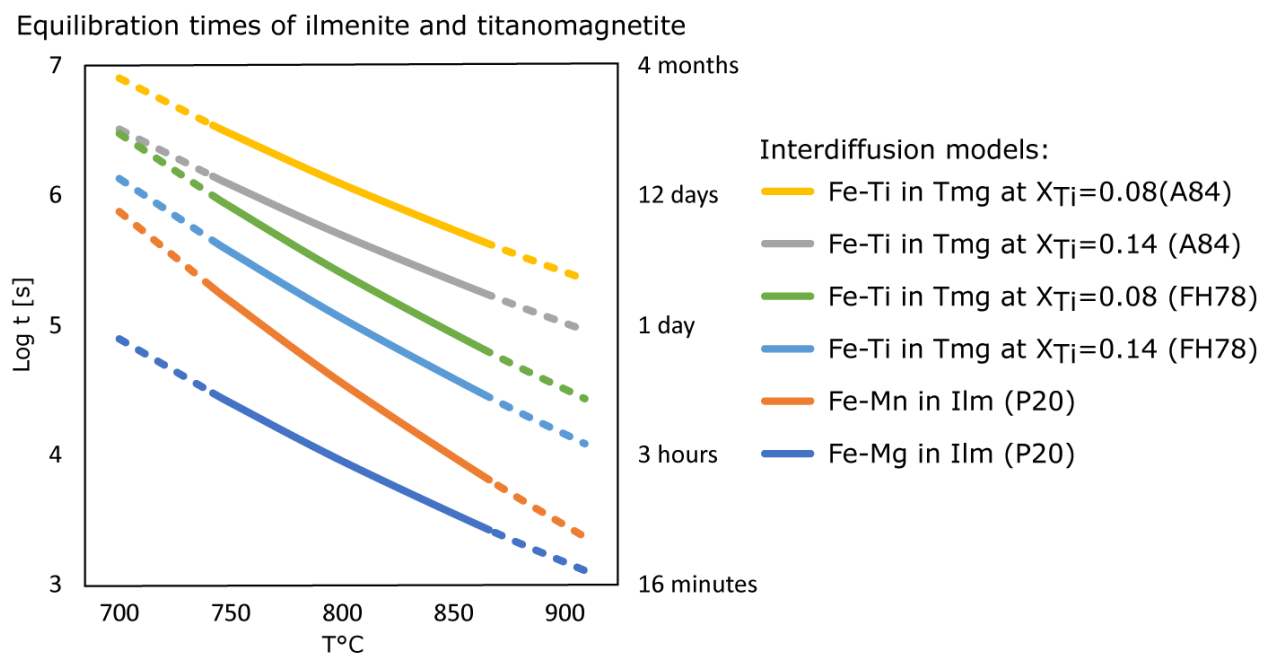


Fig. 3.12: Equilibration times plot for paired titanomagnetite-ilmenite microlites. The crystals were modeled as spheres with a representative radius of 5  $\mu\text{m}$  through interdiffusion coefficient models of FH78 (Freer and Hauptman 1978), A84 (Aragon et al. 1984), and P20 (Prissel et al. 2020) following the  $fO_2$  parameters fixed by van Orman and Crispin (2010). The dashed lines correspond to the maximum uncertainty of Fe-Ti oxides thermometry (i.e.,  $\pm 50$  °C), while  $X_{Ti}$  is the titanium mole fraction in titanomagnetite

### 3.6. Conclusions

The Azufre volcano is a stratovolcano emplaced over a 70 km long NW-SE alignment above the western boundary of the Altiplano Puna Magma Body. Its last eruption (50 – 331 ka) consists of an andesitic-dacitic (61 – 63 SiO<sub>2</sub> wt%) lava deposit that contains less evolved andesitic enclaves (58 – 60 SiO<sub>2</sub> wt%). The magmatic evolution associated with this eruption took place in a shallow ( $2 \pm 0.6$  kbar) magma reservoir ( $5.4 \pm 2.2$  km beneath the surface considering the edifice load), which was intruded and mixed by hot andesitic liquids (i.e., enclaves) that would come from APMB (20 – 30 km) or lower zones of crust (45 – 80 km). The reported enclaves are the principal evidence of the complex magmatic processes developed in the Azufre volcano's reservoir (i.e., heating, mixing, and mingling, among others). The fractionation of these intruded-less evolved andesitic liquids would generate a high-temperature (905 – 1097 ( $\pm 0 - 38$ ) °C) cumulate of olivine, Mg-rich pyroxenes, and Ca-rich plagioclase (Ca-rich cores within Ca-poor phenocrysts) together with a residual felsic melt (63 – 79 wt% SiO<sub>2</sub>). This latter would be upward transported within the reservoir and crystallized in a low-temperature (712 – 788 ( $\pm 40$ ) °C) assemblage near solidus conditions consisting of Ca-poor plagioclase, amphiboles (Group 1), biotite, quartz, and Fe-Ti oxides phenocrysts together with apatite and titanite as accessory phases. This process allowed a thermal and compositional zonation with an unknown spatial distribution within the reservoir. Nevertheless, a simple model considers the hot andesitic zone(s) settled at the bottom of the magma reservoir and surrounded by the cool silicic zone(s). The overall oxidation state of the magma reservoir was restricted to QFM+ 0.9 – 2.5 log units, while the water content within the hot andesitic zone (3.9 – 5.7 wt%) would correspond to undersaturated to saturated conditions. A simple schematic conceptual model summarizing the discussed processes is shown in Fig. 3.13.

The last eruption of the Azufre volcano would have occurred after system rejuvenation, characterized by heating, vigorous mixing, and likely, to some extent, water exsolution. In addition to enclaves, the mixing is also recorded in different crystal textures as resorbed plagioclase and quartz phenocrysts, breakdown of amphibole and biotite crystals, reverse zoning in pyroxene and plagioclases phenocrysts, and reaction rims in olivine and quartz

phenocrysts. At the time of the eruption, the lava would have flowed at temperatures as high as those of the hot zone (1028 ( $\pm$  53) °C). However, lower temperatures (742 – 866 ( $\pm$  18 – 50) °C) are recorded by Fe-Ti oxides microlites during the lava flow emplacement at sub-aerial conditions.

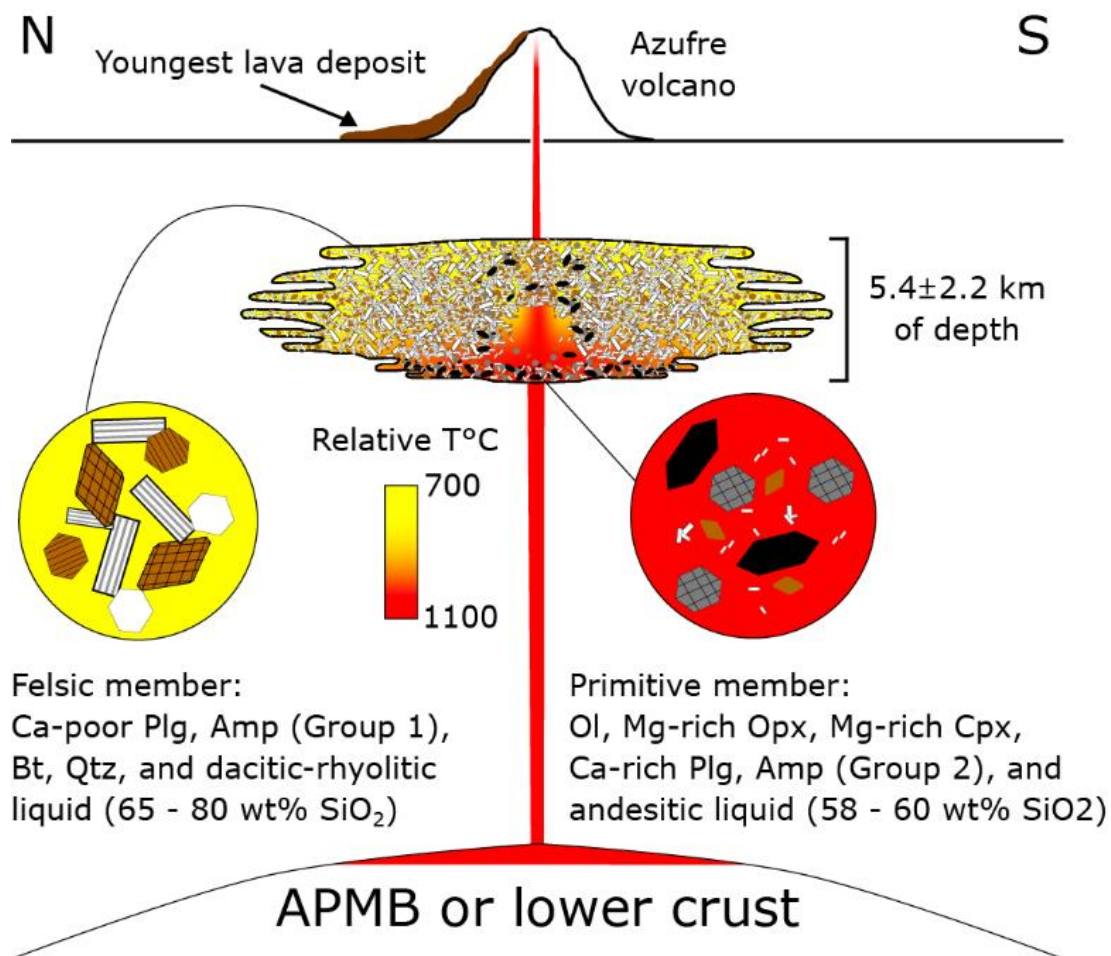


Fig. 3.13: Schematic representation (not to scale) of the processes associated with the last eruptive stage of the Azufre volcano. The intruded andesitic liquids (from APMB or lower crust zones) are mixed with hosted magma and differentiated in the shallow crust, producing a crystal mush and residual felsic melts, which give rise to thermal and compositional zonation of the reservoir

## **Acknowledgments**

We are grateful to Lorena Olivares, Rodrigo Espinoza and Vicente Méndez for their valuable assistance and discussion in the fieldwork. We also acknowledge the team of LAMARX-National University of Córdoba for aid in EMPA analyses. Helpful comments on the manuscript by Philippe Robidoux, Duncan Muir (reviewer), and Chuck Lewis (reviewer) are much appreciated. This work was funded by FONDAP-CONICYT project 15090013 "Andean Geothermal Center of Excellence" and the Department of Geology, both at the University of Chile.

## **Author contributions**

DH: conceptualization, methodology, computation, evaluation, and visualization; MAP: supervision; EM: supervision; DH wrote the original draft of the paper; all authors discussed the results and commented on the draft of the paper.

# CAPÍTULO 4: APROXIMACIÓN DEL VOLUMEN DE LA CÁMARA MAGMÁTICA QUE ORIGINÓ EL DEPÓSITO DE LAVA ESTUDIADO

## 4.1. Introducción

A partir de trabajos volcanológicos que estudian las morfologías de los edificios volcánicos y sus respectivos depósitos de lavas, se ha planteado la posibilidad de determinar parámetros asociados al sistema alimentador que sustenta la formación de dichos edificios (Castruccio et. al 2017). Tales parámetros incluyen el volumen de la cámara magmática, la profundidad a la cual se encuentra el techo de dicha cámara junto con el largo y ancho del dique alimentador del edificio volcánico.

En el presente capítulo se aplicarán parte de las metodologías propuesta por Castruccio et. al (2017) para realizar una aproximación del volumen de la cámara magmática que dio paso a la última erupción del volcán Azufre. Otros parámetros como la profundidad del techo del reservorio del volcán Azufre no fueron posibles de estimar debido a la necesidad de conocer datos complejos que están fuera de los objetivos de la nuestra tesis (e.g., sobrepresión de la cámara magmática  $\Delta P_i$  previo al comienzo de una erupción o tasas eruptivas  $Q_0$  y  $Q_h$  que son representativas de diferentes eventos eruptivos durante la evolución del edificio volcánico). El resultado obtenido para el volumen de la cámara magmática del volcán Azufre se contrasta con el modelo de tamaño crítico para cámaras magmáticas que producen erupciones volcánicas de Townsend and Huber (2020) y datos de volúmenes inferidos para cámaras magmáticas de otros sistemas volcánicos.

Para lo anterior, se determinó el volumen y densidad del depósito más joven del volcán Azufre (estudiado en el capítulo 3) junto con otro depósito que podría ser considerado uno de los más antiguos asociados al volcán ( $\sim 1,5 \pm 0,1$  Ma; Fig. 4.1). Este último corresponde a la parte sureste del domo Chanka que se encuentra al oeste del volcán Azufre (Fig. 4.2; domo DI según Hübner 2018). El planteamiento de que dicho domo corresponde a una de las unidades más antiguas se basa en una datación K-Ar realizada por Roobol et al. (1974). Sin embargo, en el trabajo de Roobol et al. (1974) no queda



clara la ubicación específica de la muestra datada, ya que según las coordenadas sexagesimales la muestra se ubicaría al este del domo DI y a una cota de ~5.500 m (Fig. 4.1 y 4.2). Sin embargo, la misma descripción del punto de muestreo aportado por Roobol et al. (1974) deja como interpretación que la datación pueda corresponder al domo DI ya que describe la unidad como “dacita de domo extrusivo al flanco SE del volcán Azufre” (Fig. 4.1). Vale la pena mencionar que otros autores (Ramírez and Huete 1981; de Silva et al. 1994; Renzulli et al. 2006) también han interpretado que la datación correspondería al domo DI.

Finalmente, se debe destacar que los rasgos morfológicos del domo DI también sustentan una mayor antigüedad relativa a la parte joven del domo Chanka (domo DII según Hübner 2018; Fig. 4.3), ya que el primero presentan una morfología cónica de flancos abruptos con textura suavizada y cúspides terminadas en forma de punta (Fig. 4.3). Por el contrario, la parte joven del domo (DII) que fue datada en ~83 ka según un análisis geocronológico de U-Th en zircones (Tierney et al. 2016), presenta una morfología cónica de textura rugosa con cúspides anchas y planas, las cuales son características de un cuerpo más joven y con poca erosión.

492	Dacita de domo extrusivo	Flanco SE del Volcán Azufre	21° 48' S	68° 15' W	1.5 ± 0.1
-----	--------------------------	-----------------------------	-----------	-----------	-----------

Fig. 4.1: Extracto de la tabla de dataciones de Roobol et al. (1974), en la cual se expone la unidad, lugar y ubicación cartográfica para estas.

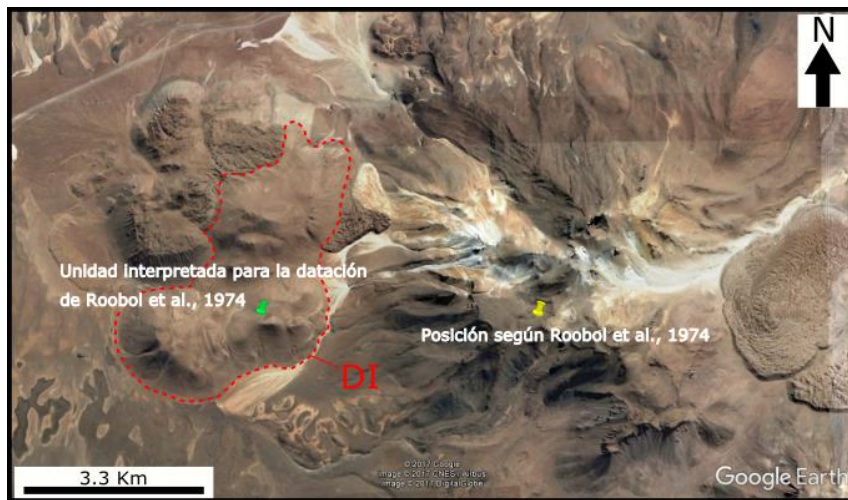


Fig. 4.2: Imagen satelital que exhibe el punto de coordenadas sexagesimales de la muestra datada por Roobol et al. (1974) más la interpretación del lugar datado según el presente documento, siendo asociado al domo DI (Hübner 2018) (modificado de Google Earth).

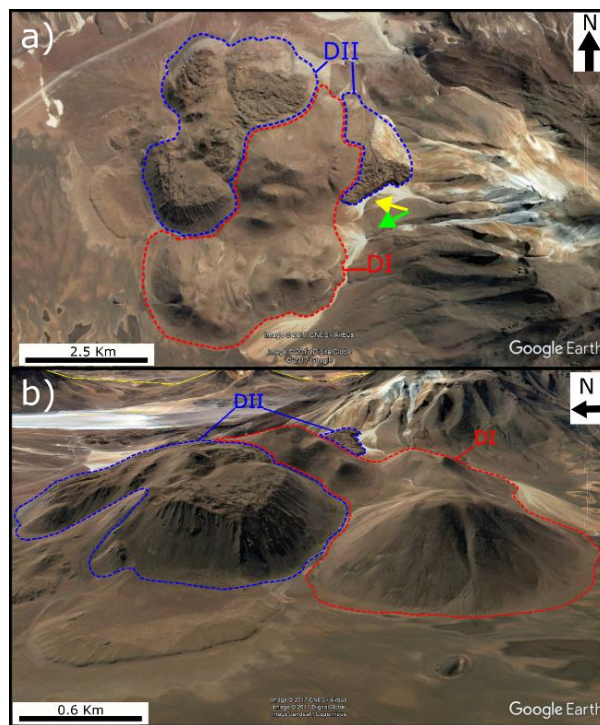


Fig. 4.3: Imagen satelital que expone las diferencias morfológicas en el domo Chanka. En a) vista en planta del domo. En b) vista lateral hacia el E, en la cual se aprecia una morfología cónica con cúspide en forma de punta para el domo DI (en rojo) y una cónica con cúspide plana para el domo DII (en azul) (modificado de Google Earth).

## 4.2. Cálculo de volúmenes y densidades

Considerando que el depósito antiguo (domo DI) se emplaza sobre una superficie prácticamente plana a una cota de 4.100 m.s.n.m. (Fig. 4.3 y 4.4), se utilizó la herramienta *Polygon Volume* de ArcGIS para determinar el volumen del depósito de domos DI. Esta metodología considera el volumen presente entre una cota base (en nuestro caso 4.100 m.s.n.m.) y la superficie topográfica del depósito, la cual fue modelada por medio de un DEM (*Digital Elevation Model*) y un TIN (*Triangulated Irregular Network*). Como resultado se obtiene un volumen de 4,1 km<sup>3</sup>.

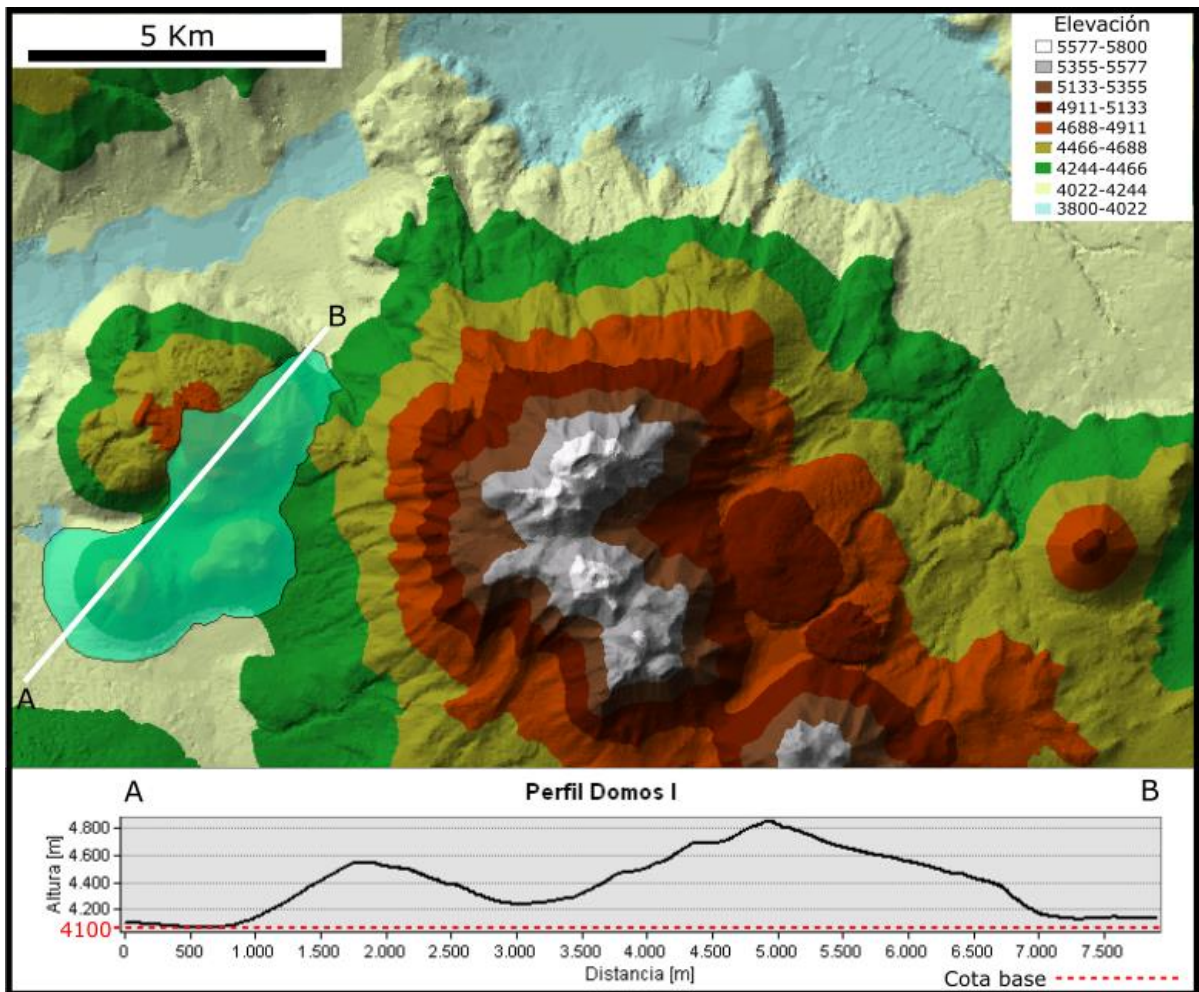


Fig. 4.4: Modelo de superficie TIN del volcán Azufre y perfil de elevación AB del domo I. En el perfil se destaca la cota de 4.100 m.s.n.m. como la base para el cálculo del volumen (modificado de ArcGIS).

Por otro lado, y debido a que a que el depósito joven del volcán Azufre se encuentra por sobre una ladera del volcán (es decir emplazado sobre una pendiente), no es posible aplicar la metodología antes mencionada (*Polygon Volume*) por no ser factible establecer una cota base que permita calcular un volumen representativo. Por lo anterior, se utilizó una combinación de herramientas existentes en el software ArcGIS.

En primer lugar, a partir del DEM se establecen las curvas de nivel asociadas al depósito de lava joven del volcán Azufre (Fig. 4.5) y su superficie TIN (Fig. 4.6). Luego, mediante el uso de las herramientas *Interpolate Shape* y *Erase* se interpolan los contactos entre las curvas de nivel y los límites del depósito de lava joven (i.e., intersección entre líneas celestes y línea roja en Fig. 4.5), lo cual permite a posterior extrae la topografía correspondiente a la colada joven y formar un nuevo TIN sin dicha morfología (Fig. 4.7). Así, es posible realizar una resta entre las dos superficies TIN (las correspondientes a las Fig. 4.6 y Fig. 4.7) mediante la herramienta *Surface Difference* y determinar así el volumen comprendido entre ellas (i.e., el volumen de la colada joven del volcán Azufre). Como resultado, se obtiene un volumen de 1,3 km<sup>3</sup>.

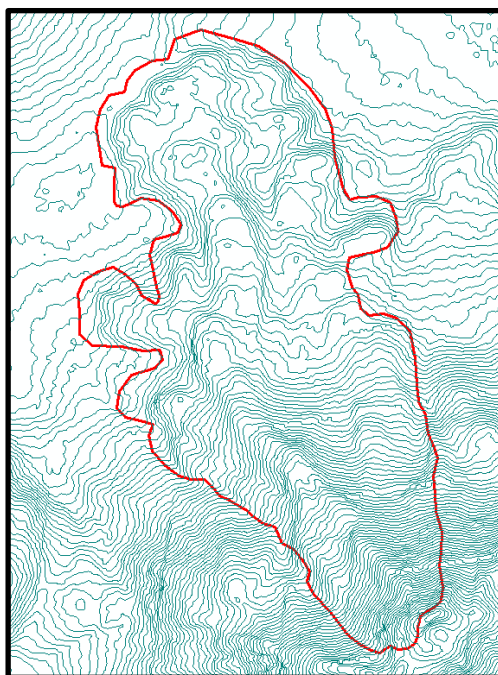


Fig. 4.5: Curvas de nivel asociadas al flanco norte del volcán Azufre y a su depósito de lava joven (delimitado en rojo; modificado de ArcGIS).

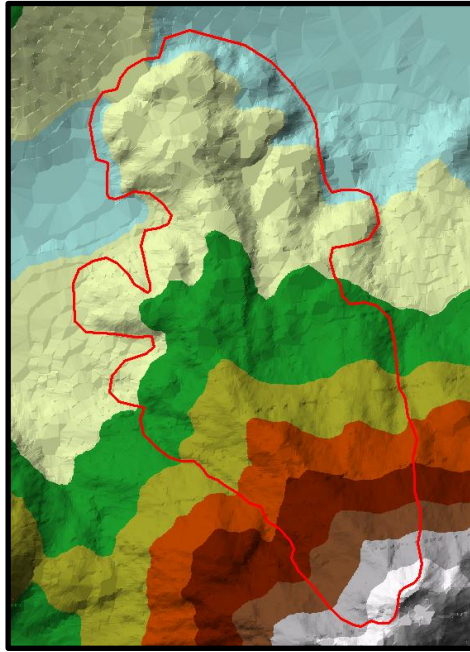


Fig. 4.6: Superficie TIN asociada al flanco norte del volcán Azufre y a su depósito de lava joven (delimitado en rojo). Gradación de colores corresponde a elevación según escala de la Fig. 5.4 (modificado de ArcGIS).

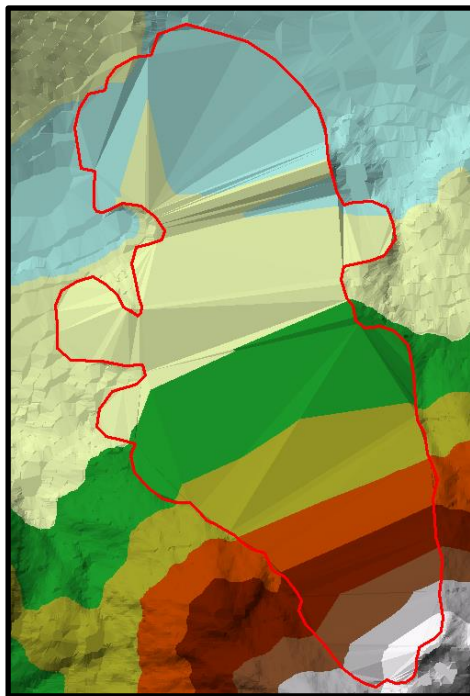


Fig. 4.7: Superficie TIN asociada al flanco norte del volcán Azufre sin su depósito de lava joven (delimitado en rojo). Gradación de colores corresponde a elevación según escala de la Fig. 5.4 (modificado de ArcGIS).

Finalmente, se determinaron las densidades correspondientes a la lava (composición de muestras más evolucionadas) y enclaves (composición de muestras más primitivas) mediante el uso de la metodología de Bottinga et al. (1982) junto con los datos de volumen y expansión termal de Lange and Carmichael (1987). De esta forma, considerando además temperaturas y contenidos de agua representativos al momento de la erupción según el Capítulo 3 ( $T=1000^{\circ}\text{C}$  y  $\text{H}_2\text{O}= 4,8 \text{ wt}\%$ ), se obtienen densidades entre  $2,33$  y  $2,38 \text{ g/cm}^3$  para las muestras Azu 14 (lava) y Azu 7 EN (enclave) a condiciones de presión de 0 kbar. Cabe destacar que estos resultados no muestran un cambio significativo (densidades entre  $2,33$  y  $2,4 \text{ g/cm}^3$ ) si se considera la presión a la cual estuvo sometido el reservorio que dio origen a la lava estudiada (i.e., 2 kbar).

### 4.3. Volumen de la cámara magmática del volcán Azufre

Considerando la metodología presentada por Castruccio et al. (2017), se busca realizar una aproximación de cuál sería el volumen de la cámara magmática del volcán Azufre, y en particular de aquella que dio origen a su última erupción.

Para determinar dicho volumen se aplica la ecuación 12 de Castruccio et al. (2017).

$$V_c = \frac{Ak'}{B\rho_mgh} \left(1 - \frac{V_h}{V_0}\right)$$

Donde:

- $V_c$  es el volumen de la cámara
- $\kappa'$  es el módulo de compresibilidad, que para un sistema con bajo contenido de cristales y volátiles se estima en  $5 \times 10^9$  Pa.
- $\rho_m$  es la densidad del magma
- $g$  es la aceleración de gravedad (9,8 m/s)
- $h$  es la altura del edificio volcánico
- $V_h$  es el volumen del depósito lava eruptado a la altura  $h$  del edificio volcánico
- $V_0$  es el volumen eruptado a la altura basal del volcán (i.e. una colada eruptada previamente a la formación del edificio volcánico)
- $\frac{A}{B}$  es un parámetro que puede ser definido por medio del volumen total de una erupción (i.e.  $\frac{A}{B} = V_e(t \rightarrow \infty)$  según Castruccio et al. (2017))

Para aplicar la ecuación 12 de Castruccio et al. (2017), se deben considerar una serie de simplificaciones que son consistentes con las realizadas por Castruccio et al. (2017) al momento de aplicar sus metodologías. Por lo anterior, tomaremos en consideración los siguientes planteamientos:

- Por su antigüedad, se considera que el domo DI es representativo de las etapas previas a la formación del edificio volcánico del volcán Azufre, pudiendo representar los primeros volúmenes expulsados desde el *vent* que con posterioridad daría paso a la formación del edificio volcánico principal. De esta forma, el volumen del domo DI ( $4,1 \text{ km}^3$ ) representa el parámetro  $V_0$ .
- Tanto la erupción del domo DI como la erupción de la colada joven del volcán Azufre provienen de una misma cámara magmática.
- $V_h$  corresponde al volumen de la lava joven del volcán Azufre ( $1,3 \text{ km}^3$ ) producida en su última erupción, la cual fue emitida desde una altura  $h$  correspondiente a la cima del edificio volcánico (1800 m de altura por sobre el *plateau* de 4.100 m.s.n.m en el cual se emplaza el edificio).
- Para establecer el parámetro  $\frac{A}{B}$ , se debe asumir que la cámara magmática no presenta variación en sus propiedades en función del tiempo. Lo anterior es fundamental en la resolución del problema, ya que según las ecuaciones 2 y 6 de Castruccio et al. (2017), se establece que  $\frac{A}{B} = \Delta V_i + \frac{V_c}{\kappa'} \Delta \rho g H$ , lo cual implica que el parámetro  $\frac{A}{B}$  es dependiente del volumen adicional de magma necesario para generar una erupción ( $\Delta V_i$ ), del volumen de la cámara ( $V_c$ ), el módulo de compresibilidad ( $\kappa'$ ), el contraste de densidad entre la corteza y el magma ( $\Delta \rho = \rho_c - \rho_m$ ), la aceleración de gravedad ( $g$ ) y la profundidad a la cual se encuentra el techo de la cámara magmática ( $H$ ). De esta forma, si el parámetro  $\frac{A}{B}$  fuera variable en el tiempo, ya sea por un cambio en los volúmenes de intrusión asociados al desencadenamiento de una erupción, a cambios en la densidad del magma inyectado, o a cambios en el volumen de la cámara o la profundidad de su techo, no sería posible aplicar el parámetro  $\frac{A}{B}$  entre diferentes erupciones asociadas a un mismo edificio o sistema volcánico.



- Dado que la colada joven es uno de los depósitos mejor preservados del volcán Azufre (i.e., una pérdida mínima debido a la erosión), se utiliza su volumen para establecer el parámetro  $\frac{A}{B} = V_e(t \rightarrow \infty) = 1,3 \text{ km}^3$ .

Considerando todos los supuestos establecidos previamente, y tomando una densidad representativa de  $2,37 \text{ g/cm}^3$  (i.e., el promedio de densidades determinadas para la lava y enclaves entre 0 y 2 kbar), se calcula que el volumen de la cámara magmática del volcán Azufre posee una dimensión en torno a los  $106 \text{ km}^3$ .

Las fuentes de error al calcular este volumen provienen de las variables  $\kappa'$ ,  $V_h$  (i.e.,  $\frac{A}{B} = V_e$ ),  $h$  y  $V_0$ , las cuales al modificarse en un 10% muestran una variación del 10%, 5%, 1% y 4% en el volumen calculado para la cámara magmática, respectivamente. Lo anterior significa que el volumen determinado de  $106 \text{ km}^3$  no posee una sensibilidad importante respecto a una incertidumbre del 10% en las variables utilizadas (e.g.,  $\kappa'$ ) o en los valores calculados para los volúmenes. Consistentemente, si se considera el rango completo de densidades calculadas para la lava y sus enclaves (i.e.,  $2,33 - 2,4 \text{ g/cm}^3$ ), el volumen calculado muestra una variación solo del 1,6%. Así, ante posibles incertidumbres en las variables utilizadas, se establece que no hay un impacto significativo en el volumen de la cámara magmática calculada para el volcán Azufre, y menos en el orden de magnitud del valor estimado.

El valor calculado de  $106 \text{ km}^3$ , sin embargo, podría ser un resultado sobrestimado si se considera el modelo de tamaño crítico de cámaras magmáticas gatilladoras de erupciones de Townsend and Huber (2020). Este último modelo, y a diferencia del planteado por Castruccio et al. (2017), toma en consideración el efecto de los volátiles exseltos en la sobrepresión crítica ( $\Delta P_i$ ) producida dentro de una cámara para generar erupciones. Así, considerando el efecto de los volátiles, Townsend and Huber (2020) plantean que cámaras magmáticas someras (4 a 10 km de profundidad) con un volumen de 10 a  $30 \text{ km}^3$  y con 1 – 10% de volátiles exseltos (en fracción de volumen), pueden producir depósitos del orden de 0,1 a  $2 \text{ km}^3$  (Fig. 4.8) como el estudiado para el volcán Azufre (i.e.,  $1,3 \text{ km}^3$ ).

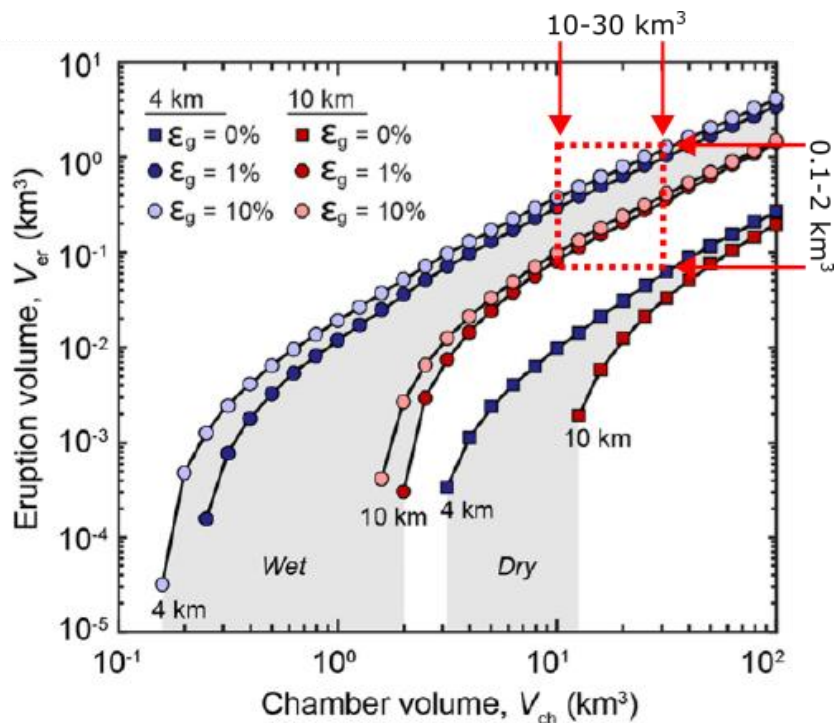


Fig. 4.8: Volumen de material eruptable (modificado de Townsend and Huber 2020), en el cual se destaca (cuadro rojo) que cámaras magmáticas entre 10 y 30  $\text{km}^3$  pueden producir erupciones con volúmenes de 0.1 a 2  $\text{km}^3$ .

Comprobar qué resultado de volumen es el más adecuado para la cámara del volcán Azufre es complejo si se considera que los únicos métodos para evaluar tal parámetro podrían provenir de estudios geofísicos de InSAR, sísmica, magnetotelúrica y gravimetría. Aun así, este tipo de estudios en general no son utilizados para determinar volúmenes de cámaras, si no que más bien (entre otras variables) volúmenes de reservorios magmáticos, tales como los que se encuentran en el contexto del APMB (Ward et al. 2014; Del Potro et al. 2013; Comeau et al. 2015, 2016). Así, se han determinados volúmenes de 500.000  $\text{km}^3$  para el APMB (Ward et al. 2014; Fig. 1.3) y de 500  $\text{km}^3$  para estructuras tipo dique que estarían alimentando reservorios (o zonas de fluidos hidrotermales) en la región donde se encuentra el volcán Uturuncu (“estructuras C3” en Fig. 4.9; Comeau et al. 2016). Sin embargo, existen algunos estudios que combinan observaciones geofísicas con modelamiento termodinámico, geoquímica y volúmenes eruptados (Ishizuka et al. 2015; Miller et al. 2016) para aproximar posibles volúmenes de cámaras magmáticas.

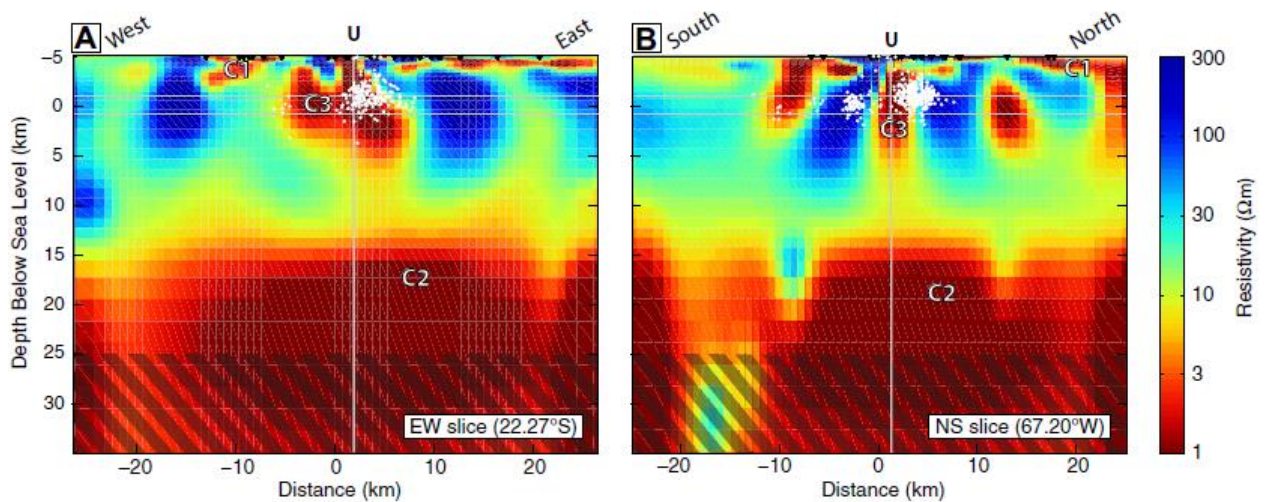


Fig. 4.9: Perfil de resistividad a partir del cual los autores (Comeau et al. 2016) establecen que las estructuras tipo dique “C3” poseen un volumen aproximado de 500 km<sup>3</sup>. Estas estructuras, que se correlacionan con hipocentros sísmicos (círculos blancos en la figura), conectarían el APMB (C2) con reservorios someros o zonas de fluido hidrotermal (C1).

El estudio de Ishizuka et al. (2015) establece que, para correlacionar la geoquímica, frecuencia eruptiva (100 – 150 años) y volúmenes eruptados (0.1 – 0.3 km<sup>3</sup>) del volcán de arco Izu-Oshima con el adyacente campo volcánico de tras arco Izu-Tobu, una cámara magmática de ~16 km<sup>3</sup> es necesaria. Otro ejemplo es el estudio de Miller et al. (2016) realizado a partir de gravimetría 3D y modelamiento termodinámico con el software MELTS, el cual establece que el sistema silíceo bajo la Laguna del Maule posee una cámara magmática de 30 km<sup>3</sup> con un 85% de material fundido que se encuentra dentro de un cuerpo de 115 km<sup>3</sup> que se interpreta como un *crystal mush* (>70% de cristales). Dicha cámara habría generado la erupción Nieblas de 2 km<sup>3</sup>.

Los resultados de los dos ejemplos anteriores tienden a ser consistente con el modelo propuestos por Townsend and Huber (2020). De esta forma, el volumen calculado de 106 km<sup>3</sup> para la cámara magmática del volcán Azufre probablemente sea un valor máximo y sobreestimado por al menos unos 70 km<sup>3</sup>.

Para evaluar de mejor manera el volumen de la cámara magmática del volcán Azufre (o de su reservorio magmático) se deberían considerar en futuros trabajos la anomalía de baja resistividad identificada bajo el volcán Azufre por Araya Vargas et al. (2019) a profundidades someras menores a 10 km (y con una extensión horizontal este-oeste de

~20 km según Fig. 4.10). Un reanálisis de los datos geofísicos de Araya Vargas et al. (2019), o la realización de nuevos estudios a escala de la corteza media o superior que complementen la resolución los resultados obtenidos a escala litosférica por Araya Vargas et al. (2019), podrían ser de gran utilidad al momento de determinar el volumen de la cámara magmática del volcán Azufre o de su reservorio magmático.

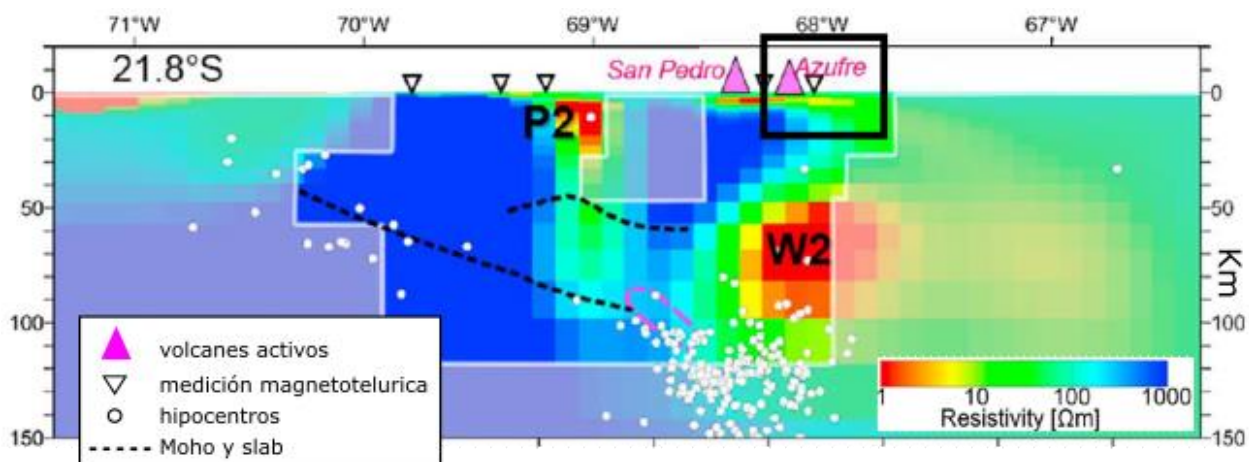


Fig. 4.10: Perfil geofísico cortical de resistividad en el cual se destaca en un cuadrado negro la ubicación del volcán Azufre y su anomalía de baja resistividad (color amarillo de ~20 km de largo). P2 y W2 corresponden a zonas de baja resistividad ubicadas debajo de la Precordillera (P) y Cordillera Occidental (W) (modificado de Araya Vargas et al. 2019).

## CAPÍTULO 5: SUPPLEMENTARY MATERIAL

### 5.1. Inferred age of last eruptive stage of the Azufre volcano

We infer an age of 50 – 331 ka for the last eruptive stage of the Azufre volcano based on the correlation of morphology and flow structures displayed by different volcanic units of the Ascotán-Inacaliri district (Sellés and Gardeweg 2017). The morphologies and volcanic structures observed in the studied lava deposit are comparable with those from volcanic units emplaced at 50 – 140 ka. The correlated volcanic units correspond to lava deposits of the San Pedro volcano and La Poruña scoria cone together with the dacitic domes Chanca, Chac Inca, and Cerro Pabellón (Table 5.1, Fig. 5.1). As the studied lava deposit, these units exhibit rough morphologies, volcanic craters, and structures flow as levees, ogives, and steep flow front. The correlation is consistent with the stratigraphy of lava deposits in the Azufre volcano (Fig. 3.1b of the main text) because the studied lava is emplaced above the Stage II of the volcano (500-700 ka; Godoy et al. 2022). Additionally, older volcanic deposits (331 ka; Fig. 5.2) belonging to Stage III show smoothed morphologies because of erosion.

Considering all the above said, an eruption age within the interval of 140 – 331 ka is an acceptable result for the studied lava deposit, and even an age between 50 – 140 ka is also feasible based on similar structures and morphologies shown by the youngest volcanic units of the Ascotán-Inacaliri district that are very near to the Azufre volcano (<25 km; Fig. 5.1). This closeness gives another quality control to the correlation, as all cited units underwent a similar erosion rate. Even heterogeneous erosion rates by glaciers would be discarded as some of the youngest units in the district are oriented to SW and SE (see Fig. 5.1), loci where glaciers are most likely to be developed, as sunlight does not reach directly due to the shadows of volcanic edifices. Therefore, we estimate an emplacement age between 50 – 331 ka as a coherent result.

Table 5.1: Dating of young volcanic units (<140 ka) of the Ascotán-Inacaliri district that show rough morphologies, volcanic craters and structures flow as levees, ogives, and steep flow front. The location of these units is displayed in Fig. 5.1

Volcanic unit	Interval age (ka)	Reference
1) Studied lava deposit of the Azufre volcano	50 – 331 (inferred)	This work
2) Chanca dome	83	Tierney et al. (2016)
3) Chac Inca dome	114	Rivera et al. (2015)
4) Cerro Pabellón dome	50 – 105	Urzua et al. (2002); Renzulli et al. (2006)
5A) Young deposit of San Pedro volcano	60 – 140	Bertin and Amigo (2019); González-Maurel et al. (2019)
5B) Young deposit of San Pedro volcano	68 – 107	Delunel et al. (2016); Bertin and Amigo (2019)
6) La Poruña scoria cone	54 – 110	Bertin and Amigo (2019); González-Maurel et al. (2019)

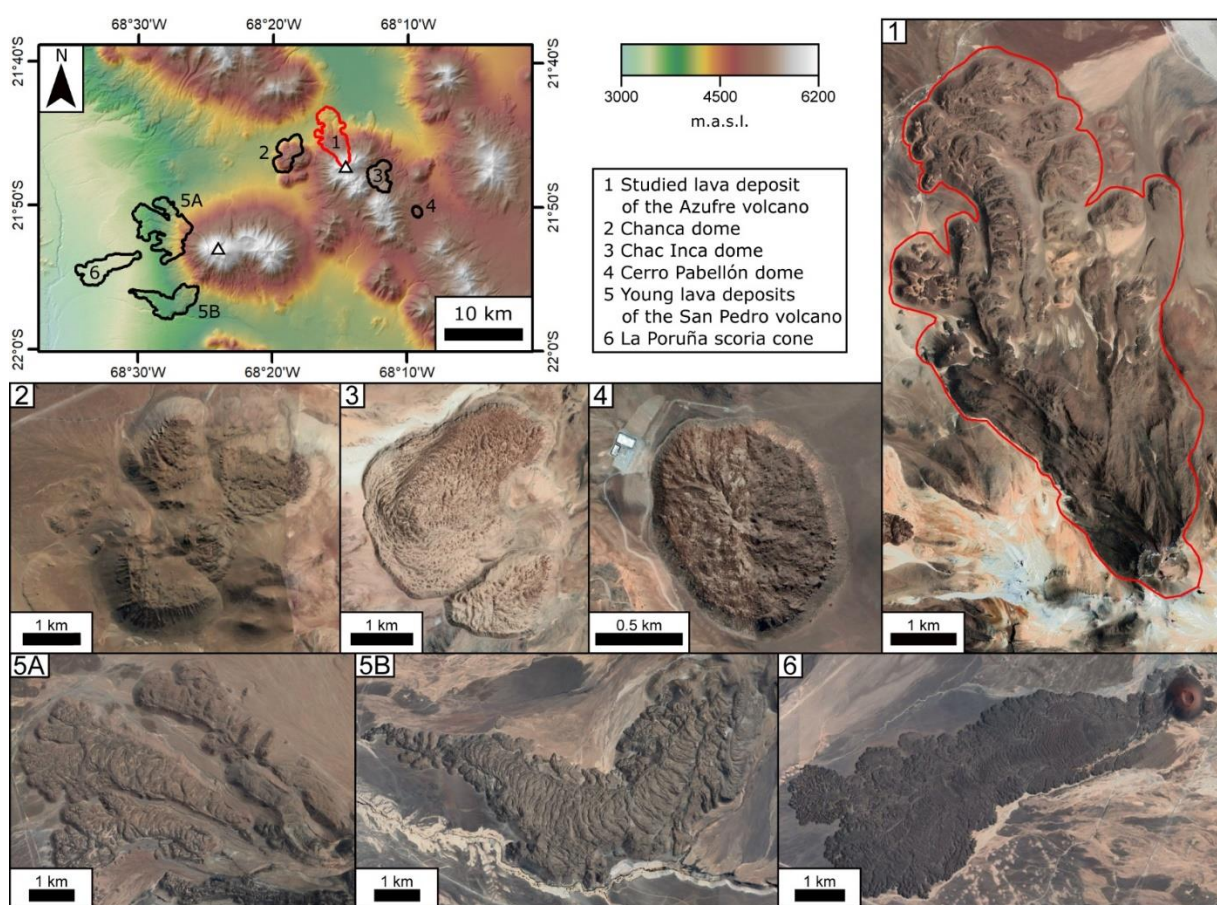


Fig. 5.1: Location of young volcanic units (50 – 140 ka) of the Ascotán-Inacaliri district that show rough morphologies, which correspond to structures as volcanic craters (studied lava deposit and La Poruña scoria cone) and flow structures as levees, ogives, and steep flow front (studied lava deposit, Chac Inca dome, young lava deposits of the San Pedro volcano, and La Poruña scoria cone). The satellite images were obtained from Google Earth® freeware

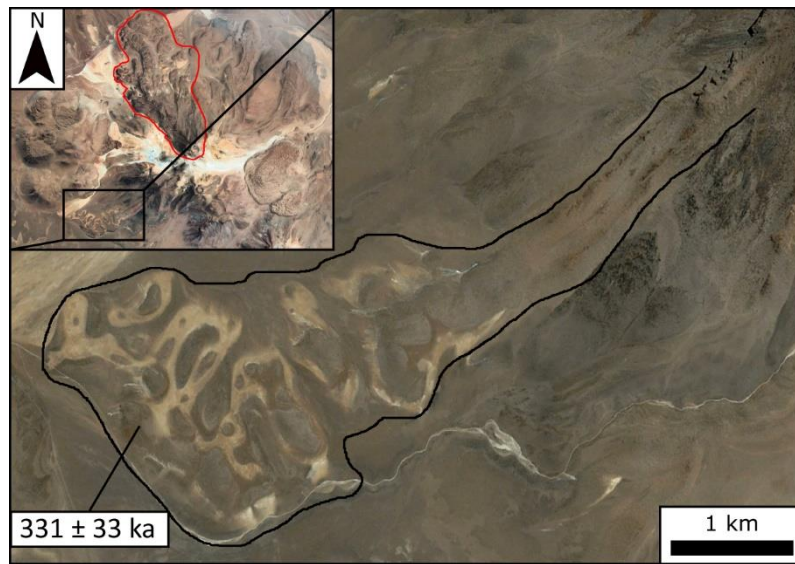


Fig. 5.2: Satellite image obtained from Google Earth® freeware that shows an eroded lava deposit of the Azufre volcano (inset), whose age is  $331 \pm 33$  ka (Bertin and Amigo 2019)

## 5.2. Sample locations

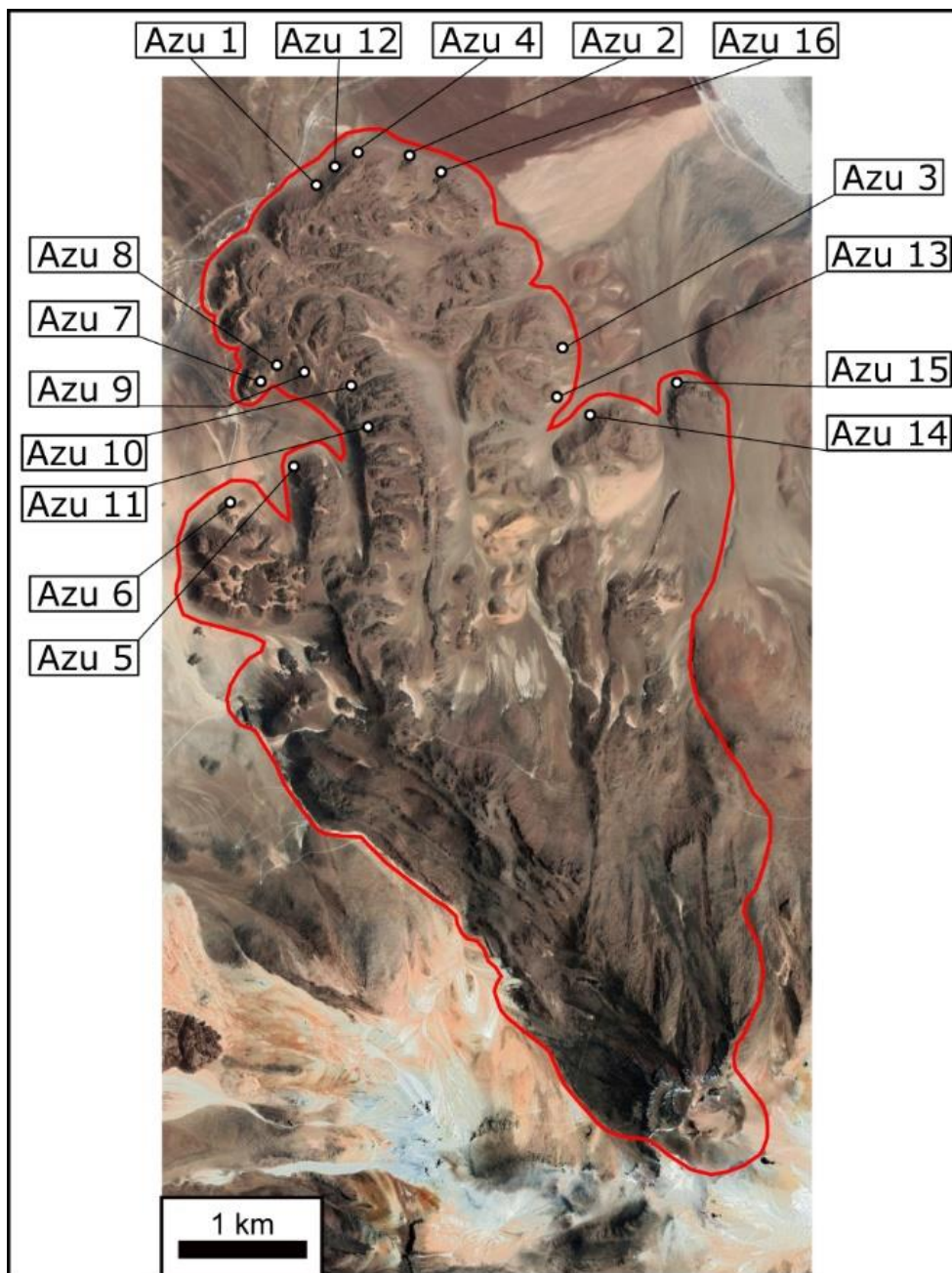


Fig. 5.3: Sample sites along the front of the studied lava deposit



Table 5.2: Coordinates of sample sites (UTM zone 19K)

Sample	comment	mS	mE	Sample	comment	mS	mE
Azu 1	lava	7597718	575511	Azu 9	lava	7596227	575402
Azu 1 EN	enclave	7597718	575511	Azu 9 EN	enclave	7596227	575402
Azu 2	lava	7597972	576242	Azu 10	lava	7596038	575813
Azu 2 EN	enclave	7597972	576242	Azu 10 EN	enclave	7596038	575813
Azu 3	lava	7596406	577396	Azu 11	lava	7595755	576012
Azu 3 EN	enclave	7596406	577396	Azu 11 EN	enclave	7595755	576012
Azu 4	lava	7598030	575758	Azu 12	lava	7597836	575687
Azu 4 EN	enclave	7598030	575758	Azu 12 EN	enclave	7597836	575687
Azu 5	lava	7595469	575348	Azu 13	lava	7596074	577420
Azu 5 EN	enclave	7595469	575348	Azu 13 EN	enclave	7596074	577420
Azu 6	lava	7595194	574830	Azu 14	lava	7595936	577728
Azu 6 EN	enclave	7595194	574830	Azu 14 EN	enclave	7595936	577728
Azu 7	lava	7596138	575011	Azu 15	lava	7596155	578362
Azu 7 EN	enclave	7596138	575011	Azu 15 EN	enclave	7596155	578362
Azu 8	lava	7596262	575174	Azu 16	lava	7597843	576493
Azu 8 EN	enclave	7596262	575174	Azu 16 EN	enclave	7597843	576493

### 5.3. Geochemistry analyses

<sup>1</sup>To calculate Fe<sub>2</sub>O<sub>3</sub>, it must be considered that samples contain iron as Fe<sup>2+</sup> and Fe<sup>3+</sup>. However, when samples are heated to measure the LOI, all Fe<sup>2+</sup> is oxidized to Fe<sup>3+</sup>. The latter, in turn, is measured by ICP analysis as Fe<sub>2</sub>O<sub>3</sub>T. Once FeO (measured by titration) and Fe<sub>2</sub>O<sub>3</sub>T are known, the original Fe<sub>2</sub>O<sub>3</sub> content of a sample can be determined as follows:

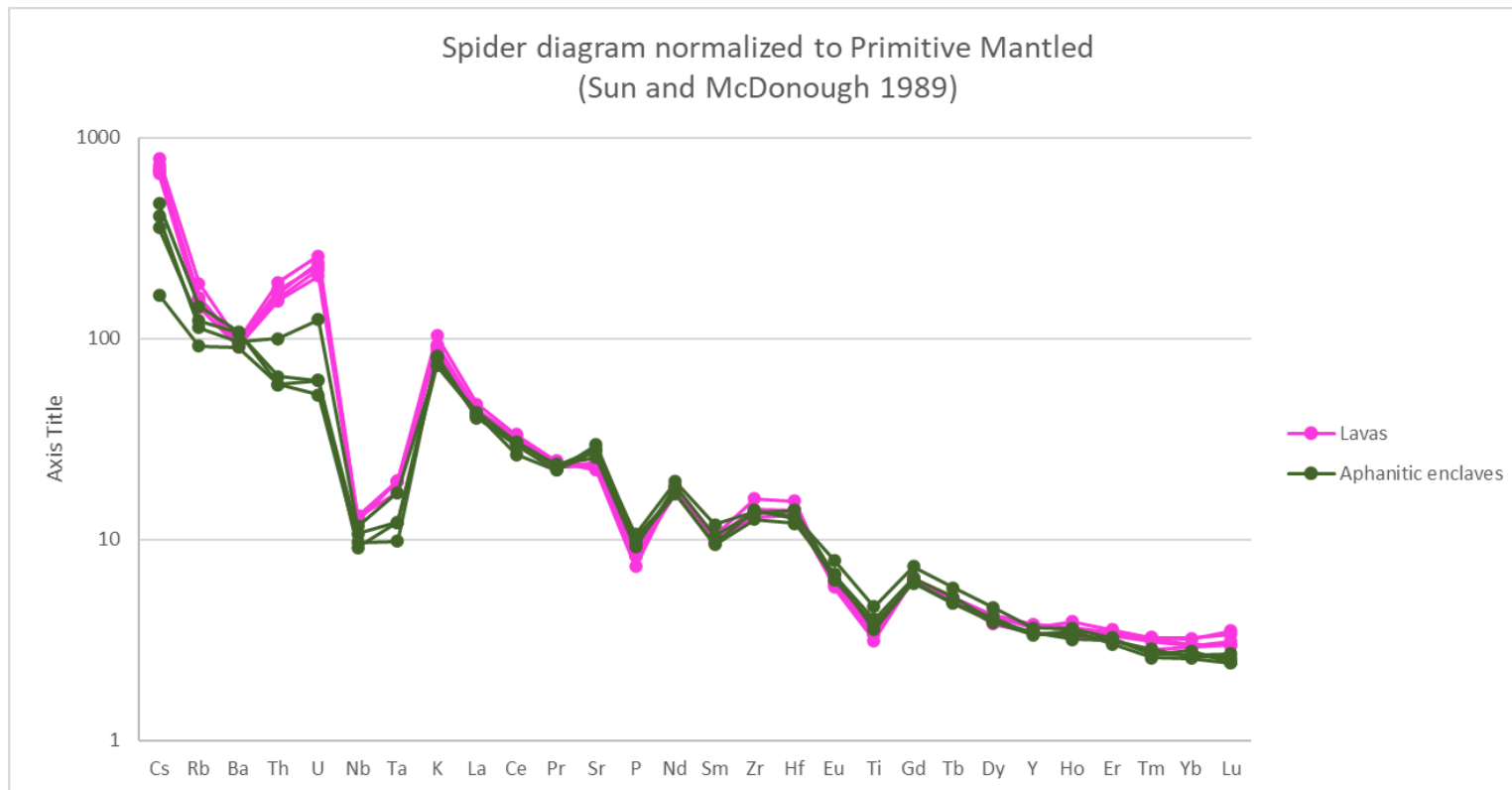
- Fe<sub>2</sub>O<sub>3</sub>T must be expressed as FeOT (i.e.  $0.8998 \cdot \text{Fe}_{2}\text{O}_{3}\text{T}$ )
- FeO must be subtracted from FeOT
- Fe<sub>2</sub>O<sub>3</sub> correspond to FeOT expressed as Fe<sup>3+</sup> (i.e.  $\text{FeOT} \cdot 1.1113$ )

<sup>2</sup>Corrected LOI does not consider the oxygen mass (%) gained by samples (negative value by convention) when it is heated due to oxidation of FeO to Fe<sub>2</sub>O<sub>3</sub>. Thus, the corrected LOI gives a better approach to the original volatile mass (%) content in the sample (mainly H<sub>2</sub>O from amphiboles and biotite), which was lost (positive value by convention) during the heating. The corrected LOI is calculated as follows:

- FeO is expressed as Fe<sub>2</sub>O<sub>3</sub> (i.e.  $\text{FeO} \cdot 1.1113$ ) and then, it is determined the oxygen (wt%) corresponded to the Fe<sub>2</sub>O<sub>3</sub> molecule (i.e.  $\text{Fe}_{2}\text{O}_{3} \cdot 3 \cdot 16 / (55.85 \cdot 2 + 16 \cdot 3)$ )
- It is determined the oxygen (wt%) corresponded to the FeO molecule (i.e.  $\text{FeO} \cdot 16 / (55.85 + 16)$ )
- Calculated oxygen of the Fe<sub>2</sub>O<sub>3</sub> molecule is subtracted from the calculated oxygen of the FeO molecule
- The result of the subtraction is added to LOI reported by the laboratory

<sup>3</sup>The corrected Sum considers the sum of SiO<sub>2</sub>, Al<sub>2</sub>O<sub>3</sub>, MgO, CaO, Na<sub>2</sub>O, K<sub>2</sub>O, TiO<sub>2</sub>, P<sub>2</sub>O<sub>5</sub>, MnO, Cr<sub>2</sub>O<sub>3</sub>, FeO, Fe<sub>2</sub>O<sub>3</sub>, and corrected LOI. It is worth noting that the corrected Sum is identical to Sum (cell O21), indicating, in turn, the coherency of calculations.

<sup>4</sup>Mg# was calculated as  $(\text{MgO}/40.3)/((\text{MgO}/40.3)+(\text{FeO}/(55.85+16)))$



Analysis method		ICP-OES												
Analyte	SiO2	Al2O3	Fe2O3T	MgO	CaO	Na2O	K2O	TiO2	P2O5	MnO	Cr2O3	LOI	Sum	
Unit	%	%	%	%	%	%	%	%	%	%	%	%	%	
MDL	0.01	0.01	0.04	0.01	0.01	0.01	0.01	0.01	0.01	0.01	0.002	-5.1	0.01	
Azu 2	60.43	16.34	5.73	3.26	5.48	3.57	2.7	0.73	0.18	0.09	0.016	1.2	99.73	
Azu 3	61.03	16.35	5.57	3.07	5.32	3.57	2.81	0.73	0.18	0.08	0.021	1	99.73	
Azu 4	60.84	16.16	5.62	3.13	5.17	3.61	2.77	0.76	0.18	0.08	0.014	1.4	99.73	
Azu 7	60.87	15.95	5.33	3.31	5.3	3.47	2.63	0.74	0.19	0.08	0.016	1.8	99.69	
Azu 7 EN	58.88	16.05	6.31	3.71	5.8	3.4	2.22	0.87	0.2	0.09	0.022	2.1	99.65	
Azu 8 EN	56.29	16.21	6.53	3.68	7.01	2.96	2.47	0.82	0.21	0.09	0.013	3.4	99.68	
Azu 10 EN	56.47	16.67	6.87	4.31	6.48	3.27	2.39	1	0.23	0.09	0.018	1.9	99.70	
Azu 14	61.88	16.37	5.06	2.32	4.82	3.62	3.1	0.68	0.16	0.08	0.007	1.6	99.70	
Azu 14 EN	58.56	17.1	5.95	2.93	6.01	3.27	2.2	0.77	0.22	0.08	0.006	2.6	99.70	
Standard														
STD SO-19 expected	61.13	13.95	7.47	2.88	6	4.11	1.29	0.69	0.32	0.13	0.5			
STD SO-19 measured	60.32	13.97	7.54	2.92	5.97	4.06	1.3	0.7	0.33	0.13	0.5	1.9	99.87	
STD SO-19 measured	60.35	14	7.45	2.92	5.98	4.08	1.31	0.7	0.33	0.13	0.503	1.9	99.87	
STD SO-19 average	60.34	13.99	7.50	2.92	5.98	4.07	1.31	0.70	0.33	0.13	0.50			
Offset from certified value	-0.80	0.04	0.03	0.04	-0.03	-0.04	0.02	0.01	0.01	0.00	0.00			
Accuracy %	1.30	0.25	0.33	1.39	0.42	0.97	1.16	1.45	3.13	0.00	0.30			
Precision 2σ	0.03	0.03	0.09	0.00	0.01	0.02	0.01	0.00	0.00	0.00	0.00			
Precision 2σ%	0.05	0.21	1.20	0.00	0.17	0.49	0.77	0.00	0.00	0.00	0.60			
Blank	0.04	<0.01	<0.04	<0.01	<0.01	<0.01	<0.01	<0.01	<0.01	<0.01	<0.002	0	0.06	

Analysis method	Titration	Calculated	Corrected from Fe <sub>2</sub> O <sub>3</sub> T and FeO concentrations	Corrected	
Analyte	FeO	Fe <sub>2</sub> O <sub>3</sub>	LOI	Sum	Mg#
Unit	%	%	%	%	
MDL	0.2				
Azu 2	2.83	2.58	1.5	99.7	0.67
Azu 3	2.76	2.50	1.3	99.7	0.66
Azu 4	2.94	2.35	1.7	99.7	0.65
Azu 7	2.8	2.22	2.1	99.7	0.68
Azu 7 EN	3.51	2.41	2.5	99.7	0.65
Azu 8 EN	3.36	2.80	3.8	99.7	0.66
Azu 10 EN	3.66	2.80	2.3	99.7	0.68
Azu 14	2.06	2.77	1.8	99.7	0.67
Azu 14 EN	2.17	3.54	2.8	99.7	0.71
<b>Standard</b>					
OREAS 700 expected	12.07				
OREAS 700 measured	12.48				
Offset from certified value	0.41				
Accuracy %	3.40				
Precision 2σ	-				
Precision 2σ%	-				
SY-4 expected	2.86				
SY-4 measured	2.85				
Offset from certified value	-0.01				
Accuracy %	0.35				
Precision 2σ	-				
Precision 2σ%	-				
<b>Duplicates</b>					
Azu 2	2.83				
Rep Azu 2 QC	2.96				

Analysis method	ICP-OES		Analysis method	ICP-MS										
Analyte	Ni	Sc	Analyte	Ba	Be	Co	Cs	Ga	Hf	Nb	Rb	Sn	Sr	Ta
Unit	PPM	PPM	Unit	PPM	PPM	PPM	PPM	PPM	PPM	PPM	PPM	PPM	PPM	PPM
MDL	20	1	MDL	1	1	0.2	0.1	0.5	0.1	0.1	0.1	1	0.5	0.1
Azu 2	33	14	Azu 2	654	3	46.9	5.4	17.5	4.3	8.8	98.6	3	509.7	0.8
Azu 3	45	13	Azu 3	644	3	33.8	5.7	18.1	4.3	9.2	100.2	1	494.5	0.8
Azu 4	27	13	Azu 4	665	<1	28.3	5.4	18	4.3	9.2	101.9	1	482.5	0.7
Azu 7	39	12	Azu 7	635	1	32.3	5.2	17.6	4.1	8.8	90.2	1	487.6	0.8
Azu 7 EN	54	14	Azu 7 EN	672	2	39.2	3.2	18.2	4.3	8.3	71.8	1	540	0.7
Azu 8 EN	36	15	Azu 8 EN	757	<1	34.9	3.7	17	3.9	6.9	91.7	1	578.6	0.4
Azu 10 EN	31	15	Azu 10 EN	631	<1	37.2	1.3	18.7	4	7.6	58.2	1	592.3	0.5
Azu 14	20	12	Azu 14	684	<1	25.6	6.2	17.4	4.8	9.3	118.9	1	466.3	0.8
Azu 14 EN	<20	14	Azu 14 EN	744	<1	40.5	2.8	17.9	3.7	6.5	77.7	1	621.8	0.5
Standard		Standard		Standard		Standard								
STD SO-19 expected	470	27	STD SO-19 expected	486	20	24	4.5	17.5	3.1	68.5	19.5	19	317.1	4.9
STD SO-19 measured	465	27	STD SO-19 measured	454	22	23.8	4.4	15	3	66.6	19.5	17	310.3	4.7
STD SO-19 measured	464	27	STD SO-19 measured	469	19	24.9	4.5	15.7	2.8	69.5	20.2	19	328.7	4.7
STD SO-19 average	464.50	27.00	STD SO-19 average	461.50	20.50	24.35	4.45	15.35	2.90	68.05	19.85	18.00	319.50	4.70
Offset from certified value	-5.50	0.00	Offset from certified value	-24.50	0.50	0.35	-0.05	-2.15	-0.20	-0.45	0.35	-1.00	2.40	-0.20
Accuracy %	1.17	0.00	Accuracy %	5.04	2.50	1.46	1.11	12.29	6.45	0.66	1.79	5.26	0.76	4.08
Precision 2σ	1.00	0.00	Precision 2σ	15.00	3.00	1.10	0.10	0.70	0.20	2.90	0.70	2.00	18.40	0.00
Precision 2σ%	0.22	0.00	Precision 2σ%	3.25	14.63	4.52	2.25	4.56	6.90	4.26	3.53	11.11	5.76	0.00
Duplicates		Duplicates		Duplicates		Duplicates								
Azu 14	20	12	Azu 14	684	<1	25.6	6.2	17.4	4.8	9.3	118.9	1	466.3	0.8
Rep Azu 14 QC			Rep Azu 14 QC	696	3	26.8	6.5	17.2	4.7	9.2	118.5	1	456.9	0.9
Blank	<20	<1	Blank	<1	<1	<0.2	<0.1	<0.5	<0.1	<0.1	<0.1	<1	<0.5	<0.1

Analysis method		ICP-MS										
Analyte	Th	U	V	W	Zr	Y	La	Ce	Pr	Nd	Sm	
Unit	PPM	PPM	PPM	PPM	PPM	PPM	PPM	PPM	PPM	PPM	PPM	
MDL	0.2	0.1	8	0.5	0.1	0.1	0.1	0.1	0.02	0.3	0.05	
Azu 2	13.4	4.6	145	129.8	153.6	17.1	29.1	54.9	6.23	23.1	4.26	
Azu 3	14.2	5	129	133	148.9	17.1	29.8	54.9	6.47	24.4	4.51	
Azu 4	14.8	4.8	134	90.5	157.3	17.2	30.4	57.4	6.5	24.2	4.53	
Azu 7	13.1	4.3	123	152.4	144.5	15.8	28.9	55.3	6.37	24.3	4.35	
Azu 7 EN	8.5	2.6	149	178.5	151.7	15.6	29.5	54.1	6.53	24.8	4.62	
Azu 8 EN	5	1.1	164	123.6	156	15.2	27.6	52	6.12	22.8	4.22	
Azu 10 EN	5	1.3	175	119.8	152.9	16.5	27.9	54.1	6.4	26.3	5.27	
Azu 14	16.2	5.4	119	113.5	178.7	16.5	32.3	59.1	6.78	25	4.62	
Azu 14 EN	5.5	1.3	146	187.6	140.5	15.3	28.8	46.9	6.09	23.1	4.19	
Standard												
STD SO-19 expected	13	19.4	165	9.8	112	35.5	71.3	161	19.4	75.7	13.7	
STD SO-19 measured	13	19.4	165	11.5	106.9	35.6	73.9	160.6	19.25	73.5	12.92	
STD SO-19 measured	13.5	20.7	170	9.6	111	37.8	76	164.6	19.85	76.1	12.9	
STD SO-19 average	13.25	20.05	167.50	10.55	108.95	36.70	74.95	162.60	19.55	74.80	12.91	
Offset from certified value	0.25	0.65	2.50	0.75	-3.05	1.20	3.65	1.60	0.15	-0.90	-0.79	
Accuracy %	1.92	3.35	1.52	7.65	2.72	3.38	5.12	0.99	0.77	1.19	5.77	
Precision 2σ	0.50	1.30	5.00	1.90	4.10	2.20	2.10	4.00	0.60	2.60	0.02	
Precision 2σ%	3.77	6.48	2.99	18.01	3.76	5.99	2.80	2.46	3.07	3.48	0.15	
Duplicates												
Azu 14	16.2	5.4	119	113.5	178.7	16.5	32.3	59.1	6.78	25	4.62	
Rep Azu 14 QC	16.4	5.3	114	110	164.9	16.1	31.9	59.7	6.67	23.8	4.27	
Blank	<0.2	<0.1	<8	0.6	0.1	<0.1	0.1	<0.1	<0.02	<0.3	<0.05	

Analysis method		ICP-MS							
Analyte	Eu	Gd	Tb	Dy	Ho	Er	Tm	Yb	Lu
Unit	PPM	PPM	PPM	PPM	PPM	PPM	PPM	PPM	PPM
MDL	0.02	0.05	0.01	0.05	0.02	0.03	0.01	0.05	0.01
Azu 2	1.03	3.84	0.55	3.1	0.6	1.66	0.24	1.57	0.26
Azu 3	1.04	3.79	0.55	3.1	0.58	1.59	0.24	1.47	0.22
Azu 4	1.06	3.75	0.54	3.08	0.6	1.6	0.23	1.46	0.23
Azu 7	1	3.76	0.55	2.8	0.54	1.49	0.21	1.43	0.22
Azu 7 EN	1.12	3.84	0.56	2.91	0.52	1.51	0.21	1.29	0.19
Azu 8 EN	1.06	3.61	0.52	2.85	0.55	1.54	0.2	1.3	0.2
Azu 10 EN	1.32	4.37	0.62	3.38	0.59	1.56	0.2	1.37	0.18
Azu 14	0.97	3.77	0.54	3.05	0.64	1.71	0.24	1.59	0.25
Azu 14 EN	1.13	3.69	0.52	3.02	0.57	1.45	0.19	1.26	0.18
Standard									
STD SO-19 expected	3.81	10.53	1.41	7.5	1.39	3.78	0.55	3.55	0.53
STD SO-19 measured	3.52	10.09	1.35	7.28	1.34	3.8	0.52	3.34	0.52
STD SO-19 measured	3.69	10.73	1.38	7.28	1.38	3.9	0.56	3.65	0.55
STD SO-19 average	3.61	10.41	1.37	7.28	1.36	3.85	0.54	3.50	0.54
Offset from certified value	-0.21	-0.12	-0.04	-0.22	-0.03	0.07	-0.01	-0.05	0.01
Accuracy %	5.38	1.14	3.19	2.93	2.16	1.85	1.82	1.55	0.94
Precision 2 $\sigma$	0.17	0.64	0.03	0.00	0.04	0.10	0.04	0.31	0.03
Precision 2 $\sigma$ %	4.72	6.15	2.20	0.00	2.94	2.60	7.41	8.87	5.61
Duplicates									
Azu 14	0.97	3.77	0.54	3.05	0.64	1.71	0.24	1.59	0.25
Rep Azu 14 QC	1	3.8	0.55	3.06	0.6	1.62	0.23	1.56	0.25
Blank	<0.02	<0.05	<0.01	<0.05	<0.02	<0.03	<0.01	<0.05	<0.01



Sample	Ba/La	La/Yb	Sm/Yb	Sr/Y	EuN/Eu*	LaN/YbN	Depth [km] (only enclave data)		
							Profeta et al. (2015)		Lieu and Stern (2019)
							Sr/Y	LaN/YbN	Sr/Y
Azu 2	22,5	18,5	2,7	29,8	0,8	13,3			
Azu 3	21,6	20,3	3,1	28,9	0,8	14,5			
Azu 4	21,9	20,8	3,1	28,1	0,8	14,9			
Azu 7	22,0	20,2	3,0	30,9	0,8	14,5			
Azu 7 EN	22,8	22,9	3,6	34,6	0,8	16,4	46,5	59,5	45,2
Azu 8 EN	27,4	21,2	3,2	38,1	0,8	15,2	50,3	58,0	48,5
Azu 10 EN	22,6	20,4	3,8	35,9	0,8	14,6	47,9	57,1	46,4
Azu 14	21,2	20,3	2,9	28,3	0,7	14,6			
Azu 14 EN	25,8	22,9	3,3	40,6	0,9	16,4	53,2	59,5	51,0

## 5.4. EMPA analyses

### Plagioclase

#### Microlites in contact with Amp microphenocrysts

Sample	Point	Comment	wt%												
			Na2O	MgO	Al2O3	SiO2	FeO	MnO	TiO2	BaO	K2O	CaO	P2O5	SrO	Total
Azu 1	15	unpaired with Amp	3.9	0.11	29.5	52.3	0.55	0.00	0.19	0.15	0.19	13.9	0.00	0.08	100.8
Azu 1	16	unpaired with Amp	4.3	0.10	29.5	53.1	0.65	0.04	0.11	0.12	0.23	13.4	0.03	0.09	101.6
Azu 1	17	unpaired with Amp	4.3	0.07	29.0	53.4	0.64	0.05	0.00	0.12	0.22	13.2	0.02	0.13	101.2
Azu 2	8		3.6	0.07	30.2	51.5	0.73	0.00	0.00	0.00	0.18	14.5	0.00	0.11	100.9
Azu 2	10		4.0	0.08	29.8	52.2	0.55	0.00	0.11	0.32	0.19	13.9	0.02	0.04	101.1
Azu 2	23		4.6	0.08	28.9	53.6	0.74	0.00	0.10	0.00	0.27	13.0	0.06	0.15	101.5
Azu 3	14		4.2	0.08	28.9	53.0	0.76	0.04	0.12	0.02	0.24	13.1	0.02	0.15	100.6
Azu 3	16		4.4	0.08	28.9	53.7	0.58	0.01	0.09	0.00	0.23	13.1	0.00	0.10	101.2
Azu 3	17		4.0	0.08	29.7	52.4	0.52	0.02	0.04	0.22	0.20	13.7	0.04	0.15	101.1
Azu 3	30		3.3	0.06	30.5	50.9	0.63	0.04	0.08	0.00	0.13	15.3	0.01	0.09	101.0
Azu 3	31		4.0	0.08	29.9	52.3	0.73	0.01	0.03	0.10	0.18	14.0	0.04	0.13	101.4
Azu 4	25		4.0	0.02	30.0	52.5	0.47	0.00	0.00	0.00	0.21	13.8	0.00	0.08	101.1
Azu 4	26		3.3	0.02	31.2	50.7	0.48	0.02	0.06	0.22	0.14	15.1	0.00	0.07	101.3
Azu 4	35	unpaired with Amp	3.9	0.06	29.5	52.5	0.63	0.05	0.06	0.00	0.19	13.9	0.02	0.12	100.9
Azu 4	36	unpaired with Amp	3.6	0.06	30.0	51.5	0.54	0.07	0.06	0.00	0.17	14.5	0.00	0.11	100.7
Azu 4	37	unpaired with Amp	4.1	0.07	29.1	53.1	0.59	0.04	0.00	0.20	0.25	13.5	0.02	0.14	101.2
Azu 4	38		4.6	0.07	28.2	53.9	0.63	0.00	0.05	0.12	0.24	12.5	0.01	0.18	100.5
Azu 4	39		4.5	0.08	28.2	53.6	0.60	0.03	0.00	0.00	0.26	12.6	0.04	0.13	100.1
Azu 4	40		4.1	0.03	29.7	52.5	0.54	0.00	0.00	0.00	0.20	13.7	0.01	0.07	100.9

Azu 4	7	4.4	0.05	29.2	53.4	0.69	0.01	0.00	0.07	0.22	13.1	0.02	0.09	101.2
Azu 4	10	4.6	0.06	28.9	53.4	0.52	0.01	0.17	0.05	0.24	13.0	0.03	0.06	101.0
Azu 7 EN	1	4.7	0.05	28.2	53.7	0.67	0.00	0.00	0.02	0.40	12.3	0.03	0.17	100.3
Azu 7 EN	2	4.4	0.07	28.5	53.1	0.61	0.02	0.09	0.00	0.34	12.7	0.02	0.08	100.0
Azu 7 EN	3	4.5	0.04	28.3	53.4	0.78	0.03	0.10	0.22	0.38	12.4	0.01	0.17	100.4
Azu 7 EN	4	3.6	0.05	29.8	51.4	0.80	0.11	0.01	0.00	0.29	14.0	0.00	0.12	100.3
Azu 8 EN	1	3.8	0.04	29.9	51.4	0.64	0.03	0.05	0.02	0.17	14.5	0.02	0.05	100.6
Azu 8 EN	2	4.0	0.06	29.2	52.4	0.65	0.00	0.16	0.00	0.27	13.7	0.01	0.21	100.7
Azu 8 EN	3	4.2	0.03	29.1	51.9	0.44	0.00	0.07	0.00	0.22	13.7	0.03	0.11	99.9
Azu 10 EN	1	3.8	0.04	29.8	51.3	0.57	0.04	0.00	0.00	0.20	14.3	0.01	0.12	100.1
Azu 10 EN	2	4.2	0.09	28.9	52.6	0.69	0.00	0.00	0.07	0.27	13.2	0.02	0.12	100.2
Azu 10 EN	3	4.3	0.06	29.0	52.2	0.51	0.02	0.00	0.25	0.20	13.4	0.01	0.09	100.0
Azu 14 EN	3	4.9	0.03	28.2	53.9	0.54	0.03	0.03	0.05	0.28	12.1	0.00	0.07	100.1
Azu 4 EN	21	4.7	0.03	28.3	54.5	0.47	0.00	0.00	0.05	0.29	12.1	0.01	0.16	100.6
Azu 4 EN	22	4.0	0.11	29.7	51.8	0.74	0.00	0.20	0.07	0.19	14.1	0.03	0.13	101.1
Azu 4 EN	23	4.1	0.05	29.0	52.9	0.51	0.00	0.00	0.00	0.21	13.4	0.06	0.08	100.2

apfu															
Sample	Point	Na	Mg	Al	Si	Fe2+	Fe+3	Mn	Ti	Ba	K	Ca	P	Sr	Total
Azu 1	15	0.34	0.01	1.6	2.4	0.00	0.02	0.00	0.01	0.00	0.01	0.67	0.00	0.00	5.0
Azu 1	16	0.37	0.01	1.6	2.4	0.00	0.02	0.00	0.00	0.00	0.01	0.64	0.00	0.00	5.0
Azu 1	17	0.38	0.00	1.5	2.4	0.00	0.02	0.00	0.00	0.00	0.01	0.64	0.00	0.00	5.0
Azu 2	8	0.31	0.00	1.6	2.3	0.00	0.03	0.00	0.00	0.00	0.01	0.70	0.00	0.00	5.0
Azu 2	10	0.35	0.01	1.6	2.4	0.00	0.02	0.00	0.00	0.01	0.01	0.67	0.00	0.00	5.0
Azu 2	23	0.40	0.01	1.5	2.4	0.00	0.03	0.00	0.00	0.00	0.02	0.62	0.00	0.00	5.0
Azu 3	14	0.37	0.01	1.5	2.4	0.00	0.03	0.00	0.00	0.00	0.01	0.64	0.00	0.00	5.0
Azu 3	16	0.38	0.01	1.5	2.4	0.00	0.02	0.00	0.00	0.00	0.01	0.63	0.00	0.00	5.0
Azu 3	17	0.35	0.01	1.6	2.4	0.00	0.02	0.00	0.00	0.00	0.01	0.66	0.00	0.00	5.0
Azu 3	30	0.29	0.00	1.6	2.3	0.00	0.02	0.00	0.00	0.00	0.01	0.74	0.00	0.00	5.0
Azu 3	31	0.35	0.01	1.6	2.3	0.00	0.03	0.00	0.00	0.00	0.01	0.67	0.00	0.00	5.0
Azu 4	25	0.35	0.00	1.6	2.4	0.00	0.02	0.00	0.00	0.00	0.01	0.66	0.00	0.00	5.0
Azu 4	26	0.29	0.00	1.7	2.3	0.00	0.02	0.00	0.00	0.00	0.01	0.73	0.00	0.00	5.0
Azu 4	35	0.34	0.00	1.6	2.4	0.00	0.02	0.00	0.00	0.00	0.01	0.67	0.00	0.00	5.0
Azu 4	36	0.32	0.00	1.6	2.3	0.00	0.02	0.00	0.00	0.00	0.01	0.70	0.00	0.00	5.0
Azu 4	37	0.36	0.00	1.5	2.4	0.00	0.02	0.00	0.00	0.00	0.01	0.65	0.00	0.00	5.0
Azu 4	38	0.41	0.00	1.5	2.4	0.00	0.02	0.00	0.00	0.00	0.01	0.60	0.00	0.00	5.0
Azu 4	39	0.40	0.01	1.5	2.4	0.00	0.02	0.00	0.00	0.00	0.02	0.61	0.00	0.00	5.0
Azu 4	40	0.36	0.00	1.6	2.4	0.00	0.02	0.00	0.00	0.00	0.01	0.66	0.00	0.00	5.0
Azu 4	7	0.38	0.00	1.5	2.4	0.00	0.03	0.00	0.00	0.00	0.01	0.63	0.00	0.00	5.0
Azu 4	10	0.40	0.00	1.5	2.4	0.00	0.02	0.00	0.01	0.00	0.01	0.63	0.00	0.00	5.0
Azu 7 EN	1	0.41	0.00	1.5	2.4	0.00	0.03	0.00	0.00	0.00	0.02	0.60	0.00	0.00	5.0
Azu 7 EN	2	0.39	0.00	1.5	2.4	0.00	0.02	0.00	0.00	0.00	0.02	0.62	0.00	0.00	5.0
Azu 7 EN	3	0.40	0.00	1.5	2.4	0.00	0.03	0.00	0.00	0.00	0.02	0.60	0.00	0.00	5.0
Azu 7 EN	4	0.32	0.00	1.6	2.3	0.00	0.03	0.00	0.00	0.00	0.02	0.68	0.00	0.00	5.0
Azu 8 EN	1	0.33	0.00	1.6	2.3	0.00	0.02	0.00	0.00	0.00	0.01	0.70	0.00	0.00	5.0
Azu 8 EN	2	0.35	0.00	1.6	2.4	0.00	0.02	0.00	0.01	0.00	0.02	0.67	0.00	0.01	5.0
Azu 8 EN	3	0.37	0.00	1.6	2.4	0.00	0.02	0.00	0.00	0.00	0.01	0.67	0.00	0.00	5.0

Azu 10 EN	1	0.33	0.00	1.6	2.3	0.00	0.02	0.00	0.00	0.00	0.01	0.69	0.00	0.00	5.0
Azu 10 EN	2	0.37	0.01	1.5	2.4	0.00	0.03	0.00	0.00	0.00	0.02	0.64	0.00	0.00	5.0
Azu 10 EN	3	0.38	0.00	1.6	2.4	0.00	0.02	0.00	0.00	0.00	0.01	0.65	0.00	0.00	5.0
Azu 14 EN	3	0.43	0.00	1.5	2.4	0.00	0.02	0.00	0.00	0.00	0.02	0.59	0.00	0.00	5.0
Azu 4 EN	21	0.41	0.00	1.5	2.5	0.01	0.01	0.00	0.00	0.00	0.02	0.58	0.00	0.00	5.0
Azu 4 EN	22	0.35	0.01	1.6	2.3	0.00	0.03	0.00	0.01	0.00	0.01	0.68	0.00	0.00	5.0
Azu 4 EN	23	0.36	0.00	1.5	2.4	0.00	0.02	0.00	0.00	0.00	0.01	0.65	0.00	0.00	5.0

---

Sample	Point	An	Ab	Or	Total	FeO(wt%) corrected	Fe2O3(wt%) calculated	Total(wt%) corrected
Azu 1	15	65.6	33.3	1.1	100	0.00	0.61	100.9
Azu 1	16	62.7	36.0	1.3	100	0.00	0.73	101.7
Azu 1	17	62.1	36.7	1.2	100	0.00	0.71	101.2
Azu 2	8	68.4	30.6	1.0	100	0.00	0.81	100.9
Azu 2	10	65.3	33.6	1.1	100	0.00	0.62	101.2
Azu 2	23	60.2	38.3	1.5	100	0.00	0.82	101.6
Azu 3	14	62.3	36.3	1.3	100	0.00	0.84	100.6
Azu 3	16	61.5	37.2	1.3	100	0.00	0.64	101.3
Azu 3	17	64.6	34.3	1.1	100	0.00	0.58	101.1
Azu 3	30	71.3	28.0	0.7	100	0.00	0.70	101.1
Azu 3	31	65.2	33.7	1.0	100	0.00	0.82	101.5
Azu 4	25	64.6	34.3	1.2	100	0.00	0.52	101.2
Azu 4	26	71.4	27.8	0.8	100	0.00	0.53	101.4
Azu 4	35	65.4	33.5	1.1	100	0.00	0.70	101.0
Azu 4	36	68.2	30.9	1.0	100	0.00	0.60	100.8
Azu 4	37	63.6	35.0	1.4	100	0.00	0.66	101.3
Azu 4	38	59.0	39.7	1.4	100	0.00	0.71	100.6
Azu 4	39	59.8	38.8	1.5	100	0.00	0.67	100.2
Azu 4	40	63.9	34.9	1.1	100	0.00	0.60	100.9
Azu 4	7	61.7	37.1	1.2	100	0.00	0.77	101.3
Azu 4	10	60.1	38.6	1.3	100	0.00	0.57	101.1
Azu 7 EN	1	58.0	39.8	2.3	100	0.00	0.75	100.3
Azu 7 EN	2	60.2	37.9	1.9	100	0.00	0.67	100.0
Azu 7 EN	3	58.8	39.0	2.1	100	0.00	0.86	100.5
Azu 7 EN	4	67.0	31.3	1.6	100	0.00	0.88	100.4
Azu 8 EN	1	67.5	31.5	0.9	100	0.00	0.71	100.7
Azu 8 EN	2	64.5	34.0	1.5	100	0.00	0.73	100.7
Azu 8 EN	3	63.4	35.4	1.2	100	0.00	0.49	100.0
Azu 10 EN	1	66.9	31.9	1.1	100	0.00	0.64	100.2

Azu 10 EN	2	62.5	35.9	1.5	100	0.00	0.76	100.2
Azu 10 EN	3	62.4	36.5	1.1	100	0.00	0.57	100.1
Azu 14 EN	3	56.9	41.5	1.6	100	0.00	0.60	100.2
Azu 4 EN	21	57.5	40.9	1.6	100	0.17	0.33	100.6
Azu 4 EN	22	65.5	33.5	1.0	100	0.00	0.83	101.2
Azu 4 EN	23	63.4	35.4	1.2	100	0.00	0.57	100.3

---

## Cores

Sample	Point	Comment	wt%												
			Na2O	MgO	Al2O3	SiO2	FeO	MnO	TiO2	BaO	K2O	CaO	P2O5	SrO	Total
Azu 1	1		4.7	0.00	28.9	53.0	0.32	0.01	0.06	0.00	0.29	12.5	0.01	0.18	99.9
Azu 1	11		2.6	0.00	32.6	49.0	0.26	0.01	0.09	0.02	0.09	17.0	0.01	0.16	101.9
Azu 2	5		4.3	0.00	29.5	52.7	0.18	0.00	0.01	0.00	0.25	13.2	0.02	0.16	100.2
Azu 2	11		5.1	0.00	28.7	55.1	0.27	0.05	0.04	0.22	0.29	12.0	0.03	0.00	101.7
Azu 2	14		3.8	0.00	30.1	51.5	0.29	0.02	0.03	0.20	0.17	14.4	0.00	0.00	100.5
Azu 3	1		1.9	0.00	33.0	47.3	0.32	0.00	0.03	0.40	0.08	17.7	0.00	0.09	100.9
Azu 3	22		4.7	0.00	29.2	53.5	0.37	0.00	0.06	0.00	0.29	12.9	0.00	0.06	101.1
Azu 4	1		2.4	0.00	32.4	48.2	0.27	0.00	0.06	0.00	0.09	16.8	0.03	0.04	100.4
Azu 4	3		4.1	0.00	29.9	52.6	0.16	0.00	0.00	0.30	0.23	13.5	0.01	0.03	100.8
Azu 4	4		4.2	0.00	30.0	52.6	0.31	0.00	0.00	0.00	0.23	13.4	0.00	0.06	100.8
Azu 4	4		3.5	0.02	30.7	51.1	0.36	0.00	0.00	0.00	0.17	14.9	0.00	0.08	100.8
Azu 4	11		3.9	0.00	30.2	52.2	0.36	0.06	0.00	0.02	0.20	14.1	0.00	0.09	101.1
Azu 4	12		3.0	0.01	31.6	50.2	0.25	0.00	0.16	0.00	0.14	15.8	0.01	0.14	101.3
Azu 4	13		4.8	0.01	28.7	54.0	0.23	0.02	0.00	0.00	0.30	12.3	0.04	0.02	100.5
Azu 7 EN	8		3.5	0.03	30.5	50.6	0.39	0.00	0.03	0.00	0.25	14.8	0.05	0.09	100.2
Azu 4 EN	26		4.6	0.00	28.8	54.0	0.17	0.03	0.10	0.07	0.29	12.5	0.03	0.10	100.6



apfu															
Sample	Point	Na	Mg	Al	Si	Fe2+	Fe+3	Mn	Ti	Ba	K	Ca	P	Sr	Total
Azu 1	1	0.41	0.00	1.5	2.4	0.00	0.01	0.00	0.00	0.00	0.02	0.61	0.00	0.00	5.0
Azu 1	11	0.23	0.00	1.7	2.2	0.00	0.01	0.00	0.00	0.00	0.00	0.82	0.00	0.00	5.0
Azu 2	5	0.37	0.00	1.6	2.4	0.00	0.01	0.00	0.00	0.00	0.01	0.64	0.00	0.00	5.0
Azu 2	11	0.44	0.00	1.5	2.5	0.00	0.01	0.00	0.00	0.00	0.02	0.57	0.00	0.00	5.0
Azu 2	14	0.33	0.00	1.6	2.3	0.00	0.01	0.00	0.00	0.00	0.01	0.70	0.00	0.00	5.0
Azu 3	1	0.17	0.00	1.8	2.2	0.00	0.01	0.00	0.00	0.01	0.00	0.86	0.00	0.00	5.0
Azu 3	22	0.40	0.00	1.5	2.4	0.00	0.01	0.00	0.00	0.00	0.02	0.62	0.00	0.00	5.0
Azu 4	1	0.21	0.00	1.7	2.2	0.00	0.01	0.00	0.00	0.00	0.01	0.82	0.00	0.00	5.0
Azu 4	3	0.36	0.00	1.6	2.4	0.00	0.01	0.00	0.00	0.01	0.01	0.65	0.00	0.00	5.0
Azu 4	4	0.37	0.00	1.6	2.4	0.00	0.01	0.00	0.00	0.00	0.01	0.65	0.00	0.00	5.0
Azu 4	4	0.31	0.00	1.6	2.3	0.00	0.01	0.00	0.00	0.00	0.01	0.72	0.00	0.00	5.0
Azu 4	11	0.34	0.00	1.6	2.4	0.00	0.01	0.00	0.00	0.00	0.01	0.68	0.00	0.00	5.0
Azu 4	12	0.26	0.00	1.7	2.3	0.00	0.01	0.00	0.01	0.00	0.01	0.76	0.00	0.00	5.0
Azu 4	13	0.42	0.00	1.5	2.4	0.00	0.01	0.00	0.00	0.00	0.02	0.59	0.00	0.00	5.0
Azu 7 EN	8	0.31	0.00	1.6	2.3	0.00	0.01	0.00	0.00	0.00	0.01	0.72	0.00	0.00	5.0
Azu 4 EN	26	0.40	0.00	1.5	2.4	0.00	0.00	0.00	0.00	0.00	0.02	0.60	0.00	0.00	5.0

Sample	Point	An	Ab	Or	Total	FeO(wt%) corrected	Fe2O3(wt%) calculated	Total(wt%) corrected
Azu 1	1	58.6	39.8	1.6	100	0.00	0.35	99.9
Azu 1	11	77.7	21.8	0.5	100	0.00	0.29	101.9
Azu 2	5	62.3	36.3	1.4	100	0.00	0.20	100.2
Azu 2	11	55.8	42.6	1.6	100	0.00	0.30	101.7
Azu 2	14	67.0	32.0	1.0	100	0.00	0.32	100.5
Azu 3	1	83.0	16.5	0.5	100	0.00	0.35	100.9
Azu 3	22	59.6	38.8	1.6	100	0.00	0.41	101.2
Azu 4	1	79.1	20.3	0.5	100	0.00	0.30	100.4
Azu 4	3	63.5	35.3	1.3	100	0.00	0.18	100.8
Azu 4	4	63.0	35.7	1.3	100	0.00	0.34	100.8
Azu 4	4	69.4	29.7	0.9	100	0.00	0.40	100.9
Azu 4	11	65.7	33.2	1.1	100	0.00	0.40	101.2
Azu 4	12	73.9	25.3	0.8	100	0.00	0.28	101.3
Azu 4	13	57.4	40.9	1.7	100	0.00	0.25	100.5
Azu 7 EN	8	69.1	29.6	1.4	100	0.00	0.43	100.3
Azu 4 EN	26	59.2	39.2	1.6	100	0.07	0.12	100.6

## External rims

Sample	Point	Comment	wt%												
			Na2O	MgO	Al2O3	SiO2	FeO	MnO	TiO2	BaO	K2O	CaO	P2O5	SrO	Total
Azu 1	14		3.9	0.10	29.4	52.4	0.55	0.00	0.05	0.00	0.23	13.7	0.03	0.13	100.5
Azu 1	19		3.9	0.11	30.0	52.1	0.45	0.03	0.19	0.00	0.18	14.0	0.03	0.16	101.1
Azu 1	21		4.3	0.08	28.9	52.9	0.70	0.00	0.05	0.00	0.24	13.0	0.02	0.13	100.3
Azu 2	7		4.0	0.06	29.5	52.2	0.64	0.00	0.00	0.00	0.18	13.8	0.03	0.00	100.4
Azu 2	13		3.9	0.09	29.6	51.8	0.65	0.02	0.00	0.02	0.16	14.1	0.01	0.13	100.5
Azu 2	18		4.2	0.07	29.2	53.3	0.62	0.03	0.00	0.20	0.23	13.3	0.02	0.21	101.4
Azu 3	8		3.1	0.02	30.6	50.1	0.45	0.04	0.00	0.27	0.16	15.2	0.01	0.01	100.0
Azu 3	12		4.3	0.08	28.9	52.6	0.61	0.00	0.15	0.00	0.22	13.2	0.00	0.09	100.2
Azu 3	24		4.2	0.08	28.9	52.0	0.63	0.00	0.00	0.17	0.23	13.3	0.00	0.10	99.6
Azu 3	29		4.0	0.08	29.4	52.4	0.65	0.00	0.00	0.07	0.22	13.8	0.04	0.08	100.8
Azu 4	21		4.0	0.07	29.5	52.0	0.75	0.03	0.00	0.10	0.20	13.8	0.01	0.14	100.6
Azu 4	2		4.2	0.08	29.8	52.1	0.53	0.00	0.01	0.02	0.23	13.8	0.02	0.10	100.8
Azu 4	6		3.9	0.09	29.8	52.4	0.67	0.00	0.10	0.40	0.21	14.0	0.00	0.08	101.5
Azu 4	9		3.8	0.10	29.8	52.0	0.59	0.00	0.11	0.12	0.19	14.2	0.04	0.10	101.1
Azu 4	15		4.2	0.09	29.3	53.2	0.69	0.00	0.05	0.05	0.20	13.4	0.00	0.15	101.3
Azu 7 EN	7		4.2	0.03	29.4	52.4	0.52	0.02	0.00	0.00	0.30	13.6	0.00	0.11	100.4
Azu 7 EN	10		4.1	0.03	29.4	52.0	0.55	0.00	0.00	0.00	0.31	13.5	0.04	0.15	100.0
Azu 10 EN	2		4.1	0.06	29.4	51.9	0.51	0.02	0.06	0.07	0.21	13.5	0.01	0.09	99.9
Azu 4 EN	19		4.0	0.06	29.8	52.3	0.54	0.00	0.09	0.05	0.21	13.9	0.02	0.18	101.2
Azu 4 EN	28		3.7	0.08	30.4	51.8	0.53	0.02	0.09	0.17	0.19	14.4	0.00	0.14	101.4

apfu															
Sample	Point	Na	Mg	Al	Si	Fe2+	Fe+3	Mn	Ti	Ba	K	Ca	P	Sr	Total
Azu 1	14	0.35	0.01	1.6	2.4	0.00	0.02	0.00	0.00	0.00	0.01	0.66	0.00	0.00	5.0
Azu 1	19	0.34	0.01	1.6	2.3	0.00	0.02	0.00	0.01	0.00	0.01	0.68	0.00	0.00	5.0
Azu 1	21	0.38	0.01	1.5	2.4	0.00	0.03	0.00	0.00	0.00	0.01	0.63	0.00	0.00	5.0
Azu 2	7	0.35	0.00	1.6	2.4	0.00	0.02	0.00	0.00	0.00	0.01	0.67	0.00	0.00	5.0
Azu 2	13	0.34	0.01	1.6	2.4	0.00	0.02	0.00	0.00	0.00	0.01	0.68	0.00	0.00	5.0
Azu 2	18	0.37	0.00	1.5	2.4	0.00	0.02	0.00	0.00	0.00	0.01	0.64	0.00	0.01	5.0
Azu 3	8	0.27	0.00	1.7	2.3	0.00	0.02	0.00	0.00	0.00	0.01	0.75	0.00	0.00	5.0
Azu 3	12	0.38	0.01	1.5	2.4	0.00	0.02	0.00	0.01	0.00	0.01	0.64	0.00	0.00	5.0
Azu 3	24	0.37	0.01	1.6	2.4	0.00	0.02	0.00	0.00	0.00	0.01	0.65	0.00	0.00	5.0
Azu 3	29	0.35	0.01	1.6	2.4	0.00	0.02	0.00	0.00	0.00	0.01	0.67	0.00	0.00	5.0
Azu 4	21	0.35	0.00	1.6	2.4	0.00	0.03	0.00	0.00	0.00	0.01	0.67	0.00	0.00	5.0
Azu 4	2	0.36	0.01	1.6	2.3	0.00	0.02	0.00	0.00	0.00	0.01	0.67	0.00	0.00	5.0
Azu 4	6	0.34	0.01	1.6	2.4	0.00	0.03	0.00	0.00	0.01	0.01	0.68	0.00	0.00	5.0
Azu 4	9	0.33	0.01	1.6	2.3	0.00	0.02	0.00	0.00	0.00	0.01	0.68	0.00	0.00	5.0
Azu 4	15	0.36	0.01	1.6	2.4	0.00	0.03	0.00	0.00	0.00	0.01	0.65	0.00	0.00	5.0
Azu 7 EN	7	0.36	0.00	1.6	2.4	0.00	0.02	0.00	0.00	0.00	0.02	0.66	0.00	0.00	5.0
Azu 7 EN	10	0.36	0.00	1.6	2.4	0.00	0.02	0.00	0.00	0.00	0.02	0.66	0.00	0.00	5.0
Azu 10 EN	2	0.36	0.00	1.6	2.4	0.00	0.02	0.00	0.00	0.00	0.01	0.66	0.00	0.00	5.0
Azu 4 EN	19	0.35	0.00	1.6	2.4	0.00	0.02	0.00	0.00	0.00	0.01	0.67	0.00	0.00	5.0
Azu 4 EN	28	0.32	0.01	1.6	2.3	0.00	0.02	0.00	0.00	0.00	0.01	0.69	0.00	0.00	5.0

Sample	Point	An	Ab	Or	Total	FeO(wt%) corrected	Fe2O3(wt%) calculated	Total(wt%) corrected
Azu 1	14	64.9	33.9	1.3	100	0.00	0.61	100.5
Azu 1	19	66.2	32.8	1.0	100	0.00	0.50	101.2
Azu 1	21	61.9	36.7	1.4	100	0.00	0.78	100.4
Azu 2	7	65.1	33.9	1.0	100	0.00	0.71	100.5
Azu 2	13	66.3	32.8	0.9	100	0.00	0.72	100.5
Azu 2	18	62.7	35.9	1.3	100	0.00	0.68	101.5
Azu 3	8	72.4	26.6	0.9	100	0.00	0.50	100.0
Azu 3	12	62.3	36.5	1.2	100	0.00	0.68	100.3
Azu 3	24	63.1	35.6	1.3	100	0.00	0.70	99.6
Azu 3	29	65.0	33.7	1.3	100	0.00	0.72	100.9
Azu 4	21	64.9	33.9	1.1	100	0.00	0.83	100.6
Azu 4	2	63.9	34.9	1.3	100	0.00	0.59	100.9
Azu 4	6	65.9	33.0	1.1	100	0.00	0.74	101.6
Azu 4	9	66.4	32.5	1.0	100	0.00	0.66	101.1
Azu 4	15	63.2	35.6	1.1	100	0.00	0.76	101.4
Azu 7 EN	7	63.3	35.1	1.7	100	0.00	0.58	100.5
Azu 7 EN	10	63.4	34.9	1.8	100	0.00	0.61	100.1
Azu 10 EN	2	63.8	35.0	1.2	100	0.00	0.57	100.0
Azu 4 EN	19	64.9	33.9	1.2	100	0.00	0.60	101.3
Azu 4 EN	28	67.6	31.4	1.1	100	0.00	0.59	101.5

## Internal rings

			wt%												
Sample	Point	Comment	Na2O	MgO	Al2O3	SiO2	FeO	MnO	TiO2	BaO	K2O	CaO	P2O5	SrO	Total
Azu 1	7		4.1	0.00	30.0	52.8	0.39	0.00	0.00	0.05	0.24	13.7	0.04	0.06	101.4
Azu 1	9		4.4	0.07	29.1	53.1	0.74	0.00	0.08	0.00	0.23	13.3	0.02	0.10	101.1
Azu 2	16		4.3	0.01	29.6	53.4	0.22	0.00	0.00	0.00	0.23	13.3	0.02	0.09	101.2
Azu 3	3		5.1	0.00	28.0	54.5	0.20	0.00	0.11	0.00	0.30	11.7	0.00	0.08	100.0
Azu 4	11		4.2	0.01	29.5	52.5	0.29	0.00	0.00	0.00	0.24	13.5	0.02	0.07	100.3
Azu 4	13		5.0	0.00	28.6	54.5	0.33	0.05	0.00	0.00	0.29	11.9	0.01	0.05	100.7
Azu 7 EN	6		4.8	0.01	28.3	54.4	0.27	0.02	0.00	0.12	0.34	12.0	0.04	0.04	100.3
Azu 4 EN	17		4.0	0.02	30.0	52.4	0.33	0.00	0.00	0.00	0.21	14.0	0.02	0.08	101.1

			apfu												
Sample	Point	Na	Mg	Al	Si	Fe2+	Fe+3	Mn	Ti	Ba	K	Ca	P	Sr	Total
Azu 1	7	0.36	0.00	1.6	2.4	0.00	0.01	0.00	0.00	0.00	0.01	0.66	0.00	0.00	5.0
Azu 1	9	0.38	0.00	1.5	2.4	0.00	0.03	0.00	0.00	0.00	0.01	0.64	0.00	0.00	5.0
Azu 2	16	0.37	0.00	1.6	2.4	0.00	0.01	0.00	0.00	0.00	0.01	0.64	0.00	0.00	5.0
Azu 3	3	0.45	0.00	1.5	2.5	0.00	0.01	0.00	0.00	0.00	0.02	0.57	0.00	0.00	5.0
Azu 4	11	0.37	0.00	1.6	2.4	0.00	0.01	0.00	0.00	0.00	0.01	0.65	0.00	0.00	5.0
Azu 4	13	0.43	0.00	1.5	2.4	0.00	0.01	0.00	0.00	0.00	0.02	0.57	0.00	0.00	5.0
Azu 7 EN	6	0.42	0.00	1.5	2.5	0.00	0.01	0.00	0.00	0.00	0.02	0.58	0.00	0.00	5.0
Azu 4 EN	17	0.35	0.00	1.6	2.4	0.00	0.01	0.00	0.00	0.00	0.01	0.67	0.00	0.00	5.0

Sample	Point	An	Ab	Or	Total	FeO(wt%) corrected	Fe2O3(wt%) calculated	Total(wt%) corrected
Azu 1	7	63.8	34.8	1.3	100	0.00	0.43	101.4
Azu 1	9	61.7	37.0	1.3	100	0.00	0.82	101.1
Azu 2	16	62.4	36.3	1.3	100	0.00	0.24	101.2
Azu 3	3	54.9	43.4	1.7	100	0.00	0.22	100.1
Azu 4	11	63.2	35.5	1.3	100	0.00	0.32	100.4
Azu 4	13	55.9	42.5	1.6	100	0.00	0.36	100.8
Azu 7 EN	6	56.9	41.2	1.9	100	0.00	0.30	100.4
Azu 4 EN	17	65.1	33.7	1.2	100	0.00	0.36	101.1

## Intermediate zones

Sample	Point	Comment	wt%												
			Na2O	MgO	Al2O3	SiO2	FeO	MnO	TiO2	BaO	K2O	CaO	P2O5	SrO	Total
Azu 1	2	with Amp inclusion	7.2	0.01	24.8	60.0	0.28	0.01	0.00	0.12	0.74	7.4	0.02	0.00	100.6
Azu 1	3	with Amp inclusion	7.1	0.00	25.3	59.4	0.23	0.00	0.02	0.00	0.65	7.8	0.00	0.04	100.4
Azu 1	4	with Amp inclusion	6.8	0.00	25.5	59.8	0.31	0.00	0.00	0.07	0.65	8.0	0.01	0.10	101.2
Azu 1	6		6.2	0.01	26.7	57.4	0.26	0.00	0.00	0.00	0.47	9.7	0.01	0.13	100.9
Azu 1	8		6.8	0.00	25.6	59.6	0.29	0.00	0.09	0.12	0.64	8.3	0.00	0.05	101.3
Azu 1	12		6.1	0.00	26.3	57.7	0.26	0.00	0.00	0.00	0.50	9.5	0.00	0.11	100.5
Azu 1	13		7.0	0.00	25.0	60.3	0.15	0.00	0.00	0.00	0.71	7.8	0.00	0.04	101.0
Azu 1	18	with Amp inclusion	7.1	0.01	24.8	60.4	0.29	0.02	0.01	0.02	0.72	7.5	0.00	0.05	101.0
Azu 1	20	with Amp inclusion	6.7	0.00	25.4	59.4	0.24	0.00	0.03	0.07	0.64	8.2	0.03	0.04	100.7
Azu 2	1		6.3	0.00	26.0	57.9	0.16	0.02	0.05	0.10	0.56	8.9	0.00	0.09	100.0
Azu 2	2		6.4	0.01	26.4	57.6	0.26	0.05	0.00	0.00	0.52	9.3	0.00	0.04	100.6
Azu 2	6		6.7	0.01	25.4	59.3	0.26	0.00	0.00	0.00	0.64	8.2	0.00	0.07	100.6
Azu 2	12		6.5	0.01	26.1	58.2	0.32	0.01	0.00	0.00	0.40	9.1	0.01	0.06	100.7
Azu 2	15		6.8	0.00	25.5	59.7	0.27	0.00	0.00	0.07	0.64	8.1	0.01	0.08	101.2
Azu 2	17		7.1	0.00	25.2	60.3	0.22	0.02	0.00	0.35	0.69	7.7	0.00	0.08	101.8
Azu 3	2		6.0	0.01	26.8	56.9	0.29	0.00	0.00	0.12	0.41	9.9	0.00	0.02	100.4
Azu 3	4		6.8	0.01	25.1	58.9	0.24	0.03	0.00	0.00	0.58	8.2	0.00	0.08	99.8
Azu 3	7		6.5	0.02	25.6	58.1	0.27	0.00	0.07	0.27	0.57	8.7	0.03	0.15	100.2
Azu 3	9		6.9	0.02	25.4	59.0	0.22	0.01	0.00	0.22	0.64	8.3	0.03	0.09	100.8
Azu 3	11		7.0	0.02	24.8	59.3	0.30	0.08	0.10	0.12	0.68	7.9	0.03	0.08	100.3
Azu 3	23		6.9	0.03	25.0	59.9	0.31	0.00	0.00	0.00	0.72	7.7	0.01	0.10	100.6
Azu 3	25		7.1	0.02	24.7	60.8	0.13	0.02	0.11	0.27	0.78	7.4	0.00	0.02	101.3
Azu 3	28		7.0	0.00	25.3	60.0	0.31	0.00	0.05	0.17	0.67	8.1	0.03	0.06	101.5
Azu 4	2	with Amp inclusion	7.0	0.02	25.1	59.8	0.25	0.00	0.00	0.00	0.65	7.8	0.03	0.07	100.7
Azu 4	6		6.6	0.00	25.8	58.9	0.29	0.06	0.09	0.15	0.64	8.6	0.00	0.02	101.1
Azu 4	7		6.6	0.01	26.0	58.5	0.18	0.01	0.00	0.05	0.60	8.7	0.00	0.04	100.6



Azu 4	8		6.8	0.00	25.3	58.9	0.23	0.03	0.00	0.00	0.64	8.3	0.02	0.09	100.3
Azu 4	10		6.7	0.01	25.2	59.6	0.26	0.00	0.09	0.15	0.71	8.0	0.03	0.10	100.8
Azu 4	12		6.4	0.00	26.2	58.0	0.17	0.00	0.00	0.00	0.57	9.1	0.01	0.04	100.5
Azu 4	14		7.1	0.01	24.9	60.4	0.15	0.00	0.01	0.00	0.76	7.3	0.00	0.06	100.7
Azu 4	15		6.5	0.00	26.5	57.9	0.29	0.07	0.02	0.07	0.49	9.3	0.00	0.07	101.2
Azu 4	16		6.8	0.01	25.1	59.7	0.27	0.03	0.09	0.00	0.68	7.9	0.00	0.16	100.6
Azu 4	17		6.1	0.02	26.6	57.4	0.34	0.08	0.07	0.07	0.50	9.6	0.02	0.07	100.8
Azu 4	18		6.9	0.01	25.4	59.1	0.29	0.02	0.17	0.05	0.65	8.1	0.00	0.06	100.7
Azu 4	20		6.7	0.03	25.7	59.3	0.26	0.00	0.00	0.12	0.64	8.5	0.00	0.08	101.3
Azu 4	27	in contact with Amp phenocrysts	6.7	0.00	25.6	59.4	0.24	0.01	0.05	0.07	0.61	8.4	0.02	0.09	101.3
Azu 4	28	in contact with Amp phenocrysts	6.5	0.01	26.4	58.5	0.28	0.01	0.11	0.00	0.53	9.1	0.04	0.00	101.5
Azu 4	1		6.9	0.00	25.2	59.2	0.32	0.00	0.10	0.12	0.64	8.1	0.01	0.00	100.6
Azu 4	5		7.0	0.00	25.2	59.5	0.26	0.00	0.00	0.00	0.70	8.0	0.03	0.11	100.8
Azu 4	8		6.9	0.02	25.4	59.4	0.27	0.03	0.00	0.02	0.66	8.2	0.02	0.06	100.9
Azu 4	14		7.1	0.02	25.3	60.0	0.22	0.00	0.04	0.00	0.71	7.8	0.00	0.05	101.3
Azu 7 EN	5		7.0	0.00	24.8	59.1	0.23	0.01	0.00	0.12	0.72	8.0	0.00	0.07	100.0
Azu 7 EN	9		6.7	0.03	24.9	59.9	0.25	0.00	0.01	0.00	0.86	7.9	0.00	0.10	100.5
Azu 10 EN	1		7.2	0.01	24.6	60.2	0.24	0.00	0.00	0.05	0.74	7.4	0.03	0.00	100.5
Azu 14 EN	1		6.8	0.03	25.2	58.9	0.33	0.01	0.05	0.02	0.64	8.4	0.00	0.08	100.5
Azu 4 EN	16		6.2	0.00	26.5	58.0	0.34	0.03	0.10	0.00	0.49	9.4	0.02	0.05	101.1
Azu 4 EN	18		6.8	0.02	25.7	59.1	0.23	0.06	0.10	0.12	0.56	8.7	0.02	0.08	101.5
Azu 4 EN	27		6.4	0.00	26.1	58.6	0.23	0.04	0.16	0.05	0.54	9.2	0.00	0.03	101.4

apfu															
Sample	Point	Na	Mg	Al	Si	Fe2+	Fe+3	Mn	Ti	Ba	K	Ca	P	Sr	Total
Azu 1	2	0.62	0.00	1.3	2.7	0.00	0.01	0.00	0.00	0.00	0.04	0.35	0.00	0.00	5.0
Azu 1	3	0.61	0.00	1.3	2.6	0.00	0.01	0.00	0.00	0.00	0.04	0.37	0.00	0.00	5.0
Azu 1	4	0.58	0.00	1.3	2.6	0.01	0.00	0.00	0.00	0.00	0.04	0.38	0.00	0.00	5.0
Azu 1	6	0.53	0.00	1.4	2.6	0.00	0.01	0.00	0.00	0.00	0.03	0.46	0.00	0.00	5.0
Azu 1	8	0.58	0.00	1.3	2.6	0.01	0.00	0.00	0.00	0.00	0.04	0.39	0.00	0.00	5.0
Azu 1	12	0.53	0.00	1.4	2.6	0.01	0.00	0.00	0.00	0.00	0.03	0.46	0.00	0.00	5.0
Azu 1	13	0.60	0.00	1.3	2.7	0.01	0.00	0.00	0.00	0.00	0.04	0.37	0.00	0.00	5.0
Azu 1	18	0.61	0.00	1.3	2.7	0.01	0.00	0.00	0.00	0.00	0.04	0.36	0.00	0.00	5.0
Azu 1	20	0.57	0.00	1.3	2.6	0.01	0.00	0.00	0.00	0.00	0.04	0.39	0.00	0.00	5.0
Azu 2	1	0.55	0.00	1.4	2.6	0.01	0.00	0.00	0.00	0.00	0.03	0.43	0.00	0.00	5.0
Azu 2	2	0.55	0.00	1.4	2.6	0.00	0.01	0.00	0.00	0.00	0.03	0.45	0.00	0.00	5.0
Azu 2	6	0.58	0.00	1.3	2.6	0.01	0.00	0.00	0.00	0.00	0.04	0.39	0.00	0.00	5.0
Azu 2	12	0.56	0.00	1.4	2.6	0.00	0.01	0.00	0.00	0.00	0.02	0.43	0.00	0.00	5.0
Azu 2	15	0.58	0.00	1.3	2.6	0.01	0.00	0.00	0.00	0.00	0.04	0.38	0.00	0.00	5.0
Azu 2	17	0.61	0.00	1.3	2.7	0.00	0.01	0.00	0.00	0.01	0.04	0.36	0.00	0.00	5.0
Azu 3	2	0.52	0.00	1.4	2.5	0.00	0.01	0.00	0.00	0.00	0.02	0.48	0.00	0.00	5.0
Azu 3	4	0.59	0.00	1.3	2.6	0.01	0.00	0.00	0.00	0.00	0.03	0.39	0.00	0.00	5.0
Azu 3	7	0.56	0.00	1.4	2.6	0.00	0.01	0.00	0.00	0.00	0.03	0.42	0.00	0.00	5.0
Azu 3	9	0.59	0.00	1.3	2.6	0.00	0.01	0.00	0.00	0.00	0.04	0.39	0.00	0.00	5.0
Azu 3	11	0.60	0.00	1.3	2.7	0.00	0.01	0.00	0.00	0.00	0.04	0.38	0.00	0.00	5.0
Azu 3	23	0.59	0.00	1.3	2.7	0.01	0.00	0.00	0.00	0.00	0.04	0.37	0.00	0.00	5.0
Azu 3	25	0.61	0.00	1.3	2.7	0.00	0.00	0.00	0.00	0.00	0.04	0.35	0.00	0.00	5.0
Azu 3	28	0.60	0.00	1.3	2.7	0.00	0.01	0.00	0.00	0.00	0.04	0.38	0.00	0.00	5.0
Azu 4	2	0.60	0.00	1.3	2.7	0.01	0.00	0.00	0.00	0.00	0.04	0.37	0.00	0.00	5.0
Azu 4	6	0.57	0.00	1.4	2.6	0.00	0.01	0.00	0.00	0.00	0.04	0.41	0.00	0.00	5.0
Azu 4	7	0.57	0.00	1.4	2.6	0.00	0.01	0.00	0.00	0.00	0.03	0.41	0.00	0.00	5.0
Azu 4	8	0.59	0.00	1.3	2.6	0.00	0.01	0.00	0.00	0.00	0.04	0.40	0.00	0.00	5.0
Azu 4	10	0.58	0.00	1.3	2.7	0.01	0.00	0.00	0.00	0.00	0.04	0.38	0.00	0.00	5.0

Azu 4	12	0.56	0.00	1.4	2.6	0.00	0.01	0.00	0.00	0.00	0.03	0.44	0.00	0.00	5.0
Azu 4	14	0.61	0.00	1.3	2.7	0.01	0.00	0.00	0.00	0.00	0.04	0.35	0.00	0.00	5.0
Azu 4	15	0.56	0.00	1.4	2.6	0.00	0.01	0.00	0.00	0.00	0.03	0.44	0.00	0.00	5.0
Azu 4	16	0.58	0.00	1.3	2.7	0.01	0.00	0.00	0.00	0.00	0.04	0.38	0.00	0.00	5.0
Azu 4	17	0.53	0.00	1.4	2.6	0.00	0.01	0.00	0.00	0.00	0.03	0.46	0.00	0.00	5.0
Azu 4	18	0.59	0.00	1.3	2.6	0.00	0.01	0.00	0.01	0.00	0.04	0.39	0.00	0.00	5.0
Azu 4	20	0.58	0.00	1.3	2.6	0.00	0.01	0.00	0.00	0.00	0.04	0.40	0.00	0.00	5.0
Azu 4	27	0.58	0.00	1.3	2.6	0.00	0.00	0.00	0.00	0.00	0.03	0.40	0.00	0.00	5.0
Azu 4	28	0.56	0.00	1.4	2.6	0.00	0.01	0.00	0.00	0.00	0.03	0.43	0.00	0.00	5.0
Azu 4	1	0.60	0.00	1.3	2.6	0.00	0.01	0.00	0.00	0.00	0.04	0.39	0.00	0.00	5.0
Azu 4	5	0.60	0.00	1.3	2.6	0.00	0.01	0.00	0.00	0.00	0.04	0.38	0.00	0.00	5.0
Azu 4	8	0.59	0.00	1.3	2.6	0.00	0.01	0.00	0.00	0.00	0.04	0.39	0.00	0.00	5.0
Azu 4	14	0.61	0.00	1.3	2.7	0.00	0.01	0.00	0.00	0.00	0.04	0.37	0.00	0.00	5.0
Azu 7 EN	5	0.61	0.00	1.3	2.6	0.00	0.01	0.00	0.00	0.00	0.04	0.38	0.00	0.00	5.0
Azu 7 EN	9	0.58	0.00	1.3	2.7	0.01	0.00	0.00	0.00	0.00	0.05	0.38	0.00	0.00	5.0
Azu 10 EN	1	0.62	0.00	1.3	2.7	0.00	0.01	0.00	0.00	0.00	0.04	0.35	0.00	0.00	5.0
Azu 14 EN	1	0.59	0.00	1.3	2.6	0.00	0.01	0.00	0.00	0.00	0.04	0.40	0.00	0.00	5.0
Azu 4 EN	16	0.54	0.00	1.4	2.6	0.01	0.01	0.00	0.00	0.00	0.03	0.45	0.00	0.00	5.0
Azu 4 EN	18	0.58	0.00	1.3	2.6	0.00	0.01	0.00	0.00	0.00	0.03	0.41	0.00	0.00	5.0
Azu 4 EN	27	0.55	0.00	1.4	2.6	0.00	0.01	0.00	0.01	0.00	0.03	0.44	0.00	0.00	5.0

Sample	Point	An	Ab	Or	Total	FeO(wt%) corrected	Fe2O3(wt%) calculated	Total(wt%) corrected
Azu 1	2	34.8	61.1	4.1	100	0.00	0.31	100.6
Azu 1	3	36.5	59.9	3.7	100	0.00	0.25	100.4
Azu 1	4	38.1	58.2	3.7	100	0.31	0.00	101.2
Azu 1	6	45.3	52.1	2.6	100	0.00	0.28	100.9
Azu 1	8	38.8	57.6	3.6	100	0.27	0.03	101.3
Azu 1	12	45.1	52.1	2.8	100	0.26	0.00	100.5
Azu 1	13	36.7	59.4	4.0	100	0.15	0.00	101.0
Azu 1	18	35.5	60.4	4.0	100	0.29	0.00	101.0
Azu 1	20	39.2	57.2	3.6	100	0.24	0.00	100.7
Azu 2	1	42.5	54.4	3.2	100	0.16	0.00	100.0
Azu 2	2	43.5	53.7	2.9	100	0.00	0.29	100.6
Azu 2	6	39.0	57.4	3.6	100	0.26	0.00	100.6
Azu 2	12	42.6	55.1	2.3	100	0.00	0.36	100.7
Azu 2	15	38.2	58.2	3.6	100	0.27	0.00	101.2
Azu 2	17	35.9	60.2	3.8	100	0.00	0.24	101.8
Azu 3	2	46.5	51.2	2.3	100	0.00	0.32	100.5
Azu 3	4	38.8	58.0	3.3	100	0.14	0.11	99.8
Azu 3	7	41.3	55.5	3.2	100	0.00	0.30	100.2
Azu 3	9	38.5	57.9	3.6	100	0.00	0.24	100.8
Azu 3	11	36.9	59.3	3.8	100	0.00	0.34	100.3
Azu 3	23	36.6	59.3	4.1	100	0.31	0.00	100.6
Azu 3	25	34.7	60.9	4.4	100	0.13	0.00	101.3
Azu 3	28	37.5	58.7	3.7	100	0.01	0.33	101.6
Azu 4	2	36.6	59.7	3.6	100	0.21	0.04	100.7
Azu 4	6	40.3	56.1	3.6	100	0.00	0.32	101.2
Azu 4	7	40.8	55.9	3.3	100	0.00	0.20	100.7
Azu 4	8	38.7	57.7	3.6	100	0.00	0.25	100.3
Azu 4	10	37.9	58.1	4.0	100	0.26	0.00	100.8
Azu 4	12	42.5	54.3	3.2	100	0.00	0.19	100.5

Azu 4	14	34.5	61.2	4.3	100	0.15	0.00	100.7
Azu 4	15	43.2	54.1	2.7	100	0.00	0.32	101.2
Azu 4	16	37.7	58.5	3.8	100	0.27	0.00	100.6
Azu 4	17	45.2	52.0	2.8	100	0.00	0.37	100.8
Azu 4	18	38.1	58.3	3.6	100	0.00	0.32	100.7
Azu 4	20	39.6	56.8	3.6	100	0.00	0.29	101.3
Azu 4	27	39.5	57.1	3.4	100	0.13	0.12	101.3
Azu 4	28	42.5	54.5	3.0	100	0.00	0.31	101.5
Azu 4	1	37.9	58.5	3.6	100	0.00	0.35	100.7
Azu 4	5	37.5	58.6	3.9	100	0.00	0.29	100.8
Azu 4	8	38.3	58.0	3.7	100	0.00	0.30	100.9
Azu 4	14	36.4	59.6	3.9	100	0.00	0.25	101.3
Azu 7 EN	5	37.0	59.0	4.0	100	0.00	0.26	100.0
Azu 7 EN	9	37.5	57.6	4.9	100	0.25	0.00	100.5
Azu 10 EN	1	34.6	61.3	4.1	100	0.05	0.22	100.5
Azu 14 EN	1	38.9	57.5	3.6	100	0.00	0.36	100.5
Azu 4 EN	16	44.3	52.9	2.8	100	0.16	0.21	101.1
Azu 4 EN	18	40.2	56.8	3.1	100	0.00	0.25	101.5
Azu 4 EN	27	43.0	54.0	3.0	100	0.08	0.17	101.4

---

## Plg inclusions in Amp microphenocrysts

Sample	Point	Comment	wt%												
			Na2O	MgO	Al2O3	SiO2	FeO	MnO	TiO2	BaO	K2O	CaO	P2O5	SrO	Total
Azu 2	24		4.6	0.09	28.9	53.0	1.02	0.07	0.19	0.00	0.26	12.7	0.01	0.08	101.0
Azu 3	5		4.4	0.08	28.4	53.3	0.68	0.00	0.04	0.17	0.26	12.5	0.02	0.17	100.1
Azu 3	6		4.2	0.06	29.1	53.1	0.62	0.02	0.07	0.00	0.24	13.1	0.02	0.19	100.8
Azu 3	13		4.4	0.06	28.8	53.6	0.68	0.02	0.07	0.25	0.23	13.0	0.01	0.08	101.1
Azu 3	21		4.3	0.08	28.8	52.6	0.71	0.00	0.09	0.22	0.20	13.2	0.00	0.15	100.5
Azu 3	36		4.2	0.09	29.3	52.2	0.93	0.00	0.05	0.00	0.21	13.6	0.03	0.10	100.6
Azu 4	34		3.9	0.08	30.2	52.0	0.72	0.00	0.05	0.22	0.18	14.2	0.03	0.11	101.6
Azu 4	3		3.8	0.05	29.9	52.0	0.71	0.05	0.00	0.15	0.21	14.2	0.01	0.05	101.2

Sample	Point	apfu													
		Na	Mg	Al	Si	Fe2+	Fe+3	Mn	Ti	Ba	K	Ca	P	Sr	Total
Azu 2	24	0.40	0.01	1.5	2.4	0.00	0.04	0.00	0.01	0.00	0.01	0.61	0.00	0.00	5.0
Azu 3	5	0.39	0.01	1.5	2.4	0.00	0.03	0.00	0.00	0.00	0.02	0.61	0.00	0.00	5.0
Azu 3	6	0.37	0.00	1.5	2.4	0.00	0.02	0.00	0.00	0.00	0.01	0.64	0.00	0.00	5.0
Azu 3	13	0.39	0.00	1.5	2.4	0.00	0.03	0.00	0.00	0.00	0.01	0.62	0.00	0.00	5.0
Azu 3	21	0.38	0.01	1.5	2.4	0.00	0.03	0.00	0.00	0.00	0.01	0.64	0.00	0.00	5.0
Azu 3	36	0.36	0.01	1.6	2.4	0.00	0.04	0.00	0.00	0.00	0.01	0.66	0.00	0.00	5.0
Azu 4	34	0.34	0.01	1.6	2.3	0.00	0.03	0.00	0.00	0.00	0.01	0.68	0.00	0.00	5.0
Azu 4	3	0.34	0.00	1.6	2.3	0.00	0.03	0.00	0.00	0.00	0.01	0.69	0.00	0.00	5.0

Sample	Point	An	Ab	Or	Total	FeO(wt%) corrected	Fe2O3(wt%) calculated	Total(wt%) corrected
Azu 2	24	59.4	39.1	1.4	100	0.00	1.13	101.1
Azu 3	5	60.1	38.4	1.5	100	0.00	0.76	100.1
Azu 3	6	62.3	36.3	1.4	100	0.00	0.69	100.8
Azu 3	13	61.0	37.7	1.3	100	0.00	0.76	101.2
Azu 3	21	62.0	36.8	1.1	100	0.00	0.79	100.5
Azu 3	36	63.5	35.3	1.2	100	0.00	1.03	100.7
Azu 4	34	66.1	32.9	1.0	100	0.00	0.80	101.7
Azu 4	3	66.3	32.5	1.2	100	0.00	0.79	101.2

## Plg inclusions in Amp phenocrysts

Sample	Point	Comment	wt%												
			Na2O	MgO	Al2O3	SiO2	FeO	MnO	TiO2	BaO	K2O	CaO	P2O5	SrO	Total
Azu 1	10		6.8	0.01	25.5	59.6	0.40	0.02	0.12	0.00	0.67	8.1	0.02	0.03	101.3
Azu 4	29		6.7	0.04	26.1	59.0	0.40	0.05	0.14	0.10	0.73	8.7	0.00	0.01	102.0
Azu 4	31		6.3	0.02	26.0	58.5	0.31	0.01	0.02	0.10	0.58	8.9	0.01	0.05	100.8

Sample	Point	apfu													
		Na	Mg	Al	Si	Fe2+	Fe+3	Mn	Ti	Ba	K	Ca	P	Sr	Total
Azu 1	10	0.59	0.00	1.3	2.6	0.01	0.01	0.00	0.00	0.00	0.04	0.39	0.00	0.00	5.0
Azu 4	29	0.57	0.00	1.4	2.6	0.00	0.01	0.00	0.00	0.00	0.04	0.41	0.00	0.00	5.0
Azu 4	31	0.55	0.00	1.4	2.6	0.01	0.00	0.00	0.00	0.00	0.03	0.43	0.00	0.00	5.0

Sample	Point	An	Ab	Or	Total	FeO(wt%) corrected	Fe2O3(wt%) calculated	Total(wt%) corrected
Azu 1	10	38.2	58.1	3.8	100	0.16	0.27	101.3
Azu 4	29	40.0	56.0	4.0	100	0.00	0.44	102.0
Azu 4	31	42.3	54.4	3.3	100	0.31	0.00	100.8



## Plg inclusions in Bt phenocrysts

Sample	Point	Comment	wt%												
			Na2O	MgO	Al2O3	SiO2	FeO	MnO	TiO2	BaO	K2O	CaO	P2O5	SrO	Total
Azu 2	4		6.5	0.04	26.0	57.7	0.30	0.00	0.00	0.00	0.53	9.0	0.02	0.05	100.2
Azu 2	9		6.9	0.01	25.5	59.1	0.38	0.00	0.00	0.00	0.65	8.1	0.00	0.00	100.6
Azu 2	20		6.7	0.02	25.6	59.5	0.30	0.02	0.00	0.00	0.63	8.4	0.00	0.00	101.2
Azu 2	22		6.7	0.00	26.4	58.9	0.45	0.00	0.05	0.00	0.62	8.9	0.00	0.05	102.0
Azu 3	19		6.7	0.00	25.0	58.8	0.33	0.00	0.00	0.00	0.67	8.1	0.00	0.04	99.6
Azu 3	20		6.6	0.00	25.7	58.6	0.30	0.04	0.09	0.00	0.59	8.6	0.01	0.08	100.6
Azu 3	35	Ca rim	4.5	0.06	29.1	53.8	0.56	0.00	0.07	0.00	0.29	12.9	0.03	0.06	101.4
Azu 4	22		6.5	0.02	25.7	58.6	0.21	0.00	0.05	0.15	0.58	8.7	0.00	0.13	100.7
Azu 4	24		6.6	0.00	26.1	58.5	0.33	0.02	0.00	0.10	0.56	8.7	0.00	0.00	100.9
Azu 4	32		6.9	0.01	25.7	59.6	0.33	0.03	0.00	0.02	0.64	8.2	0.01	0.03	101.4
Azu 4	33		7.0	0.00	25.7	59.9	0.36	0.00	0.06	0.00	0.65	8.2	0.02	0.07	102.0

apfu															
Sample	Point	Na	Mg	Al	Si	Fe2+	Fe+3	Mn	Ti	Ba	K	Ca	P	Sr	Total
Azu 2	4	0.56	0.00	1.4	2.6	0.00	0.01	0.00	0.00	0.00	0.03	0.43	0.00	0.00	5.0
Azu 2	9	0.60	0.00	1.3	2.6	0.00	0.01	0.00	0.00	0.00	0.04	0.39	0.00	0.00	5.0
Azu 2	20	0.58	0.00	1.3	2.6	0.01	0.00	0.00	0.00	0.00	0.04	0.40	0.00	0.00	5.0
Azu 2	22	0.57	0.00	1.4	2.6	0.00	0.02	0.00	0.00	0.00	0.03	0.42	0.00	0.00	5.0
Azu 3	19	0.58	0.00	1.3	2.6	0.01	0.00	0.00	0.00	0.00	0.04	0.39	0.00	0.00	5.0
Azu 3	20	0.57	0.00	1.4	2.6	0.00	0.01	0.00	0.00	0.00	0.03	0.41	0.00	0.00	5.0
Azu 3	35	0.39	0.00	1.5	2.4	0.00	0.02	0.00	0.00	0.00	0.02	0.62	0.00	0.00	5.0
Azu 4	22	0.57	0.00	1.4	2.6	0.00	0.01	0.00	0.00	0.00	0.03	0.42	0.00	0.00	5.0
Azu 4	24	0.57	0.00	1.4	2.6	0.00	0.01	0.00	0.00	0.00	0.03	0.42	0.00	0.00	5.0
Azu 4	32	0.59	0.00	1.3	2.6	0.00	0.01	0.00	0.00	0.00	0.04	0.39	0.00	0.00	5.0
Azu 4	33	0.60	0.00	1.3	2.6	0.00	0.01	0.00	0.00	0.00	0.04	0.39	0.00	0.00	5.0

Sample	Point	An	Ab	Or	Total	FeO(wt%) corrected	Fe2O3(wt%) calculated	Total(wt%) corrected
Azu 2	4	42.0	55.0	3.0	100	0.00	0.34	100.2
Azu 2	9	37.9	58.5	3.6	100	0.00	0.43	100.7
Azu 2	20	39.3	57.2	3.5	100	0.19	0.12	101.2
Azu 2	22	40.9	55.7	3.4	100	0.00	0.51	102.1
Azu 3	19	38.6	57.6	3.8	100	0.31	0.02	99.6
Azu 3	20	40.4	56.3	3.3	100	0.00	0.34	100.6
Azu 3	35	60.3	38.0	1.6	100	0.00	0.62	101.4
Azu 4	22	40.9	55.8	3.3	100	0.00	0.24	100.7
Azu 4	24	40.9	56.0	3.1	100	0.00	0.36	100.9
Azu 4	32	38.1	58.4	3.5	100	0.00	0.36	101.4
Azu 4	33	38.0	58.5	3.6	100	0.00	0.40	102.0

## Amphibole

### Phenocrysts and inclusions in Plg

Sample	Point	Comment	wt%													Total
			F	Na2O	MgO	Al2O3	SiO2	TiO2	Cr2O3	MnO	FeO	ZnO	Cl	K2O	CaO	
Azu 1	1	inclusion in Plg	0.17	1.1	14.4	6.5	47.8	1.4	0.00	0.47	13.6	0.00	0.09	0.57	12.5	98.6
Azu 1	2	with Plg inclusion	0.11	1.5	13.9	7.8	45.9	1.8	0.00	0.43	14.2	0.00	0.10	0.87	12.4	99.0
Azu 1	3	with Plg inclusion	0.18	1.5	13.6	7.9	45.0	1.6	0.09	0.51	14.6	0.00	0.14	0.92	12.3	98.2
Azu 1	4		0.23	1.3	14.1	7.3	46.9	1.4	0.00	0.47	14.2	0.01	0.10	0.77	12.4	99.2
Azu 1	5		0.17	1.1	15.2	6.3	48.6	1.4	0.03	0.56	13.1	0.18	0.08	0.60	12.5	99.8
Azu 1	6		0.24	1.3	13.8	7.5	46.4	1.7	0.04	0.54	13.5	0.02	0.11	0.86	12.6	98.6
Azu 1	7	inclusion in Plg	0.31	1.5	13.7	7.9	46.6	1.9	0.02	0.51	14.5	0.11	0.12	0.85	12.4	100.2
Azu 1	9		0.19	1.6	12.7	8.5	45.1	1.9	0.00	0.47	15.1	0.00	0.11	0.89	12.3	98.8
Azu 1	10		0.15	1.4	14.1	7.7	46.4	1.3	0.00	0.51	14.9	0.02	0.11	0.82	12.4	99.6
Azu 4	1	in contact with Plg phenocrysts	0.20	1.3	14.1	7.3	47.5	1.7	0.00	0.36	13.4	0.13	0.10	0.70	12.5	99.1
Azu 4	2	in contact with Plg phenocrysts	0.14	1.5	12.8	8.8	45.0	2.0	0.00	0.45	14.6	0.12	0.13	1.01	12.4	99.0
Azu 4	3	in contact with Plg phenocrysts	0.10	1.1	14.1	7.0	47.0	1.4	0.00	0.41	13.3	0.08	0.09	0.71	12.4	97.9
Azu 4	5	in contact with Plg phenocrysts	0.09	1.5	13.5	7.7	45.7	1.6	0.05	0.40	14.4	0.03	0.10	0.76	12.4	98.2
Azu 4	9	inclusion in Plg	0.28	1.3	13.4	7.7	45.8	1.6	0.00	0.41	13.5	0.00	0.17	0.89	12.5	97.6
Azu 4	1		0.22	1.3	14.1	6.8	47.8	1.5	0.02	0.40	14.1	0.00	0.10	0.66	12.4	99.3
Azu 4	2		0.16	1.3	13.0	7.8	47.7	1.5	0.01	0.47	13.9	0.12	0.11	0.95	12.3	99.3

apfu

Sample	Point	Si	Al IV	Ti	T	Ti	Al VI	Cr	Fe3+	Zn	Mn2+	Fe2+	Mg	C	Mn2+	Fe2+	Mg	Ca	Na	B	Ca	Na	K	A	Sum T,C,B,A	O (non-W)	OH	F	Cl	O	W
Azu 1	1	6.9	1.1		8.0	0.15	0.05		0.35		0.03	1.31	3.1	5.0	0.03			1.9	0.03	2.0	0.29	0.11	0.39	15.4	22.0	1.9	0.08	0.02		2.0	
Azu 1	2	6.7	1.3		8.0	0.20	0.02		0.38		0.02	1.35	3.0	5.0	0.03			1.9	0.04	2.0	0.39	0.16	0.55	15.5	22.0	1.9	0.05	0.03		2.0	
Azu 1	3	6.6	1.4		8.0	0.17	0.00	0.01	0.48		0.04	1.32	3.0	5.0	0.03			1.9	0.03	2.0	0.39	0.17	0.57	15.6	22.0	1.9	0.08	0.03		2.0	
Azu 1	4	6.8	1.2		8.0	0.15	0.04		0.41	0.00	0.02	1.32	3.1	5.0	0.03			1.9	0.04	2.0	0.34	0.14	0.48	15.5	22.0	1.9	0.11	0.03		2.0	
Azu 1	5	6.9	1.1	0.00	8.0	0.15		0.00	0.44	0.02	0.02	1.13	3.2	5.0	0.04			1.9	0.05	2.0	0.26	0.11	0.37	15.4	22.0	1.9	0.08	0.02		2.0	
Azu 1	6	6.8	1.2		8.0	0.19	0.09	0.01	0.24	0.00	0.05	1.42	3.0	5.0	0.02			2.0	0.02	2.0	0.36	0.16	0.52	15.5	22.0	1.9	0.11	0.03		2.0	
Azu 1	7	6.7	1.3		8.0	0.21	0.06	0.00	0.32	0.01	0.02	1.43	2.9	5.0	0.04			1.9	0.05	2.0	0.36	0.16	0.52	15.5	22.0	1.8	0.14	0.03		2.0	
Azu 1	9	6.6	1.4		8.0	0.21	0.11		0.28		0.03	1.57	2.8	5.0	0.03			1.9	0.03	2.0	0.43	0.17	0.59	15.6	22.0	1.9	0.09	0.03		2.0	
Azu 1	10	6.7	1.3		8.0	0.14	0.01		0.56	0.00	0.02	1.24	3.0	5.0	0.04			1.9	0.05	2.0	0.33	0.15	0.49	15.5	22.0	1.9	0.07	0.03		2.0	
Azu 4	1	6.9	1.1		8.0	0.18	0.12		0.20	0.01	0.01	1.43	3.0	5.0	0.03			1.9	0.04	2.0	0.34	0.13	0.47	15.5	22.0	1.9	0.09	0.03		2.0	
Azu 4	2	6.6	1.4		8.0	0.22	0.14		0.27	0.01	0.03	1.53	2.8	5.0	0.02			2.0	0.03	2.0	0.39	0.19	0.58	15.6	22.0	1.9	0.06	0.03		2.0	
Azu 4	3	6.9	1.1		8.0	0.16	0.09		0.32	0.01	0.03	1.31	3.1	5.0	0.02			2.0	0.03	2.0	0.30	0.13	0.43	15.4	22.0	1.9	0.05	0.02		2.0	
Azu 4	5	6.7	1.3		8.0	0.18	0.06	0.01	0.34	0.00	0.03	1.43	3.0	5.0	0.02			2.0	0.02	2.0	0.39	0.14	0.53	15.5	22.0	1.9	0.04	0.03		2.0	
Azu 4	9	6.8	1.2		8.0	0.18	0.14		0.18		0.05	1.49	3.0	5.0	0.01			2.0	0.01	2.0	0.37	0.17	0.54	15.5	22.0	1.8	0.13	0.04		2.0	
Azu 4	1	6.9	1.1		8.0	0.16	0.08	0.00	0.28		0.01	1.43	3.0	5.0	0.04			1.9	0.04	2.0	0.32	0.12	0.44	15.4	22.0	1.9	0.10	0.02		2.0	
Azu 4	2	6.9	1.1		8.0	0.16	0.28	0.00	0.05	0.01	0.03	1.65	2.8	5.0	0.03			1.9	0.06	2.0	0.31	0.18	0.48	15.5	22.0	1.9	0.07	0.03		2.0	

Sample	Point	O=F,Cl	Total-OH-F-Cl	FeO(wt%) corrected	Fe2O3(wt%) calculated	H2O wt% calculated	Total(wt%) corrected
Azu 1	1	-0.09	98.5	10.8	3.2	2.0	100.8
Azu 1	2	-0.07	98.9	11.1	3.4	2.0	101.2
Azu 1	3	-0.11	98.1	10.7	4.3	1.9	100.4
Azu 1	4	-0.12	99.1	10.8	3.8	1.9	101.4
Azu 1	5	-0.09	99.8	9.4	4.1	2.0	102.1
Azu 1	6	-0.12	98.5	11.6	2.1	1.9	100.6
Azu 1	7	-0.16	100.1	11.9	3.0	1.9	102.2
Azu 1	9	-0.11	98.7	12.8	2.5	1.9	100.9
Azu 1	10	-0.09	99.5	10.2	5.1	1.9	101.9
Azu 4	1	-0.11	99.0	11.8	1.8	1.9	101.1
Azu 4	2	-0.09	98.9	12.5	2.4	1.9	101.1
Azu 4	3	-0.06	97.8	10.7	2.9	2.0	100.1
Azu 4	5	-0.06	98.1	11.6	3.0	2.0	100.4
Azu 4	9	-0.16	97.4	12.0	1.6	1.9	99.5
Azu 4	1	-0.11	99.2	11.8	2.6	1.9	101.4
Azu 4	2	-0.09	99.2	13.5	0.4	1.9	101.2

Sample	Point	Fe <sup>3+</sup> /Fe <sub>tot</sub>	Mg# (Mg/Mg+Fe <sup>2+</sup> )	Altot	<sup>A</sup> (Na+K+2Ca)	<sup>C</sup> (Al+Fe <sup>3+</sup> +Cr+2Ti)	Name
Azu 1	1	0.21	0.70	1.1	0.39	0.70	magnesio-ferri-hornblende
Azu 1	2	0.22	0.69	1.3	0.55	0.79	magnesio-hastingsite
Azu 1	3	0.27	0.69	1.4	0.57	0.84	magnesio-hastingsite
Azu 1	4	0.24	0.70	1.2	0.48	0.76	magnesio-ferri-hornblende
Azu 1	5	0.28	0.74	1.1	0.37	0.74	magnesio-ferri-hornblende
Azu 1	6	0.14	0.68	1.3	0.52	0.70	magnesio-hastingsite
Azu 1	7	0.18	0.67	1.3	0.52	0.80	magnesio-hastingsite
Azu 1	9	0.15	0.64	1.5	0.59	0.81	magnesio-hastingsite
Azu 1	10	0.31	0.71	1.3	0.49	0.85	magnesio-ferri-hornblende
Azu 4	1	0.12	0.68	1.2	0.47	0.69	magnesio-ferri-hornblende
Azu 4	2	0.15	0.65	1.5	0.58	0.84	magnesio-hastingsite
Azu 4	3	0.20	0.70	1.2	0.43	0.73	magnesio-ferri-hornblende
Azu 4	5	0.19	0.67	1.3	0.53	0.77	magnesio-hastingsite
Azu 4	9	0.11	0.67	1.3	0.54	0.67	magnesio-hastingsite
Azu 4	1	0.17	0.68	1.2	0.44	0.68	magnesio-ferri-hornblende
Azu 4	2	0.03	0.63	1.3	0.48	0.64	magnesio-hornblende

## Microphenocrysts

Sample	Point	Comment	F	Na2O	MgO	Al2O3	SiO2	TiO2	Cr2O3	MnO	FeO	ZnO	Cl	K2O	CaO	Total
Azu 2	2		0.17	2.2	13.6	11.8	40.4	2.6	0.00	0.21	13.6	0.00	0.03	0.61	11.6	96.8
Azu 2	3		0.19	2.2	15.7	10.7	43.4	2.4	0.05	0.25	11.9	0.07	0.03	0.52	11.7	99.2
Azu 3	1	with Plg inclusion	0.29	2.2	14.7	12.0	42.0	3.0	0.00	0.13	11.3	0.09	0.03	0.64	11.8	98.1
Azu 3	6		0.23	2.6	14.1	11.8	42.2	3.4	0.02	0.29	12.1	0.07	0.03	0.64	11.9	99.3
Azu 3	7	with Plg inclusion	0.23	2.3	15.0	12.0	41.9	2.4	0.00	0.15	11.3	0.00	0.02	0.61	12.0	98.0
Azu 3	8		0.19	2.1	15.3	10.0	44.3	2.9	0.00	0.15	11.0	0.00	0.04	0.69	12.1	98.6
Azu 3	9	with Plg inclusion	0.33	2.0	14.9	9.8	44.3	3.0	0.00	0.19	11.6	0.08	0.04	0.73	12.1	99.1
Azu 3	10	with Plg inclusion	0.28	2.3	14.5	11.6	41.9	3.4	0.00	0.16	12.1	0.00	0.03	0.64	12.1	99.0
Azu 3	11	with Plg inclusion	0.23	2.4	14.7	10.5	43.1	2.8	0.00	0.24	11.7	0.00	0.04	0.69	12.0	98.4
Azu 3	14		0.24	2.1	15.1	10.7	43.1	2.7	0.00	0.17	11.5	0.12	0.03	0.74	12.1	98.6
Azu 4	7		0.09	2.0	13.5	11.2	42.7	3.3	0.02	0.30	13.0	0.00	0.04	0.69	12.1	99.0
Azu 4	10		0.28	2.0	14.7	10.0	44.2	2.7	0.00	0.21	12.3	0.15	0.04	0.80	12.0	99.5
Azu 4	11		0.13	2.0	14.0	10.3	43.1	2.8	0.00	0.28	13.0	0.00	0.04	0.78	12.1	98.5
Azu 4	12	with Plg inclusion	0.29	2.2	15.0	10.7	43.0	2.8	0.00	0.13	11.4	0.06	0.03	0.67	12.1	98.3
Azu 4	13	with Plg inclusion	0.17	2.1	15.8	9.5	45.5	1.8	0.04	0.22	11.2	0.00	0.04	0.64	11.9	99.1
Azu 4	14		0.18	2.3	13.7	12.4	41.8	3.1	0.00	0.13	13.2	0.00	0.03	0.65	11.7	99.1
Azu 4	15		0.05	2.0	15.0	9.2	44.5	2.5	0.03	0.29	11.9	0.01	0.06	0.77	11.9	98.3
Azu 4	9		0.13	2.5	13.6	12.1	41.7	3.1	0.01	0.21	12.6	0.08	0.02	0.64	11.7	98.3
Azu 4	10	with Plg inclusion	0.35	2.1	14.9	9.9	44.3	3.0	0.03	0.18	11.2	0.05	0.05	0.71	11.9	98.5
Azu 4	12		0.12	2.3	15.0	10.6	44.0	2.9	0.02	0.21	11.3	0.00	0.02	0.73	12.1	99.3
Azu 4	13		0.30	2.2	15.0	10.6	43.8	3.1	0.06	0.16	11.3	0.00	0.02	0.69	12.2	99.5
Azu 4	14		0.16	2.4	14.7	11.2	42.9	2.9	0.00	0.15	12.4	0.02	0.02	0.58	11.5	98.8
Azu 8 EN	2		0.46	2.3	14.6	12.0	41.2	4.4	0.05	0.09	11.1	0.00	0.06	1.00	11.9	99.0
Azu 8 EN	3		0.30	2.3	13.6	12.8	41.2	3.0	0.03	0.11	11.7	0.08	0.05	0.73	12.0	97.9
Azu 10 EN	1		0.16	2.1	15.1	10.0	43.6	3.4	0.00	0.18	10.8	0.07	0.03	0.73	12.0	98.3
Azu 10 EN	3		0.22	2.3	12.9	12.6	41.7	2.8	0.01	0.30	13.8	0.03	0.03	0.72	11.8	99.2
Azu 10 EN	4		0.02	2.2	14.6	11.5	43.3	2.6	0.00	0.12	11.8	0.00	0.03	0.61	11.7	98.4

Azu 14 EN	1	0.05	2.4	12.2	13.6	40.1	2.9	0.01	0.12	14.2	0.00	0.03	0.64	11.5	97.9
Azu 14 EN	2	0.27	2.1	14.3	12.3	42.9	2.1	0.00	0.13	12.2	0.03	0.04	0.58	11.4	98.3
Azu 14 EN	3	0.17	2.3	14.6	12.4	42.5	1.9	0.00	0.20	12.2	0.11	0.04	0.61	11.4	98.4
Azu 4 EN	3	0.20	2.0	14.9	9.9	44.6	3.1	0.04	0.21	11.8	0.12	0.05	0.78	12.2	99.7
Azu 4 EN	4	0.25	2.1	15.1	9.4	45.4	2.7	0.02	0.24	11.6	0.16	0.07	0.74	11.9	99.8
Azu 4 EN	5	0.20	2.3	14.4	12.5	41.9	2.8	0.00	0.14	11.5	0.00	0.02	0.62	11.9	98.3
Azu 4 EN	6	0.13	2.2	13.7	11.8	41.1	3.0	0.05	0.17	13.3	0.02	0.03	0.61	11.7	97.7
Azu 4 EN	7	0.17	2.2	15.0	10.3	43.6	2.4	0.02	0.19	11.9	0.01	0.03	0.70	12.0	98.6
Azu 4 EN	8	0.10	2.1	15.2	10.1	44.4	2.3	0.00	0.19	11.8	0.12	0.04	0.69	12.0	99.0

---



apfu

Sample	Point	Si	Al IV	Ti	T	Ti	Al VI	Cr	Fe3+	Zn	Mn2+	Fe2+	Mg	C	Mn2+	Fe2+	Mg	Ca	Na	B	Ca	Na	K	A	Sum T,C,B,A	O (non-W)	OH	F	Cl	O	W
Azu 2	2	6.0	2.0	8.0	0.29	0.07			0.77			0.87	3.0	5.0	0.03	0.05	1.8	0.09	2.0	0.56	0.12	0.67		15.7	22.0	1.9	0.08	0.01		2.0	
Azu 2	3	6.2	1.8	8.0	0.26	0.01	0.01		0.76	0.01		0.60	3.4	5.0	0.03	0.06	1.8	0.11	2.0	0.51	0.10	0.60		15.6	22.0	1.9	0.09	0.01		2.0	
Azu 3	1	6.1	1.9	8.0	0.33	0.16			0.48	0.01		0.83	3.2	5.0	0.02	0.06	1.8	0.08	2.0	0.55	0.12	0.67		15.7	22.0	1.9	0.14	0.01		2.0	
Azu 3	6	6.1	1.9	8.0	0.37	0.13	0.00		0.32	0.01		1.11	3.1	5.0	0.04	0.03	1.9	0.08	2.0	0.65	0.12	0.77		15.8	22.0	1.9	0.11	0.01		2.0	
Azu 3	7	6.1	1.9	8.0	0.26	0.16			0.58			0.75	3.2	5.0	0.02	0.04	1.9	0.07	2.0	0.59	0.11	0.71		15.7	22.0	1.9	0.11	0.01		2.0	
Azu 3	8	6.4	1.6	8.0	0.31	0.11			0.28			1.00	3.3	5.0	0.02	0.04	1.9	0.07	2.0	0.52	0.13	0.65		15.6	22.0	1.9	0.09	0.01		2.0	
Azu 3	9	6.4	1.6	8.0	0.33	0.08			0.29	0.01		1.07	3.2	5.0	0.02	0.04	1.9	0.07	2.0	0.50	0.14	0.64		15.6	22.0	1.8	0.15	0.01		2.0	
Azu 3	10	6.1	1.9	8.0	0.38	0.05			0.51			0.92	3.1	5.0	0.02	0.04	1.9	0.07	2.0	0.57	0.12	0.69		15.7	22.0	1.9	0.13	0.01		2.0	
Azu 3	11	6.3	1.7	8.0	0.31	0.08			0.33			1.08	3.2	5.0	0.03	0.03	1.9	0.06	2.0	0.62	0.13	0.75		15.8	22.0	1.9	0.11	0.01		2.0	
Azu 3	14	6.2	1.8	8.0	0.30	0.07			0.49	0.01		0.87	3.3	5.0	0.02	0.03	1.9	0.06	2.0	0.53	0.14	0.66		15.7	22.0	1.9	0.11	0.01		2.0	
Azu 4	7	6.2	1.8	8.0	0.36	0.15	0.00		0.33			1.24	2.9	5.0	0.04	0.02	1.9	0.06	2.0	0.52	0.13	0.64		15.6	22.0	1.9	0.04	0.01		2.0	
Azu 4	10	6.4	1.6	8.0	0.30	0.08			0.41	0.02		1.03	3.2	5.0	0.03	0.04	1.9	0.08	2.0	0.47	0.15	0.62		15.6	22.0	1.9	0.13	0.01		2.0	
Azu 4	11	6.3	1.7	8.0	0.30	0.08			0.42			1.16	3.0	5.0	0.03	0.01	1.9	0.05	2.0	0.50	0.15	0.65		15.6	22.0	1.9	0.06	0.01		2.0	
Azu 4	12	6.3	1.7	8.0	0.30	0.09			0.44	0.01		0.91	3.3	5.0	0.02	0.04	1.9	0.06	2.0	0.55	0.12	0.67		15.7	22.0	1.9	0.13	0.01		2.0	
Azu 4	13	6.5	1.5	8.0	0.20	0.13	0.01		0.44			0.85	3.4	5.0	0.03	0.05	1.8	0.09	2.0	0.49	0.12	0.60		15.6	22.0	1.9	0.08	0.01		2.0	
Azu 4	14	6.1	1.9	8.0	0.34	0.17			0.55			0.98	3.0	5.0	0.02	0.07	1.8	0.10	2.0	0.53	0.12	0.65		15.7	22.0	1.9	0.08	0.01		2.0	
Azu 4	15	6.5	1.5	8.0	0.28	0.06	0.00		0.34	0.00		1.07	3.2	5.0	0.04	0.03	1.9	0.07	2.0	0.49	0.14	0.64		15.6	22.0	2.0	0.02	0.01		2.0	
Azu 4	9	6.1	1.9	8.0	0.34	0.19	0.00		0.39	0.01		1.09	3.0	5.0	0.03	0.05	1.8	0.09	2.0	0.61	0.12	0.73		15.7	22.0	1.9	0.06	0.01		2.0	
Azu 4	10	6.5	1.5	8.0	0.33	0.14	0.00		0.15	0.01		1.14	3.2	5.0	0.02	0.07	1.9	0.06	2.0	0.52	0.13	0.65		15.6	22.0	1.8	0.16	0.01		2.0	
Azu 4	12	6.3	1.7	8.0	0.32	0.14	0.00		0.26			1.07	3.2	5.0	0.03	0.04	1.9	0.07	2.0	0.57	0.13	0.70		15.7	22.0	1.9	0.06	0.01		2.0	
Azu 4	13	6.3	1.7	8.0	0.34	0.11	0.01		0.28			1.04	3.2	5.0	0.02	0.04	1.9	0.06	2.0	0.56	0.13	0.69		15.7	22.0	1.9	0.14	0.01		2.0	
Azu 4	14	6.2	1.8	8.0	0.31	0.10			0.55	0.00		0.86	3.2	5.0	0.02	0.09	1.8	0.12	2.0	0.54	0.11	0.65		15.6	22.0	1.9	0.08	0.01		2.0	
Azu 8 EN	2	6.0	2.0	8.0	0.48	0.05	0.01		0.28			1.02	3.2	5.0	0.01	0.05	1.9	0.07	2.0	0.59	0.19	0.77		15.8	22.0	1.8	0.21	0.01		2.0	
Azu 8 EN	3	6.1	1.9	8.0	0.33	0.27	0.00		0.33	0.01		1.08	3.0	5.0	0.01	0.04	1.9	0.06	2.0	0.60	0.14	0.74		15.7	22.0	1.8	0.14	0.01		2.0	
Azu 10 EN	1	6.3	1.7	8.0	0.38	0.06			0.24	0.01		1.04	3.3	5.0	0.02	0.04	1.9	0.07	2.0	0.54	0.14	0.67		15.7	22.0	1.9	0.07	0.01		2.0	
Azu 10 EN	3	6.1	1.9	8.0	0.30	0.24	0.00		0.47	0.00		1.18	2.8	5.0	0.04	0.03	1.8	0.08	2.0	0.56	0.13	0.69		15.7	22.0	1.9	0.10	0.01		2.0	
Azu 10 EN	4	6.3	1.7	8.0	0.29	0.22			0.43			0.92	3.1	5.0	0.02	0.07	1.8	0.10	2.0	0.51	0.11	0.62		15.6	22.0	2.0	0.01	0.01		2.0	
Azu 14 EN	1	5.9	2.1	8.0	0.33	0.29	0.00		0.51			1.18	2.7	5.0	0.02	0.07	1.8	0.09	2.0	0.59	0.12	0.71		15.7	22.0	2.0	0.03	0.01		2.0	

Azu 14 EN	2	6.2	1.8	8.0	0.23	0.30		0.58	0.00	0.80	3.1	5.0	0.02	0.09	1.8	0.13	2.0	0.47	0.11	0.58	15.6	22.0	1.9	0.12	0.01	2.0
Azu 14 EN	3	6.1	1.9	8.0	0.21	0.25		0.70	0.01	0.69	3.1	5.0	0.02	0.09	1.8	0.13	2.0	0.51	0.11	0.62	15.6	22.0	1.9	0.08	0.01	2.0
Azu 4 EN	3	6.4	1.6	8.0	0.33	0.08	0.00	0.29	0.01	1.09	3.2	5.0	0.03	0.03	1.9	0.06	2.0	0.48	0.14	0.62	15.6	22.0	1.9	0.09	0.01	2.0
Azu 4 EN	4	6.5	1.5	8.0	0.29	0.12	0.00	0.18	0.02	1.15	3.2	5.0	0.03	0.07	1.8	0.06	2.0	0.52	0.14	0.65	15.7	22.0	1.9	0.11	0.02	2.0
Azu 4 EN	5	6.1	1.9	8.0	0.31	0.23		0.45		0.90	3.1	5.0	0.02	0.05	1.9	0.08	2.0	0.58	0.11	0.69	15.7	22.0	1.9	0.09	0.01	2.0
Azu 4 EN	6	6.0	2.0	8.0	0.33	0.09	0.01	0.63	0.00	0.95	3.0	5.0	0.02	0.06	1.8	0.09	2.0	0.53	0.11	0.65	15.6	22.0	1.9	0.06	0.01	2.0
Azu 4 EN	7	6.3	1.7	8.0	0.26	0.10	0.00	0.43	0.00	0.98	3.2	5.0	0.02	0.04	1.9	0.07	2.0	0.56	0.13	0.69	15.7	22.0	1.9	0.08	0.01	2.0
Azu 4 EN	8	6.4	1.6	8.0	0.25	0.11		0.44	0.01	0.93	3.3	5.0	0.02	0.04	1.9	0.08	2.0	0.52	0.13	0.65	15.6	22.0	1.9	0.05	0.01	2.0

Sample	Point	O=F,Cl	Total-OH-F-Cl	FeO(wt%) corrected	Fe2O3(wt%) calculated	H2O wt% calculated	Total(wt%) corrected
Azu 2	2	-0.08	96.7	7.4	6.9	1.9	99.3
Azu 2	3	-0.09	99.1	5.6	7.1	2.0	101.8
Azu 3	1	-0.13	98.0	7.3	4.4	1.9	100.4
Azu 3	6	-0.1	99.2	9.4	2.9	1.9	101.4
Azu 3	7	-0.1	97.9	6.5	5.3	1.9	100.3
Azu 3	8	-0.09	98.5	8.6	2.6	2.0	100.7
Azu 3	9	-0.15	98.9	9.2	2.7	1.9	101.1
Azu 3	10	-0.12	98.8	7.9	4.7	1.9	101.2
Azu 3	11	-0.11	98.3	9.0	3.0	1.9	100.5
Azu 3	14	-0.11	98.5	7.4	4.5	1.9	100.9
Azu 4	7	-0.05	98.9	10.3	3.0	2.0	101.2
Azu 4	10	-0.13	99.3	8.9	3.8	1.9	101.6
Azu 4	11	-0.06	98.4	9.6	3.9	2.0	100.8
Azu 4	12	-0.13	98.1	7.8	4.0	1.9	100.5
Azu 4	13	-0.08	99.0	7.6	4.1	2.0	101.4
Azu 4	14	-0.08	99.0	8.7	5.0	2.0	101.5
Azu 4	15	-0.03	98.2	9.0	3.2	2.0	100.6
Azu 4	9	-0.06	98.2	9.4	3.5	2.0	100.6
Azu 4	10	-0.16	98.4	9.9	1.4	1.9	100.4
Azu 4	12	-0.05	99.3	9.2	2.4	2.0	101.5
Azu 4	13	-0.13	99.3	8.9	2.6	1.9	101.5
Azu 4	14	-0.07	98.7	7.8	5.1	2.0	101.2
Azu 8 EN	2	-0.2	98.8	8.8	2.6	1.8	100.9
Azu 8 EN	3	-0.14	97.8	9.1	2.9	1.9	100.0
Azu 10 EN	1	-0.07	98.2	8.8	2.2	2.0	100.4
Azu 10 EN	3	-0.1	99.1	9.9	4.3	1.9	101.4
Azu 10 EN	4	-0.01	98.4	8.2	3.9	2.0	100.8
Azu 14 EN	1	-0.03	97.8	10.1	4.5	2.0	100.3
Azu 14 EN	2	-0.12	98.2	7.4	5.3	1.9	100.6

Azu 14 EN	3	-0.08	98.3	6.4	6.4	2.0	100.9
Azu 4 EN	3	-0.1	99.6	9.3	2.7	1.9	101.8
Azu 4 EN	4	-0.12	99.7	10.2	1.6	1.9	101.8
Azu 4 EN	5	-0.09	98.2	7.8	4.1	2.0	100.5
Azu 4 EN	6	-0.06	97.6	8.1	5.7	2.0	100.2
Azu 4 EN	7	-0.08	98.5	8.4	3.9	2.0	100.9
Azu 4 EN	8	-0.05	99.0	8.1	4.1	2.0	101.4

---

Sample	Point	Fe <sup>3+</sup> /Fe <sub>tot</sub>	Mg# (Mg/Mg+Fe <sup>2+</sup> )	Altot	<sup>A</sup> (Na+K+2Ca)	<sup>C</sup> (Al+Fe <sup>3+</sup> +Cr+2Ti)	Name
Azu 2	2	0.45	0.76	2.1	0.67	1.41	magnesio-hastingsite
Azu 2	3	0.53	0.83	1.8	0.60	1.30	magnesio-hastingsite
Azu 3	1	0.35	0.78	2.1	0.67	1.31	Ti-rich magnesio-hastingsite
Azu 3	6	0.22	0.73	2.0	0.77	1.19	Ti-rich magnesio-hastingsite
Azu 3	7	0.42	0.80	2.1	0.71	1.27	magnesio-hastingsite
Azu 3	8	0.21	0.76	1.7	0.65	1.01	Ti-rich magnesio-hastingsite
Azu 3	9	0.21	0.74	1.7	0.64	1.03	Ti-rich magnesio-hastingsite
Azu 3	10	0.35	0.77	2.0	0.69	1.31	Ti-rich magnesio-hastingsite
Azu 3	11	0.23	0.74	1.8	0.75	1.03	Ti-rich magnesio-hastingsite
Azu 3	14	0.35	0.78	1.8	0.66	1.15	magnesio-hastingsite
Azu 4	7	0.21	0.70	1.9	0.64	1.19	Ti-rich magnesio-hastingsite
Azu 4	10	0.28	0.75	1.7	0.62	1.08	magnesio-hastingsite
Azu 4	11	0.27	0.72	1.8	0.65	1.11	Ti-rich magnesio-hastingsite
Azu 4	12	0.32	0.77	1.8	0.67	1.13	Ti-rich magnesio-hastingsite
Azu 4	13	0.33	0.79	1.6	0.60	0.97	magnesio-hastingsite
Azu 4	14	0.34	0.74	2.1	0.65	1.40	Ti-rich magnesio-hastingsite
Azu 4	15	0.24	0.75	1.6	0.64	0.96	magnesio-hastingsite
Azu 4	9	0.25	0.72	2.1	0.73	1.26	Ti-rich magnesio-hastingsite
Azu 4	10	0.11	0.73	1.7	0.65	0.96	Ti-rich magnesio-hastingsite
Azu 4	12	0.19	0.74	1.8	0.70	1.03	Ti-rich magnesio-hastingsite
Azu 4	13	0.21	0.75	1.8	0.69	1.07	Ti-rich magnesio-hastingsite
Azu 4	14	0.37	0.77	1.9	0.65	1.28	Ti-rich magnesio-hastingsite
Azu 8 EN	2	0.21	0.75	2.1	0.77	1.30	Ti-rich magnesio-hastingsite
Azu 8 EN	3	0.23	0.73	2.2	0.74	1.27	Ti-rich magnesio-hastingsite
Azu 10 EN	1	0.18	0.75	1.7	0.67	1.05	Ti-rich magnesio-hastingsite
Azu 10 EN	3	0.28	0.70	2.2	0.69	1.32	Ti-rich magnesio-hastingsite
Azu 10 EN	4	0.30	0.76	2.0	0.62	1.22	magnesio-hastingsite
Azu 14 EN	1	0.29	0.68	2.4	0.71	1.45	Ti-rich magnesio-hastingsite
Azu 14 EN	2	0.39	0.78	2.1	0.58	1.33	magnesio-hastingsite

Azu 14 EN	3	0.47	0.80	2.1	0.62	1.37	magnesio-hastingsite
Azu 4 EN	3	0.21	0.74	1.7	0.62	1.04	Ti-rich magnesio-hastingsite
Azu 4 EN	4	0.13	0.73	1.6	0.65	0.88	magnesio-hastingsite
Azu 4 EN	5	0.32	0.77	2.1	0.69	1.30	Ti-rich magnesio-hastingsite
Azu 4 EN	6	0.39	0.75	2.0	0.65	1.39	Ti-rich magnesio-hastingsite
Azu 4 EN	7	0.30	0.76	1.8	0.69	1.05	magnesio-hastingsite
Azu 4 EN	8	0.31	0.77	1.7	0.65	1.04	magnesio-hastingsite

---

## Biotite

### Phenocrysts

wt%																
Sample	Point	Comment	F	Na2O	MgO	Al2O3	SiO2	TiO2	Cr2O3	MnO	FeO	ZnO	Cl	K2O	CaO	Total
Azu 2	1		0.14	0.49	13.7	13.4	36.7	5.1	0.00	0.23	16.7	0.04	0.18	9.3	0.00	96.0
Azu 2	2		0.12	0.85	15.3	13.5	37.1	4.7	0.00	0.26	14.6	0.17	0.16	9.0	0.03	95.6
Azu 2	3		0.30	0.78	14.7	13.5	36.8	4.5	0.01	0.14	15.3	0.00	0.14	8.7	0.05	94.9
Azu 4	1		0.11	0.50	13.3	13.4	36.8	4.5	0.02	0.23	17.5	0.03	0.17	9.4	0.04	95.9
Azu 4	1		0.38	0.56	13.6	13.4	36.8	4.3	0.03	0.16	16.9	0.00	0.17	9.2	0.05	95.5
Azu 4	2		0.14	0.53	13.5	13.3	36.3	4.9	0.01	0.25	17.4	0.05	0.16	9.2	0.05	95.7

apfu																											
Sampl e	Poin t	Si	Al IV	Fe <sup>3+</sup>	T	Al VI	M g	Fe <sup>2+</sup>	Fe <sup>3+</sup>	Ti	Cr	Mn	Ni	Zn	Li	M	M vacancy	K	Na	Ba	Ca	A	A vacancy	F	Cl	O H	O <sup>2-</sup>
Azu 2	1	2.8	0.95	0.22	4.0	0.27	1.6	0.72	0.14	0.29	0.00	0.00	0.00	0.00	0.00	3.1	0.00	0.86	0.00	0.00	0.00	0.93	0.07	0.12	0.00	1.3	0.57
Azu 2	2	2.8	0.98	0.18	4.0	0.24	1.8	0.54	0.21	0.20	0.00	0.00	0.00	0.00	0.00	3.1	0.00	0.83	0.10	0.00	0.00	0.96	0.04	0.09	0.00	1.2	0.65
Azu 2	3	2.8	0.99	0.18	4.0	0.24	1.7	0.61	0.19	0.20	0.00	0.00	0.00	0.00	0.00	3.1	0.00	0.82	0.10	0.00	0.00	0.96	0.06	0.12	0.00	1.2	0.62
Azu 4	1	2.8	0.92	0.24	4.0	0.30	1.6	0.75	0.11	0.20	0.00	0.00	0.00	0.00	0.00	3.1	0.00	0.80	0.00	0.00	0.00	0.99	0.05	0.10	0.00	1.3	0.54
Azu 4	1	2.8	0.93	0.23	4.0	0.29	1.6	0.73	0.11	0.20	0.00	0.00	0.00	0.00	0.00	3.1	0.00	0.80	0.00	0.00	0.00	0.99	0.05	0.10	0.00	1.3	0.53
Azu 4	2	2.8	0.97	0.21	4.0	0.24	1.6	0.75	0.11	0.20	0.00	0.00	0.00	0.00	0.00	3.1	0.00	0.80	0.00	0.00	0.00	0.99	0.06	0.10	0.00	1.3	0.54

Sample	Point	-O=F+Cl	FeO(wt%) corrected	Fe2O3(wt%) calculated	H2O wt% calculated	Total(wt%) corrected
Azu 2	1	0.10	5.6	12.4	2.5	99.6
Azu 2	2	0.08	6.0	9.4	2.4	98.8
Azu 2	3	0.16	5.8	10.6	2.4	98.3
Azu 4	1	0.09	5.9	12.9	2.6	99.6
Azu 4	1	0.20	5.6	12.5	2.5	99.1
Azu 4	2	0.10	5.8	12.8	2.5	99.3

Sample	Point	Al IV error	Al VI error	Fe2+ error	Fe3+ error	OH error	O <sup>2-</sup> error	Fe <sup>2+</sup> /(Fe <sup>2+</sup> +Mg)	PhI (#Mg)	Fe <sup>3+</sup> /Fe <sub>tot</sub>	Mg/(Fe <sup>2+</sup> +Mg) error	Fe <sup>3+</sup> /Fe <sub>tot</sub> error
Azu 2	1	±0.2 apfu	±0.3 apfu	±0.2 apfu	±0.3 apfu	±0.2 apfu	±0.3 apfu	0.31	0.69	0.33	0.1	0.19
Azu 2	2	±0.2 apfu	±0.3 apfu	±0.2 apfu	±0.3 apfu	±0.2 apfu	±0.3 apfu	0.23	0.77	0.42	0.1	0.21
Azu 2	3	±0.2 apfu	±0.3 apfu	±0.2 apfu	±0.3 apfu	±0.2 apfu	±0.3 apfu	0.26	0.74	0.38	0.1	0.20
Azu 4	1	±0.2 apfu	±0.3 apfu	±0.2 apfu	±0.3 apfu	±0.2 apfu	±0.3 apfu	0.32	0.68	0.34	0.1	0.19
Azu 4	1	±0.2 apfu	±0.3 apfu	±0.2 apfu	±0.3 apfu	±0.2 apfu	±0.3 apfu	0.31	0.69	0.33	0.1	0.19
Azu 4	2	±0.2 apfu	±0.3 apfu	±0.2 apfu	±0.3 apfu	±0.2 apfu	±0.3 apfu	0.32	0.68	0.34	0.1	0.19



## Pyroxenes

## Microlites

Sample	Point	Comment	wt%									Total
			Na2O	MgO	Al2O3	MnO	TiO2	SiO2	CaO	FeO	Cr2O3	
Azu 1	22		0.02	27.9	3.0	0.27	0.35	54.0	1.5	13.0	0.06	100.0
Azu 1	23		0.03	26.2	2.7	0.28	0.35	53.4	1.9	15.0	0.00	99.9
Azu 2	1		0.02	29.0	1.0	0.34	0.30	55.9	1.9	11.7	0.22	100.4
Azu 2	2		0.01	29.8	1.3	0.23	0.04	56.7	1.6	11.3	0.25	101.1
Azu 2	7		0.02	26.2	3.8	0.34	0.19	53.6	1.8	14.7	0.07	100.7
Azu 2	9		0.02	28.4	1.4	0.24	0.14	56.5	2.0	11.9	0.30	101.0
Azu 1	21		0.32	15.0	5.1	0.25	1.27	49.4	19.8	9.0	0.10	100.2
Azu 1	24		0.32	15.1	4.5	0.18	0.93	50.7	20.4	9.0	0.10	101.3
Azu 2	1		0.34	14.9	4.7	0.15	1.13	50.3	20.2	9.2	0.05	100.9
Azu 2	3		0.31	15.7	5.2	0.25	1.30	50.1	18.9	9.4	0.18	101.3
Azu 2	4		0.31	15.2	4.4	0.16	0.90	50.9	21.0	7.8	0.28	100.9
Azu 2	5		0.37	15.6	4.1	0.17	0.74	51.8	20.4	7.7	0.47	101.4
Azu 2	6		0.29	15.7	4.0	0.18	0.86	51.5	20.5	7.6	0.42	101.1
Azu 2	8		0.35	15.1	5.1	0.22	1.16	50.5	19.6	9.2	0.05	101.2
Azu 3	10		0.37	14.5	5.5	0.11	1.53	49.6	19.8	9.1	0.12	100.6
Azu 7 EN	15		0.11	22.9	1.8	0.62	0.43	52.9	2.1	18.2	0.01	99.1
Azu 7 EN	17		0.02	28.8	1.6	0.13	0.12	54.6	1.4	11.8	0.33	98.8
Azu 7 EN	18		0.05	27.7	3.4	0.23	0.53	54.0	1.2	12.4	0.36	99.8
Azu 7 EN	19		0.02	25.8	1.6	0.41	0.14	54.3	1.6	15.4	0.02	99.2
Azu 7 EN	21		0.04	24.6	2.0	0.50	0.28	52.0	1.9	16.6	0.03	98.0
Azu 7 EN	22		0.03	25.2	2.2	0.32	0.43	53.5	1.6	15.8	0.02	99.0
Azu 7 EN	23		0.05	25.7	1.0	0.43	0.22	53.6	1.8	15.8	0.03	98.6
Azu 8 EN	3		0.06	24.9	2.3	0.38	0.38	54.3	1.6	16.3	0.03	100.3

Azu 8 EN	4	0.02	22.8	2.9	0.48	0.31	52.9	1.7	18.9	0.00	99.9
Azu 8 EN	6	0.06	24.9	1.5	0.48	0.20	55.0	1.8	17.1	0.03	101.1
Azu 8 EN	7	0.05	24.4	2.5	0.65	0.39	54.2	1.6	17.0	0.17	101.1
Azu 8 EN	10	0.04	25.7	2.8	0.41	0.45	53.4	1.4	15.2	0.05	99.5
Azu 14 EN	5	0.02	26.8	2.0	0.45	0.42	54.8	2.4	13.8	0.00	100.6
Azu 14 EN	6	0.01	23.3	2.0	0.79	0.15	52.6	1.4	18.3	0.00	98.5
Azu 14 EN	7	0.07	24.6	2.1	0.56	0.33	54.0	2.0	15.9	0.02	99.5
Azu 14 EN	8	0.06	24.6	2.1	0.63	0.22	53.3	1.5	16.1	0.03	98.6
Azu 14 EN	9	0.03	24.0	2.1	0.53	0.30	53.3	1.6	17.8	0.00	99.5
Azu 7 EN	14	0.40	12.6	4.2	0.38	1.31	48.2	20.1	11.1	0.01	98.4
Azu 7 EN	16	0.27	14.0	3.9	0.27	0.94	50.4	20.1	10.7	0.00	100.6
Azu 7 EN	20	0.30	13.3	3.9	0.25	1.35	49.8	20.9	10.2	0.01	100.0
Azu 8 EN	1	0.47	14.4	4.5	0.30	1.33	50.3	20.5	9.2	0.02	101.0
Azu 8 EN	2	0.31	14.0	4.5	0.27	1.23	50.2	20.4	9.8	0.01	100.7
Azu 8 EN	5	0.50	14.7	3.7	0.19	0.55	51.1	20.5	9.3	0.03	100.6
Azu 8 EN	8	2.19	11.9	12.7	0.26	2.83	41.1	11.8	14.7	0.03	97.4
Azu 8 EN	9	0.26	16.0	1.6	0.36	0.41	53.6	19.7	9.3	0.03	101.1
Azu 10 EN	6	2.12	13.1	12.0	0.18	3.43	41.2	11.4	12.0	0.00	95.5
Azu 10 EN	7	1.90	14.2	10.5	0.20	2.83	43.7	11.8	11.6	0.00	96.8
Azu 10 EN	8	2.31	13.4	11.4	0.12	2.92	43.3	11.9	12.1	0.03	97.5
Azu 14 EN	4	0.37	14.2	4.3	0.24	0.91	50.4	19.9	9.9	0.00	100.2
Azu 14 EN	10	2.20	11.8	13.3	0.23	1.89	41.3	11.9	13.8	0.00	96.4
Azu 14 EN	11	2.32	11.4	13.4	0.17	2.06	41.0	11.9	14.2	0.00	96.5

apfu												
Sample	Point	Na	Mg	Al	Mn	Ti	Si	Ca	Fe2+	Fe+3	Cr	Total
Azu 1	22	0.00	1.5	0.13	0.01	0.01	1.9	0.06	0.39	0.00	0.00	4.0
Azu 1	23	0.00	1.4	0.11	0.01	0.01	1.9	0.07	0.44	0.01	0.00	4.0
Azu 2	1	0.00	1.5	0.04	0.01	0.01	2.0	0.07	0.34	0.00	0.01	4.0
Azu 2	2	0.00	1.6	0.05	0.01	0.00	2.0	0.06	0.33	0.00	0.01	4.0
Azu 2	7	0.00	1.4	0.16	0.01	0.01	1.9	0.07	0.44	0.00	0.00	4.0
Azu 2	9	0.00	1.5	0.06	0.01	0.00	2.0	0.07	0.35	0.00	0.01	4.0
Azu 1	21	0.02	0.8	0.22	0.01	0.04	1.8	0.78	0.20	0.08	0.00	4.0
Azu 1	24	0.02	0.8	0.19	0.01	0.03	1.9	0.80	0.21	0.07	0.00	4.0
Azu 2	1	0.02	0.8	0.20	0.00	0.03	1.8	0.79	0.22	0.06	0.00	4.0
Azu 2	3	0.02	0.9	0.22	0.01	0.04	1.8	0.74	0.22	0.07	0.01	4.0
Azu 2	4	0.02	0.8	0.19	0.01	0.02	1.9	0.82	0.19	0.05	0.01	4.0
Azu 2	5	0.03	0.8	0.18	0.01	0.02	1.9	0.79	0.21	0.03	0.01	4.0
Azu 2	6	0.02	0.9	0.17	0.01	0.02	1.9	0.80	0.20	0.03	0.01	4.0
Azu 2	8	0.03	0.8	0.22	0.01	0.03	1.8	0.77	0.23	0.05	0.00	4.0
Azu 3	10	0.03	0.8	0.24	0.00	0.04	1.8	0.78	0.24	0.05	0.00	4.0
Azu 7 EN	15	0.01	1.3	0.08	0.02	0.01	2.0	0.08	0.56	0.00	0.00	4.0
Azu 7 EN	17	0.00	1.5	0.07	0.00	0.00	2.0	0.05	0.35	0.00	0.01	4.0
Azu 7 EN	18	0.00	1.5	0.14	0.01	0.01	1.9	0.04	0.37	0.00	0.01	4.0
Azu 7 EN	19	0.00	1.4	0.07	0.01	0.00	2.0	0.06	0.47	0.00	0.00	4.0
Azu 7 EN	21	0.00	1.4	0.09	0.02	0.01	1.9	0.08	0.48	0.04	0.00	4.0
Azu 7 EN	22	0.00	1.4	0.09	0.01	0.01	2.0	0.06	0.48	0.00	0.00	4.0
Azu 7 EN	23	0.00	1.4	0.04	0.01	0.01	2.0	0.07	0.48	0.01	0.00	4.0
Azu 8 EN	3	0.00	1.3	0.10	0.01	0.01	2.0	0.06	0.49	0.00	0.00	4.0
Azu 8 EN	4	0.00	1.3	0.13	0.01	0.01	1.9	0.06	0.58	0.00	0.00	4.0
Azu 8 EN	6	0.00	1.3	0.06	0.01	0.01	2.0	0.07	0.52	0.00	0.00	4.0
Azu 8 EN	7	0.00	1.3	0.11	0.02	0.01	2.0	0.06	0.51	0.00	0.00	4.0
Azu 8 EN	10	0.00	1.4	0.12	0.01	0.01	1.9	0.06	0.46	0.00	0.00	4.0
Azu 14 EN	5	0.00	1.4	0.08	0.01	0.01	2.0	0.09	0.41	0.00	0.00	4.0
Azu 14 EN	6	0.00	1.3	0.09	0.02	0.00	2.0	0.06	0.57	0.00	0.00	4.0

Azu 14 EN	7	0.01	1.3	0.09	0.02	0.01	2.0	0.08	0.48	0.00	0.00	4.0
Azu 14 EN	8	0.00	1.3	0.09	0.02	0.01	2.0	0.06	0.50	0.00	0.00	4.0
Azu 14 EN	9	0.00	1.3	0.09	0.02	0.01	2.0	0.06	0.55	0.00	0.00	4.0
Azu 7 EN	14	0.03	0.7	0.19	0.01	0.04	1.8	0.82	0.26	0.09	0.00	4.0
Azu 7 EN	16	0.02	0.8	0.17	0.01	0.03	1.9	0.80	0.28	0.05	0.00	4.0
Azu 7 EN	20	0.02	0.7	0.17	0.01	0.04	1.9	0.84	0.27	0.05	0.00	4.0
Azu 8 EN	1	0.03	0.8	0.19	0.01	0.04	1.8	0.81	0.21	0.07	0.00	4.0
Azu 8 EN	2	0.02	0.8	0.20	0.01	0.03	1.9	0.81	0.26	0.04	0.00	4.0
Azu 8 EN	5	0.04	0.8	0.16	0.01	0.02	1.9	0.81	0.20	0.09	0.00	4.0
Azu 8 EN	8	0.16	0.7	0.57	0.01	0.08	1.6	0.48	0.16	0.31	0.00	4.0
Azu 8 EN	9	0.02	0.9	0.07	0.01	0.01	2.0	0.77	0.28	0.00	0.00	4.0
Azu 10 EN	6	0.16	0.8	0.54	0.01	0.10	1.6	0.47	0.14	0.24	0.00	4.0
Azu 10 EN	7	0.14	0.8	0.47	0.01	0.08	1.7	0.48	0.17	0.20	0.00	4.0
Azu 10 EN	8	0.17	0.8	0.51	0.00	0.08	1.6	0.48	0.14	0.24	0.00	4.0
Azu 14 EN	4	0.03	0.8	0.19	0.01	0.03	1.9	0.79	0.26	0.05	0.00	4.0
Azu 14 EN	10	0.16	0.7	0.60	0.01	0.05	1.6	0.49	0.14	0.30	0.00	4.0
Azu 14 EN	11	0.17	0.7	0.60	0.01	0.06	1.6	0.49	0.14	0.31	0.00	4.0

Sample	Point	FeO(wt%) corrected	Fe2O3(wt%) calculated	Total(wt%) corrected	Mg#	Wo	En	Fe	Total
Azu 1	22	13.0	0.05	100.0	0.79	2.9	77.0	20.1	100.0
Azu 1	23	14.6	0.48	99.9	0.76	3.8	73.3	22.9	100.0
Azu 2	1	11.7	0.00	100.4	0.82	3.7	78.6	17.7	100.0
Azu 2	2	11.3	0.00	101.1	0.82	3.0	79.9	17.1	100.0
Azu 2	7	14.7	0.00	100.7	0.76	3.7	73.3	23.0	100.0
Azu 2	9	11.9	0.00	101.0	0.81	3.8	77.8	18.3	100.0
Azu 1	21	6.4	2.86	100.5	0.81	43.4	45.6	10.9	100.0
Azu 1	24	6.7	2.50	101.5	0.80	43.7	45.1	11.2	100.0
Azu 2	1	7.1	2.29	101.1	0.79	43.4	44.6	12.0	100.0
Azu 2	3	7.2	2.42	101.5	0.79	40.8	47.0	12.2	100.0
Azu 2	4	6.2	1.77	101.1	0.81	44.7	45.0	10.4	100.0
Azu 2	5	6.9	0.93	101.5	0.80	42.9	45.7	11.3	100.0
Azu 2	6	6.6	1.11	101.2	0.81	43.2	45.9	10.9	100.0
Azu 2	8	7.7	1.65	101.3	0.78	42.1	45.0	12.9	100.0
Azu 3	10	7.7	1.64	100.8	0.77	43.1	43.9	13.0	100.0
Azu 7 EN	15	18.2	0.00	99.1	0.69	4.4	66.2	29.4	100.0
Azu 7 EN	17	11.8	0.00	98.8	0.81	2.7	79.1	18.2	100.0
Azu 7 EN	18	12.4	0.00	99.8	0.80	2.4	78.0	19.7	100.0
Azu 7 EN	19	15.4	0.00	99.2	0.75	3.3	72.5	24.2	100.0
Azu 7 EN	21	15.4	1.26	98.2	0.74	4.0	71.0	25.0	100.0
Azu 7 EN	22	15.8	0.00	99.0	0.74	3.3	71.6	25.1	100.0
Azu 7 EN	23	15.5	0.41	98.6	0.75	3.6	72.0	24.3	100.0
Azu 8 EN	3	16.3	0.00	100.3	0.73	3.3	70.6	26.1	100.0
Azu 8 EN	4	18.9	0.00	99.9	0.68	3.4	66.0	30.6	100.0
Azu 8 EN	6	17.1	0.00	101.1	0.72	3.7	69.5	26.9	100.0
Azu 8 EN	7	17.0	0.00	101.1	0.72	3.4	69.5	27.1	100.0
Azu 8 EN	10	15.2	0.00	99.5	0.75	2.9	73.0	24.1	100.0
Azu 14 EN	5	13.8	0.00	100.6	0.78	4.8	73.8	21.4	100.0
Azu 14 EN	6	18.3	0.00	98.5	0.69	3.0	67.3	29.7	100.0
Azu 14 EN	7	15.9	0.00	99.5	0.73	4.1	70.4	25.5	100.0

Azu 14 EN	8	16.1	0.00	98.6	0.73	3.1	70.8	26.1	100.0
Azu 14 EN	9	17.8	0.00	99.5	0.71	3.2	68.3	28.4	100.0
Azu 7 EN	14	8.2	3.15	98.7	0.73	45.6	39.8	14.6	100.0
Azu 7 EN	16	8.9	1.96	100.7	0.74	43.2	41.9	15.0	100.0
Azu 7 EN	20	8.6	1.71	100.2	0.73	45.2	40.2	14.6	100.0
Azu 8 EN	1	6.9	2.55	101.3	0.79	44.7	43.6	11.7	100.0
Azu 8 EN	2	8.3	1.61	100.9	0.75	44.0	42.0	14.0	100.0
Azu 8 EN	5	6.5	3.08	100.9	0.80	44.5	44.5	11.0	100.0
Azu 8 EN	8	5.0	10.79	98.5	0.81	36.5	51.3	12.1	100.0
Azu 8 EN	9	9.2	0.06	101.1	0.76	40.1	45.3	14.6	100.0
Azu 10 EN	6	4.5	8.37	96.3	0.84	34.4	55.0	10.6	100.0
Azu 10 EN	7	5.3	6.96	97.5	0.83	33.1	55.3	11.6	100.0
Azu 10 EN	8	4.5	8.41	98.3	0.84	34.8	54.8	10.3	100.0
Azu 14 EN	4	8.3	1.78	100.4	0.75	43.1	42.9	14.0	100.0
Azu 14 EN	10	4.5	10.40	97.4	0.82	37.4	51.6	11.0	100.0
Azu 14 EN	11	4.4	10.93	97.6	0.82	38.0	51.0	11.0	100.0

---

## Mg-rich rims

Sample	Point	Comment	wt%									Total
			Na2O	MgO	Al2O3	MnO	TiO2	SiO2	CaO	FeO	Cr2O3	
Azu 1	3		0.04	28.7	2.4	0.28	0.29	54.2	1.4	12.7	0.35	100.4
Azu 1	8		0.01	28.9	2.2	0.18	0.08	54.4	1.3	12.2	0.36	99.7
Azu 1	10		0.01	28.4	2.8	0.24	0.21	53.4	1.3	12.6	0.53	99.5
Azu 2	10		0.03	28.7	1.9	0.27	0.26	56.1	1.5	12.3	0.10	101.1
Azu 2	12		0.00	28.5	2.7	0.18	0.42	54.8	1.6	11.6	0.52	100.2
Azu 2	15		0.01	29.5	1.4	0.16	0.19	55.9	1.4	11.1	0.28	100.0
Azu 2	18		0.01	29.4	2.2	0.15	0.32	55.9	1.3	11.2	0.50	100.9
Azu 2	21		0.01	28.8	2.1	0.24	0.32	55.7	1.5	11.3	0.40	100.4
Azu 2	28		0.02	28.8	1.7	0.30	0.00	55.8	1.7	12.3	0.05	100.6
Azu 2	31		0.01	28.0	2.0	0.21	0.08	55.0	1.7	12.8	0.06	99.7
Azu 2	36		0.01	29.2	1.6	0.27	0.17	56.4	1.4	11.9	0.15	101.1
Azu 3	2		0.03	29.3	1.3	0.28	0.21	57.1	1.5	12.1	0.18	101.9
Azu 3	5		0.04	27.2	3.5	0.18	0.07	54.5	1.4	12.8	0.26	99.9
Azu 3	6		0.02	29.0	1.3	0.28	0.05	56.4	1.5	12.1	0.24	100.8
Azu 3	9		0.04	28.5	2.5	0.20	0.08	55.2	1.4	12.0	0.44	100.4
Azu 3	15		0.02	30.0	2.5	0.16	0.09	55.3	1.2	10.2	0.61	100.1
Azu 3	19		0.04	28.9	2.2	0.30	0.19	55.8	1.3	12.0	0.27	101.0
Azu 4	1		0.02	28.5	2.5	0.26	0.20	55.6	1.3	12.0	0.51	100.9
Azu 4	3		0.03	28.5	2.3	0.29	0.26	55.9	1.9	11.8	0.34	101.4
Azu 4	5		0.02	28.6	2.4	0.24	0.13	55.7	1.3	12.0	0.49	101.0
Azu 4	8		0.01	28.8	1.9	0.17	0.12	55.5	1.4	11.6	0.52	100.0
Azu 4	2		0.03	29.3	1.6	0.20	0.27	55.4	1.4	11.7	0.34	100.2
Azu 4	4		0.05	28.9	2.5	0.22	0.22	55.2	1.2	11.3	0.62	100.3
Azu 4	6		0.05	29.6	1.7	0.23	0.12	55.8	1.3	11.3	0.54	100.6
Azu 1	5		0.33	15.0	5.2	0.19	1.11	48.5	20.0	9.0	0.11	99.4
Azu 1	13		0.24	17.3	2.3	0.20	0.34	52.6	18.7	8.8	0.14	100.6
Azu 1	16		0.33	15.1	4.8	0.10	0.91	49.6	19.9	8.7	0.19	99.5

Azu 1	20	0.30	15.2	4.5	0.16	1.04	50.0	20.1	8.8	0.35	100.4
Azu 2	24	0.30	16.5	4.0	0.23	0.84	52.0	19.2	7.8	0.40	101.2
Azu 2	27	0.36	15.2	4.1	0.13	0.58	51.9	22.2	6.8	0.48	101.8
Azu 2	29	0.29	16.0	2.1	0.25	0.64	53.2	21.6	7.2	0.07	101.4
Azu 2	34	0.30	16.0	2.6	0.21	0.58	52.3	21.5	6.9	0.22	100.4
Azu 3	21	0.26	16.0	2.6	0.20	0.47	53.5	21.8	7.1	0.16	102.0
Azu 3	22	0.36	14.6	4.0	0.18	0.72	51.7	21.9	8.0	0.10	101.5
Azu 3	23	0.20	16.9	2.2	0.15	0.45	53.7	20.3	7.5	0.16	101.6
Azu 3	25	0.36	15.8	3.5	0.18	0.63	52.6	21.2	7.4	0.38	102.0
Azu 3	29	0.20	18.2	2.1	0.20	0.36	54.0	17.5	8.8	0.02	101.3
Azu 3	30	0.35	14.8	5.7	0.18	1.43	49.9	20.1	8.6	0.14	101.2
Azu 3	32	0.33	14.3	5.2	0.09	1.14	49.8	21.1	8.4	0.10	100.4
Azu 7 EN	2	0.02	27.8	2.9	0.23	0.25	54.4	1.3	13.1	0.30	100.2
Azu 7 EN	3	0.04	28.5	2.5	0.18	0.25	54.6	1.3	12.0	0.52	99.9
Azu 7 EN	5	0.04	28.0	3.0	0.19	0.21	54.8	1.3	12.4	0.47	100.4
Azu 7 EN	8	0.05	29.8	1.9	0.29	0.06	55.4	1.4	10.7	0.35	99.9
Azu 7 EN	11	0.08	28.6	1.5	0.27	0.20	55.1	1.5	11.7	0.21	99.1
Azu 7 EN	13	0.06	28.2	1.7	0.23	0.15	55.1	1.4	12.2	0.37	99.3
Azu 10 EN	2	0.04	28.2	1.7	0.27	0.20	55.1	1.3	12.5	0.19	99.5
Azu 10 EN	3	0.03	28.2	2.1	0.29	0.09	54.8	1.3	12.8	0.06	99.6
Azu 4 EN	12	0.01	29.3	2.5	0.25	0.14	55.5	1.3	11.2	0.62	100.9
Azu 4 EN	13	0.02	29.1	2.8	0.19	0.22	55.1	1.2	11.3	0.64	100.5
Azu 4 EN	14	0.01	29.1	1.9	0.28	0.19	55.8	1.3	11.8	0.13	100.4



apfu												
Sample	Point	Na	Mg	Al	Mn	Ti	Si	Ca	Fe2+	Fe+3	Cr	Total
Azu 1	3	0.00	1.5	0.10	0.01	0.01	1.9	0.05	0.35	0.03	0.01	4.0
Azu 1	8	0.00	1.5	0.09	0.01	0.00	1.9	0.05	0.35	0.01	0.01	4.0
Azu 1	10	0.00	1.5	0.12	0.01	0.01	1.9	0.05	0.34	0.03	0.02	4.0
Azu 2	10	0.00	1.5	0.08	0.01	0.01	2.0	0.05	0.36	0.00	0.00	4.0
Azu 2	12	0.00	1.5	0.11	0.01	0.01	1.9	0.06	0.34	0.00	0.01	4.0
Azu 2	15	0.00	1.6	0.06	0.00	0.01	2.0	0.05	0.33	0.00	0.01	4.0
Azu 2	18	0.00	1.5	0.09	0.00	0.01	2.0	0.05	0.33	0.00	0.01	4.0
Azu 2	21	0.00	1.5	0.09	0.01	0.01	2.0	0.06	0.33	0.00	0.01	4.0
Azu 2	28	0.00	1.5	0.07	0.01	0.00	2.0	0.06	0.36	0.00	0.00	4.0
Azu 2	31	0.00	1.5	0.08	0.01	0.00	2.0	0.06	0.38	0.00	0.00	4.0
Azu 2	36	0.00	1.5	0.06	0.01	0.00	2.0	0.05	0.35	0.00	0.00	4.0
Azu 3	2	0.00	1.5	0.05	0.01	0.01	2.0	0.06	0.35	0.00	0.00	4.0
Azu 3	5	0.00	1.4	0.15	0.01	0.00	1.9	0.05	0.38	0.00	0.01	4.0
Azu 3	6	0.00	1.5	0.05	0.01	0.00	2.0	0.06	0.36	0.00	0.01	4.0
Azu 3	9	0.00	1.5	0.10	0.01	0.00	2.0	0.05	0.36	0.00	0.01	4.0
Azu 3	15	0.00	1.6	0.10	0.00	0.00	1.9	0.05	0.30	0.00	0.02	4.0
Azu 3	19	0.00	1.5	0.09	0.01	0.00	2.0	0.05	0.35	0.00	0.01	4.0
Azu 4	1	0.00	1.5	0.10	0.01	0.01	2.0	0.05	0.35	0.00	0.01	4.0
Azu 4	3	0.00	1.5	0.10	0.01	0.01	2.0	0.07	0.35	0.00	0.01	4.0
Azu 4	5	0.00	1.5	0.10	0.01	0.00	2.0	0.05	0.35	0.00	0.01	4.0
Azu 4	8	0.00	1.5	0.08	0.01	0.00	2.0	0.05	0.34	0.00	0.01	4.0
Azu 4	2	0.00	1.5	0.07	0.01	0.01	2.0	0.05	0.35	0.00	0.01	4.0
Azu 4	4	0.00	1.5	0.11	0.01	0.01	1.9	0.05	0.33	0.00	0.02	4.0
Azu 4	6	0.00	1.5	0.07	0.01	0.00	2.0	0.05	0.33	0.00	0.02	4.0
Azu 1	5	0.02	0.8	0.23	0.01	0.03	1.8	0.80	0.15	0.13	0.00	4.0
Azu 1	13	0.02	0.9	0.10	0.01	0.01	1.9	0.73	0.22	0.05	0.00	4.0
Azu 1	16	0.02	0.8	0.21	0.00	0.03	1.8	0.79	0.19	0.08	0.01	4.0
Azu 1	20	0.02	0.8	0.19	0.01	0.03	1.8	0.79	0.19	0.08	0.01	4.0
Azu 2	24	0.02	0.9	0.17	0.01	0.02	1.9	0.75	0.22	0.01	0.01	4.0

Azu 2	27	0.03	0.8	0.18	0.00	0.02	1.9	0.86	0.16	0.05	0.01	4.0
Azu 2	29	0.02	0.9	0.09	0.01	0.02	1.9	0.84	0.19	0.03	0.00	4.0
Azu 2	34	0.02	0.9	0.11	0.01	0.02	1.9	0.84	0.17	0.04	0.01	4.0
Azu 3	21	0.02	0.9	0.11	0.01	0.01	1.9	0.84	0.20	0.02	0.00	4.0
Azu 3	22	0.03	0.8	0.17	0.01	0.02	1.9	0.85	0.20	0.04	0.00	4.0
Azu 3	23	0.01	0.9	0.09	0.00	0.01	1.9	0.79	0.23	0.00	0.00	4.0
Azu 3	25	0.03	0.8	0.15	0.01	0.02	1.9	0.82	0.19	0.03	0.01	4.0
Azu 3	29	0.01	1.0	0.09	0.01	0.01	2.0	0.68	0.27	0.00	0.00	4.0
Azu 3	30	0.02	0.8	0.25	0.01	0.04	1.8	0.79	0.22	0.05	0.00	4.0
Azu 3	32	0.02	0.8	0.23	0.00	0.03	1.8	0.83	0.20	0.06	0.00	4.0
Azu 7 EN	2	0.00	1.5	0.12	0.01	0.01	1.9	0.05	0.39	0.00	0.01	4.0
Azu 7 EN	3	0.00	1.5	0.10	0.01	0.01	1.9	0.05	0.36	0.00	0.01	4.0
Azu 7 EN	5	0.00	1.5	0.13	0.01	0.01	1.9	0.05	0.37	0.00	0.01	4.0
Azu 7 EN	8	0.00	1.6	0.08	0.01	0.00	2.0	0.05	0.32	0.00	0.01	4.0
Azu 7 EN	11	0.01	1.5	0.06	0.01	0.01	2.0	0.06	0.35	0.00	0.01	4.0
Azu 7 EN	13	0.00	1.5	0.07	0.01	0.00	2.0	0.05	0.36	0.00	0.01	4.0
Azu 10 EN	2	0.00	1.5	0.07	0.01	0.01	2.0	0.05	0.37	0.00	0.01	4.0
Azu 10 EN	3	0.00	1.5	0.09	0.01	0.00	2.0	0.05	0.38	0.00	0.00	4.0
Azu 4 EN	12	0.00	1.5	0.10	0.01	0.00	1.9	0.05	0.33	0.00	0.02	4.0
Azu 4 EN	13	0.00	1.5	0.11	0.01	0.01	1.9	0.05	0.33	0.00	0.02	4.0
Azu 4 EN	14	0.00	1.5	0.08	0.01	0.01	2.0	0.05	0.35	0.00	0.00	4.0

---

Sample	Point	FeO(wt%) corrected	Fe2O3(wt%) calculated	Total(wt%) corrected	Mg#	Wo	En	Fe	Total
Azu 1	3	11.7	1.12	100.5	0.81	2.8	79.1	18.1	100.0
Azu 1	8	11.8	0.41	99.7	0.81	2.6	79.2	18.2	100.0
Azu 1	10	11.4	1.23	99.6	0.82	2.7	79.4	17.9	100.0
Azu 2	10	12.3	0.00	101.1	0.81	2.9	78.4	18.8	100.0
Azu 2	12	11.6	0.00	100.2	0.81	3.1	78.9	18.0	100.0
Azu 2	15	11.1	0.00	100.0	0.83	2.8	80.3	17.0	100.0
Azu 2	18	11.2	0.00	100.9	0.82	2.6	80.3	17.1	100.0
Azu 2	21	11.3	0.00	100.4	0.82	2.9	79.5	17.6	100.0
Azu 2	28	12.3	0.00	100.6	0.81	3.3	78.1	18.6	100.0
Azu 2	31	12.8	0.00	99.7	0.80	3.3	77.0	19.7	100.0
Azu 2	36	11.9	0.00	101.1	0.81	2.8	79.1	18.1	100.0
Azu 3	2	12.1	0.00	101.9	0.81	2.9	78.9	18.2	100.0
Azu 3	5	12.8	0.00	99.9	0.79	2.8	76.9	20.3	100.0
Azu 3	6	12.1	0.00	100.8	0.81	2.9	78.6	18.5	100.0
Azu 3	9	12.0	0.00	100.4	0.81	2.8	78.6	18.6	100.0
Azu 3	15	10.2	0.00	100.1	0.84	2.4	81.9	15.7	100.0
Azu 3	19	12.0	0.00	101.0	0.81	2.5	79.1	18.5	100.0
Azu 4	1	12.0	0.00	100.9	0.81	2.7	78.7	18.6	100.0
Azu 4	3	11.8	0.00	101.4	0.81	3.8	78.0	18.2	100.0
Azu 4	5	12.0	0.00	101.0	0.81	2.6	78.8	18.6	100.0
Azu 4	8	11.6	0.00	100.0	0.82	2.7	79.4	17.9	100.0
Azu 4	2	11.7	0.00	100.2	0.82	2.8	79.5	17.7	100.0
Azu 4	4	11.3	0.00	100.3	0.82	2.4	80.1	17.5	100.0
Azu 4	6	11.3	0.00	100.6	0.82	2.5	80.3	17.2	100.0
Azu 1	5	4.9	4.62	99.8	0.85	44.7	46.7	8.5	100.0
Azu 1	13	7.1	1.80	100.8	0.81	38.7	49.8	11.5	100.0
Azu 1	16	6.2	2.81	99.8	0.81	43.5	46.0	10.5	100.0
Azu 1	20	6.3	2.81	100.7	0.81	43.5	45.8	10.6	100.0
Azu 2	24	7.4	0.47	101.3	0.80	40.0	48.0	12.0	100.0
Azu 2	27	5.2	1.68	102.0	0.84	46.7	44.7	8.6	100.0

Azu 2	29	6.4	0.93	101.5	0.82	44.2	45.6	10.2	100.0
Azu 2	34	5.5	1.60	100.6	0.84	44.8	46.3	8.9	100.0
Azu 3	21	6.5	0.66	102.1	0.81	44.4	45.3	10.3	100.0
Azu 3	22	6.6	1.59	101.7	0.80	46.3	42.9	10.8	100.0
Azu 3	23	7.5	0.00	101.6	0.80	40.9	47.3	11.8	100.0
Azu 3	25	6.4	1.15	102.1	0.82	44.1	45.6	10.3	100.0
Azu 3	29	8.8	0.00	101.3	0.79	35.2	51.0	13.8	100.0
Azu 3	30	7.1	1.74	101.4	0.79	43.5	44.6	12.0	100.0
Azu 3	32	6.4	2.32	100.7	0.80	45.9	43.3	10.8	100.0
Azu 7 EN	2	13.1	0.00	100.2	0.79	2.6	77.1	20.3	100.0
Azu 7 EN	3	12.0	0.00	99.9	0.81	2.6	78.7	18.7	100.0
Azu 7 EN	5	12.4	0.00	100.4	0.80	2.7	78.0	19.3	100.0
Azu 7 EN	8	10.7	0.00	99.9	0.83	2.7	81.0	16.3	100.0
Azu 7 EN	11	11.7	0.00	99.1	0.81	2.9	79.0	18.1	100.0
Azu 7 EN	13	12.2	0.00	99.3	0.80	2.7	78.3	19.0	100.0
Azu 10 EN	2	12.5	0.00	99.5	0.80	2.5	78.0	19.4	100.0
Azu 10 EN	3	12.8	0.00	99.6	0.80	2.6	77.7	19.7	100.0
Azu 4 EN	12	11.2	0.00	100.9	0.82	2.5	80.3	17.2	100.0
Azu 4 EN	13	11.3	0.00	100.5	0.82	2.4	80.2	17.4	100.0
Azu 4 EN	14	11.8	0.00	100.4	0.82	2.6	79.4	18.0	100.0

## Mg-poor cores

Sample	Point	Comment	wt%									Total
			Na2O	MgO	Al2O3	MnO	TiO2	SiO2	CaO	FeO	Cr2O3	
Azu 1	7		0.05	25.2	7.3	0.31	0.45	50.3	1.4	15.4	0.03	100.4
Azu 2	14		0.02	25.3	3.2	0.36	0.63	52.8	1.4	16.1	0.01	99.8
Azu 2	17		0.05	24.8	2.9	0.40	0.49	53.9	1.5	17.0	0.01	100.9
Azu 2	20		0.01	25.7	2.5	0.43	0.29	53.6	1.3	16.1	0.03	100.0
Azu 2	30		0.02	23.0	2.1	0.50	0.29	52.6	1.4	19.9	0.01	99.8
Azu 2	32		0.01	23.3	2.4	0.76	0.34	52.7	1.5	18.6	0.02	99.6
Azu 2	35		0.03	25.1	2.3	0.32	0.28	53.7	1.5	16.8	0.03	100.0
Azu 3	1		0.03	27.5	2.0	0.36	0.01	55.8	1.3	13.7	0.24	100.9
Azu 3	18		0.04	26.6	2.5	0.25	0.09	54.1	1.3	15.1	0.05	100.1
Azu 4	7		0.04	24.4	4.5	0.29	0.37	52.1	1.3	17.0	0.06	100.1
Azu 4	1		0.04	24.9	3.3	0.76	0.26	52.4	0.4	16.9	0.11	99.1
Azu 2	23		0.31	13.7	2.7	0.39	0.49	52.2	21.3	10.0	0.00	101.1
Azu 2	26		0.29	14.7	1.6	0.37	0.24	53.1	20.5	10.3	0.00	101.1
Azu 2	33		0.41	13.4	3.7	0.44	1.00	50.3	20.7	10.7	0.00	100.6
Azu 7 EN	1		0.01	25.3	1.9	0.70	0.00	54.2	0.7	17.0	0.00	99.7
Azu 7 EN	7		0.06	24.7	3.0	0.58	0.20	52.3	1.2	17.1	0.04	99.2
Azu 7 EN	10		0.06	26.1	1.9	0.34	0.21	54.1	1.6	15.0	0.05	99.4
Azu 10 EN	4		0.01	24.1	1.4	0.42	0.00	54.2	0.8	18.6	0.05	99.6

apfu												
Sample	Point	Na	Mg	Al	Mn	Ti	Si	Ca	Fe2+	Fe+3	Cr	Total
Azu 1	7	0.00	1.3	0.31	0.01	0.01	1.8	0.05	0.40	0.07	0.00	4.0
Azu 2	14	0.00	1.4	0.14	0.01	0.02	1.9	0.05	0.49	0.00	0.00	4.0
Azu 2	17	0.00	1.3	0.12	0.01	0.01	1.9	0.06	0.51	0.00	0.00	4.0
Azu 2	20	0.00	1.4	0.11	0.01	0.01	1.9	0.05	0.49	0.00	0.00	4.0
Azu 2	30	0.00	1.3	0.09	0.02	0.01	1.9	0.05	0.61	0.00	0.00	4.0
Azu 2	32	0.00	1.3	0.10	0.02	0.01	1.9	0.06	0.57	0.00	0.00	4.0
Azu 2	35	0.00	1.4	0.10	0.01	0.01	2.0	0.06	0.51	0.00	0.00	4.0
Azu 3	1	0.00	1.4	0.08	0.01	0.00	2.0	0.05	0.41	0.00	0.01	4.0
Azu 3	18	0.00	1.4	0.11	0.01	0.00	1.9	0.05	0.45	0.00	0.00	4.0
Azu 4	7	0.00	1.3	0.19	0.01	0.01	1.9	0.05	0.52	0.00	0.00	4.0
Azu 4	1	0.00	1.4	0.14	0.02	0.01	1.9	0.02	0.52	0.00	0.00	4.0
Azu 2	23	0.02	0.8	0.12	0.01	0.01	1.9	0.84	0.29	0.02	0.00	4.0
Azu 2	26	0.02	0.8	0.07	0.01	0.01	2.0	0.81	0.29	0.02	0.00	4.0
Azu 2	33	0.03	0.7	0.16	0.01	0.03	1.9	0.82	0.26	0.07	0.00	4.0
Azu 7 EN	1	0.00	1.4	0.08	0.02	0.00	2.0	0.03	0.52	0.00	0.00	4.0
Azu 7 EN	7	0.00	1.4	0.13	0.02	0.01	1.9	0.05	0.50	0.02	0.00	4.0
Azu 7 EN	10	0.00	1.4	0.08	0.01	0.01	2.0	0.06	0.46	0.00	0.00	4.0
Azu 10 EN	4	0.00	1.3	0.06	0.01	0.00	2.0	0.03	0.57	0.00	0.00	4.0

Sample	Point	FeO(wt%) corrected	Fe2O3(wt%) calculated	Total(wt%) corrected	Mg#	Wo	En	Fe	Total
Azu 1	7	13.2	2.43	100.7	0.77	3.0	75.0	22.0	100.0
Azu 2	14	16.1	0.00	99.8	0.74	2.8	71.5	25.6	100.0
Azu 2	17	17.0	0.00	100.9	0.72	3.0	70.0	26.9	100.0
Azu 2	20	16.1	0.00	100.0	0.74	2.7	72.1	25.3	100.0
Azu 2	30	19.9	0.09	99.8	0.67	2.8	65.5	31.8	100.0
Azu 2	32	18.6	0.00	99.6	0.69	3.0	67.0	30.0	100.0
Azu 2	35	16.8	0.00	100.0	0.73	2.9	70.5	26.5	100.0
Azu 3	1	13.7	0.00	100.9	0.78	2.6	76.1	21.3	100.0
Azu 3	18	15.1	0.00	100.1	0.76	2.6	73.9	23.5	100.0
Azu 4	7	17.0	0.00	100.1	0.72	2.7	69.9	27.4	100.0
Azu 4	1	16.9	0.00	99.1	0.73	0.9	71.8	27.2	100.0
Azu 2	23	9.4	0.75	101.1	0.72	44.7	39.9	15.4	100.0
Azu 2	26	9.5	0.80	101.1	0.73	42.4	42.2	15.4	100.0
Azu 2	33	8.4	2.54	100.8	0.74	45.1	40.6	14.3	100.0
Azu 7 EN	1	17.0	0.00	99.7	0.73	1.4	71.6	27.0	100.0
Azu 7 EN	7	16.3	0.89	99.3	0.73	2.5	71.1	26.4	100.0
Azu 7 EN	10	15.0	0.00	99.4	0.76	3.1	73.2	23.7	100.0
Azu 10 EN	4	18.6	0.00	99.6	0.70	1.6	68.7	29.7	100.0

### Mg-rich Opx patches in Mg-rich rims of Cpx

			wt%									
Sample	Point	Comment	Na2O	MgO	Al2O3	MnO	TiO2	SiO2	CaO	FeO	Cr2O3	Total
Azu 1	6		0.00	26.5	3.1	0.27	0.40	52.3	1.5	14.5	0.02	98.7
Azu 1	11		0.02	28.0	1.7	0.26	0.13	54.8	2.4	12.5	0.32	100.1
Azu 1	17		0.04	27.0	3.6	0.38	0.22	52.5	2.0	13.5	0.31	99.6
Azu 1	19		0.04	27.2	2.1	0.28	0.25	54.3	2.3	13.0	0.14	99.6
Azu 2	25		0.02	27.8	3.2	0.26	0.26	54.9	2.0	12.1	0.35	100.9
Azu 3	20		0.01	27.5	1.6	0.26	0.02	55.7	1.6	13.3	0.03	100.0
Azu 3	24		0.03	27.2	2.7	0.31	0.29	55.2	1.7	13.4	0.15	101.0
Azu 3	28		0.03	27.2	3.4	0.28	0.36	53.8	1.9	13.1	0.21	100.3
Azu 3	31		0.02	27.7	1.2	0.25	0.07	55.8	1.8	13.3	0.06	100.2

			apfu									
Sample	Point	Na	Mg	Al	Mn	Ti	Si	Ca	Fe2+	Fe+3	Cr	Total
Azu 1	6	0.00	1.4	0.13	0.01	0.01	1.9	0.06	0.41	0.03	0.00	4.0
Azu 1	11	0.00	1.5	0.07	0.01	0.00	2.0	0.09	0.36	0.01	0.01	4.0
Azu 1	17	0.00	1.4	0.15	0.01	0.01	1.9	0.08	0.36	0.05	0.01	4.0
Azu 1	19	0.00	1.5	0.09	0.01	0.01	2.0	0.09	0.39	0.00	0.00	4.0
Azu 2	25	0.00	1.5	0.13	0.01	0.01	1.9	0.08	0.36	0.00	0.01	4.0
Azu 3	20	0.00	1.5	0.07	0.01	0.00	2.0	0.06	0.40	0.00	0.00	4.0
Azu 3	24	0.00	1.4	0.11	0.01	0.01	2.0	0.06	0.40	0.00	0.00	4.0
Azu 3	28	0.00	1.4	0.14	0.01	0.01	1.9	0.07	0.39	0.00	0.01	4.0
Azu 3	31	0.00	1.5	0.05	0.01	0.00	2.0	0.07	0.40	0.00	0.00	4.0



Sample	Point	FeO(wt%) corrected	Fe <sub>2</sub> O <sub>3</sub> (wt%) calculated	Total(wt%) corrected	Mg#	Wo	En	Fe	Total
Azu 1	6	13.4	1.22	98.8	0.78	3.1	75.5	21.3	100.0
Azu 1	11	12.2	0.26	100.2	0.88	4.8	76.5	18.7	100.0
Azu 1	17	11.8	1.84	99.8	0.80	4.2	76.9	18.9	100.0
Azu 1	19	13.0	0.00	99.6	0.79	4.6	75.2	20.2	100.0
Azu 2	25	12.1	0.00	100.9	0.80	4.0	77.2	18.8	100.0
Azu 3	20	13.3	0.00	100.0	0.79	3.1	76.2	20.7	100.0
Azu 3	24	13.4	0.00	101.0	0.78	3.4	75.6	21.0	100.0
Azu 3	28	13.1	0.00	100.3	0.79	3.8	75.7	20.5	100.0
Azu 3	31	13.3	0.00	100.2	0.79	3.5	76.1	20.4	100.0

## Fe-Ti oxides

### Paired Fe-Ti oxides microlites

Sample	Point	Comment	wt%											
			MgO	Al2O3	SiO2	TiO2	V2O3	Cr2O3	FeO	CaO	ZnO	NiO	MnO	Total
Azu 2	3		2.4	1.0	3.61	41.8	0.47	0.00	48.6	0.39	0.00	0.03	0.56	98.9
Azu 2	4		1.0	1.5	0.12	8.0	0.68	0.00	81.5	0.06	0.17	0.00	0.38	93.4
Azu 2	6		1.0	1.9	0.12	6.0	0.73	0.13	82.1	0.06	0.17	0.01	0.38	92.6
Azu 2	7		2.1	0.2	0.19	40.5	0.60	0.09	54.2	0.08	0.11	0.00	0.54	98.7
Azu 2	8		1.1	1.8	0.15	7.0	0.67	0.00	82.2	0.05	0.27	0.03	0.46	93.7
Azu 2	15		2.2	0.1	0.11	46.4	0.52	0.07	48.7	0.06	0.09	0.00	0.71	98.9
Azu 2	16		1.0	1.7	0.15	7.5	0.79	0.00	82.2	0.06	0.16	0.00	0.46	93.9
Azu 8 EN	1		1.4	1.7	0.21	11.4	0.67	0.00	79.0	0.08	0.06	0.04	0.47	95.1
Azu 8 EN	2		2.7	0.2	0.13	45.9	0.60	0.09	48.6	0.17	0.02	0.03	0.59	99.0
Azu 8 EN	3		1.4	1.6	0.25	11.4	0.57	0.04	79.8	0.07	0.11	0.00	0.55	95.8

apfu														
Sample	Point	Mg	Al	Si	Ti	V	Cr	Fe2+	Fe3+	Ca	Zn	Ni	Mn	Total
Azu 2	3	0.09	0.03	0.09	0.77	0.01	0.00	0.75	0.25	0.01		0.00	0.01	2.0
Azu 2	4	0.06	0.07	0.00	0.23	0.02	0.00	1.16	1.44	0.00	0.00	0.00	0.01	3.0
Azu 2	6	0.06	0.08	0.00	0.17	0.02	0.00	1.10	1.54	0.00	0.00	0.00	0.01	3.0
Azu 2	7	0.08	0.01	0.00	0.76	0.01	0.00	0.67	0.46	0.00	0.00	0.00	0.01	2.0
Azu 2	8	0.06	0.08	0.01	0.20	0.02	0.00	1.12	1.49	0.00	0.01	0.00	0.01	3.0
Azu 2	15	0.08	0.00	0.00	0.87	0.01	0.00	0.77	0.24	0.00	0.00	0.00	0.01	2.0
Azu 2	16	0.06	0.08	0.01	0.21	0.02	0.00	1.14	1.46	0.00	0.00	0.00	0.01	3.0
Azu 8 EN	1	0.08	0.07	0.01	0.32	0.02	0.00	1.23	1.25	0.00	0.00	0.00	0.02	3.0
Azu 8 EN	2	0.10	0.01	0.00	0.85	0.01	0.00	0.74	0.27	0.00	0.00	0.00	0.01	2.0
Azu 8 EN	3	0.08	0.07	0.01	0.32	0.02	0.00	1.22	1.26	0.00	0.00	0.00	0.02	3.0

Sample	Point	FeO(wt%) corrected	Fe2O3(wt%) calculated	Total(wt%) corrected
Azu 2	3	36.5	13.5	100.3
Azu 2	4	36.2	50.3	98.4
Azu 2	6	34.2	53.2	97.9
Azu 2	7	32.2	24.5	101.1
Azu 2	8	35.2	52.3	98.9
Azu 2	15	37.1	12.8	100.2
Azu 2	16	36.0	51.3	99.1
Azu 8 EN	1	39.1	44.3	99.5
Azu 8 EN	2	35.8	14.3	100.5
Azu 8 EN	3	39.3	44.9	100.3

Sample	Point	Mol			TiO2 norm	FeO norm	Fe2O3 norm	Total	X'Usp	X'Illm	XTi
		TiO2	FeO	Fe2O3							
Azu 2	3	0.52	0.51	0.08	46.9	45.5	7.6	100.0		0.86	
Azu 2	4	0.10	0.50	0.31	10.9	54.9	34.3	100.0	0.24		0.10
Azu 2	6	0.07	0.48	0.33	8.5	53.9	37.7	100.0	0.18		0.08
Azu 2	7	0.51	0.45	0.15	45.8	40.4	13.8	100.0		0.76	
Azu 2	8	0.09	0.49	0.33	9.6	54.1	36.2	100.0	0.21		0.09
Azu 2	15	0.58	0.52	0.08	49.3	43.9	6.8	100.0		0.87	
Azu 2	16	0.09	0.50	0.32	10.2	54.7	35.1	100.0	0.22		0.10
Azu 8 EN	1	0.14	0.54	0.28	14.7	56.5	28.8	100.0	0.34		0.14
Azu 8 EN	2	0.57	0.50	0.09	49.4	42.9	7.7	100.0		0.86	
Azu 8 EN	3	0.14	0.55	0.28	14.6	56.4	29.0	100.0	0.33		0.14

## Olivine

			wt%									
Sample	Point	Comment	MgO	Al2O3	SiO2	MnO	TiO2	FeO	CaO	Cr2O3	NiO	Total
Azu 1	1	core	44.4	0.00	39.8	0.20	0.00	17.6	0.12	0.02	0.08	102.2
Azu 1	2	core	42.6	0.03	39.0	0.41	0.02	19.5	0.13	0.06	0.09	101.9
Azu 2	1	core	44.5	0.00	39.6	0.25	0.00	15.7	0.10	0.06	0.14	100.4
Azu 2	1	rim	39.2	0.05	38.2	0.43	0.07	22.1	0.11	0.00	0.05	100.2
Azu 3	1	core	42.1	0.00	38.8	0.27	0.02	18.9	0.12	0.04	0.06	100.4
Azu 3	2	core	44.8	0.01	39.2	0.24	0.05	15.8	0.12	0.04	0.18	100.4
Azu 3	3	rim	39.6	0.01	38.4	0.56	0.03	21.8	0.10	0.05	0.17	100.6
Azu 3	4	core	41.9	0.04	38.6	0.29	0.10	19.1	0.11	0.14	0.14	100.3
Azu 10 EN	1	core	41.3	0.01	38.1	0.32	0.03	19.4	0.13	0.00	0.02	99.3

			apfu									
Sample	Point	Mg	Al	Si	Mn	Ti	Fe2+	Fe3+	Ca	Cr	Ni	Total
Azu 1	1	1.6	0.00	1.0	0.00	0.00	0.34	0.03	0.00	0.00	0.00	3.0
Azu 1	2	1.6	0.00	1.0	0.01	0.00	0.37	0.04	0.00	0.00	0.00	3.0
Azu 2	1	1.7	0.00	1.0	0.01	0.00	0.32	0.01	0.00	0.00	0.00	3.0
Azu 2	1	1.5	0.00	1.0	0.01	0.00	0.46	0.02	0.00	0.00	0.00	3.0
Azu 3	1	1.6	0.00	1.0	0.01	0.00	0.38	0.02	0.00	0.00	0.00	3.0
Azu 3	2	1.7	0.00	1.0	0.01	0.00	0.30	0.03	0.00	0.00	0.00	3.0
Azu 3	3	1.5	0.00	1.0	0.01	0.00	0.45	0.02	0.00	0.00	0.00	3.0
Azu 3	4	1.6	0.00	1.0	0.01	0.00	0.38	0.03	0.00	0.00	0.00	3.0
Azu 10 EN	1	1.6	0.00	1.0	0.01	0.00	0.39	0.03	0.00	0.00	0.00	3.0

Sample	Point	FeO(wt%) corrected	Fe2O3(wt%) calculated	Total(wt%) corrected	Fo (#Mg)	Fa	Total
Azu 1	1	16.3	1.4	102.4	83.0	17.0	100.0
Azu 1	2	17.7	2.0	102.1	81.1	18.9	100.0
Azu 2	1	15.1	0.6	100.4	84.0	16.0	100.0
Azu 2	1	21.3	0.8	100.3	76.6	23.4	100.0
Azu 3	1	17.9	1.1	100.5	80.7	19.3	100.0
Azu 3	2	14.2	1.7	100.6	84.9	15.1	100.0
Azu 3	3	20.8	1.0	100.7	77.2	22.8	100.0
Azu 3	4	17.9	1.3	100.5	80.7	19.3	100.0
Azu 10 EN	1	18.0	1.6	99.5	80.4	19.6	100.0

## Standards

Internal standards			
Ideal formula	Phase	Standard code	Type locality
NaAlSi <sub>3</sub> O <sub>8</sub>	Albite	LAMARX standard	Palermo #1 mine, New Hampshire, USA
CaAl <sub>2</sub> Si <sub>2</sub> O <sub>8</sub>	Anorthite	NMNH 137041	Great Sitkin Island, Alaska, USA
(NaK)AlSi <sub>3</sub> O <sub>8</sub>	Anorthoclase	NMNH 133868	Kakanui, New Zealand
BaSO <sub>4</sub>	Baryte	LAMARX standard	Unknown locality
SrSO <sub>4</sub>	Celestine	LAMARX standard	Manjaka, Madagascar
FeCr <sub>2</sub> O <sub>4</sub>	Chromite	USGS OXBU	Bushveld, South Africa
Fe <sub>2</sub> SiO <sub>4</sub>	Fayalite	NMNH 85276	Rockport, Massachusetts, USA
Mg <sub>2</sub> SiO <sub>4</sub>	Forsterite	NMNH 111312-44	San Carlos, Arizona, USA
Fe <sub>2</sub> O <sub>3</sub>	Hematite	LAMARX standard	Payún Matrú volcano, Mendoza, Argentina
FeTiO <sub>3</sub>	Ilmenite	NMNH 96189	Ilmen Mountains, Miask, Russian
Cu <sub>2</sub> PO <sub>4</sub> OH	Libethenite	LAMARX standard	Vila Viçosa, Portugal
MgO	MgO (synthetic)	LAMARX standard	Synthetic, University of New Orleans, USA
NiAs	Nickeline	LAMARX standard	Copper Pass Deposit, Great Slave Lake, Northwestern Territories, Canada
KAlSi <sub>3</sub> O <sub>8</sub>	Orthoclase	USGS FSBO	Benson Mines, St. Lawrence County, New York, USA
MnO <sub>2</sub>	Pyrolusite	LAMARX standard	Unknown locality
ScVO <sub>4</sub>	ScVO <sub>4</sub> (synthetic)	LAMARX standard	Synthetic, University of New Orleans, USA
Na <sub>4</sub> (Si <sub>3</sub> Al <sub>3</sub> O <sub>6</sub> ) <sub>2</sub> Cl	Sodalite	LAMARX standard	Brazil
Ti	Ti	LAMARX standard	Synthetic, University of Córdoba, Argentina
CaTiSiO <sub>5</sub>	Titanite	USGS SPHC	Hemet Quadrangle, California USA
Al <sub>2</sub> SiO <sub>4</sub> (OH,F) <sub>2</sub>	Topaz	USGS TPTM	Topaz Mountain, Utah, USA
CaSiO <sub>3</sub>	Wollastonite	USGS PXWO	Mammoth Lakes, Mono County, California
ZnO	ZnO (synthetic)	LAMARX standard	Synthetic, University of New Orleans, USA
ZrO <sub>2</sub>	ZrO <sub>2</sub> (synthetic)	LAMARX standard	Synthetic, University of Córdoba, Argentina

External standards									
Standard composition (wt.%)									
Phase	Standard code	P <sub>2</sub> O <sub>5</sub>	nB <sub>2</sub> O <sub>5</sub>	SiO <sub>2</sub>	TiO <sub>2</sub>	Al <sub>2</sub> O <sub>3</sub>	Cr <sub>2</sub> O <sub>3</sub>	Fe <sub>2</sub> O <sub>3</sub>	FeO
Olivine	NMNH 111312-44	0,0		40,8					9,6
Plagioclase	NMNH 115900			51,3	0,1	30,9		0,3	0,2
Clinopyroxene	AS1150-AB			55,4	0,1	0,1			0,1
Amphibola	NMNH 111356	<0,01		41,5	1,4	15,5		5,6	6,4
Ilmenite	NMNH 96189		0,9		45,7			11,6	36,1
Chromite	NMNH 117075					9,9	60,5		13,0
Measured composition (wt.%)									
Phase	Standard code	P <sub>2</sub> O <sub>5</sub>	nB <sub>2</sub> O <sub>5</sub>	SiO <sub>2</sub>	TiO <sub>2</sub>	Al <sub>2</sub> O <sub>3</sub>	Cr <sub>2</sub> O <sub>3</sub>	Fe <sub>2</sub> O <sub>3</sub>	FeO
Olivine	NMNH 111312-44			40,0					
Plagioclase	NMNH 115900			51,7	0,1	30,5			
Clinopyroxene	AS1150-AB			55,5		0,1			
Amphibola	NMNH 111356			41,9	1,4	15,3			
Ilmenite	NMNH 96189				46,5				
Chromite	NMNH 117075					10,0	61,0		
Uncertainty (relative wt.%)									
Phase	Standard code	P <sub>2</sub> O <sub>5</sub>	nB <sub>2</sub> O <sub>5</sub>	SiO <sub>2</sub>	TiO <sub>2</sub>	Al <sub>2</sub> O <sub>3</sub>	Cr <sub>2</sub> O <sub>3</sub>	Fe <sub>2</sub> O <sub>3</sub>	FeO
Olivine	NMNH 111312-44			1,9					
Plagioclase	NMNH 115900			0,9	15,0	1,2			
Clinopyroxene	AS1150-AB			0,2		1,0			
Amphibola	NMNH 111356			1,1	1,9	1,7			
Ilmenite	NMNH 96189				1,8				
Chromite	NMNH 117075					1,2	0,8		



External standards

Phase	Standard code	Standard composition (wt.%)								
		FeO <sub>T</sub>	MgO	MnO	NiO	CaO	Na <sub>2</sub> O	K <sub>2</sub> O	H <sub>2</sub> O	Total
Olivine	NMNH 111312-44	9,6	49,4	0,1	0,4	<0,05				100,3
Plagioclase	NMNH 115900	0,5	0,1	0,0		13,6	3,5	0,2	0,1	100,2
Clinopyroxene	AS1150-AB	0,1	18,6	0,1		25,7				100,0
Amphibola	NMNH 111356	11,5	14,2	0,2		11,6	1,9	0,2	1,2	99,1
Ilmenite	NMNH 96189	46,5	0,3	4,8						99,4
Chromite	NMNH 117075	13,0	15,2	0,1						98,8

Phase	Standard code	Measured composition (wt.%)								
		FeO <sub>T</sub>	MgO	MnO	NiO	CaO	Na <sub>2</sub> O	K <sub>2</sub> O	H <sub>2</sub> O	Total
Olivine	NMNH 111312-44	9,6	50,4	0,1	0,4					100,6
Plagioclase	NMNH 115900	0,5	0,2			13,8	3,5	0,2		100,4
Clinopyroxene	AS1150-AB		18,7	0,1		25,8				100,3
Amphibola	NMNH 111356	11,5	14,0	0,1		11,4	1,9	0,2		97,9
Ilmenite	NMNH 96189	47,1	0,3	5,1						99,1
Chromite	NMNH 117075	13,2	15,6	0,1						99,9

Phase	Standard code	Uncertainty (relative wt.%)							
		FeO <sub>T</sub>	MgO	MnO	NiO	CaO	Na <sub>2</sub> O	K <sub>2</sub> O	H <sub>2</sub> O
Olivine	NMNH 111312-44	0,3	1,9	3,5	5,1				
Plagioclase	NMNH 115900	12,0	18,0			1,0	0,3	3,6	
Clinopyroxene	AS1150-AB		0,4	2,0		0,3			
Amphibola	NMNH 111356	0,6	1,5	2,4		1,4	1,6	2,3	
Ilmenite	NMNH 96189	1,3	2,6	6,6					
Chromite	NMNH 117075	0,9	2,6	18,0					

## 5.5. P-T- felsic melt composition-fO2- Solubility calculations

### Pressure calculations (kbar)

#### Amphibole

Amp	Sample	Point	Ridolfi et al., 2010	Ridolfi et al., 2010 (error $\pm 11\%$ )	Ridolfi and Renzulli, 2012 (error $\pm 0.43$ )	Mutch et al., 2016	Mutch et al., 2016 (error $\pm 16\%$ )
Phenocrysts and inclusion in Plg	Azu 1	1	0.95	0.1	1.0	2.1	0.3
	Azu 1	2	1.30	0.1	1.3	2.7	0.4
	Azu 1	3	1.38	0.2	1.4	2.8	0.5
	Azu 1	4	1.14	0.1	1.1	2.4	0.4
	Azu 1	5	0.88	0.1	1.0	2.0	0.3
	Azu 1	6	1.24	0.1	1.3	2.6	0.4
	Azu 1	7	1.31	0.1	1.4	2.7	0.4
	Azu 1	9	1.61	0.2	1.5	3.2	0.5
	Azu 1	10	1.24	0.1	1.3	2.6	0.4
	Azu 4	1	1.14	0.1	1.2	2.4	0.4
	Azu 4	2	1.72	0.2	1.7	3.3	0.5
	Azu 4	3	1.10	0.1	1.1	2.4	0.4
	Azu 4	5	1.31	0.1	1.3	2.7	0.4
	Azu 4	9	1.32	0.1	1.3	2.7	0.4
	Azu 4	11	1.01	0.1	1.0	2.2	0.4
	Azu 4	12	1.32	0.1	1.4	2.7	0.4

## Amphibole-plagioclase

Amp	Sample	Point	Plg	Sample	Point	Anderson and Smith, 1995 Holland and Blundy, 1994 eq. B (error $\pm 0.6$ )
	Azu 1	1		Azu 1	2	1.9
	Azu 1	1	central zones	Azu 1	3	1.8
	Azu 1	1		Azu 1	4	1.8
	Azu 1	2		Azu 1	10	2.7
	Azu 1	3	Plg inclusions in Amp phenocrysts	Azu 1	10	3.1
	Azu 1	7		Azu 1	18	2.0
	Azu 4	1		Azu 4	27	1.8
	Azu 4	2		Azu 4	27	2.6
	Azu 4	3		Azu 4	27	1.7
Phenocrysts and inclusion in Plg	Azu 4	5	central zones	Azu 4	27	2.0
	Azu 4	1		Azu 4	28	1.6
	Azu 4	2		Azu 4	28	2.4
	Azu 4	3		Azu 4	28	1.6
	Azu 4	5		Azu 4	28	1.7
	Azu 4	1		Azu 4	29	1.8
	Azu 4	2		Azu 4	29	2.5
	Azu 4	3		Azu 4	29	1.7
	Azu 4	5		Azu 4	29	1.9
	Azu 4	1	Plg inclusions in Amp phenocrysts	Azu 4	31	1.6
	Azu 4	2		Azu 4	31	2.4
	Azu 4	3		Azu 4	31	1.6
	Azu 4	5		Azu 4	31	1.7
	Azu 4	9	central zones	Azu 4	2	2.9

## Temperature calculations (°C)

### Amphibole-plagioclase

Amp	Sample	Point	Plg	Sample	Point	Anderson and Smith, 1995 Holland and Blundy, 1994 eq. B (error ±40) at P=2 kbar	Anderson and Smith, 1995 Holland and Blundy, 1994 eq. A (error ±40) at P=2 kbar
	Azu 1	1		Azu 1	2	715.6	747.4
	Azu 1	1	central zones	Azu 1	3	720.9	750.3
	Azu 1	1		Azu 1	4	726.7	754.5
	Azu 1	2	Plg inclusions in	Azu 1	10	731.6	809.6
	Azu 1	3	Amp phenocrysts	Azu 1	10	711.7	826.7
	Azu 1	7		Azu 1	18	770.6	785.4
Phenocrysts and inclusion in Plg	Azu 4	1		Azu 4	27	756.8	750.2
	Azu 4	2		Azu 4	27	777.5	795.1
	Azu 4	3		Azu 4	27	755.1	756.0
	Azu 4	5	central zones	Azu 4	27	771.7	801.9
	Azu 4	1		Azu 4	28	767.1	757.3
	Azu 4	2		Azu 4	28	787.5	803.3
	Azu 4	3		Azu 4	28	765.3	762.9
	Azu 4	5		Azu 4	28	781.9	810.0

Phenocrysts and inclusion in Plg	Azu 4	1		Azu 4	29	759.5	753.1
	Azu 4	2		Azu 4	29	780.1	798.5
	Azu 4	3		Azu 4	29	757.7	758.8
	Azu 4	5	Plg inclusions in	Azu 4	29	774.3	805.2
	Azu 4	1	Amp phenocrysts	Azu 4	31	767.0	757.7
	Azu 4	2		Azu 4	31	787.5	803.9
	Azu 4	3		Azu 4	31	765.2	763.3
	Azu 4	5		Azu 4	31	781.8	810.5
	Azu 4	9	central zones	Azu 4	2	719.1	753.7

---

## Amphibole

Amp	Sample	Point	Ridolfi et al., 2010 (error $\pm 22$ )	Ridolfi and Renzulli, 2012 (error $\pm 23.5$ ) at P=2 kbar	Putirka, 2016 eq. 5 (error $\pm 30$ ; 53)	Putirka, 2016 eq. 6 (error $\pm 28$ ; 52) at P=2 kbar	Putirka, 2016 eq. 8 (error $\pm 47$ ) at P=2 kbar
phenocrysts and inclusion in Plg	Azu 1	1	810.2	774.0	787.7	790.3	812.5
	Azu 1	2	854.9	821.9	830.4	828.4	848.6
	Azu 1	3	866.7	843.7	829.5	826.4	846.2
	Azu 1	4	832.4	799.3	805.1	804.9	826.2
	Azu 1	5	811.7	824.3	790.7	793.7	820.0
	Azu 1	6	845.0	819.7	819.8	819.8	833.0
	Azu 1	7	847.9	843.3	825.7	824.4	840.7
	Azu 1	9	867.9	827.6	836.8	833.3	843.9
	Azu 1	10	846.4	815.1	808.7	807.1	830.2
	Azu 4	1	827.4	796.1	809.2	810.4	825.2
	Azu 4	2	874.7	837.2	841.2	838.1	845.2
	Azu 4	3	825.5	784.9	799.7	801.5	819.0
	Azu 4	5	850.2	811.4	821.9	820.2	836.5
	Azu 4	9	847.9	786.0	818.1	817.7	827.8
	Azu 4	1	813.9	777.4	793.6	795.2	815.7
	Azu 4	2	823.1	792.1	797.7	799.0	800.7

## Orthopyroxene-clinopyroxene

Opx	Sample	Point	Cpx	Sample	Point	Putirka, 2008 eq. 37 (error $\pm 38$ ) at P=2 kbar
	Azu 1	3		Azu 2	24	1059.3
	Azu 1	8		Azu 2	24	1061.4
	Azu 1	10		Azu 2	24	1060.1
	Azu 2	10		Azu 2	24	1054.0
	Azu 2	12		Azu 2	24	1071.4
	Azu 2	21		Azu 2	24	1062.6
	Azu 2	28		Azu 2	24	1051.6
	Azu 2	31		Azu 2	24	1057.3
	Azu 2	36		Azu 2	24	1054.6
	Azu 3	2		Azu 2	24	1058.6
	Azu 3	5		Azu 2	24	1050.8
	Azu 3	6		Azu 2	24	1057.6
	Azu 3	9		Azu 2	24	1061.5
	Azu 3	19		Azu 2	24	1051.1
	Azu 4	1		Azu 2	24	1057.4
	Azu 4	3		Azu 2	24	1064.0
	Azu 4	5		Azu 2	24	1058.1
	Azu 4	8		Azu 2	24	1067.6
	Azu 4	2		Azu 2	24	1068.8
	Azu 4	4		Azu 2	24	1063.7
	Azu 7 EN	2		Azu 2	24	1055.0
	Azu 7 EN	3		Azu 2	24	1067.0
	Azu 7 EN	5		Azu 2	24	1060.2
	Azu 7 EN	11		Azu 2	24	1060.5

Mg-rich rims

Mg-rich rims

Mg-rich rims

Azu 7 EN	13
Azu 10 EN	2
Azu 10 EN	3
Azu 4 EN	12
Azu 4 EN	13
Azu 4 EN	14
Azu 1	3
Azu 1	8
Azu 1	10
Azu 2	10
Azu 2	12
Azu 2	15
Azu 2	18
Azu 2	21
Azu 2	28
Azu 2	31
Azu 2	36
Azu 3	2
Azu 3	6
Azu 3	9
Azu 3	19
Azu 4	1
Azu 4	3
Azu 4	5
Azu 4	8
Azu 4	2
Azu 4	4
Azu 4	6

Mg-rich rims

Azu 2	24	1063.9
Azu 2	24	1054.3
Azu 2	24	1046.4
Azu 2	24	1058.9
Azu 2	24	1064.4
Azu 2	24	1050.7
Azu 2	27	927.5
Azu 2	27	929.1
Azu 2	27	928.2
Azu 2	27	923.4
Azu 2	27	936.8
Azu 2	27	934.6
Azu 2	27	935.7
Azu 2	27	930.1
Azu 2	27	921.6
Azu 2	27	926.0
Azu 2	27	923.9
Azu 2	27	927.0
Azu 2	27	926.2
Azu 2	27	929.2
Azu 2	27	921.2
Azu 2	27	926.1
Azu 2	27	931.2
Azu 2	27	926.6
Azu 2	27	933.9
Azu 2	27	934.8
Azu 2	27	930.9
Azu 2	27	932.6



Mg-rich rims

Azu 7 EN	2
Azu 7 EN	3
Azu 7 EN	5
Azu 7 EN	11
Azu 7 EN	13
Azu 10 EN	2
Azu 10 EN	3
Azu 4 EN	12
Azu 4 EN	13
Azu 4 EN	14
Azu 1	3
Azu 1	8
Azu 1	10
Azu 2	10
Azu 2	12
Azu 2	15
Azu 2	18
Azu 2	21
Azu 2	28
Azu 2	31
Azu 2	36
Azu 3	2
Azu 3	6
Azu 3	9
Azu 3	19
Azu 4	1
Azu 4	3
Azu 4	5

Mg-rich rims

Azu 2	27	924.2
Azu 2	27	933.4
Azu 2	27	928.2
Azu 2	27	928.5
Azu 2	27	931.0
Azu 2	27	923.7
Azu 2	27	917.6
Azu 2	27	927.2
Azu 2	27	931.4
Azu 2	27	920.9
Azu 2	34	949.3
Azu 2	34	951.0
Azu 2	34	950.0
Azu 2	34	945.0
Azu 2	34	959.1
Azu 2	34	956.7
Azu 2	34	957.9
Azu 2	34	952.0
Azu 2	34	943.2
Azu 2	34	947.7
Azu 2	34	945.6
Azu 2	34	948.8
Azu 2	34	948.0
Azu 2	34	951.1
Azu 2	34	942.8
Azu 2	34	947.8
Azu 2	34	953.1
Azu 2	34	948.3

Mg-rich rims

Azu 4	8
Azu 4	2
Azu 4	4
Azu 4	6
Azu 7 EN	3
Azu 7 EN	5
Azu 7 EN	8
Azu 7 EN	11
Azu 7 EN	13
Azu 10 EN	2
Azu 10 EN	3
Azu 4 EN	12
Azu 4 EN	13
Azu 4 EN	14

Mg-rich rims

Azu 2	34	956.0
Azu 2	34	956.9
Azu 2	34	952.8
Azu 2	34	954.6
Azu 2	34	955.5
Azu 2	34	950.1
Azu 2	34	946.0
Azu 2	34	950.3
Azu 2	34	953.0
Azu 2	34	945.3
Azu 2	34	939.0
Azu 2	34	949.0
Azu 2	34	953.4
Azu 2	34	942.4

---

Opx	Sample	Point	Cpx	Sample	Point	Putirka, 2008 eq. 37 (error $\pm 38$ ) at P=2 kbar
	Azu 1	7		Azu 2	23	883.1
	Azu 2	14		Azu 2	23	897.3
	Azu 2	17		Azu 2	23	896.1
	Azu 2	20		Azu 2	23	891.0
	Azu 2	35		Azu 2	23	900.6
Mg-poor cores	Azu 4	7	Mg-poor cores	Azu 2	23	893.0
	Azu 4	1		Azu 2	23	860.2
	Azu 7 EN	1		Azu 2	23	866.4
	Azu 7 EN	7		Azu 2	23	879.5
	Azu 10 EN	4		Azu 2	23	885.1
	Azu 1	7		Azu 2	26	922.5
	Azu 2	14		Azu 2	26	938.0
	Azu 2	17		Azu 2	26	936.7
	Azu 2	20		Azu 2	26	931.1
	Azu 2	35		Azu 2	26	941.7

Mg-poor cores

Azu 3	18
Azu 4	7
Azu 4	1
Azu 7 EN	1
Azu 7 EN	7
Azu 7 EN	10
Azu 2	17
Azu 2	32
Azu 2	35
Azu 4	7
Azu 4	1
Azu 7 EN	1
Azu 7 EN	7
Azu 10 EN	4

Mg-poor cores

Azu 2	26	940.6
Azu 2	26	933.3
Azu 2	26	897.5
Azu 2	26	904.3
Azu 2	26	918.5
Azu 2	26	943.3
Azu 2	33	928.0
Azu 2	33	904.9
Azu 2	33	932.9
Azu 2	33	924.7
Azu 2	33	889.5
Azu 2	33	896.3
Azu 2	33	910.2
Azu 2	33	916.2

---

Opx	Sample	Point	Cpx	Sample	Point	Putirka, 2008 eq. 37 (error $\pm 38$ ) at P=2 kbar
Mg-rich Opx patches in Cpx	Azu 1	6	Mg-rich rims	Azu 1	5	1011.9
	Azu 1	11		Azu 1	13	1078.0
	Azu 1	17		Azu 1	16	1014.4
	Azu 1	19		Azu 1	16	1030.8
	Azu 1	17		Azu 1	20	1009.2
	Azu 1	19		Azu 1	20	1025.5
	Azu 2	25		Azu 2	24	1062.5
	Azu 3	24		Azu 3	22	916.2
	Azu 3	24		Azu 3	25	970.2
	Azu 3	28		Azu 3	29	1093.5
	Azu 3	31		Azu 3	29	1096.6
	Azu 3	28		Azu 3	30	1021.0
	Azu 3	31		Azu 3	30	1023.7
	Azu 3	28		Azu 3	32	966.1
	Azu 3	31		Azu 3	32	968.6

## Plagioclase-liquid

Plg	Sample	Point	Xliq Azu 7 EN		Putirka, 2005 eq. B (error $\pm 53^\circ\text{C}$ ) at P=2 kbar
Microlites and inclusions in Amp microphenocrysts	Azu 1	15	SiO <sub>2</sub>	0.56	1028.0
	Azu 2	8	AlO <sub>1.5</sub>	0.18	1021.6
	Azu 3	30	CaO	0.06	1014.7
	Azu 4	26			1013.8
	Azu 4	34			1027.9
	Azu 4	36			1022.9
	Azu 4	3			1025.7
	Azu 7 EN	4			1019.8
	Azu 8 EN	1			1024.9
	Azu 10 EN	1			1024.7
rims	Azu 1	19			1027.6
	Azu 2	13			1028.3
	Azu 3	8			1008.5
	Azu 4	6			1026.9
	Azu 4	9			1026.4
	Azu 4 EN	28			1023.3
	Azu 1	11			988.2
Cores	Azu 2	14			1025.7
	Azu 3	1			957.2
	Azu 4	1			979.9
	Azu 4	4			1019.4
	Azu 4	11			1027.7
	Azu 4	12			1003.7
	Azu 7 EN	8			1016.4

## Fe-Ti oxides

Tmg	Sample	Point	Ilm	Sample	Point	Ghiorso and Evans, 2008 Fe-Ti exchange (error $\pm 18$ )	Sauerzapf et al., 2008 (error $\pm 50$ )
Paired Tmg-Ilm microlites	Azu 2	4	Paired Tmg-Ilm microlites	Azu 2	3	826	809.2
	Azu 2	6		Azu 2	7	742	797.1
	Azu 2	8		Azu 2	7	822	823.4
	Azu 2	16		Azu 2	15	748	749.8
	Azu 8 EN	1		Azu 8 EN	2	866	858.8
	Azu 8 EN	3		Azu 8 EN	2	864	856.1

## fO<sub>2</sub> (log units)

### Amphibole

Amp	Sample	Point	Ridolfi et al., 2010 LogfO <sub>2</sub> (error ±0.4 log units) at T=HB1994B	Ridolfi et al., 2010 ΔQFM (error ±0.4 log units) at T=HB1994B
Phenocrysts and inclusion in Plg	Azu 1	1	-14.4	2.1
	Azu 1	1	-14.2	2.1
	Azu 1	1	-14.1	2.1
	Azu 1	2	-14.3	1.8
	Azu 1	3	-14.7	1.8
	Azu 1	7	-13.5	1.6
	Azu 4	1	-13.6	1.8
	Azu 4	2	-13.6	1.3
	Azu 4	3	-13.5	2.0
	Azu 4	5	-13.4	1.7
	Azu 4	1	-13.4	1.8
	Azu 4	2	-13.4	1.3
	Azu 4	3	-13.3	2.0
	Azu 4	5	-13.2	1.7
	Azu 4	1	-13.6	1.8
	Azu 4	2	-13.6	1.3
	Azu 4	3	-13.4	2.0
	Azu 4	5	-13.4	1.7
	Azu 4	1	-13.4	1.8
	Azu 4	2	-13.4	1.3
	Azu 4	3	-13.3	2.0
	Azu 4	5	-13.2	1.7
	Azu 4	9	-14.7	1.6



## Fe-Ti oxides

Tmg	Sample	Point	Ilm	Sample	Point	Ghiorso and Evans, 2008 Log $fO_2$ (error $\pm 0.1$ log units)	Ghiorso and Evans, 2008 $\Delta QFM$ (error $\pm 0.1$ log units)	Sauerzapf et al., 2008 Log $fO_2$ (error $\pm 0.4$ log units) at P=1 atm	Sauerzapf et al., 2008 $\Delta QFM$ (error $\pm 0.4$ log units) at P=1 atm
Paired Tmg-Ilm microlites	Azu 2	4	Paired Tmg-Ilm microlites	Azu 2	3	-12.5	1.4	-12.35	1.9
	Azu 2	6		Azu 2	7	-13.7	2.0	-12.05	2.5
	Azu 2	8		Azu 2	7	-12.2	1.8	-11.69	2.3
	Azu 2	16		Azu 2	15	-14.6	1.1	-13.74	1.8
	Azu 8 EN	1		Azu 8 EN	2	-12.2	0.9	-11.99	1.3
	Azu 8 EN	3		Azu 8 EN	2	-12.2	0.9	-12.03	1.3

## Liquid

T°C	Kress and Carmichael, 1991 $\Delta QFM$ at P=1 atm and $XFe_2O_3/XFeO = 0.69$ (Azu 7 EN sample)
712	1.3
740	1.5
870	2.0
900	2.1
1000	2.4
1097	2.5

## H<sub>2</sub>O solubility (wt%)

### Liquid

Liquid Azu 7 EN						
Xliq Azu 7 EN		T°C	Moore et al., 1998 (error ±0,5 wt%) at 2 kbar	Zhang et al., 2007 (error ±0,68 wt%) at 2 kbar		
SiO <sub>2</sub>	58,88	900	5,90	5,43		
Al <sub>2</sub> O <sub>3</sub>	16,05	901	5,90	5,43		
Fe <sub>2</sub> O <sub>3</sub> T	6,31	902	5,89	5,43		
FeOT	5,7	903	5,89	5,43		
MgO	3,71	904	5,88	5,43		
CaO	5,8	905	5,88	5,42		
Na <sub>2</sub> O	3,4	906	5,87	5,42		
K <sub>2</sub> O	2,22	907	5,86	5,42		
TiO <sub>2</sub>	0,87	908	5,86	5,42		
P <sub>2</sub> O <sub>5</sub>	0,2	909	5,85	5,42		
MnO	0,09	910	5,85	5,41		
Cr <sub>2</sub> O <sub>3</sub>	0,022	911	5,84	5,41		
LOI	2,1	912	5,84	5,41		
Total	99,0	913	5,83	5,41		
		914	5,83	5,41		
		915	5,82	5,40		
		916	5,82	5,40		
		917	5,81	5,40		
		918	5,81	5,40		
		919	5,80	5,40		
		920	5,80	5,40		
		921	5,79	5,39		

922	5,78	5,39
923	5,78	5,39
924	5,77	5,39
925	5,77	5,39
926	5,76	5,38
927	5,76	5,38
928	5,75	5,38
929	5,75	5,38
930	5,74	5,38
931	5,74	5,37
932	5,73	5,37
933	5,73	5,37
934	5,72	5,37
935	5,72	5,37
936	5,71	5,37
937	5,71	5,36
938	5,70	5,36
939	5,70	5,36
940	5,69	5,36
941	5,69	5,36
942	5,68	5,35
943	5,68	5,35
944	5,67	5,35
945	5,67	5,35
946	5,66	5,35
947	5,66	5,35
948	5,65	5,34
949	5,65	5,34
950	5,64	5,34
951	5,64	5,34
952	5,63	5,34

953	5,63	5,33
954	5,62	5,33
955	5,62	5,33
956	5,61	5,33
957	5,61	5,33
958	5,60	5,33
959	5,60	5,32
960	5,60	5,32
961	5,59	5,32
962	5,59	5,32
963	5,58	5,32
964	5,58	5,32
965	5,57	5,31
966	5,57	5,31
967	5,56	5,31
968	5,56	5,31
969	5,55	5,31
970	5,55	5,30
971	5,54	5,30
972	5,54	5,30
973	5,53	5,30
974	5,53	5,30
975	5,53	5,30
976	5,52	5,29
977	5,52	5,29
978	5,51	5,29
979	5,51	5,29
980	5,50	5,29
981	5,50	5,29
982	5,49	5,28
983	5,49	5,28

984	5,49	5,28
985	5,48	5,28
986	5,48	5,28
987	5,47	5,28
988	5,47	5,27
989	5,46	5,27
990	5,46	5,27
991	5,45	5,27
992	5,45	5,27
993	5,45	5,27
994	5,44	5,26
995	5,44	5,26
996	5,43	5,26
997	5,43	5,26
998	5,42	5,26
999	5,42	5,26
1000	5,42	5,25
1001	5,41	5,25
1002	5,41	5,25
1003	5,40	5,25
1004	5,40	5,25
1005	5,39	5,25
1006	5,39	5,24
1007	5,39	5,24
1008	5,38	5,24
1009	5,38	5,24
1010	5,37	5,24
1011	5,37	5,24
1012	5,36	5,23
1013	5,36	5,23
1014	5,36	5,23

1015	5,35	5,23
1016	5,35	5,23
1017	5,34	5,23
1018	5,34	5,22
1019	5,34	5,22
1020	5,33	5,22
1021	5,33	5,22
1022	5,32	5,22
1023	5,32	5,22
1024	5,32	5,21
1025	5,31	5,21
1026	5,31	5,21
1027	5,30	5,21
1028	5,30	5,21
1029	5,30	5,21
1030	5,29	5,20
1031	5,29	5,20
1032	5,28	5,20
1033	5,28	5,20
1034	5,28	5,20
1035	5,27	5,20
1036	5,27	5,20
1037	5,26	5,19
1038	5,26	5,19
1039	5,26	5,19
1040	5,25	5,19
1041	5,25	5,19
1042	5,24	5,19
1043	5,24	5,18
1044	5,24	5,18
1045	5,23	5,18

1046	5,23	5,18
1047	5,23	5,18
1048	5,22	5,18
1049	5,22	5,17
1050	5,21	5,17
1051	5,21	5,17
1052	5,21	5,17
1053	5,20	5,17
1054	5,20	5,17
1055	5,19	5,17
1056	5,19	5,16
1057	5,19	5,16
1058	5,18	5,16
1059	5,18	5,16
1060	5,18	5,16
1061	5,17	5,16
1062	5,17	5,16
1063	5,16	5,15
1064	5,16	5,15
1065	5,16	5,15
1066	5,15	5,15
1067	5,15	5,15
1068	5,15	5,15
1069	5,14	5,14
1070	5,14	5,14
1071	5,14	5,14
1072	5,13	5,14
1073	5,13	5,14
1074	5,12	5,14
1075	5,12	5,14
1076	5,12	5,13

1077	5,11	5,13
1078	5,11	5,13
1079	5,11	5,13
1080	5,10	5,13
1081	5,10	5,13
1082	5,10	5,13
1083	5,09	5,12
1084	5,09	5,12
1085	5,09	5,12
1086	5,08	5,12
1087	5,08	5,12
1088	5,08	5,12
1089	5,07	5,12
1090	5,07	5,11
1091	5,06	5,11
1092	5,06	5,11
1093	5,06	5,11
1094	5,05	5,11
1095	5,05	5,11
1096	5,05	5,11
1097	5,04	5,10
1098	5,04	5,10
1099	5,04	5,10
1100	5,03	5,10



## 5.6. Cr<sub>2</sub>O<sub>3</sub> (wt%) contents in pyroxenes

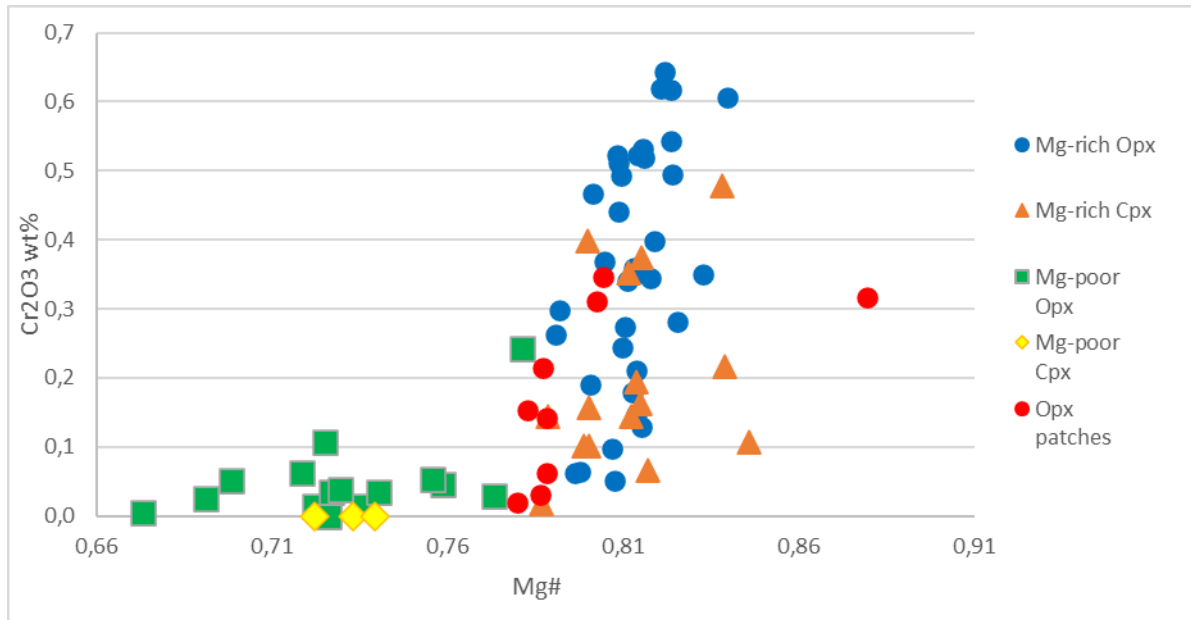


Fig. 5.4: Diagram displaying the contrasting Cr<sub>2</sub>O<sub>3</sub> (wt%) concentrations between Mg-poor and Mg-rich (including patches) pyroxene phenocrysts. Although we did not use a secondary standard to quantify the uncertainty of Cr<sub>2</sub>O<sub>3</sub> (wt%) measurement, the data show a notorious difference in Cr<sub>2</sub>O<sub>3</sub> (wt%) concentration.

## 5.7. Equilibrium tests

Mineral-liquid test (Roeder and Emslie 1970; Putirka 2008, 2016) considering the enclave samples Azu 7 EN, Azu 8 EN, Azu 10 EN, and Azu 14 EN as liquid composition.

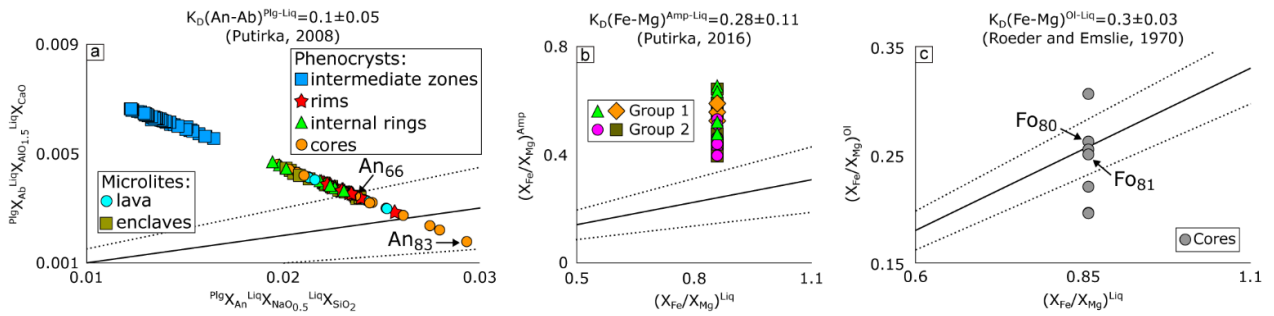


Fig. 5.5: Mineral-liquid test plots considering the composition of the enclave sample Azu 7 EN as liquid composition. The results show that cores of plagioclase phenocryst (An<sub>66</sub>–<sub>83</sub>) and olivine phenocrysts (Fo<sub>80</sub>–<sub>81</sub>) are in equilibrium with the considered liquid composition, whereas amphiboles are in disequilibrium

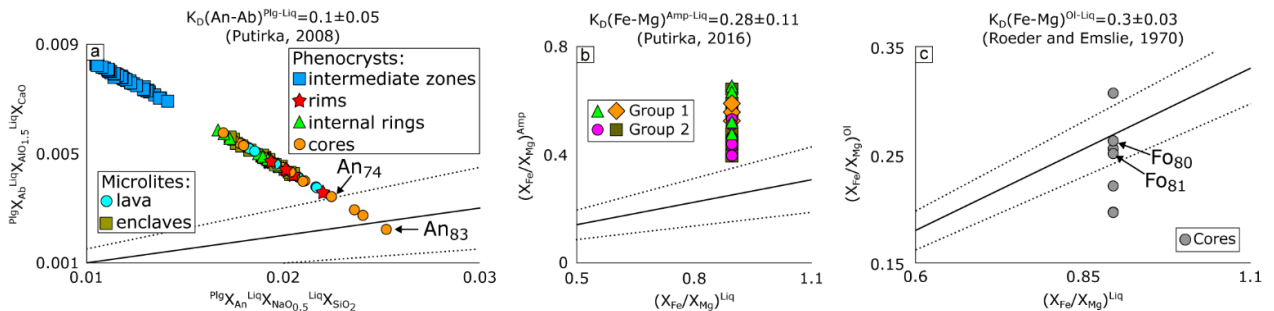


Fig. 5.6: Mineral-liquid test plots considering the composition of the enclave sample Azu 8 EN as liquid composition. The results show that cores of plagioclase phenocryst (An<sub>74</sub>–<sub>83</sub>) and olivine phenocrysts (Fo<sub>80</sub>–<sub>81</sub>) are in equilibrium with the considered liquid composition, whereas amphiboles are in disequilibrium

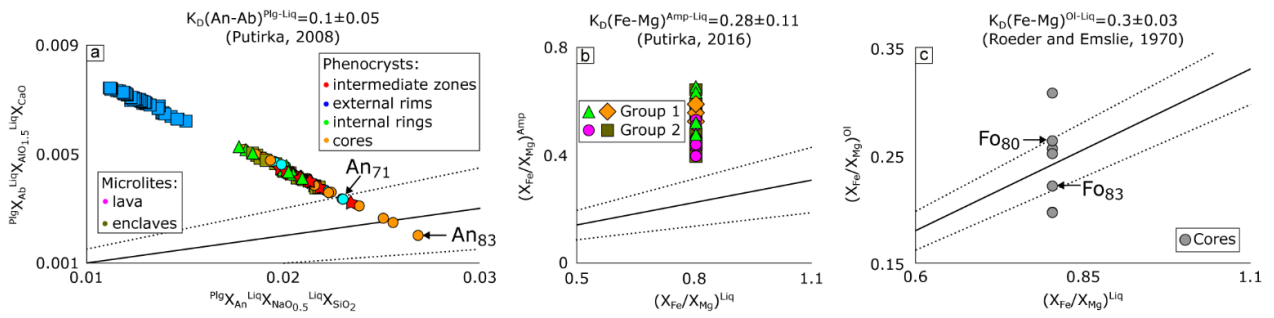


Fig. 5.7: Mineral-liquid test plots considering the composition of the enclave sample Azu 10 EN as liquid composition. The results show that cores and external rims of plagioclase phenocrysts and plagioclase microlites with composition between An<sub>71–83</sub> are in equilibrium with the considered liquid composition. Cores of olivine phenocrysts (Fo<sub>80–83</sub>) are also in equilibrium, whereas amphiboles are in disequilibrium

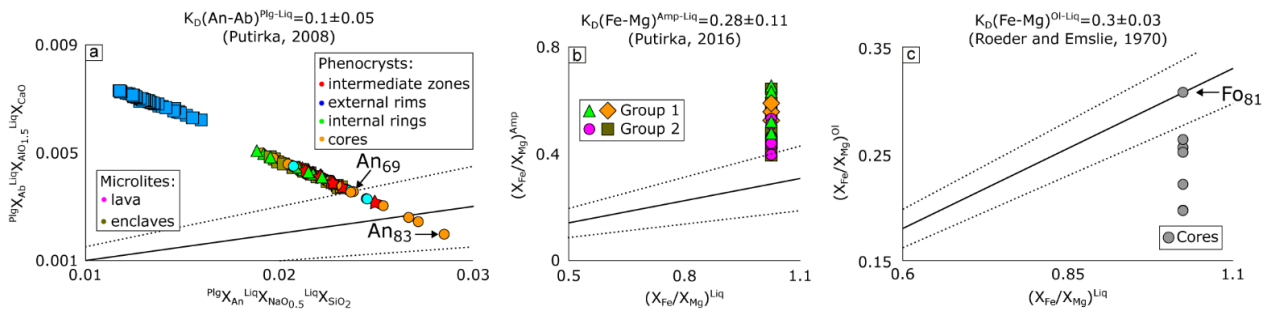


Fig. 5.8: Mineral-liquid test plots considering the composition of the enclave sample Azu 14 EN as liquid composition. The results show that cores and external rims of plagioclase phenocrysts and plagioclase microlites with composition between An<sub>69–83</sub> are in equilibrium with the considered liquid composition. Cores of olivine phenocrysts (Fo<sub>80</sub>) are also in equilibrium, whereas amphiboles are in disequilibrium

## 5.8. Temperatures not considered for amphiboles of Group 1

Among all crystallization temperatures calculated for Group 1 amphiboles (Fig. 5.9), we only consider those of edenite-richterite calibration (712 – 788 ( $\pm 40$ ) °C; Fig. 5.9a) due to the following reasons:

- 1) Holland and Blundy (1994) noted that edenite-tremolite calibration ( $T_A$ ) gives systematically higher temperatures than edenite-richterite calibration ( $T_B$ ) when it is applied to quartz-undersaturated systems. This observation was reaffirmed by Bachmann and Dungan (2002), who identified no quartz inclusions on amphiboles, establishing that  $T_A - T_B$  is systematically  $\sim 50^\circ\text{C}$ .

Group 1 amphiboles yielded low and high differences between  $T_A - T_B$ . Thus, when  $T_A < 800^\circ\text{C}$  (more than half of data as is indicated by median value in Fig. 5.9b) the average value of  $T_A - T_B$  ( $\pm \sigma$ ) is 14 ( $\pm 11$ ) °C, whereas if  $T_A > 800^\circ\text{C}$  this difference is 43 ( $\pm 33$ ) °C. Thus, despite of quartz and amphibole phenocrysts were not found in contact, we interpret the high silica content of melt in equilibrium with Group 1 amphiboles (63 – 79 wt% of  $\text{SiO}_2$ ; see the following section) and the narrow correlation between  $T_A$  and  $T_B$  when  $T_A < 800^\circ\text{C}$  as representative of amphibole crystallization (or re-equilibration) in a quartz-saturated system at low temperatures ( $< 800^\circ\text{C}$ ).

- 2) Empirical geothermometers of Ridolfi et al. (2010) and Ridolfi and Renzulli (2012) tend to overestimate the temperature of amphiboles crystallized below  $800^\circ\text{C}$  (see Figure 5a of Putirka 2016) due to their calibrations are made with experimental amphibole crystallized in equilibrium with high glass percentages (average 73% of glass) and above of  $850^\circ\text{C}$  (only a few experimental data are between  $800 - 850^\circ\text{C}$ ). Similar overestimations are given by equation 8 of Putirka (2016) and to a lesser degree by its equations 5 and 6 (see Figure 5g, 5h, and 8a of Putirka 2016). Presumably, Ridolfi (2021) also gives overestimated temperature results, as it uses the same thermometric equation of Ridolfi and Renzulli (2012) but with some new calibration data (between  $885 - 1060^\circ\text{C}$ ).
- 3) Holland and Blundy (1994) geothermometers are calibrated over a thermodynamic principle that considers the stability of two mineral phases, representing better scientific fundamentals than thermometry based on empirical correlations (Ridolfi et al. 2010; Ridolfi and Renzulli 2012; Putirka 2016) with a likely limited database

(e.g., at low temperatures < 800 °C) that does not cover the large and complex chemical substitutions of amphiboles in accordance with temperature, pressure, oxygen fugacity or water content variation.

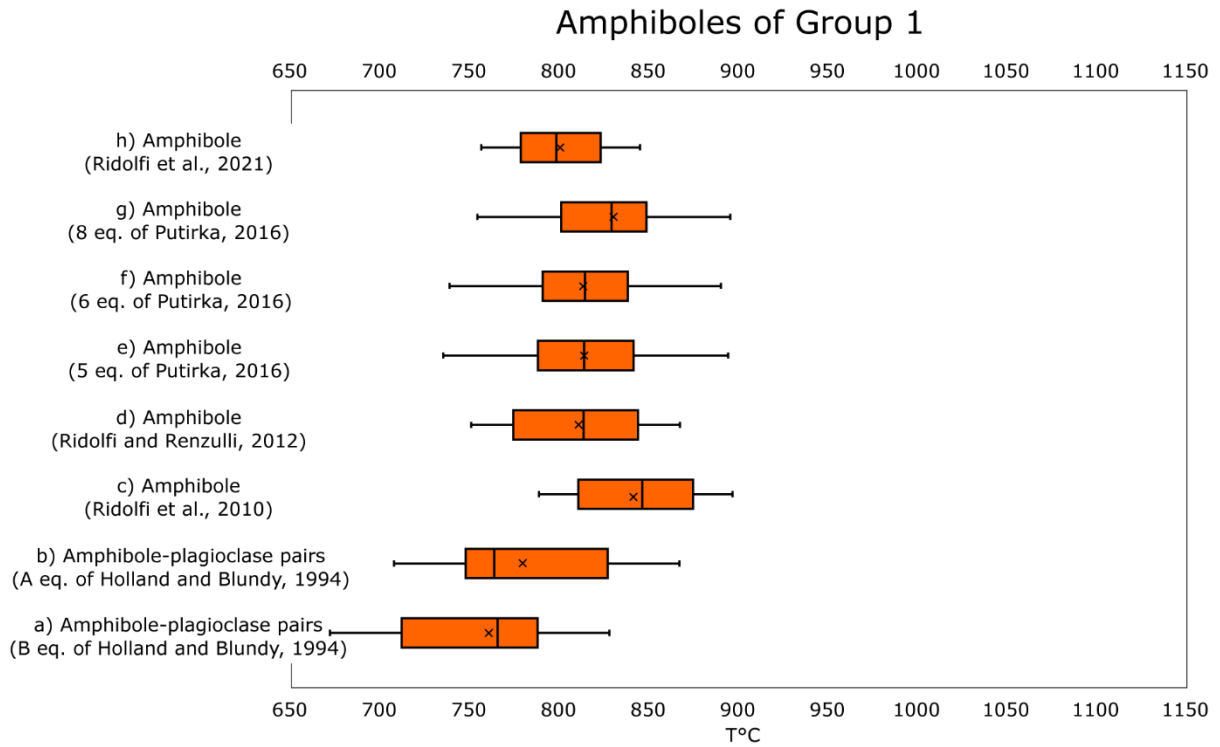


Fig. 5.9: Box plots showing temperature crystallization of Group 1 amphiboles according to different geothermometers (a – h) at 2 kbar of pressure. The phases and equation references involved in the calculations are on the left side of the diagram

## 5.9. Felsic melt composition

We determined the composition ( $\text{SiO}_2$ ,  $\text{K}_2\text{O}$ ,  $\text{Al}_2\text{O}_3$ ,  $\text{CaO}$ ,  $\text{FeO}$ ,  $\text{MgO}$ , and  $\text{TiO}_2$ ) of the liquid equilibrated with Group 1 amphiboles considering the following points:

- 1) To avoid bias to P-T conditions determined by different thermometers and barometers in the main text, we performed the calculations in a wide P-T field of 1 – 5 kbar and 700 – 900 °C. Oxides contents (wt%) calculated within these ranges show low variance. For example,  $\text{SiO}_2$  concentrations between 2 – 5 kbar are almost the same (~79.8 wt%) when Ridolfi and Renzulli's (2012) method is applied (Fig. 5.10a), and only at 1 kbar display a significant 11% drop (~70.4 wt%) from the determinations at higher pressures. Similarly, when chemometric calibrations of Putirka (2016) and Zhang et al. (2017) are applied, no significant variation is observed in each method except for the first mentioned (Fig. 5.10b and c), which at 700 °C exhibits an 11% variation (~62.3 wt%) from calculations at higher temperatures (~70.7 wt%). In the case of  $\text{Al}_2\text{O}_3$  and  $\text{K}_2\text{O}$  determination using Ridolfi and Renzulli's (2012) method, no significative difference is seen between 2 – 5 kbar (~13.2 and ~4.8 wt%, respectively). Nevertheless, at 1 kbar a rise of 37% and 10% is recorded (~18.1 and ~5.4 wt%, respectively). In summary, the dacitic-rhyolitic composition determined for the melt in equilibrium with Group 1 amphiboles does not change within the considered P-T field. The complete set of calculated major oxide compositions can be found in the Excel file "P-T-felsic melt composition-fO2-Solubility calculations".
- 2) Some results were not considered because these were out of calibrated boundaries of each method. For example, we did not consider  $\text{SiO}_2$  results obtained from Ridolfi and Renzulli's (2012) calibration larger than 78.1 (wt%) because this value is the upper limit of the method. The upper and lower boundaries of the applied method can be found in the Excel file "P-T-felsic melt composition-fO2-Solubility calculations". The origin of out-of-bounds results would come from the bias to high temperature amphiboles (> 850 °C) data used to perform the calibrations.
- 3) The considered error for each oxide content was the highest among all methods used. For example, the highest error for  $\text{SiO}_2$  and  $\text{K}_2\text{O}$  calculations ( $\pm 3.8$  and  $\pm 0.6$ ) came from Zhang et al.'s (2017) calibrations. The error of each method can be found in the Excel file "P-T-felsic melt composition-fO2-H2O-Solubility calculations".

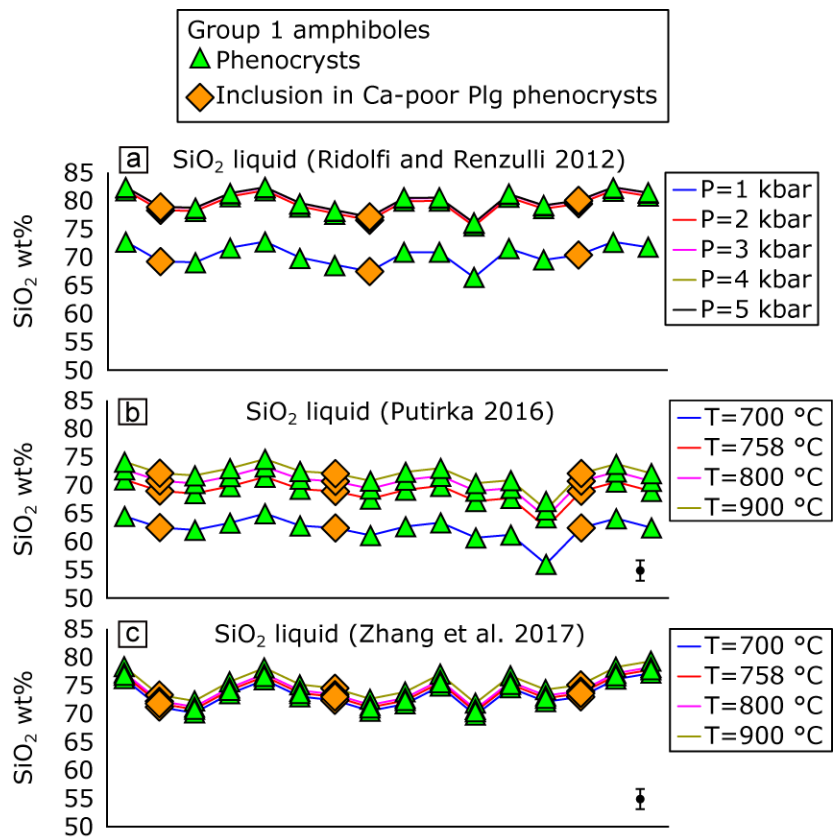


Fig. 5.10: Diagrams showing the SiO<sub>2</sub> (wt%) content in the liquid equilibrated with Group 1 amphiboles at different P-T conditions. X axis represents different spot analysis of amphibole (triangles and diamond). The uncertainties associated with Ridolfi and Renzulli's (2012) method is ± 1.3 wt% (smaller than symbols), while those of Putirka (2016) and Zhang et al. (2017) are ± 3.6 wt% for both. In (a) plot the pressure curves at 2, 3, 4, and 5 kbar are superposed

## 5.10. MELTS simulations

Diagrams of Fig. 5.11 to Fig. 5.13 show the P-T- $fO_2$  conditions and initial H<sub>2</sub>O contents for which modellings via Rhyolite-MELTS (Gualda et al. 2012) reproduced olivine, Mg-rich pyroxenes (co-crystallized orthopyroxene and clinopyroxene), and Ca-rich plagioclase compositions consistent with those observed in the lava samples of the Azufre volcano. Although plagioclase and pyroxenes modellings gave coincident compositions in wide P-T- $fO_2$ -H<sub>2</sub>O conditions (Fig. 5.11 to Fig. 5.13), olivine crystallization is restricted to oxygen fugacity buffer conditions of QFM and QFM+1 (Fig. 5.11). Therefore, the observed high-temperature mineralogy is reproduced with the widest temperature intervals at P- $fO_2$  conditions of 2 kbar and QFM+1 together with initial water contents between 4 – 5 (wt%) as stated in Fig. 5.11. MELTS modellings can be consult in the file “MELTS simulations.rar”

It is worth noting that each modelling at determined P- $fO_2$  conditions was performed with an initial water content indicated by the number on the right side of each modelling line (Fig. 5.11 to Fig. 5.13).

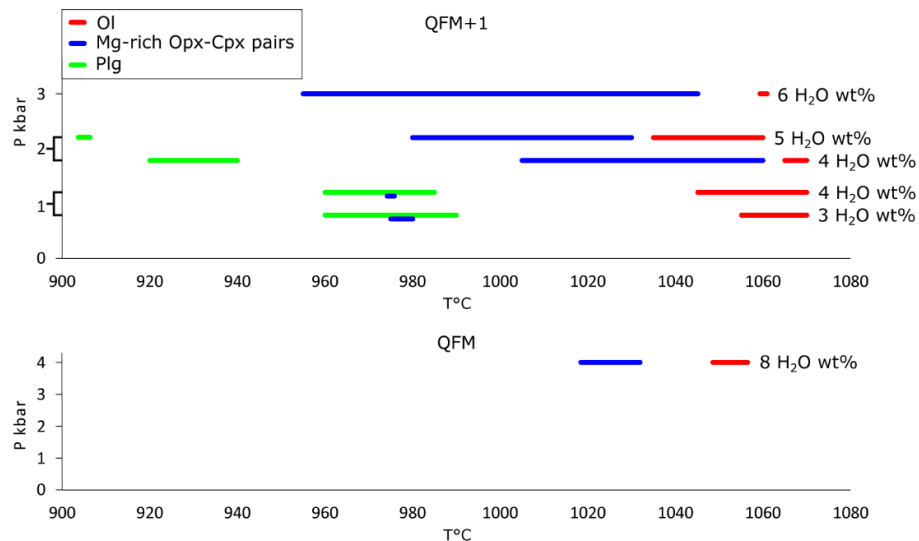


Fig. 5.11: Diagrams showing P-T- $fO_2$  conditions and initial H<sub>2</sub>O contents in which Rhyolite-MELTS modellings reproduced crystallization sequence of olivine, Mg-rich pyroxenes (co-crystallized orthopyroxene and clinopyroxene), and Ca-rich plagioclase with An<sub>≥66</sub>, which is consistent with the composition observed in lava samples



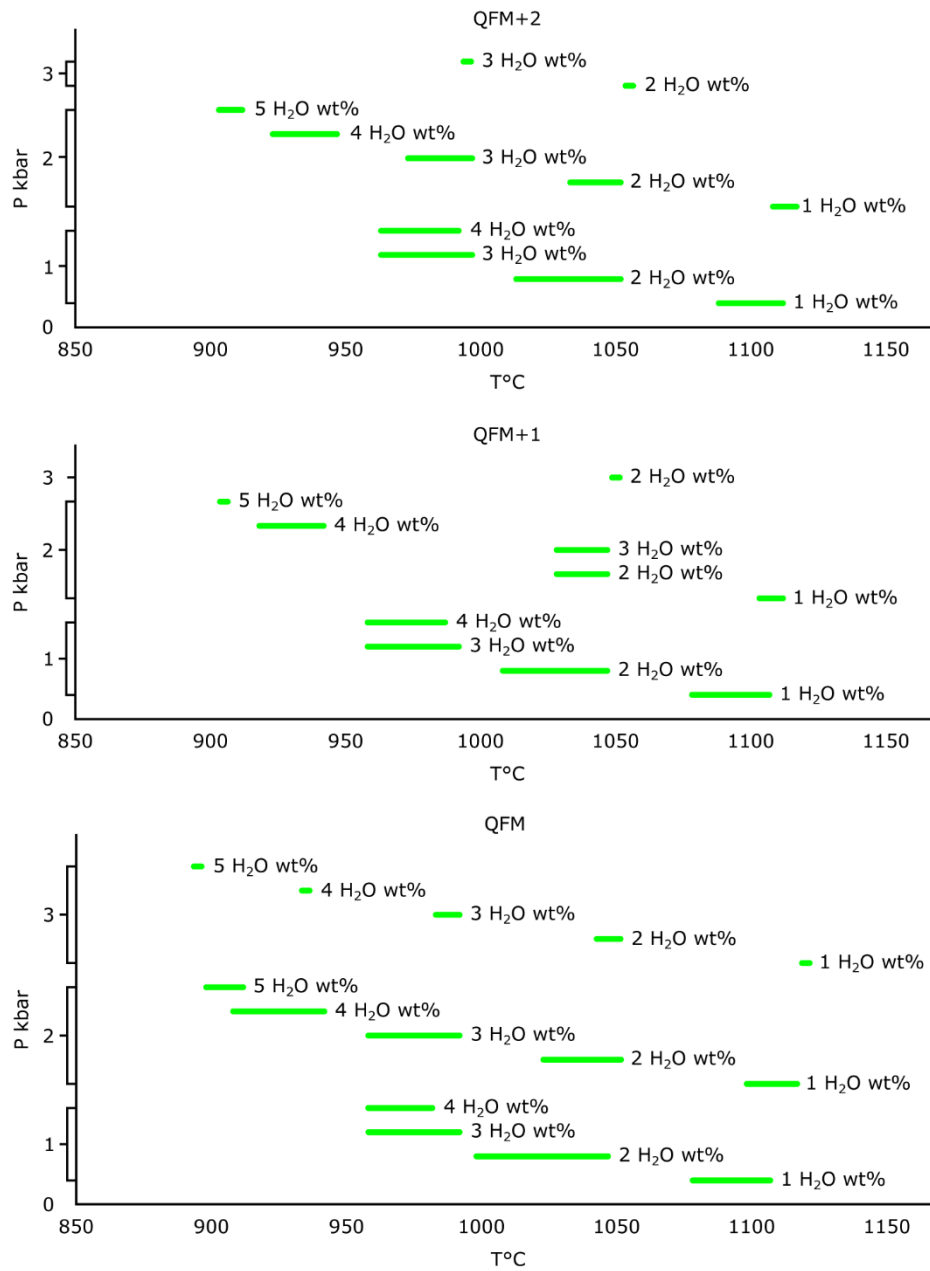


Fig. 5.12: Diagrams showing P-T-*f*O<sub>2</sub> conditions and initial H<sub>2</sub>O contents in which Rhyolite-MELT modellings reproduced Ca-rich plagioclase (An<sub>≥66</sub>)

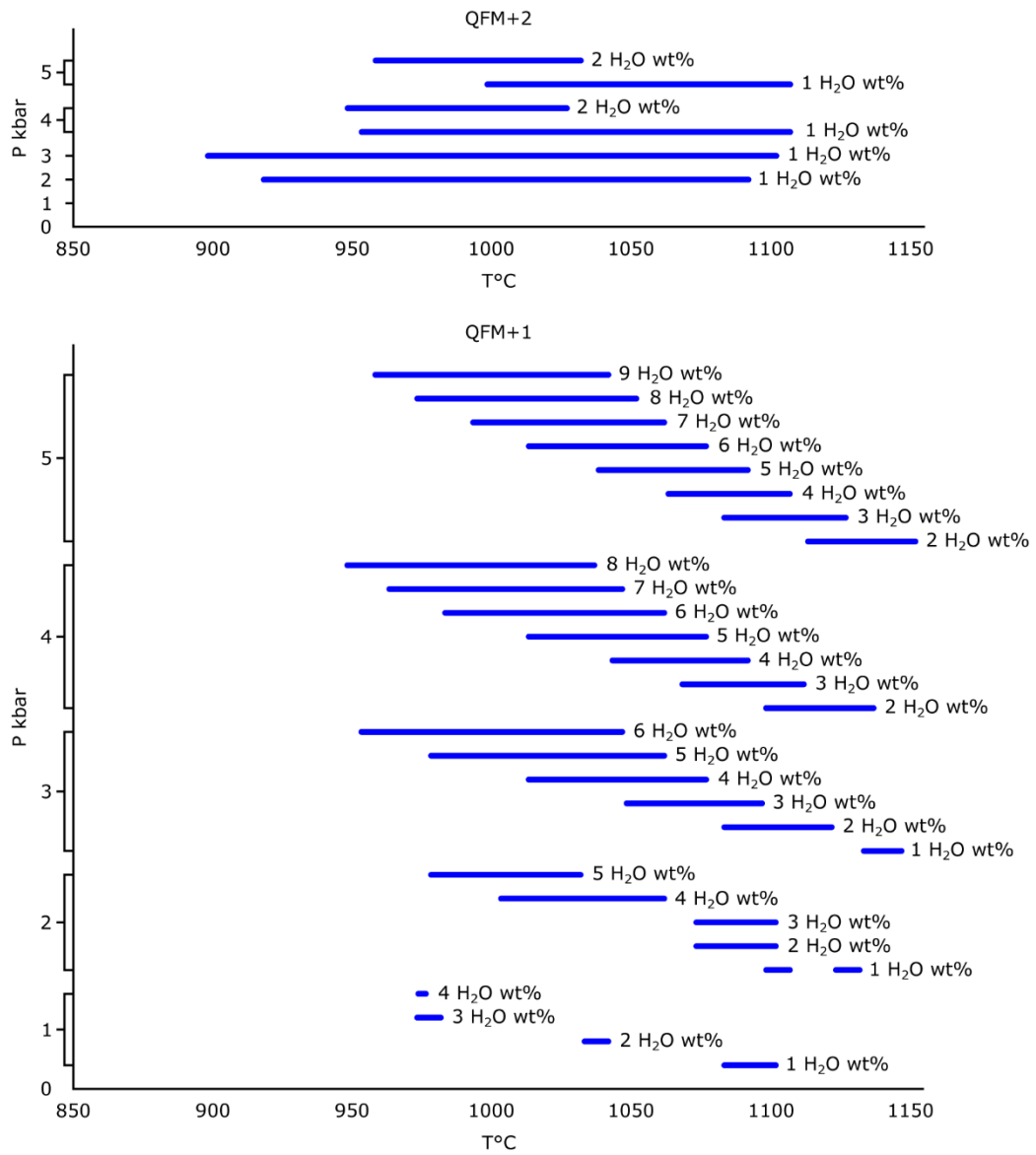


Fig. 5.13: Diagrams showing P-T-fO<sub>2</sub> conditions and initial H<sub>2</sub>O contents in which Rhyolite-MELT modellings reproduced the Mg-rich pyroxenes compositions (co-crystallized ortho- and clinopyroxene) consistent with those observed in lava samples

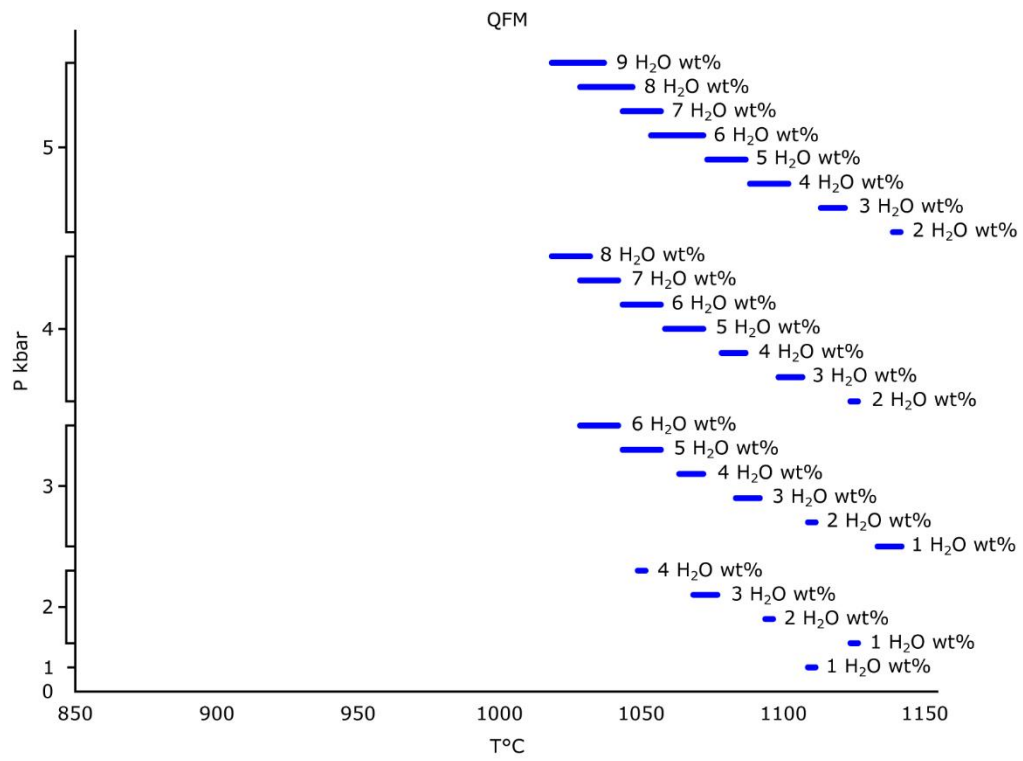


Fig. 5.14: Continued diagram of Fig. 5.13

## 5.11. Shallow Mg-rich pyroxenes and olivine crystallization data

As it is shown in the Table 5.3, a basaltic andesite (55,2 wt% SiO<sub>2</sub>) crystallized the association olivine (Fo<sub>83</sub>) + clinopyroxene (En<sub>44</sub>Fe<sub>10</sub>Wo<sub>46</sub>) + plagioclase (An<sub>89</sub>), while an andesite (62,6 wt% SiO<sub>2</sub>) crystallized orthopyroxene (En<sub>77</sub>Fe<sub>22</sub>Wo<sub>2</sub>) + clinopyroxene (En<sub>48</sub>Fe<sub>10</sub>Wo<sub>42</sub>) + plagioclase (An<sub>76</sub>) + amphibole. Except for plagioclases, which are more calcic than plagioclase microlites from Azufre volcano, the other phases of both associations have a mineral chemistry equivalent to those of olivine, Mg-rich pyroxenes, and amphibole microphenocrysts belonged to Azufre volcano products. These experimental runs crystallized at similar thermodynamic conditions to those inferred from MELTS, except for  $fO_2$  buffer, which is 1 log unit more oxidizing. Similarly, Table 5.4 displays melting experiments on basaltic andesite liquid, whose results support olivine composition and intensive variables inferred from MELTS for its crystallization at the shallow reservoir of the Azufre volcano.

It should be noted that the results of these experiments kinds are strongly sensitive to liquid composition and PH<sub>2</sub>O- $fO_2$  conditions (Grove et al. 1997; Moore and Carmichael 1998; Martel et al. 1999). Thus, it is expected that experimental results should not wholly coincide with the mineral compositions of the Azufre volcano. However, the main conclusion from these data (Table 5.3 and Table 5.4) is the possibility of a shallow origin of olivine and Mg-rich pyroxenes from the Azufre volcano.

Table 5.3: Features of the melting experiments on andesite (spessartite) and basaltic andesite of Moore and Carmichael (1998).

Sample	Spessartite (Mas-12)					Basaltic andesite (Mas-22)			
Run	PEM12-10					PEM22-18			
P (kbar)	1.45					2.04			
T (°C)	950					1025			
H <sub>2</sub> O (wt%)	4.5					5.1			
<i>f</i> O <sub>2</sub>	QFM+2 <sup>a</sup>					QFM+2.3 <sup>a</sup>			
	Sample Mas-12	Opx	Plg	Cpx	Amp	Sample Mas-22	OI	Plg	Cpx
SiO <sub>2</sub>	62.64	53.8	52.1	51.7	44.6	55.25	40.1	47.2	50.5
TiO <sub>2</sub>	0.63	0.2	0.02	1.08	1.68	0.74	0.04	0.11	0.71
Al <sub>2</sub> O <sub>3</sub>	17.25	2.5	29.9	2.7	12.2	17.41	0.8	32.6	4.2
Fe <sub>2</sub> O <sub>3</sub> <sup>b</sup>	2.01					1.96			
FeO <sup>b</sup>	2.01	14.21	0.65	6.18	9.96	4.22	15.55	0.8	6.08
MgO	2.65	27.6	0.05	16.6	15.6	6.68	42.4	0.2	15.4
CaO	5.64	1.26	12.48	19.9	11.17	7.28	0.35	16.39	22
Na <sub>2</sub> O	4.05	0.01	4.2	0.8	2.1	3.97	0.1	2.1	0.3
K <sub>2</sub> O	1.61		0.09		0.37	1.18	0.04	0.08	
P <sub>2</sub> O <sub>5</sub>	0.24					0.27			
Total	99.53	99.6	99.5	99	97.7	99.57	99.4	99.5	99.2
		En <sub>77</sub> Fe <sub>22</sub> WO <sub>2</sub>	An <sub>76</sub>	En <sub>48</sub> Fe <sub>10</sub> WO <sub>42</sub>			FO <sub>83</sub>	An <sub>89</sub>	En <sub>44</sub> Fe <sub>10</sub> WO <sub>46</sub>

Table 5.4: Features of the melting experiment on basaltic andesite of Groove et al. (1997).

Sample	Inclusion 1140mf		
	Run	1140mf-18	1140mf-22
P (kbar)		1	1
T (°C)		1050	1015
H <sub>2</sub> O (wt%)		3.5 <sup>a</sup>	3.5 <sup>a</sup>
<i>f</i> O <sub>2</sub>		<u>QFM+0.7<sup>b</sup></u>	<u>QFM+0.7<sup>b</sup></u>
	Sample 1140mf	OI	OI
SiO <sub>2</sub>	56.3	39.3	39.4
TiO <sub>2</sub>	0.95	0.04	0.03
Al <sub>2</sub> O <sub>3</sub>	17.4	0.04	0.02
Cr <sub>2</sub> O <sub>3</sub>			0.02
FeO <sup>c</sup>	7.17	20.2	20.9
MnO	0.12	0.31	0.29
MgO	4.42	40.2	40.8
CaO	7.88	0.29	0.22
NiO		0.09	0.07
Na <sub>2</sub> O	3.54		
K <sub>2</sub> O	1.26		
P <sub>2</sub> O <sub>5</sub>	0.18		
Total	99.22	100.5	101.8
		F <sub>O78</sub>	F <sub>O78</sub>

## 5.12. Equilibrium time of ilmenite and titanomagnetite

Interdiffusion modellings of paired titanomagnetite-ilmenite microlites were performed considering a spherical geometry for their crystals and the following equation from Prissel et al. (2020) and references therein:

$$f \approx 1 - \frac{6}{\pi^2} \exp\left(-\frac{\pi^2 Dt}{r^2}\right)$$

where  $f$  is the fractional approach to equilibrium with a value of 0.95,  $D$  diffusion coefficient taken at given temperature ( $\text{m}^2\text{s}^{-1}$ ),  $r$  grain radius (m), and  $t$  the time (s) since the perturbation. We determined a representative radius of 5  $\mu\text{m}$  from the average of both semi-minor axis and semi-major axis of ilmenites crystals found in the lava samples of the Azufre volcano (Fig. 5.15). The interdiffusion modellings were performed with titanomagnetite crystals that have titanium mole fraction ( $X_{\text{Ti}}$ ) between 0.08 – 0.14. Calculation details are shown in Excel file “Equilibrium time of ilmenite and titanomagnetite”.

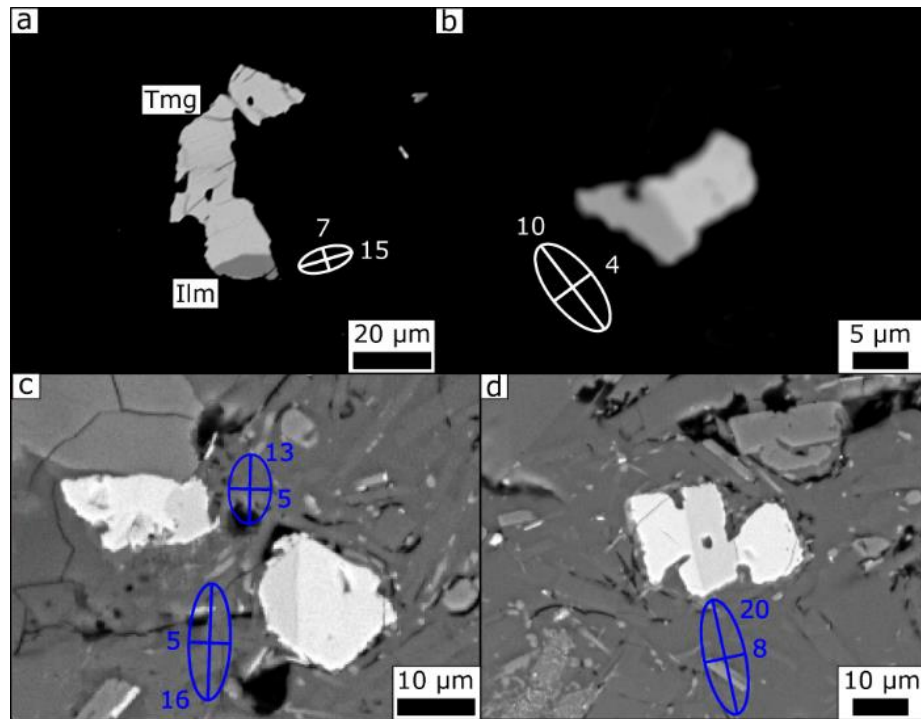


Fig. 5.15: Paired titanomagnetite-ilmenite microlites founded in the lava samples of the Azufre volcano. Different ellipses are drawn next to the small ilmenite crystals with the length of their minor and major axis to determine a representative sphere geometry with a radius of 5 μm



## CAPÍTULO 6: CONCLUSIÓN

La presente investigación establece que la última erupción del volcán Azufre (50 – 331 ka) consiste en una lava de composición andesita-dacítica (61 – 63 SiO<sub>2</sub> wt%) que porta enclaves andesíticos más primitivos (58 – 60 SiO<sub>2</sub> wt%). La erupción se originó producto de procesos magmáticos desarrollados en un reservorio de la corteza superior ( $2 \pm 0,6$  kbar, i.e.,  $5,4 \pm 2,2$  km bajo la superficie si se considera la carga del edificio volcánico). Los enclaves y las distintas fases minerales presentes en el depósito de lava estudiado dan cuenta que el reservorio desarrolló una zonación termal y composicional. Cristales de anfíbola (Grupo 1) y plagioclasa podres en Ca evidencian que el reservorio presentó una zona(s) con magmas de baja temperatura ( $712 - 788 \pm 40$  °C) y en equilibrio con un fundido félsico muy evolucionado ( $\sim 74 \pm 3,3$  SiO<sub>2</sub> wt%), lo cual obedece a condiciones cercanas al *solidus* (680 °C para un sistema granítico saturado en agua). Sin embargo, los enclaves junto con los cristales de olivino, piroxenos ricos en Mg y plagioclasa rica en Ca (An $\geq$ 66) evidencian que existieron intrusiones de un magma más primitivo y caliente ( $905 - 1097 \pm 38$  °C) cuyo origen se asocia a la corteza profunda (45 – 80 km). La intrusión de este magma caliente desencadenaría una serie de procesos tales como el fraccionamiento de fases minerales de alta temperatura, *mixing* con el magma frío, calentamiento del reservorio, producción de líquidos residuales de composición intermedia (evidenciado en piroxenos de bajo Mg) a composición félsica (evidenciado en la asociación amphibola (Grupo 1) + plagioclasa Ca + biotita + cuarzo + óxidos de Fe-Ti + apatito + titanite). Entre todos estos procesos, el *mixing* jugaría un rol preponderante en gatillar la última erupción del volcán Azufre por medio del calentamiento del sistema y un eventual aporte de volátiles (agua principalmente) que sufrieron exsolución.

Adicionalmente, también se determinó que la evolución magmática se desarrolló en condiciones de oxidación correspondientes a QFM + 0.9 – 2.5 unidades logarítmicas y bajo contenidos mínimos de H<sub>2</sub>O entre 3,9 – 5,7 wt% en una cámara magmática con un máximo de 106 km<sup>3</sup> de volumen. Otras fuentes de agua se podrían haberse generado a partir de la descomposición de anfíbolos y biotitas.

Es probable que las observaciones, datos y parámetros determinados sólo cubran una pequeña parte de la evolución del reservorio, lo cual llama a perseverar en la investigación relativa con este volcán y otros que pudiesen representar fuentes de calor en sistemas geotermales activos como el de Cerro Pabellón. Por lo anterior, nuestro modelo presenta limitaciones al momento de definir este reservorio como una posible fuente de calor del sistema geotermal de Cerro Pabellón, ya que no da cuenta de la longevidad del reservorio, su evolución termal en una línea de tiempo mayor en la escala de miles de años ni de la difusión térmica hacia la corteza.

No obstante, nuestro modelo representa un avance significativo en la dirección de establecer que los reservorios magmáticos del volcán Azufre y los domos dacíticos emplazados alrededor de él (domos Chanca, Chac Inca y Cerro Pabellón) podrían ser la principal fuente de calor del sistema geotermal de Cerro Pabellón. Incluso, si se considera la cercanía entre estas unidades volcánicas, la similitud geoquímica mostrada por sus enclaves y el probable control estructural extensivo del lineamiento NW-SE de 70 km en sus emplazamientos, se podría sugerir que comparten el mismo reservorio magmático somero. De esta forma, los domos dacíticos podrían representar la extracción de un magma silíceo (como el identificado para la zona fría del volcán Azufre) con un menor grado de mixing en relación con el que generó la lava andesítica estudiada.

En síntesis, esta investigación entrega antecedentes novedosos en la perspectiva de plantear el reservorio magmático del volcán Azufre como una posible fuente de calor del sistema geotermal de Cerro Pabellón (Fig. 6.1), el cual es el único en explotación para producir corriente eléctrica en Sudamérica.

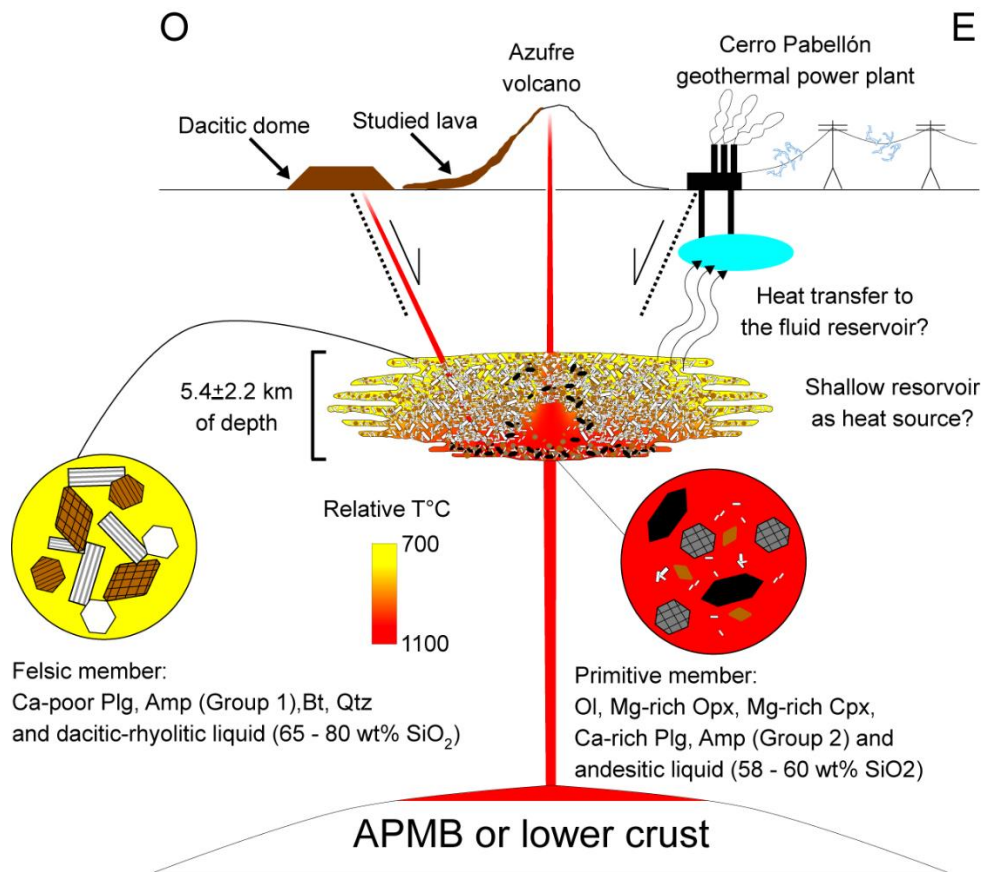


Fig. 6.1: Modelo conceptual que plantea al reservorio magmático del volcán Azufre como una posible fuente de calor del sistema geotermal de Cerro Pabellón. Adicionalmente, se destaca también el posible rol que podría jugar el lineamiento NW-SE (estructura extensiva) en el ascenso de los magmas que originaron los domos dacíticos y la lava andesítica estudiada del volcán Azufre a partir de un mismo reservorio.

## BIBLIOGRAPHY

Allmendinger RW, Jordan TE, Kay SM, Isacks BL (1997) The evolution of the Altiplano-Puna plateau of the Central Andes. *Annu Rev Earth Planet Sci* 25:139–174. <https://doi.org/10.1146/annurev.earth.25.1.139>

Anderson JL, Smith DR (1995) The effects of temperature and  $fO_2$  on the Al-in-hornblende barometer. *American Mineralogist* 80:549–559. <https://doi.org/10.2138/am-1995-5-614>

Annen C, Blundy JD, Sparks RSJ (2006) The genesis of intermediate and silicic magmas in deep crustal hot zones. *Journal of Petrology* 47:505–539. <https://doi.org/10.1093/petrology/egi084>

Aragon R, McCallister RH, Harrison HR (1984) Cation diffusion in titanomagnetites. *Contributions to Mineralogy and Petrology* 85:174–185. <https://doi.org/10.1007/BF00371707>

Aravena A, Gutiérrez FJ, Parada MA, et al (2017) Compositional zonation of the shallow La Gloria pluton (Central Chile) by late-stage extraction/redistribution of residual melts by channelization: Numerical modeling. *Lithos* 284–285:578–587. <https://doi.org/10.1016/J.LITHOS.2017.05.013>

Aravena D, Muñoz M, Morata D, et al (2016) Assessment of high enthalpy geothermal resources and promising areas of Chile. *Geothermics* 59:1–13. <https://doi.org/10.1016/j.geothermics.2015.09.001>

Araya Vargas J, Meqbel NM, Ritter O, et al (2019) Fluid distribution in the Central Andes Subduction Zone imaged with magnetotellurics. *J Geophys Res Solid Earth* 124:4017–4034. <https://doi.org/10.1029/2018JB016933>

Audétat A, Simon AC (2012) Magmatic Controls on Porphyry Copper Genesis. In: Hedenquist J. W., Harris M., Camus F. (eds) *Geology and Genesis of Major Copper Deposits and Districts of the World: A Tribute to Richard H. Sillitoe*. Society of Economic Geologists, pp 553–572

Bachmann O, Dungan MA (2002) Temperature-induced Al-zoning in hornblendes of the Fish Canyon magma, Colorado. *American Mineralogist* 87:1062–1076. <https://doi.org/10.2138/am-2002-8-903>

Bachmann O, Bergantz GW (2004) On the origin of crystal-poor rhyolites: Extracted from batholithic crystal mushes. *Journal of Petrology* 45:1565–1582. <https://doi.org/10.1093/petrology/egh019>

Bachmann O, Bergantz GW (2008) Deciphering magma chamber dynamics from styles of compositional zoning in large silicic ash flow sheets. *Rev Mineral Geochem* 69:651–674. <https://doi.org/10.2138/rmg.2008.69.17>

Bachmann O, Huber C (2016) Silicic magma reservoirs in the Earth's crust. *American Mineralogist* 101:2377–2404. <https://doi.org/10.2138/am-2016-5675>

Bacon CR, Hirschmann MM (1988) Mg/Mn partitioning as a test for equilibrium between coexisting Fe-Ti oxides. *American Mineralogist* 73:57–61

Bardintzeff JM, Bonin B (1987) The amphibole effect: A possible mechanism for triggering explosive eruptions. *Journal of Volcanology and Geothermal Research* 33:255–262. [https://doi.org/10.1016/0377-0273\(87\)90017-5](https://doi.org/10.1016/0377-0273(87)90017-5)

Beck SL, Zandt G (2002) The nature of orogenic crust in the central Andes. *J Geophys Res Solid Earth* 107:1–16. <https://doi.org/10.1029/2000jb000124>

Bell AS, Simon A (2011) Experimental evidence for the alteration of the  $\text{Fe}^{3+}/\Sigma\text{Fe}$  of silicate melt caused by the degassing of chlorine-bearing aqueous volatiles. *Geology* 39:499–502

Bergantz GW, Schleicher JM, Burgisser A (2015) Open-system dynamics and mixing in magma mushes. *Nat Geosci* 8:793–796. <https://doi.org/10.1038/ngeo2534>

Bertin D, Amigo A (2019) Geología del volcán San Pedro, región de Antofagasta. Servicio Nacional de Geología y Minería, Carta Geológica de Chile, Serie Geología Básica, mapa escala 1:50.000. Santiago, Chile.

Blatter DL, Sisson TW, Hankins WB (2013) Crystallization of oxidized, moderately hydrous arc basalt at mid- to lower-crustal pressures: Implications for andesite genesis.

Contributions to Mineralogy and Petrology 166:861–886. <https://doi.org/10.1007/s00410-013-0920-3>

Bottinga Y, Weill D, Richet P (1982) Density calculations for silicate liquids. I. Revised method for aluminosilicate compositions. *Geochimica et Cosmochimica Acta*, 46(6), 909–919.

Browne BL, Gardner JE (2006) The influence of magma ascent path on the texture, mineralogy, and formation of hornblende reaction rims. *Earth Planet Sci Lett* 246:161–176. <https://doi.org/10.1016/J.EPSL.2006.05.006>

Buckley VJE, Sparks RSJ, Wood BJ (2006) Hornblende dehydration reactions during magma ascent at Soufrière Hills Volcano, Montserrat. *Contributions to Mineralogy and Petrology* 151:121–140. <https://doi.org/10.1007/S00410-005-0060-5>

Buddington AF, Lindsley DH (1964) Iron-titanium oxide minerals and synthetic equivalents. *Journal of Petrology* 5:310–357. <https://doi.org/10.1093/petrology/5.2.310>

Burns DH, de Silva SL, Tepley F, et al (2015) Recording the transition from flare-up to steady-state arc magmatism at the Purico-Chascon volcanic complex, northern Chile. *Earth Planet Sci Lett* 422:75–86. <https://doi.org/10.1016/j.epsl.2015.04.002>

Burov E, Jaupart C, Guillou-Frottier L (2003) Ascent and emplacement of buoyant magma bodies in brittle-ductile upper crust. *J Geophys Res Solid Earth* 108:2177. <https://doi.org/10.1029/2002jb001904>

Cappetti G, Giorgi N, Arias A, Volpi G, Rivera G, Cei M, Baccarin F (2020). The Cerro Pabellón Geothermal Project (Chile): from surface exploration to energy production. In *Proceedings of the World Geothermal Congress (Vol. 1)*.

Caricchi L, Townsend M, Rivalta E, Namiki A (2021) The build-up and triggers of volcanic eruptions. *Nat Rev Earth Environ* 2:458–476. <https://doi.org/10.1038/s43017-021-00174-8>

Cashman K, Blundy J (2013) Petrological cannibalism: The chemical and textural consequences of incremental magma body growth. *Contributions to Mineralogy and Petrology* 166:703–729. <https://doi.org/10.1007/s00410-013-0895-0>

Cashman K v., Sparks RSJ, Blundy JD (2017) Vertically extensive and unstable magmatic systems: A unified view of igneous processes. *Science* 355: <https://doi.org/10.1126/science.aag3055>

Castro A (2014) The off-crust origin of granite batholiths. *Geoscience Frontiers* 5:63–75. <https://doi.org/10.1016/j.gsf.2013.06.006>

Castruccio A, Diez M, Gho R (2017). The influence of plumbing system structure on volcano dimensions and topography. *Journal of Geophysical Research: Solid Earth*, 122(11), 8839-8859.

Charrier R, Muñoz N (1994). Jurassic Cretaceous Palaeogeographic evolution of the Chilean Andes at 23–24 S latitude and 34–35 S latitude: A comparative analysis. In *Tectonics of the Southern Central Andes: Structure and Evolution of an Active Continental Margin* (pp. 233-242). Berlin, Heidelberg: Springer Berlin Heidelberg.

Charrier R, Pinto L, Rodriguez MP (2007) Tectonostatigraphic evolution of the Andean Orogen in Chile. In: Moreno T, Gibbons W (eds) *The Geology of Chile*. The Geological Society, pp 21–114

Chelle-Michou C, Rottier B, Caricchi L, Simpson G (2017) Tempo of magma degassing and the genesis of porphyry copper deposits. *Scientific Reports* 7:1–12. <https://doi.org/10.1038/srep40566>

Chernicoff C J, Richards J P, Zappettini E O (2002). Crustal lineament control on magmatism and mineralization in northwestern Argentina: geological, geophysical, and remote sensing evidence. *Ore Geology Reviews*, 21(3-4), 127-155.

Chmielowski J, Zandt G, Haberland C (1999) The Central Andean Altiplano-Puna magma body. *Geophys Res Lett* 26:783–786. <https://doi.org/10.1029/1999GL900078>

Comeau MJ, Unsworth MJ, Ticona F, Sunagua M (2015) Magnetotelluric images of magma distribution beneath Volcán Uturuncu, Bolivia: Implications for magma dynamics. *Geology* 43:243–246. <https://doi.org/10.1130/G36258.1>

Comeau MJ, Unsworth MJ, Cordell D (2016). New constraints on the magma distribution and composition beneath Volcán Uturuncu and the southern Bolivian Altiplano from magnetotelluric data. *Geosphere*, 12(5), 1391-1421.

Cooper KM, Kent AJR (2014) Rapid remobilization of magmatic crystals kept in cold storage. *Nature* 506:480–483. <https://doi.org/10.1038/nature12991>

Cornejo P C, Mahood G A (1997). Seeing past the effects of re-equilibration to reconstruct magmatic gradients in plutons: La Gloria Pluton, central Chilean Andes. *Contributions to Mineralogy and Petrology*, 127, 159-175.

de Silva SL (1989a) Geochronology and stratigraphy of the ignimbrites from the 21°30'S to 23°30'S portion of the Central Andes of northern Chile. *Journal of Volcanology and Geothermal Research* 37:93–131. [https://doi.org/10.1016/0377-0273\(89\)90065-6](https://doi.org/10.1016/0377-0273(89)90065-6)

de Silva SL (1989b) Altiplano-Puna volcanic complex of the central Andes. *Geology* 17:1102–1106. [https://doi.org/https://doi.org/10.1130/0091-7613\(1989\)017<1102:APVCOT>2.3.CO;2](https://doi.org/10.1130/0091-7613(1989)017<1102:APVCOT>2.3.CO;2)

de Silva S L, Self S, Francis P W, Carlos R R (1994) Effusive silicic volcanism in the Central Andes: The Chao dacite and other young lavas of the Altiplano-Puna Volcanic Complex. *Journal of Geophysical Research: Solid Earth*, 99(B9): 17805-17825.

de Silva SL, Gosnold WD (2007) Episodic construction of batholiths: Insights from the spatiotemporal development of an ignimbrite flare-up. *Journal of Volcanology and Geothermal Research* 167:320–335. <https://doi.org/10.1016/J.JVOLGEORES.2007.07.015>

de Silva SL, Kay SM (2018) Turning up the heat: High-flux magmatism in the Central Andes. *Elements* 14:245–250. <https://doi.org/10.2138/gselements.14.4.245>

de Silva SL, Zandt G, Trumbull R, et al (2006) Large ignimbrite eruptions and volcano-tectonic depressions in the Central Andes: A thermomechanical perspective. In: Troise C, de Natale G, Kilburn CRJ (eds) *Mechanisms of Activity and Unrest at Large Calderas*. Geological Society of London, pp 47–63



Deer WA, Howie RA, Zussman J (1992) An introduction to the rock-forming minerals, 2nd edition. Longman Scientific & Technical, Harlow, UK

del Potro R, Díez M, Blundy J, et al (2013) Diapiric ascent of silicic magma beneath the Bolivian Altiplano. *Geophys Res Lett* 40:2044–2048. <https://doi.org/10.1002/grl.50493>

Delunel R, Blard PH, Martin LCP, et al (2016) Long term low latitude and high elevation cosmogenic  $^3\text{He}$  production rate inferred from a 107 ka-old lava flow in northern Chile; 22°S-3400 m.a.s.l. *Geochim Cosmochim Acta* 184:71–87. <https://doi.org/10.1016/j.gca.2016.04.023>

Dufek J, Bachmann O (2010) Quantum magmatism: Magmatic compositional gaps generated by melt-crystal dynamics. *Geology* 38:687–690. <https://doi.org/10.1130/G30831.1>

Erdmann S, Martel C, Pichavant M, Kushnir A (2014) Amphibole as an archivist of magmatic crystallization conditions: problems, potential, and implications for inferring magma storage prior to the paroxysmal 2010 eruption of Mount Merapi, Indonesia. *Contributions to Mineralogy and Petrology* 167:1–23. <https://doi.org/10.1007/s00410-014-1016-4>

Evans K A, Elburg M A, Kamenetsky V S (2012) Oxidation state of subarc mantle. *Geology*, 40(9), 783-786.

Feeley T C, Davidson J P (1994). Petrology of calc-alkaline lavas at Volcán Ollagüe and the origin of compositional diversity at central Andean stratovolcanoes. *Journal of Petrology*, 35(5), 1295-1340.

Fiedrich AM, Martin LHJ, Storck JC, et al (2018) The influence of water in silicate melt on aluminium excess in plagioclase as a potential hygrometer. *Sci Rep* 8:1–8. <https://doi.org/10.1038/s41598-018-29178-z>

Freer R, Hauptman Z (1978) An experimental study of magnetite-titanomagnetite interdiffusion. *Physics of the Earth and Planetary Interiors* 16:223–231. [https://doi.org/10.1016/0031-9201\(78\)90015-8](https://doi.org/10.1016/0031-9201(78)90015-8)

Freytmuth H, Brandmeier M, Wörner G (2015). The origin and crust/mantle mass balance of Central Andean ignimbrite magmatism constrained by oxygen and strontium isotopes and erupted volumes. *Contributions to Mineralogy and Petrology*, 169, 1-24.

Frost BR (1991) Introduction to oxygen fugacity and its petrologic importance. In: Lindsley DH (ed) *Oxide Minerals: Petrologic and Magnetic Significance*. *Reviews in Mineralogy*, pp 1–10

Gelman SE, Gutiérrez FJ, Bachmann O (2013) On the longevity of large upper crustal silicic magma reservoirs. *Geology* 41:759–762. <https://doi.org/10.1130/G34241.1>

Ghiorso MS, Evans BW (2008) Thermodynamics of rhombohedral oxide solid solutions and a revision of the Fe-Ti two-oxide geothermometer and oxygen-barometer. *Am J Sci* 308:957–1039. <https://doi.org/10.2475/09.2008.01>

Giambiagi L, Alvarez P, Spagnotto S (2016). Temporal variation of the stress field during the construction of the central Andes: Constrains from the volcanic arc region (22–26 S), Western Cordillera, Chile, during the last 20 Ma. *Tectonics*, 35(9), 2014-2033.

Giordano D, Russell J K, Dingwell D B (2008). Viscosity of magmatic liquids: a model. *Earth and Planetary Science Letters*, 271(1-4), 123-134.

Giordano G, Caricchi L (2022). Determining the state of activity of transcrustal magmatic systems and their volcanoes. *Annual Review of Earth and Planetary Sciences*, 50, 231-259.

Glazner AF, Bartley JM, Coleman DS, et al (2004) Are pluton assembled over millions of years by amalgamation from small magma chambers? *GSA Today* 14:4–11. [https://doi.org/10.1130/1052-5173\(2004\)014<0004:APAOMO>2.0.CO;2](https://doi.org/10.1130/1052-5173(2004)014<0004:APAOMO>2.0.CO;2)

Godoy B, Wörner G, Kojima S, Aguilera F, Simon K, Hartmann G (2014). Low-pressure evolution of arc magmas in thickened crust: The San Pedro–Linzor volcanic chain, Central Andes, Northern Chile. *Journal of South American earth sciences*, 52, 24-42.

Godoy B, Wörner G, le Roux P, et al (2017) Sr- and Nd- isotope variations along the Pleistocene San Pedro – Linzor volcanic chain, N. Chile: Tracking the influence of the

upper crustal Altiplano-Puna Magma Body. *Journal of Volcanology and Geothermal Research* 341:172–186. <https://doi.org/10.1016/j.jvolgeores.2017.05.030>

Godoy B, Taussi M, González-Maurel O, et al (2022) Evolution of the Azufre volcano (northern Chile): Implications for the Cerro Pabellón Geothermal Field as inferred from long lasting eruptive activity. *Journal of Volcanology and Geothermal Research* 423:107472. <https://doi.org/10.1016/J.JVOLGEORES.2022.107472>

González-Maurel O, Godoy B, le Roux P, et al (2019) Magmatic differentiation at La Poruña scoria cone, Central Andes, northern Chile: Evidence for assimilation during turbulent ascent processes, and genetic links with mafic eruptions at adjacent San Pedro volcano. *Lithos* 338–339:128–140. <https://doi.org/10.1016/j.lithos.2019.03.033>

Gorini A, Ridolfi F, Piscaglia F, et al (2018) Application and reliability of calcic amphibole thermobarometry as inferred from calc-alkaline products of active geothermal areas in the Andes. *Journal of Volcanology and Geothermal Research* 358:58–76. <https://doi.org/10.1016/j.jvolgeores.2018.03.018>

Grove TL, Donnelly-Nolan JM, Housh T (1997) Magmatic processes that generated the rhyolite of Glass Mountain, Medicine Lake volcano, N. California. *Contributions to Mineralogy and Petrology* 127:205–223. <https://doi.org/10.1007/s004100050276>

Gualda GAR, Ghiorso MS, Lemons R v., Carley TL (2012) Rhyolite-MELTS: A modified calibration of MELTS optimized for silica-rich, fluid-bearing magmatic systems. *Journal of Petrology* 53:875–890. <https://doi.org/10.1093/petrology/egr080>

Gutiérrez F, Parada MA (2010) Numerical Modeling of Time-dependent Fluid Dynamics and Differentiation of a Shallow Basaltic Magma Chamber. *Journal of Petrology* 51:731–762. <https://doi.org/10.1093/petrology/egp101>

Gutiérrez F, Payacán I, Gelman SE, et al (2013) Late-stage magma flow in a shallow felsic reservoir: Merging the anisotropy of magnetic susceptibility record with numerical simulations in La Gloria Pluton, central Chile. *J Geophys Res Solid Earth* 118:1984–1998. <https://doi.org/10.1002/JGRB.50164>

Gutiérrez F, Payacán I, Szymanowski D, et al (2018) Lateral magma propagation during the emplacement of La Gloria Pluton, central Chile. *Geology* 46:1051–1054. <https://doi.org/10.1130/G45361.1>

Hammond PA, Taylor LA (1982) The ilmenite/titano-magnetite assemblage: kinetics of re-equilibration. *Earth Planet Sci Lett* 61:143–150. [https://doi.org/10.1016/0012-821X\(82\)90047-4](https://doi.org/10.1016/0012-821X(82)90047-4)

Hawthorne FC, Oberti R, Harlow GE, et al (2012) Ima report: Nomenclature of the amphibole supergroup. *American Mineralogist* 97:2031–2048. <https://doi.org/10.2138/am.2012.4276>

Hedenquist JW, Lowenstern JB (1994) The role of magmas in the formation of hydrothermal ore deposits. *Nature* 370:519–527. <https://doi.org/10.1038/370519a0>

Henton de Angelis S, Larsen J, Coombs M, et al (2015) Amphibole reaction rims as a record of pre-eruptive magmatic heating: An experimental approach. *Earth Planet Sci Lett* 426:235–245. <https://doi.org/10.1016/j.epsl.2015.06.051>

Hildreth W (1981) Gradients in silicic magma chambers: implications for lithospheric magmatism. *J Geophys Res* 86:10153–10192. <https://doi.org/10.1029/JB086iB11p10153>

Hildreth W (2004) Volcanological perspectives on Long Valley, Mammoth Mountain, and Mono Craters: Several contiguous but discrete systems. *Journal of Volcanology and Geothermal Research* 136:169–198. <https://doi.org/10.1016/j.jvolgeores.2004.05.019>

Hildreth W, Moorbath S (1988) Crustal contributions to arc magmatism in the Andes of Central Chile. *Contributions to Mineralogy and Petrology* 98:455–489. <https://doi.org/10.1007/BF00372365>

Hirose K, Kawamoto T (1995) Hydrous partial melting of lherzolite at 1 GPa: the effect of H<sub>2</sub>O on the genesis of basaltic magmas. *Earth and planetary Science letters*, 133(3-4), 463-473.

Holland T, Blundy J (1994) Non-ideal interactions in calcic amphiboles and their bearing on amphibole-plagioclase thermometry. *Contributions to Mineralogy and Petrology* 116:433–447. <https://doi.org/10.1007/BF00310910>

Holtz F, Johannes W, Tamic N, Behrens H (2001) Maximum and minimum water contents of granitic melts generated in the crust: A reevaluation and implications. *Lithos* 56:1–14. [https://doi.org/10.1016/S0024-4937\(00\)00056-6](https://doi.org/10.1016/S0024-4937(00)00056-6)

Holtz F, Sato H, Lewis J, et al (2005) Experimental petrology of the 1991-1995 Unzen dacite, Japan. Part I: Phase relations, phase composition and pre-eruptive conditions. *Journal of Petrology* 46:319–337. <https://doi.org/10.1093/petrology/egh077>

Huber C, Townsend M, Degruyter W, Bachmann O (2019) Optimal depth of subvolcanic magma chamber growth controlled by volatiles and crust rheology. *Nat Geosci* 12:762–768. <https://doi.org/10.1038/s41561-019-0415-6>

Hübner (2018) Evolución geológica del Volcán Azufre, II Región de Antofagasta. Tesis de grado, Universidad de Chile, Santiago.

Humphreys MCS, Brooker RA, Fraser DG, et al (2015) Coupled Interactions between Volatile Activity and Fe Oxidation State during Arc Crustal Processes. *Journal of Petrology* 56:795–814

Huppert HE, Sparks RSJ (1984) Double-Diffusive Convection Due to Crystallization in Magmas. *Annu Rev Earth Planet Sci* 12:11–37. <https://doi.org/10.1146/ANNUREV.EA.12.050184.000303>

Irvine TN, Baragar WRA (1971) A guide to the chemical classification of the common volcanic rocks. *Can J Earth Sci* 8:523–548. <https://doi.org/10.1139/e71-055>

Isacks BL (1988) Uplift of the central Andean Plateau and bending of the Bolivian Orocline. *J Geophys Res* 93:3211–3231. <https://doi.org/10.1029/JB093iB04p03211>

Ishizuka O, Taylor RN, Geshi N, Oikawa T, Kawanabe Y, Ogitsu I (2015). Progressive mixed-magma recharging of Izu-Oshima volcano, Japan: A guide to magma chamber volume. *Earth and Planetary Science Letters*, 430, 19-29.

Jackson MD, Blundy J, Sparks RSJ (2018) Chemical differentiation, cold storage and remobilization of magma in the Earth's crust. *Nature* 564:405–409. <https://doi.org/10.1038/s41586-018-0746-2>

Johnson MC, Rutherford MJ (1989) Experimental calibration of the aluminum-in-hornblende geobarometer with application to Long Valley caldera (California) volcanic rocks. *Geology* 17:837–841. [https://doi.org/10.1130/0091-7613\(1989\)017<0837:ECOTAI>2.3.CO;2](https://doi.org/10.1130/0091-7613(1989)017<0837:ECOTAI>2.3.CO;2)

Johnson SE, Fletcher JM, Fanning CM, et al (2003) Structure, emplacement and lateral expansion of the San José tonalite pluton, Peninsular Ranges batholith, Baja California, México. *J Struct Geol* 25:1933–1957. [https://doi.org/10.1016/S0191-8141\(03\)00015-4](https://doi.org/10.1016/S0191-8141(03)00015-4)

Karakas O, Degruyter W, Bachmann O, Dufek J (2017) Lifetime and size of shallow magma bodies controlled by crustal-scale magmatism. *Nat Geosci* 10:446–450. <https://doi.org/10.1038/ngeo2959>

Kay SM, Coira BL, Caffè PJ, Chen CH (2010) Regional chemical diversity, crustal and mantle sources and evolution of central Andean Puna plateau ignimbrites. *Journal of Volcanology and Geothermal Research* 198:81–111. <https://doi.org/10.1016/J.JVOLGEORES.2010.08.013>

Kelley K A, Cottrell E (2009) Water and the oxidation state of subduction zone magmas. *Science*, 325(5940), 605-607.

Kiser E, Palomeras I, Levander A, et al (2016) Magma reservoirs from the upper crust to the Moho inferred from high-resolution Vp and Vs models beneath Mount St. Helens, Washington State, USA. *Geology* 44:411–414. <https://doi.org/10.1130/G37591.1>

Kress VC, Carmichael ISE (1991) The compressibility of silicate liquids containing Fe<sub>2</sub>O<sub>3</sub> and the effect of composition, temperature, oxygen fugacity and pressure on their redox states. *Contributions to Mineralogy and Petrology* 108:82–92. <https://doi.org/10.1007/BF00307328>

Lahsen A, Rojas J, Morata D, Aravena D (2015). Geothermal exploration in Chile: country update. In *Proceedings, World Geothermal Congress*.

Landi P, Métrich N, Bertagnini A, Rosi M (2004) Dynamics of magma mixing and degassing recorded in plagioclase at Stromboli (Aeolian Archipelago, Italy). *Contributions to Mineralogy and Petrology* 147:213–227. <https://doi.org/10.1007/s00410-004-0555-5>

Lange R A (1994) The effects of H<sub>2</sub>O, CO<sub>2</sub> and F on the density and viscosity of silicate melts. In: Volatiles in Magmas. Reviews in Mineralogy, 30.

Laumonier M, Gaillard F, Muir D, et al (2017) Giant magmatic water reservoirs at mid-crustal depth inferred from electrical conductivity and the growth of the continental crust. *Earth Planet Sci Lett* 457:173–180. <https://doi.org/10.1016/j.epsl.2016.10.023>

Laumonier M, Scaillet B, Pichavant M, et al (2014) On the conditions of magma mixing and its bearing on andesite production in the crust. *Nat Commun* 5:1–12. <https://doi.org/10.1038/ncomms6607>

le Bas MJ, le Maitre RW, Streckeisen A, Zanettin B (1986) A chemical classification of volcanic rocks based on the total alkali-silica diagram. *Journal of Petrology* 27:745–750. <https://doi.org/10.1093/petrology/27.3.745>

Lee CT, Dee S (2019) Does volcanism cause warming or cooling? *Geology* 47:687–688. <https://doi.org/10.1130/focus072019.1>

Lee KC (2001) Classification of geothermal resources by exergy. *Geothermics* 30:431–442. [https://doi.org/10.1016/S0375-6505\(00\)00056-0](https://doi.org/10.1016/S0375-6505(00)00056-0)

Li X, Zhang C, Behrens H, Holtz F (2020) Calculating biotite formula from electron microprobe analysis data using a machine learning method based on principal components regression. *Lithos* 356–357:105371. <https://doi.org/10.1016/j.lithos.2020.105371>

Lieu WK, Stern RJ (2019) The robustness of Sr/Y and La/Yb as proxies for crust thickness in modern arcs. *Geosphere* 15:621–641. <https://doi.org/10.1130/GES01667.1>

Lindsay JM, Schmitt AK, Trumbull RB, et al (2001) Magmatic evolution of the La Pacana caldera system, Central Andes, Chile: Compositional variation of two cogenetic, large-volume felsic ignimbrites. *Journal of Petrology* 42:459–486. <https://doi.org/10.1093/petrology/42.3.459>

Locock AJ (2014) An Excel spreadsheet to classify chemical analyses of amphiboles following the IMA 2012 recommendations. *Comput Geosci* 62:1–11. <https://doi.org/10.1016/j.cageo.2013.09.011>

Marsh BD (1996) Solidification fronts and magmatic evolution. *Mineral Mag* 60:5–40. <https://doi.org/10.1180/MINMAG.1996.060.398.03>

Martel C, Pichavant M, Holtz F, et al (1999) Effects of fO<sub>2</sub> and H<sub>2</sub>O on andesite phase relations between 2 and 4 kbar. *J Geophys Res Solid Earth* 104:29453–29470. <https://doi.org/10.1029/1999JB900191>

Mather TA, Pyle DM, Allen AG (2004) Volcanic source for fixed nitrogen in the early Earth's atmosphere. *Geology* 32:905–908. <https://doi.org/10.1130/G20679.1>

Mattioli M, Renzulli A, Menna M, Holm P M (2006). Rapid ascent and contamination of magmas through the thick crust of the CVZ (Andes, Ollagüe region): Evidence from a nearly aphyric high-K andesite with skeletal olivines. *Journal of Volcanology and Geothermal Research*, 158(1-2), 87-105.

Maza SN, Collo G, Morata D, et al (2021) Active and fossil hydrothermal zones of the Apacheta volcano: Insights for the Cerro Pabellón hidden geothermal system (Northern Chile). *Geothermics* 96:102206. <https://doi.org/10.1016/J.GEOTHERMICS.2021.102206>

McBirney A R, Murase T (1984). Rheological properties of magmas. *Annual Review of Earth and Planetary Sciences*, 12(1), 337-357.

Menand T, Annen C, Blanquat M de saint (2015) Rates of magma transfer in the crust: Insights into magma reservoir recharge and pluton growth. *Geology* 43:199–202. <https://doi.org/10.1130/G36224.1>

Miller CA, Williams-Jones G, Fournier D, Witter J (2017). 3D gravity inversion and thermodynamic modelling reveal properties of shallow silicic magma reservoir beneath Laguna del Maule, Chile. *Earth and Planetary Science Letters*, 459, 14-27.

Moeck IS (2014) Catalog of geothermal play types based on geologic controls. *Renewable and Sustainable Energy Reviews* 37:867–882

Moore G, Carmichael ISE (1998) The hydrous phase equilibria (to 3 kbar) of an andesite and basaltic andesite from western Mexico: Constraints on water content and conditions of phenocryst growth. *Contributions to Mineralogy and Petrology* 130:304–319. <https://doi.org/10.1007/s004100050367>



Moore G, Vennemann T, Carmichael ISE (1998) An empirical model for the solubility of H<sub>2</sub>O in magmas to 3 kilobars. *American Mineralogist* 83:36–42. <https://doi.org/10.2138/AM-1998-1-203>

Morgado E, Morgan DJ, Castruccio A, et al (2019) Old magma and a new, intrusive trigger: using diffusion chronometry to understand the rapid-onset Calbuco eruption, April 2015 (Southern Chile). *Contributions to Mineralogy and Petrology* 174:61. <https://doi.org/10.1007/s00410-019-1596-0>

Moussallam Y, Oppenheimer C, Scaillet B, et al (2014) Tracking the changing oxidation state of Erebus magmas, from mantle to surface, driven by magma ascent and degassing. *Earth Planet Sci Lett* 393:200–209

Mpodosis C, Ramos V A (2008). Tectónica jurásica en Argentina y Chile: extensión, subducción oblicua, rifting, deriva y colisiones?. *Revista de la Asociación geológica Argentina*, 63(4), 481-497.

Muir DD, Blundy JD, Hutchinson MC, Rust AC (2014a) Petrological imaging of an active pluton beneath Cerro Uturuncu, Bolivia. *Contributions to Mineralogy and Petrology* 167:1–25. <https://doi.org/10.1007/S00410-014-0980-Z/FIGURES/14>

Muir DD, Blundy JD, Rust AC, Hickey J (2014b) Experimental constraints on dacite pre-eruptive magma storage conditions beneath uturuncu volcano. *Journal of Petrology* 55:749–767. <https://doi.org/10.1093/petrology/egu005>

Mutch E J F, Blundy JD, Tattitch BC, et al (2016) An experimental study of amphibole stability in low-pressure granitic magmas and a revised Al-in-hornblende geobarometer. *Contributions to Mineralogy and Petrology* 171:85. <https://doi.org/10.1007/s00410-016-1298-9>

Noble S R, Aspden J A, Jemielita R (1997). Northern Andean crustal evolution: New U-Pb geochronological constraints from Ecuador. *Geological Society of America Bulletin*, 109(7), 789-798.

Pardo-Casas F, Molnar P (1987) Relative motion of the Nazca (Farallon) and South American plates since Late Cretaceous time. *Tectonics*, 6(3), 233-248.

- Payacán I, Gutiérrez F, Gelman S E, Bachmann O, Parada M Á (2014) Comparing magnetic and magmatic fabrics to constrain the magma flow record in La Gloria pluton, central Chile. *Journal of Structural Geology*, 69, 32-46.
- Peacock S M (1993) Large-scale hydration of the lithosphere above subducting slabs. *Chemical Geology*, 108(1-4), 49-59.
- Pearce J A, Peate D W (1995) Tectonic implications of the composition of volcanic arc magmas. *Annual review of Earth and planetary sciences*, 23(1), 251-285.
- Perkins JP, Ward KM, de Silva SL, et al (2016) Surface uplift in the Central Andes driven by growth of the Altiplano Puna Magma Body. *Nat Commun* 7:1–10. <https://doi.org/10.1038/ncomms13185>
- Petford N, Cruden AR, McCaffrey KJW, Vigneresse JL (2000) Granite magma formation, transport and emplacement in the Earth's crust. *Nature* 408:669–673. <https://doi.org/10.1038/35047000>
- Prezzi CB, Götze HJ, Schmidt S (2009) 3D density model of the Central Andes. *Physics of the Earth and Planetary Interiors* 177:217–234. <https://doi.org/10.1016/j.pepi.2009.09.004>
- Prissel KB, Krawczynski MJ, van Orman JA (2020) Fe–Mg and Fe–Mn interdiffusion in ilmenite with implications for geospeedometry using oxides. *Contributions to Mineralogy and Petrology* 175:62. <https://doi.org/10.1007/s00410-020-01695-z>
- Profeta L, Ducea MN, Chapman JB, et al (2015) Quantifying crustal thickness over time in magmatic arcs. *Scientific Reports* 2015 5:1 5:1–7. <https://doi.org/10.1038/srep17786>
- Putirka KD (2005) Igneous thermometers and barometers based on plagioclase + liquid equilibria: Tests of some existing models and new calibrations. *American Mineralogist* 90:336–346. <https://doi.org/10.2138/AM.2005.1449>
- Putirka KD (2008) Thermometers and barometers for volcanic systems. In: Putirka KD, Tepley III FJ (eds) *Minerals, Inclusions and Volcanic Processes*. *Reviews in Mineralogy and Geochemistry*, pp 61–120

Putirka K (2016) Special collection: Rates and depths of magma ascent on earth: Amphibole thermometers and barometers for igneous systems and some implications for eruption mechanisms of felsic magmas at arc volcanoes. *American Mineralogist* 101:841–858. <https://doi.org/10.2138/am-2016-5506>

Putirka K (2016) Amphibole thermometers and barometers for igneous systems and some implications for eruption mechanisms of felsic magmas at arc volcanoes. *American Mineralogist* 101:841–858. <https://doi.org/10.2138/am-2016-5506>

Ramírez C, Huete C (1980) Carta Geológica Regional N°40: Hoja Ollague. Servicio Nacional de Geología y Minería.

Renzulli A, Menna M, Tibaldi A, Flude S (2006) New data of surface geology, petrology and Ar-Ar geochronology of the Altiplano-Puna Volcanic Complex (norther Chile) in the framework of future geothermal exploration. In: *Actas XI Congreso Geológico Chileno*, Antofagasta, Chile. pp 307–310

Reymer A, Schubert G (1984) Phanerozoic addition rates to the continental crust and crustal growth. *Tectonics*, 3(1), 63-77.

Richards J P (2003) Tectono-magmatic precursors for porphyry Cu-(Mo-Au) deposit formation. *Economic geology*, 98(8), 1515-1533.

Ridolfi F (2021) Amp-TB2: An Updated Model for Calcic Amphibole Thermobarometry. *Minerals* 2021 11:324. <https://doi.org/10.3390/MIN11030324>

Ridolfi F, Renzulli A (2012) Calcic amphiboles in calc-alkaline and alkaline magmas: Thermobarometric and chemometric empirical equations valid up to 1,130°C and 2.2 GPa. *Contributions to Mineralogy and Petrology* 163:877–895. <https://doi.org/10.1007/s00410-011-0704-6>

Ridolfi F, Renzulli A, Puerini M (2010) Stability and chemical equilibrium of amphibole in calc-alkaline magmas: An overview, new thermobarometric formulations and application to subduction-related volcanoes. *Contributions to Mineralogy and Petrology* 160:45–66. <https://doi.org/10.1007/s00410-009-0465-7>

- Risacher F, Fritz B, Hauser A (2011) Origin of components in Chilean thermal waters. *J South Am Earth Sci* 31:153–170. <https://doi.org/10.1016/j.jsames.2010.07.002>
- Rivera G, Morata D, Ramírez C (2015) Evolución vulcanológica y tectónica del área del cordón volcánico Cerro del Azufre-Cerro de Inacaliri y su relación con el sistema geotérmico de Pampa Apacheta, II Región de Antofagasta, Chile. In: *Actas del XIV Congreso Geológico Chileno, La Serena, Chile*. pp 556–559
- Roeder PL, Emslie RF (1970) Olivine-liquid equilibrium. *Contributions to Mineralogy and Petrology* 29:275–289. <https://doi.org/10.1007/BF00371276>
- Roobol M J, Francis P W, RIDLEY W I, RHODES M, WALKER G P L (1974) Physicochemical characters of the Andean volcanic chain between latitudes 21 and 22 South. *Bull. Volcanol.*
- Rutherford MJ, Hill PM (1993) Magma ascent rates from amphibole breakdown: An experimental study applied to the 1980–1986 Mount St. Helens eruptions. *J Geophys Res Solid Earth* 98:19667–19685. <https://doi.org/10.1029/93JB01613>
- Samadi R, Torabi G, Kawabata H, Miller NR (2021) Biotite as a petrogenetic discriminator: Chemical insights from igneous, meta-igneous and meta-sedimentary rocks in Iran. *Lithos* 386–387:106016. <https://doi.org/10.1016/J.LITHOS.2021.106016>
- Samrock F, Grayver A V, Eysteinnsson H, Saar M O (2018). Magnetotelluric image of transcrustal magmatic system beneath the Tulu Moye geothermal prospect in the Ethiopian Rift. *Geophysical Research Letters*, 45(23), 12-847.
- Sauerzapf U, Lattard D, Burchard M, Engelmann R (2008) The titanomagnetite-ilmenite equilibrium: New experimental data and thermo-oxybarometric application to the crystallization of basic to intermediate rocks. *Journal of Petrology* 49:1161–1185. <https://doi.org/10.1093/petrology/egn021>
- Schmidt MW (1992) Amphibole composition in tonalite as a function of pressure: an experimental calibration of the Al-in-hornblende barometer. *Contributions to Mineralogy and Petrology* 110:304–310. <https://doi.org/10.1007/BF00310745>

Schmitt AK, de Silva SL, Trumbull RB, Emmermann R (2001) Magma evolution in the Purico ignimbrite complex, northern Chile: Evidence for zoning of a dacitic magma by injection of rhyolitic melts following mafic recharge. *Contributions to Mineralogy and Petrology* 140:680–700. <https://doi.org/10.1007/s004100000214>

Sellés D, Gardeweg M (2017) Geología del área Ascotán-Cerro Inacaliri, Región de Antofagasta. Servicio Nacional de Geología y Minería, Carta Geológica de Chile, Serie Geología Básica 190:73 p, 1 mapa escala 1:100000 Santiago, Chile. <https://doi.org/10.13140/RG.2.2.30946.84165>

Shea T, Hammer JE (2013) Kinetics of cooling- and decompression-induced crystallization in hydrous mafic-intermediate magmas. *Journal of Volcanology and Geothermal Research* 260:127–145. <https://doi.org/10.1016/j.jvolgeores.2013.04.018>

Sillitoe RH (2010) Porphyry copper systems. *Economic Geology* 105:3–41. <https://doi.org/10.2113/gsecongeo.105.1.3>

Solano JMS, Jackson MD, Sparks RSJ, et al (2012) Melt Segregation in Deep Crustal Hot Zones: a Mechanism for Chemical Differentiation, Crustal Assimilation and the Formation of Evolved Magmas. *Journal of Petrology* 53:1999–2026. <https://doi.org/10.1093/PETROLOGY/EGS041>

Spang A, Baumann TS, Kaus BJP (2021) A Multiphysics Approach to Constrain the Dynamics of the Altiplano-Puna Magmatic System. *J Geophys Res Solid Earth* 126:1–18. <https://doi.org/10.1029/2021JB021725>

Sparks R S J, Folkes C B, Humphreys M C, Barfod D N, Clavero J, Sunagua M C, McNutt S R, Pritchard M E (2008). Uturuncu volcano, Bolivia: Volcanic unrest due to mid-crustal magma intrusion. *American Journal of Science*, 308(6), 727-769.

Stern CR (2004) Active Andean volcanism: Its geologic and tectonic setting. *Revista Geologica de Chile* 31:161–206. <https://doi.org/10.4067/S0716-02082004000200001>

Stern C R, Moreno H, López-Escobar L, Clavero J E, Lara L E, Naranjo J A, Parada M G, Skewes A (2007). Chilean volcanoes In: Moreno T, Gibbons W (eds) *The Geology of Chile*. The Geological Society, pp 147–178

Stormer JC (1983) The effects of recalculation on estimates of temperature and oxygen fugacity from analyses of multicomponent iron-titanium oxides. *American Mineralogist* 68:586–594

Streck MJ (2008) Mineral Textures and Zoning as Evidence for Open System Processes. *Rev Mineral Geochem* 69:595–622. <https://doi.org/10.2138/rmg.2008.69.15>

Sun SS, McDonough WF (1989) Chemical and isotopic systematics of oceanic basalts: Implications for mantle composition and processes. In: Saunders AD, Norry MJ (eds) *Magmatism in the Ocean Basins*. Geological Society, London, Special Publications, pp 313–345

Szymanowski D, Wotzlaw JF, Ellis BS, et al (2017) Protracted near-solidus storage and pre-eruptive rejuvenation of large magma reservoirs. *Nat Geosci* 10:777–782. <https://doi.org/10.1038/ngeo3020>

Tait S, Jaupart C, Vergnolle S (1989) Pressure, gas content and eruption periodicity of a shallow, crystallising magma chamber. *Earth Planet Sci Lett* 92:107–123. [https://doi.org/10.1016/0012-821X\(89\)90025-3](https://doi.org/10.1016/0012-821X(89)90025-3)

Tatsumi Y, Hamilton D L, Nesbitt R W (1986) Chemical characteristics of fluid phase released from a subducted lithosphere and origin of arc magmas: evidence from high-pressure experiments and natural rocks. *Journal of volcanology and geothermal research*, 29(1-4), 293-309.

Taussi M, Godoy B, Piscaglia F, et al (2019) The upper crustal magma plumbing system of the Pleistocene Apacheta-Aguilucho Volcanic Complex area (Altiplano-Puna, northern Chile) as inferred from the erupted lavas and their enclaves. *Journal of Volcanology and Geothermal Research* 373:179–198. <https://doi.org/10.1016/j.jvolgeores.2019.01.021>

Thorpe R S, Francis P W, Harmon R S (1981) Andean andesites and crustal growth. *Philosophical Transactions of the Royal Society of London. Series A, Mathematical and Physical Sciences*, 301(1461), 305-320.

Tibaldi A, Corazzato C, Roviada A (2009). Miocene–Quaternary structural evolution of the Uyuni–Atacama region, Andes of Chile and Bolivia. *Tectonophysics*, 471(1-2), 114-135.

- Tibaldi A, Bonali F L, Corazzato C (2017). Structural control on volcanoes and magma paths from local-to orogen-scale: The central Andes case. *Tectonophysics*, 699, 16-41.
- Tierney CR, Schmitt AK, Lovera OM, de Silva SL (2016) Voluminous plutonism during volcanic quiescence revealed by thermochemical modeling of zircon. *Geology* 44:683–686. <https://doi.org/10.1130/G37968.1>
- Townsend M, Huber C, (2020) A critical magma chamber size for volcanic eruptions. *Geology*, 48(5): 431-435. <https://doi.org/10.1130/G47045.1>
- Trail D, Watson EB, Tailby ND (2011) The oxidation state of Hadean magmas and implications for early Earth's atmosphere. *Nature* 480:79–82. <https://doi.org/10.1038/nature10655>
- Tramontano S, Gualda GAR, Ghiorso MS (2017) Internal triggering of volcanic eruptions: tracking overpressure regimes for giant magma bodies. *Earth Planet Sci Lett* 472:142–151. <https://doi.org/10.1016/J.EPSL.2017.05.014>
- Tsuchiyama A (1985) Dissolution kinetics of plagioclase in the melt of the system diopside-albite-anorthite, and origin of dusty plagioclase in andesites. *Contributions to Mineralogy and Petrology* 89:1–16. <https://doi.org/10.1007/BF01177585>
- Tsuchiyama A (1986) Experimental study of olivine-melt reaction and its petrological implications. *Journal of Volcanology and Geothermal Research* 29:245–264. [https://doi.org/10.1016/0377-0273\(86\)90047-8](https://doi.org/10.1016/0377-0273(86)90047-8)
- Turner JS (1980) A fluid-dynamical model of differentiation and layering in magma chambers. *Nature* 285:213–215. <https://doi.org/10.1038/285213a0>
- Urzua L, Powell T, Cumming WB, Dobson P (2002) Apacheta, a new geothermal prospect in Northern Chile. *Geothermal Resources Council Transactions* 26:65–69
- Urzua L, Powell T, Cumming W B, Dobson P (2002). Apacheta, a new geothermal prospect in northern Chile. Lawrence Berkeley National Lab, Berkeley, California, United States.
- van Orman JA, Crispin KL (2010) Diffusion in Oxides. In: Zhang Y, Cherniak DJ (eds) *Diffusion in Minerals and Melts*. *Reviews in Mineralogy and Geochemistry*, pp 757–826

Venezky DY, Rutherford MJ (1999) Petrology and Fe-Ti oxide reequilibration of the 1991 Mount Unzen mixed magma. *Journal of Volcanology and Geothermal Research* 89:213–230. [https://doi.org/10.1016/S0377-0273\(98\)00133-4](https://doi.org/10.1016/S0377-0273(98)00133-4)

Vidal J, Patrier P, Beaufort D, Maza S, Rivera G, Volpi G, Morata D (2022). Clay Minerals in the Deep Reservoir of the Cerro Pabellón Geothermal System (Northern Chile). *Minerals*, 12(10), 1244.

Vidal J, Patrier P, Beaufort D, Maza S, Rivera G, Volpi G, Morata D (2023). Structural control of the graben fault on hydrothermal alteration in the Cerro Pabellón geothermal system (Andean Cordillera, Northern Chile). *Geothermal Energy*, 11(1), 18.

Walker BA, Klemetti EW, Grunder AL, et al (2013) Crystal reaming during the assembly, maturation, and waning of an eleven-million-year crustal magma cycle: Thermobarometry of the Aucanquilcha Volcanic Cluster. *Contributions to Mineralogy and Petrology* 165:663–682. <https://doi.org/10.1007/s00410-012-0829-2>

Ward KM, Zandt G, Beck SL, et al (2014) Seismic imaging of the magmatic underpinnings beneath the Altiplano-Puna volcanic complex from the joint inversion of surface wave dispersion and receiver functions. *Earth Planet Sci Lett* 404:43–53. <https://doi.org/10.1016/j.epsl.2014.07.022>

Watts R B, de Silva S L, Jimenez de Rios G, Croudace I (1999). Effusive eruption of viscous silicic magma triggered and driven by recharge: a case study of the Cerro Chascon-Runtu Jarita Dome Complex in Southwest Bolivia. *Bulletin of Volcanology*, 61, 241-264.

Wilson G, Wilson TM, Deligne NI, Cole JW (2014) Volcanic hazard impacts to critical infrastructure: A review. *Journal of Volcanology and Geothermal Research* 286:148–182. <https://doi.org/10.1016/j.jvolgeores.2014.08.030>

Wörner G, Mamani M, Blum-Oeste M (2018) Magmatism in the Central Andes. *Elements* 14:237–244. <https://doi.org/10.2138/gselements.14.4.237>

Zhang J, Humphreys MCS, Cooper GF, et al (2017) Magma mush chemistry at subduction zones, revealed by new melt major element inversion from calcic amphiboles. *American Mineralogist* 102:1353–1367. <https://doi.org/10.2138/AM-2017-5928>



Zhang Y, Xu Z, Zhu M, Wang H (2007) Silicate melt properties and volcanic eruptions. *Reviews of Geophysics* 45:.. <https://doi.org/10.1029/2006RG000216>

## Anexo A: Otras publicaciones asociadas al PhD

Journal of Volcanology and Geothermal Research 423 (2022) 107472



Contents lists available at ScienceDirect

Journal of Volcanology and Geothermal Research

journal homepage: [www.elsevier.com/locate/jvolgeores](http://www.elsevier.com/locate/jvolgeores)

## Evolution of the Azufre volcano (northern Chile): Implications for the Cerro Pabellón Geothermal Field as inferred from long lasting eruptive activity



Benigno Godoy<sup>a,\*</sup>, Marco Taussi<sup>b</sup>, Osvaldo González-Maurel<sup>c</sup>, Darío Hübner<sup>a,d</sup>, James Lister<sup>c</sup>, Daniel Sellés<sup>e,1</sup>, Petrus le Roux<sup>c</sup>, Alberto Renzulli<sup>b</sup>, Germain Rivera<sup>f</sup>, Diego Morata<sup>a</sup>

<sup>a</sup> Centro de Excelencia en Geotermia de los Andes (CEGA) y Departamento de Geología, Facultad de Ciencias Físicas y Matemáticas, Universidad de Chile, Plaza Ercilla 803, Santiago, Chile

<sup>b</sup> Dipartimento di Scienze Pure e Applicate, Università degli Studi di Urbino Carlo Bo, Via Ca' Le Suore 2/4, Urbino, Italy

<sup>c</sup> Department of Geological Sciences, University of Cape Town, Rondebosch 7700, South Africa

<sup>d</sup> Programa de Doctorado en Ciencias, Mención Geología, Departamento de Geología, Facultad de Ciencias Físicas y Matemáticas, Universidad de Chile, Plaza Ercilla 803, Santiago, Chile

<sup>e</sup> ALRUM Consultores Ltda, Del Inca 4446, of 701, Las Condes, Chile

<sup>f</sup> Enel Green Power Chile y Puñes Andinos, Av. Presidente Bisco 5335, Piso 14, Las Condes, Santiago, Chile

## ARTICLE INFO

## Article history:

Received 10 June 2021

Received in revised form 7 January 2022

Accepted 10 January 2022

Available online 18 January 2022

## Keywords:

Central Andes

Azufre volcano

Geothermal field

Volcanic evolution

## ABSTRACT

Azufre volcano (21°47'S, 68°15'W) is part of the Pleistocene NW-SE trending Azufre-Inacaliri Volcanic Chain, located in the Chilean Central Volcanic Zone of the Andes, near the currently exploited Cerro Pabellón Geothermal Field. Geochronological data and geomorphological features indicate that Azufre was constructed between ~1300 and ~120 ka through four magmatic Stages (namely Stage I, II, III and IV), with eruptions from different vents that generated the Northern (Stages II and IV) and Southern (Stages I and III) edifices. Whole rock geochemical data indicates that lavas erupted in Stage II (700–500 ka) and Stage IV (300–120 ka) mainly show lower Al<sub>2</sub>O<sub>3</sub>, Na<sub>2</sub>O and Sr concentrations, and higher FeO, MgO and TiO<sub>2</sub> concentrations at similar SiO<sub>2</sub> contents than those of Stage I (1,300–700 ka) and Stage III (500–300 ka). These differences suggest dominant plagioclase and Fe–Mg rich mineral phases (i.e. olivine and orthopyroxene) fractionations in the Northern edifice with respect to the Southern one. This is in agreement with petrographic characters that reveal more olivine and orthopyroxene contents in less evolved (<60 wt% SiO<sub>2</sub>) lavas of the Northern edifice whilst those of the Southern edifice shows higher amphibole content at similar SiO<sub>2</sub> compositions. Finally, mineral chemistry of samples of the Northern edifice was used to establish a preliminary estimation of the physical conditions of the magma below Azufre volcano. Two-pyroxene thermobarometry gave temperature values spanning from 1000 °C up to 1060 °C (±39 °C), and fractionation pressures between 350 and 470 (±370) MPa, whereas amphibole thermobarometry indicated pressures of magma fractionation between 140 and 220 (±115%) MPa, with temperature ranging from 810 °C to 890 °C (±23.5 °C). These thermobarometric conditions are similar to those previously published of the nearby Apacheta-Aguilucho Volcanic Complex (~1050–600 ka) and the young (<150 ka) dacitic domes of Chanka, Chac-Inca and Pabellón, therefore suggesting common petrogenetic systems. Evolution of Azufre volcano fill the time gap of the volcanic activity between the growth of the adjacent Apacheta-Aguilucho Volcanic Complex and the emplacement of the young dacitic domes surrounding the Cerro Pabellón Geothermal Field. This possibly unravels a long lasting (more than 1 Ma) active magmatic system in the northeastern-most sectors of the Azufre-Inacaliri Volcanic Chain and new constraints on the longevity of the heat source regions of the high-enthalpy Cerro Pabellón Geothermal Field, possibly opening new perspectives in the geothermal exploration of this area.

© 2022 Elsevier B.V. All rights reserved.

## 1. Introduction

Understanding the architectural evolution of the magmatic system that feeds a geothermal field is of paramount importance to determine the processes that sustain these systems through time (e.g., Agostini et al., 2006; Lucci et al., 2020; Rosenberg et al., 2020). The Central Andes comprises several geothermal systems, mostly distributed in

\* Corresponding author.

E-mail address: [bgodoy@uchile.cl](mailto:bgodoy@uchile.cl) (B. Godoy).<sup>1</sup> Present address: Teck Resources Chile Ltda, Alonso de Córdova 4580 piso 10, las Condes, Chile



Contents lists available at ScienceDirect

Journal of South American Earth Sciences

journal homepage: [www.elsevier.com/locate/jsames](http://www.elsevier.com/locate/jsames)

## Contrasting sources and conditions of shallow magmatic reservoirs of the Fui Group small eruptive centres associated with the Liquiñe-Ofqui Fault Zone (Chilean Andes)

Francisca Mallea-Lillo <sup>a,b,\*</sup>, Miguel A. Parada <sup>a,b</sup>, Eduardo Morgado <sup>c</sup>, Claudio Contreras <sup>d</sup>, Darío Hübner <sup>a,b</sup>

<sup>a</sup> Departamento de Geología, Facultad de Ciencias Físicas y Matemáticas, Universidad de Chile, 803 Plaza Ercilla, 8370450 Santiago, Chile

<sup>b</sup> Centro de Excelencia en Geotermia de los Andes (CEGA), Universidad de Chile, 803 Plaza Ercilla, 8370450 Santiago, Chile

<sup>c</sup> Escuela de Geología, Universidad Mayor, Manuel Montt 367, Providencia, Chile

<sup>d</sup> School of Earth Sciences, University of Bristol, Wills Memorial Building, Bristol BS8 1RJ, UK

### ARTICLE INFO

#### Keywords:

Fui group  
Pre-eruptive conditions  
Shallow reservoir  
Small eruptive centres  
Southern volcanic zone of the andes

### ABSTRACT

Along the Southern Volcanic Zone of the Andes, the Liquiñe Ofqui Fault Zone controls the occurrence and distribution of small eruptive centres and stratovolcanoes. The Fui Group are clusters of Holocene small eruptive centres within the vicinity of ~5.5 km west of the Liquiñe Ofqui Fault Zone and 8–16 km ENE from the Mocho-Choshuenco Volcanic Complex. Although separated ~2 km from each other, the Fui Norte (north) volcanic products are olivine-rich basalts (49–52 wt% SiO<sub>2</sub>) and enriched in incompatible elements, whilst the Fui Sur (south) materials are basaltic andesites to andesites (55–58 wt% SiO<sub>2</sub>) with less amount of olivine but more plagioclase and clinopyroxene and depleted in incompatible elements. Crystal clots of olivine, plagioclase and clinopyroxene are abundant in all the studied samples. We found two compositional zones of olivine and plagioclase: High-Fo, High-An (Zone 1, Fo<sub>78-89</sub> and An<sub>76-93</sub>) and Low-Fo, Low-An (Zone 2, Fo<sub>60-78</sub> and An<sub>57-73</sub>); only Zone 2 are in equilibrium with the groundmass (representing the melt) compositions. We determined shallow magmatic reservoir conditions (2–8 km and 6–19 km in the Fui Norte and Fui Sur eruptive centres, respectively) for Zone 2 crystallisation using geothermobarometers and thermodynamic modelling by rhyolite-MELTS v.1.0.2 freeware. Additionally, we determined water content dissolved in melt of 1–2.5 wt% and 2–3.8 wt% for Zone 2 compositions of the Fui Norte and Fui Sur small eruptive centres, respectively, and oxidation conditions for Zone 2 of QFM, QFM-1 and NNO. The relatively more primitive compositions of Zone 1 and the common occurrence of crystal clots with compositions of Zone 1 crystals, suggest an earlier stage of crystallisation in a mushy zone of the shallow reservoirs. Although their geographical proximity, we propose that the magmatic origins of Fui Norte and Fui Sur small eruptive centres are independent due to their differing petrographic and geochemical features and the likely genetic relation of Fui Sur magmas with those erupted from Mocho-Choshuenco Volcanic Complex, where the structures associated to the Liquiñe Ofqui Fault Zone aids the magmatic ascent and emplacement of the volcanic products.

### 1. Introduction

Monogenetic volcanoes or Small Eruptive Centres (SECs; see Németh and Kereszturi, 2015; Cañón Tapia, 2016; McGee and Smith, 2016; for recent discussion about this term) are the most common form of volcanism on Earth (Németh and Kereszturi, 2015) and are present in every known tectonic settings (Németh, 2010; Cañón-Tapia, 2016).

This type of volcanism is characterised by a small amount of erupted material (<1 km<sup>3</sup>; Németh and Kereszturi, 2015) produced during a geologically short time frame from days to some years (≤10 years; Németh and Kereszturi, 2015). The compositions of these volcanic products are not restricted to a specific range, nevertheless, they are commonly basaltic (Valentine and Gregg, 2008; Németh, 2010).

Volcanism of SECs was commonly considered as a simple batch of

\* Corresponding author. Centro de Excelencia en Geotermia de los Andes (CEGA), Universidad de Chile, 803 Plaza Ercilla, 8370450 Santiago, Chile.

E-mail addresses: [francisca.mallea@ug.uchile.cl](mailto:francisca.mallea@ug.uchile.cl) (F. Mallea-Lillo), [maparada@cec.uchile.cl](mailto:maparada@cec.uchile.cl) (M.A. Parada), [eduardo.morgado@umayor.cl](mailto:eduardo.morgado@umayor.cl) (E. Morgado), [claudio.contreras@bristol.ac.uk](mailto:claudio.contreras@bristol.ac.uk) (C. Contreras), [dario.hubner@ing.uchile.cl](mailto:dario.hubner@ing.uchile.cl) (D. Hübner).

<https://doi.org/10.1016/j.jsames.2022.103875>

Received 3 April 2022; Received in revised form 2 June 2022; Accepted 3 June 2022

Available online 9 June 2022

0895-9811/© 2022 Elsevier Ltd. All rights reserved.

## Anexo B: Participación en congresos



**XV CONGRESO GEOLÓGICO CHILENO**  
"GEOCIENCIAS HACIA LA COMUNIDAD"  
18 AL 23 DE NOVIEMBRE DE 2016, UNIVERSIDAD DE CONCEPCIÓN,  
CONCEPCIÓN, CHILE



### **VOLC-1: Volcanismo de la Zona Volcánica Andina Central (ZVAC)**

**Geological evolution of the Azufre Volcano: A case of stratovolcano emplaced over the western border of the Altiplano-Puna Magma Body**

Dario Hübner<sup>1,2</sup>, Benigno Godoy<sup>2</sup>, Miguel Ángel Parada<sup>1,2</sup>, Osvaldo González-Maurel<sup>3,4</sup>.

(1) Departamento de Geología, Facultad de Ciencias Físicas y Matemáticas, Universidad de Chile, Santiago, Chile

(2) Departamento de Geología, Facultad de Ciencias Físicas y Matemáticas, Universidad de Chile, Centro de Excelencia en Geotermia de los Andes (CEGA), Santiago, Chile

(3) Departamento de Ciencias Geológicas, Facultad de Ingeniería y Ciencias Geológicas, Universidad Católica del Norte, Antofagasta, Chile

(4) Department of Geological Sciences, Science Faculty, University of Cape Town, Cape Town, South Africa

The Azufre Volcano, located in the Western Cordillera at 21°47'S and 68°14', is a Pleistocene stratovolcano belonging to the Central Volcanic Zone of the Andes. This volcano is emplaced on the western border of the Altiplano-Puna Volcanic Complex, an area dominated by a siliceous volcanism that corresponds to the exogenous manifestation of the Altiplano-Puna Magma Body. The Azufre Volcano is part of a 75 km long NW-SE volcanic chain, which is delimited by the Palpana Volcano to the north and the Inacaliri Graben to the south. Additionally, Cerro Pabellón, the first geothermal power plant of South America, is located 6 km to the SE of Azufre Volcano. The Azufre Volcano is built over a Miocene ignimbrite basement and is composed of four lava units with ages that range from the Middle to Upper Pleistocene. The eruptive products correspond to highly crystalline (~45 vol%) blocky andesite and dacite lavas, that show a high-K calc-alkaline trend. The mineralogy of the lavas corresponds to zoned plagioclase, clinopyroxene, orthopyroxene, hornblende and biotite phenocrysts, plagioclase microlites and small crystals of zircon and apatite as accessory phases. Oval-shaped enclaves are commonly observed; they consist of clinopyroxene and orthopyroxene, which occur as resorbed phenocrysts and forming part of hornblende reaction rims, along with microphenocrysts of plagioclase and hornblende in a cumulate texture. The geology of Azufre Volcano also includes Chanka dacitic and Chac Inca domes, located on the W and E flank of the volcano respectively, glacial deposits on the SW flank and a hydrothermal alteration zone at the central part of the edifice, which shows signs of recent activity. The dacitic domes and the lavas of the last eruption stages (< 150 ky) along with the Cerro Pabellón Dome, located 6 km to SE of the Azufre Volcano, are the most modern extrusive products of the NW-SE volcanic chain. Therefore, this study provides the necessary basic geologic information to assess the role of the studied volcanic system as a heat source of the Cerro Pabellón geothermal system.

# SHALLOW MAGMA MIXING ABOVE THE OCCIDENTAL BOUNDARY OF ALTIPLANO PUNA MAGMA BODY: CONSTRAINING THE GEOTHERMAL HEAT SOURCES THROUGH THE CASE OF AZUFRE VOLCANO

DARÍO HÜBNER<sup>1,2</sup>, MIGUEL ANGEL PARADA<sup>1,2</sup>,  
EDUARDO MORGADO<sup>2,3</sup> AND FRANCISCA MALLEA-  
LILLO<sup>1,2</sup>

<sup>1</sup>University of Chile

<sup>2</sup>Andean Geothermal Center of Excellence, CEGA

<sup>3</sup>University of Leeds

Presenting Author: [dariosalvadorhubner@gmail.com](mailto:dariosalvadorhubner@gmail.com)

In the context of researching the heat sources that feed the Cerro Pabellón geothermal system (Northern Chile), we study the origin of the youngest andesitic (61–63 SiO<sub>2</sub> wt%) lava flow from the Azufre volcano (21°47'7"S; 68°14'23"W). This stratovolcano is emplaced over a 70 km long NW-SE alignment above the occidental boundary of Altiplano Puna Magma Body (which is the largest active magma body on Earth) and located 10 km NW from the first geothermal power plant of South America. The significance of this volcano relies on the younger volcanic units developed around it (<150 ky), which correspond to dacitic domes (Chanca, Chac Inca and Cerro Pabellón; see figure 1) and our studied holocrystalline lava flow. This flow comprises aphanitic andesite enclaves (58–60 SiO<sub>2</sub> wt%) and phenocrysts of plagioclase, amphibole, biotite and orthopyroxene (15, 4, 4, 2 in vol%, respectively) together with scarce phenocrysts of clinopyroxene, quartz and olivine (~1 in vol% each one). The groundmass of lava and enclaves is made up of the same mineral chemistry, displaying amphibole microphenocrysts and microlites of plagioclase, pyroxenes and Fe-Ti oxides.

We use different geobarometric and geothermometric techniques in phenocrysts and microlites along with crystallization simulations performed in MELTS freeware to study the magmatic evolution and identify a zoned crystal-mush magma reservoir emplaced at shallow crustal levels (~6,4 km of depth). In this way, based on textural features, mineral chemistry and thermometry results, an open system with two zones (Zone A and B) was identified for the magmatic system that fed the youngest lava flow of the Azufre volcano. Zone A (at high temperatures in the range of 916–1097°C) would represent a deep recharge zone where primitive melt (of composition similar to enclaves) intruded the bottom of the Zone B, which corresponds to a more evolved siliceous crystal-mush reservoir (at lower temperatures between 712–799°C). Thereby, during this incomplete magma mixing was made the magma chamber that triggered the last eruption stage of the Azufre volcano.

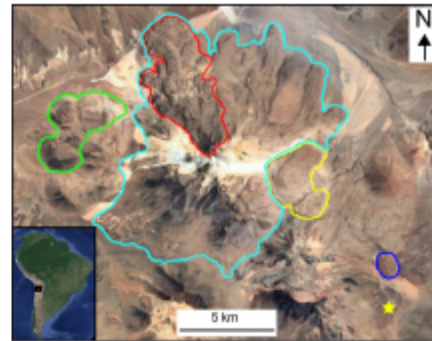


Figure 1. Satellite image highlighting the locations of the geothermal power plant (yellow star), the Azufre volcano (cyan line), the holocrystalline lava flow studied (red line) and the others younger volcanic units: Cerro Pabellón dome (blue line), Chac Inca dome (yellow line) and Chanca dome (green line).



## La historia de una lava desde su reservorio somero zonado hasta la superficie: El caso del volcán Azufre en el contexto del Altiplano Puna Magma Body (Norte de Chile)

### Presentaciones Orales

AT 1: INVESTIGACIÓN BÁSICA EN GEOCIENCIAS , AT1-8: Procesos magmáticos durante la evolución volcánica en Chile: desde el manto hacia la superficie / Magmatic processes during volcanic evolution in Chile: from mantle to surface.

**Darío Hübner** <sup>1, 2,</sup> Miguel-Ángel Parada <sup>1, 2,</sup> Eduardo Morgado <sup>2, 3,</sup> Francisca Mallea-Lillo <sup>1, 2, 4,</sup>

(1) Universidad de Chile, Departamento de Geología, Chile.

(2) Centro de Excelencia en Geotermia de Los Andes, CEGA, Chile.

(3) Universidad Mayor, Escuela de Geología, Chile.

(4) University of Adelaide, Earth Sciences, School of Physical Sciences, Adelaide, Australia.

dariosalvadorhubner@gmail.com

El volcán Azufre (21°47'S; 68°14'W) se encuentra emplazado sobre un lineamiento volcánico NO-SE de 70 km de largo por sobre el borde occidental del Altiplano Puna Magma Body, el cual es el mayor cuerpo magmático activo de la Tierra (~500.000 km<sup>3</sup> de volumen; Ward et al. 2014). El depósito de lava más joven del volcán Azufre fue seleccionado para un estudio detallado debido a la importante información petrológica que se podría obtener al entender las condiciones de su reservorio como una potencial fuente de calor del sistema geotermal de Cerro Pabellón que se encuentra a menos 5km hacia el SE. El depósito corresponde a una lava tipo bloque de composición andesita-dacita (61 - 63 SiO<sub>2</sub> wt%) que pertenece a las unidades más jóvenes (<331 ka) de esta parte de los Andes Centrales. Su mineralogía comprende fenocristales de plagioclasa, anfíbol (Grupo 1), biotita y ortopiroxeno (15, 4, 4, 2 vol%, respectivamente) junto con escasos fenocristales de clinopiroxeno, cuarzo, olivino y óxidos de Fe-Ti (~1 vol% cada uno). El depósito de lava incluye también la presencia de enclaves afaníticos de composición andesítica (58 - 60 SiO<sub>2</sub> wt%), cuyas masas fundamentales presentan la misma mineralogía y química mineral de la masa fundamental de las muestras de lava, consistiendo en microfenocristales de anfíbol (Grupo 2) y microlitos de plagioclasa, piroxenos y óxidos de Fe-Ti. Abundantes